First-Principles Study of Electronic Structure, Transport, and Chiral Magnetism of Emergent Quantum Materials.

by

Dimple Rani

PHYS11202104021

National Institute of Science Education and Research, Bhubaneswar

A thesis submitted to the

Board of Studies in Physical Sciences

In partial fulfillment of requirements

for the Degree of

DOCTOR OF PHILOSOPHY

of

HOMI BHABHA NATIONAL INSTITUTE

May, 2026

Homi Bhabha National Institute

Recommendations of the Viva Voce Committee

As members of the Viva Voce Committee, we certify that we have read the dissertation prepared by **Dimple Rani** entitled **"First-Principles Study of Electronic Structure, Transport, and Chiral Magnetism of Emergent Quantum Materials"** and recommend that it may be accepted as fulfilling the thesis requirement for the award of Degree of Doctor of Philosophy.

S. No.	Doctoral Committee	Name	Signature	Date	In-Person /Online
1.	Chairman	Dr. Kartikeswar Senapati		02/09/26	In person
2.	Guide/Convener	Dr. Prasanjit Samal		2-9-26	In person
3.	Co-Guide	Prof. Manish Kumar Niranjan		02/09/26	In person
4.	Examiner	Prof. Manish Jain		2/9/26	In person
5.	Member - 1	Dr. A.V. Anil Kumar		2/9/26	In person
6.	Member - 2	Dr. Joydeep Bhattacharjee		2/9/26	In person
7.	Member - 3	Dr. Anuj Goyal		02/09/26	Online
8.	Technology Advisor (if any)				

Final approval and acceptance of this thesis is contingent upon the candidate's submission of the final copies of the thesis to HBNI.

I hereby certify that I have read this thesis prepared under my direction and recommend that it may be accepted as fulfilling the thesis requirement.

Date : September 02, 2026

Place : NISER Bhubaneswar

Signature

Co-guide

Signature

Guide

STATEMENT BY AUTHOR

This dissertation has been submitted in partial fulfillment of requirements for an advanced degree at Homi Bhabha National Institute (HBNI) and is deposited in the Library to be made available to borrowers under rules of the HBNI.

Brief quotations from this dissertation are allowable without special permission, provided that accurate acknowledgement of source is made. Requests for permission for extended quotation from or reproduction of this manuscript in whole or in part may be granted by the Competent Authority of HBNI when in his or her judgment the proposed use of the material is in the interests of scholarship. In all other instances, however, permission must be obtained from the author.

Date : September 02, 2026

Place : NISER Bhubaneswar

(Dimple Rani)

DECLARATION

I hereby declare that I am the sole author of this thesis in partial fulfillment of the requirements for a postgraduate degree from National Institute of Science Education and Research (NISER). I authorize NISER to lend this thesis to other institutions or individuals for the purpose of scholarly research.

Date : September 02, 2026

Place : NISER Bhubaneswar

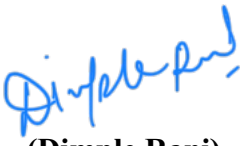

(Dimple Rani)

CERTIFICATION ON ACADEMIC INTEGRITY

Undertaking by the Student:

1. I, **Dimple Rani**, HBNI Enrolment No. **PHYS11202104021**, hereby undertake that the thesis, titled **"First-Principles Study of Electronic Structure, Transport, and Chiral Magnetism of Emergent Quantum Materials"**, is prepared by me and is the original work undertaken by me.

2. I also hereby undertake that this document has been duly checked through a plagiarism detection tool and the document is found to be plagiarism-free as per the guidelines of the Institute/UGC.

3. I am aware and undertake that if plagiarism is detected in my thesis at any stage in the future, suitable penalty will be imposed as applicable as per the guidelines of the Institute/UGC.

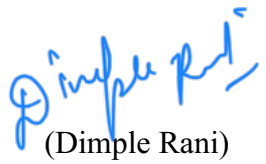

(Dimple Rani)

Endorsed by the Thesis Supervisor:

I certify that the thesis written by the Researcher is plagiarism-free as mentioned above by the student.

Signature of the Thesis Supervisor with date

Name : Dr. Prasanjit Samal

Designation : Associate Professor

Department/Centre : School of Physical Sciences

Name of the CI/OCC : National Institute of Science Education and Research

Academic Contributions

Publications within the thesis

1. "First-principle investigation of structural, electronic, and phase stabilities in chalcopyrite semiconductors: insights from Meta-GGA functionals", **Dimple Rani**, Subrata Jana, Manish K. Niranjan, and Prasanjit Samal, Journal of Physics: Condensed Matter, 2024, 36, 165502.

2. "Thermoelectric Characteristics of Silver-Based Chalcopyrite Semiconductors: An Ab Initio Study Based on the Nonempirical Range-Separated Dielectric-Dependent Hybrid", **Dimple Rani**, Subrata Jana, Manish K. Niranjan, and Prasanjit Samal, The Journal of Physical Chemistry C, 2025, 129, 3784–3797.

3. "Strain- and correlation-tuned magnetic anisotropy and Dzyaloshinskii-Moriya interaction in two-dimensional $FeTe_2$", **Dimple Rani**, B. R. K. Nanda, and Prasanjit Samal, Physical Review B, 2025, 112, 174401.

4. "Activating Dzyaloshinskii–Moriya Interactions in 2D Ti_2Si through Selective Heavy-Atom Incorporation for Chiral Spintronic Nanodevices", **Dimple Rani**, Gayatri Panda, Subrata Jana, and Prasanjit Samal, ACS Applied Nano Materials, 2026.

5. "Engineering Skyrmions in 2D $FeTe_2$/Pt Heterostructures through Interfacial Spin–Orbit Coupling", **Dimple Rani**, B. R. K. Nanda, and Prasanjit Samal, To be submitted.

Publications outside the thesis

1. "Accurate and efficient prediction of the band gaps and optical spectra of chalcopyrite semiconductors from a nonempirical range-separated dielectric-dependent hybrid: Comparison with many-body perturbation theory", Arghya Ghosh, Subrata Jana, **Dimple Rani**, Manoar Hossain, Manish K. Niranjan, and Prasanjit Samal, Physical Review B, 2024, 109, 045133.

2. “Nonempirical dielectric dependent hybrid as an accurate starting point for the single shot G_0W_0 calculation of chalcopyrite semiconductors”, Subrata Jana, Arghya Ghosh, Abhishek Bhattacharjee, **Dimple Rani**, Manoar Hossain, and Prasanjit Samal, The Journal of Chemical Physics, 2025, 162, 064104.

3. “Advancing excited-state properties of two-dimensional materials using a dielectric-dependent hybrid functional”, Arghya Ghosh, Subrata Jana, Manoar Hossain, **Dimple Rani**, Szymon Smiga, and Prasanjit Samal, Physical Review B, 2025, 112, 045128.

4. “Accurate surface and interfacial properties from a nonempirical range-separated dielectric-dependent hybrid functional”, Arghya Ghosh, Subrata Jana, **Dimple Rani**, Szymon Smiga, Manish K. Niranjan, and Prasanjit Samal, Physical Review B, 2026, 113, 085122.

5. ”Symmetry-Engineered Nonlinear Hall Response and Optical Response in Strained Monolayer Janus AsTeBr”, **Dimple Rani**, Ritesh Ranjan Badhai, Gayatri Panda, Subrata Jana and Prasanjit Samal, (Under Review).

Conference Presentations and Participation

1. Joint ICTP MARVEL College: Materials simulations in the age of AI (2026), ICTP, Italy (Poster Presentation).

2. 2026 School on Electron-Phonon Physics and Many-body Perturbation Theory (2026), ICTP, Italy (Poster Presentation).

3. American Physical Society (APS) Global Physics March Meeting (2026), Colorado Convention Center, Denver, USA (Oral Presentation).

4. 36th Annual General Meeting of the Materials Research Society of India (MRSI) and 7th Indian Materials Conclave on Emerging Materials (2025), NISER Bhubaneswar, India (Poster Presentation).

5. Psi-k Conference on Electronic Structure Calculations of Materials (2025), École Polytechnique Fédérale de Lausanne (EPFL), Lausanne, Switzerland (Poster Presentation).

6. APALi Psi-k nternational Conference on Density Functional Theory and Applications (2025), Indian Institute of Science Education and Research (IISER) Pune, India (Poster Presentation).

7. Evolution of Electronic Structure Theory and Experimental Realization (EESTER 2025), Indian Institute of Technology (IIT) Madras, India (Poster Presentation).

8. 20th International Conference on Density Functional Theory and its Applications (DFT-2024), ParisTech Chemistry, PSL University, Paris, France (Poster Presentation).

9. Annual Conference on QUANTUM CONDENSED MATTER (QMAT) Conference (2023), NISER Bhubaneswar, India (Poster Presentation).

10. Namma Psi-k Conference on Electronic Structure and Materials Modeling (2023), Indian Institute of Science (IISc) Bangalore, India (Poster Presentation).

11. Physics of Quantum Matter School (PQMS) (2023), NISER Bhubaneswar, India (Attended).

12. APCTP-IACS-SNBNCBS Workshop on Computational Methods for Emergent Quantum Matter: From Theoretical Concepts to Experimental Realization, S.N. Bose National Centre for Basic Sciences (SNBNCBS) Workshop (2022), Kolkata, India (Attended).

Date : September 02, 2026

Place : NISER Bhubaneswar

(Dimple Rani)

DEDICATED TO

To the journey itself, for all it asked, all it taught,
and all it quietly left behind.

ACKNOWLEDGMENTS

I would like to express my sincere gratitude to my Ph.D. supervisor, Prof. Prasanjit Samal, for his constant encouragement and cheerful support throughout my doctoral journey. More than a supervisor, he has been a mentor and a friend whose trust, patience, and positive attitude have always motivated me during both the smooth and challenging phases of my research.

I am deeply grateful to my co-guide, Prof. Manish Kumar Niranjan, for his continuous guidance, insightful discussions, and willingness to help whenever I encountered difficulties in my research work. His suggestions and support have greatly contributed to this thesis.

I sincerely thank Prof. B. R. K. Nanda for hosting me at IIT Madras and for the valuable collaboration during my research visit. I also cherish the wonderful friendships I formed there, especially with Kaushik and Ayushmin, whose support and companionship made my time at IIT Madras truly memorable. I am thankful to my doctoral committee members, Prof. Kartikeswar Senapati, Prof. A. V. Anil Kumar, Prof. Joydeep Bhattacharjee, and Prof. Anuj Goyal, for their valuable suggestions, constructive criticism, and insightful comments during my presentations.

I gratefully acknowledge my seniors, Dr. Bikash Patra, Dr. Abhilash Patra, and Dr. Ashish Kumar, for their constant support and readiness to help whenever needed. Special thanks are also due to Dr. Subrata Jana for his continuous motivation, support, and constant push throughout my Ph.D. journey.

I am especially grateful to Parashar Chatterjee, for his unwavering support, encouragement, and cheerful presence throughout these years. His companionship made this journey much more meaningful and enjoyable. I would also like to thank my lab juniors, Jeet, Gayatri, and Ritesh, for creating a friendly and supportive environment in the lab.

Most importantly, I would like to express my deepest gratitude to my family for their unconditional love and sacrifices. I am especially indebted to my mother, Seema Jindal, whose constant hard work, strength, and unwavering support made it possible for me to reach this stage of my life. Her sacrifices and encouragement have been the foundation of everything I have achieved.

Finally, I gratefully acknowledge the support and facilities provided by NISER Bhubaneswar

and all the funding agencies that supported this research work.

Date : September 02, 2026

Place : NISER Bhubaneswar

(Dimple Rani)

ABSTRACT

This thesis investigates electronic structure, transport properties, and chiral magnetism in quantum materials using first-principles methods. In bulk semiconductor systems, the electronic structure and phase stability of Cu- and Ag-based chalcopyrites are studied using advanced exchange-correlation functionals within density functional theory (DFT). The rMGGAC meta-GGA functional yields band gaps in close agreement with experiment, while r^{2}SCAN provides reliable thermodynamic phase stability, together establishing an accurate computational framework for chalcopyrite materials. Their thermoelectric performance is evaluated using the dielectric-dependent hybrid (DDH) functional combined with Boltzmann transport theory, showing that band dispersion, effective mass, and carrier scattering collectively govern the Seebeck coefficient and power factor. Among the systems studied, the quaternary compound Ag_2ZnGeS_4 achieves the highest figure of merit $ZT = 2.57$ at 800 K, identifying Ag-based quaternary chalcopyrites as promising candidates for high-temperature thermoelectric applications. In two-dimensional systems, reduced dimensionality, inversion symmetry breaking, and spin–orbit coupling (SOC) strongly influence magnetic behavior. In the non-centrosymmetric H-phase $FeTe_2$ monolayer, biaxial strain and electronic correlations enable continuous tuning of the magnetic anisotropy energy (MAE) and Dzyaloshinskii-Moriya interaction (DMI), with the micromagnetic DMI constant reaching 3.06 mJ/m^2. In T-$FeTe_2$/Pt van der Waals heterostructures, interfacial SOC from the heavy-metal substrate activates a large DMI of 1.33 meV, and micromagnetic simulations confirm the stabilization of Néel-type skyrmions under an applied magnetic field. In the centrosymmetric Ti_2Si monolayer, Co and Pt co-doping simultaneously breaks inversion symmetry and enhances SOC, generating finite DMI and enabling chiral spin textures in an otherwise magnetically trivial system. These results establish a direct link between electronic structure and emergent magnetic phenomena, providing a predictive pathway for designing quantum materials with tunable transport and spintronic functionalities across different dimensional regimes.

Contents

SUMMARY

This thesis presents a comprehensive first-principles investigation of electronic structure, transport properties, and chiral magnetism in emergent quantum materials, with a particular emphasis on the interplay between symmetry, dimensionality, and spin–orbit coupling (SOC). The central objective is to develop a unified understanding of how electronic structure governs both conventional properties in bulk semiconductors and emergent magnetic phenomena in low-dimensional systems.

The first part of the thesis focuses on bulk semiconductor materials, where electronic structure provides a well-established framework for understanding transport and energy-related properties. Using density functional theory (DFT) along with advanced exchange-correlation functionals, the electronic structure and phase stability of Cu- and Ag-based chalcopyrite semiconductors are systematically examined. Particular attention is given to accurately describing band gaps, band dispersion, and thermodynamic stability. Building on this, the thermoelectric properties of ternary and quaternary chalcopyrite systems are analyzed, with emphasis on the role of band structure, density of states, and carrier transport in determining the Seebeck coefficient, electrical conductivity, and overall efficiency. This part of the work highlights the importance of electronic structure engineering in optimizing materials for energy conversion applications.

The second part of the thesis addresses two-dimensional (2D) materials, where reduced dimensionality fundamentally alters symmetry, electronic screening, and magnetic interactions. In these systems, inversion symmetry breaking and strong SOC play a decisive role in shaping electronic and magnetic behavior. The study examines noncollinear magnetism in 2D monolayers and explores how external factors such as strain, interfacial effects, and chemical modification can be used to tailor magnetic properties. Special emphasis is placed on transition metal dichalcogenides (TMDCs) and transition metal silicides (TMS), where different structural phases exhibit distinct symmetry characteristics, providing a natural platform for investigating symmetry-driven phenomena. To obtain microscopic insight into magnetic interactions, the electronic structure from first-principles calculations is further mapped onto Wannier-based tight-binding Hamiltonians. This approach enables an orbital-resolved description of exchange interactions and provides a direct connection

between electronic structure and magnetic anisotropy as well as antisymmetric exchange interactions. A key focus of this work is the Dzyaloshinskii–Moriya interaction (DMI), which arises from the combined effect of broken inversion symmetry and SOC, and plays a central role in stabilizing chiral magnetic textures. The thesis investigates the microscopic origin and tunability of DMI in a range of systems, including pristine 2D materials, van der Waals heterostructures, and chemically modified compounds. In particular, heterostructures involving heavy-metal substrates are considered as a route to enhance SOC and induce interfacial DMI, while chemical doping is explored as a complementary strategy for symmetry breaking and interaction tuning. These studies provide a framework for understanding the emergence and control of topological spin textures such as skyrmions.

Overall, this thesis establishes a coherent connection between electronic structure, transport properties, and chiral magnetism across different classes of materials. By combining first-principles calculations with atomistic and micromagnetic modeling approaches, the work contributes to the fundamental understanding and rational design of materials for next-generation energy and spintronic applications.

List of Figures

List of Tables

Chapter 1

Introduction

1.1 Emergent Quantum Materials

The twentieth century witnessed remarkable progress in understanding the electronic properties of solids through the framework of band theory and Fermi liquid theory. Within this paradigm, electrons in a crystal are treated as weakly interacting quasiparticles moving in a periodic potential, and materials are classified as metals, semiconductors, or insulators depending on the position of the Fermi level relative to the band gap [4, 5]. This framework successfully accounts for the electrical, optical, and thermal properties of a vast range of conventional materials, from simple metals such as copper and aluminum to technologically important semiconductors such as silicon and germanium, particularly in their bulk form.

However, a growing class of materials has been identified whose properties lie fundamentally beyond the reach of this conventional picture. These are the so-called *emergent quantum materials*, systems in which quantum mechanical effects, acting collectively on a macroscopic number of electrons, give rise to entirely new states of matter and physical phenomena that have no analogue in the physics of individual atoms or weakly correlated electron gases [6, 7]. The defining feature of emergent quantum materials is that their most striking properties are not encoded in the individual constituents but arise from the cooperative interplay of charge, spin, orbital, and lattice degrees of freedom. Even small changes in external parameters such as temperature, pressure, chemical composition, dimensional confinement, or applied fields can trigger dramatic phase transitions and the emergence of qualitatively new behaviors.

The landscape of emergent quantum materials is extraordinarily broad and encompasses several distinct classes. *Strongly correlated electron systems*, including transition metal oxides such as V_2O_3 and NiO, heavy fermion compounds such as $CeCu_6$ and URu_2Si_2, and Mott insulators such as La_2CuO_4, are characterized by large on-site Coulomb repulsion between electrons occupying narrow d or f bands, which drives them far from the weakly interacting limit and can produce metal–insulator transitions, colossal magnetoresistance, and unconventional superconductivity [8, 9]. *Topological materials*, including topological insulators such as Bi_2Se_3 and Bi_2Te_3, and Weyl and Dirac semimetals such as TaAs and Cd_3As_2, are characterized by non-trivial topology of their electronic band structures, which gives rise to protected surface states and unusual transport responses [10, 11]. *Two-dimensional van der Waals materials*, including graphene and transition metal dichalcogenides (TMDCs) such as MoS_2 and WS_2, exhibit a unique combination of reduced dimensionality, tunable electronic structure, and strong many-body effects when assembled into heterostructures [12, 13]. *Magnetically ordered and multifunctional materials*, including multiferroics and non-collinear antiferromagnets such as Mn_3Sn, represent another important class in which spin, charge, and lattice degrees of freedom are strongly coupled, leading to complex magnetic and transport behavior [14].

A particularly important distinction within this broad class of quantum materials lies between bulk systems and low-dimensional systems. In bulk materials, electronic properties are governed by three-dimensional band dispersion and screening effects, which often stabilize conventional phases, although strong correlations can still drive complex electronic and magnetic behavior. Representative examples include conventional semiconductors such as Si and GaAs [15], as well as correlated oxides such as $SrVO_3$ and La_2CuO_4, where electronic interactions lead to rich phase diagrams [8]. In contrast, low-dimensional systems, especially two-dimensional materials, exhibit enhanced quantum confinement, reduced coordination, and stronger sensitivity to symmetry breaking. These effects lead to pronounced

modifications in electronic structure and interactions, often resulting in phenomena that are either weak or entirely absent in bulk counterparts. Notable examples include graphene, with its Dirac-like electronic dispersion [16], and TMDCs such as MoS_2 and WSe_2, which exhibit layer-dependent band gaps and strong spin–orbit coupling effects [17, 18].

What unites these diverse classes of materials is a set of common physical ingredients: quantum fluctuations, strong electron correlations, reduced dimensionality, and symmetry breaking. It is the interplay of these factors that gives rise to emergent phenomena and makes quantum materials a rich platform for exploring new physics and functionalities.

1.2 Bulk Semiconductors

Semiconductors constitute a fundamental class of materials that underpin modern electronic, optoelectronic, and energy technologies. Their defining feature is the presence of a finite band gap separating the valence and conduction bands, which enables controlled manipulation of charge carriers through doping, temperature, and external fields. Prototypical semiconductors such as silicon (Si) and gallium arsenide (GaAs) have been extensively studied and widely used in electronic devices due to their well-characterized electronic structures and favorable transport properties [15]. In addition, wide-band-gap semiconductors such as gallium nitride (GaN) and silicon carbide (SiC) play a crucial role in high-power and high-frequency applications owing to their superior thermal stability and breakdown characteristics [19, 20]. Understanding the electronic structure of semiconductors is essential for predicting and optimizing their physical properties. The relationship between electronic structure and material functionality forms the foundation for the design of next-generation semiconductor devices.

1.2.1 Electronic Structure and Its Role in Material Properties

The electronic structure of a material governs its fundamental properties, including electrical conductivity, optical response, and carrier dynamics. In semiconductors, key quantities such as the band structure, density of states (DOS), and band gap determine the behavior of charge carriers and their interaction with external perturbations [21]. The band structure describes the dispersion of electronic states in momentum space and determines whether a material behaves as a metal, semiconductor, or insulator. The density of states characterizes the distribution of available electronic states and directly influences transport and thermodynamic properties. The curvature of bands near the band edges defines the effective mass of charge carriers, which strongly affects carrier mobility and conductivity [22]. The nature of the band gap (direct or indirect) is crucial for optoelectronic applications. Direct band gap materials such as GaAs and GaN enable efficient light emission and absorption, whereas indirect band gap materials such as Si are less efficient for radiative processes but remain central to modern electronics [15]. These distinctions highlight how electronic structure directly dictates material functionality. These features are schematically illustrated in Fig. 1.1(a,b), showing the band structure and density of states near the Fermi level.

Accurate determination of electronic structure relies on a combination of experimental and theoretical approaches. Experimental techniques such as angle-resolved photoemission spectroscopy (ARPES) and optical spectroscopy provide direct insight into band dispersion and carrier dynamics [23, 24]. Complementarily, first-principles methods based on density functional theory (DFT), along with beyond-DFT approaches such as hybrid functionals and the GW approximation, enable predictive modeling of band gaps, effective masses, and electronic properties across a wide range of materials [25, 26, 27, 28].

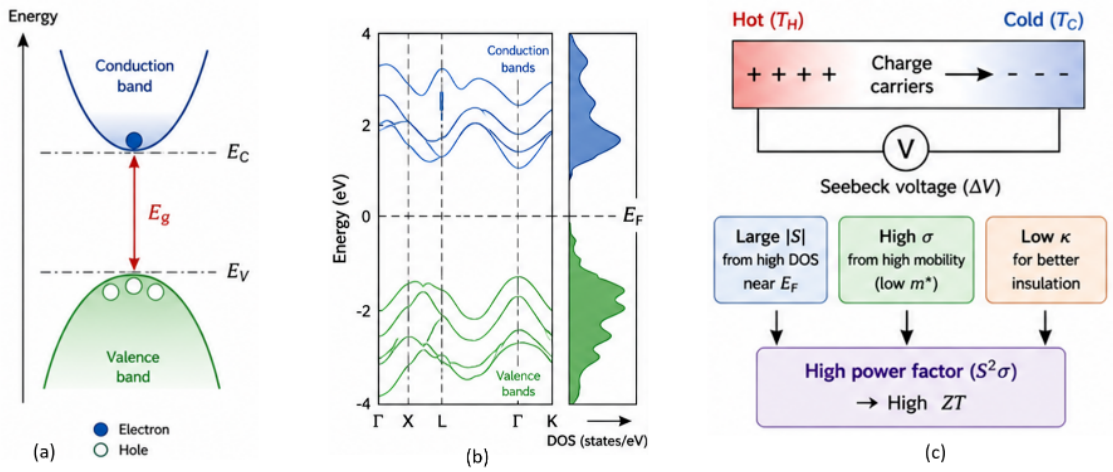

Figure 1.1: (a) Schematic representation of the electronic band structure of a semiconductor showing the valence band, conduction band, and band gap (E_g). (b) Representative band structure and DOS, illustrating the role of electronic structure near the Fermi level (E_F). (c) Thermoelectric transport based on the Seebeck effect and key parameters governing performance.

1.2.2 Electronic Structure in Energy Applications

The electronic structure of semiconductors critically determines their performance in energy conversion and storage applications. In photovoltaic devices, the band gap is the primary descriptor of solar energy harvesting efficiency. Si, with an indirect band gap of 1.1 eV, dominates commercial solar cells due to its near-optimal band gap and earth abundance [15]. GaAs, with a direct band gap of 1.43 eV, achieves higher efficiencies and is widely used in high-performance concentrator solar cells [29]. Emerging absorber materials such as $MAPbI_3$ perovskites, with tunable band gaps in the range of approximately 1.5–1.7 eV, have demonstrated rapid improvements in power conversion efficiency due to their favorable electronic structure and strong optical absorption [29, 30]. In thermoelectric energy harvesting, efficiency is quantified by the dimensionless figure of merit ZT, defined as

$$ZT = \frac{S^2 \sigma T}{\kappa}, \tag{1.1}$$

where S is the Seebeck coefficient, σ is the electrical conductivity, κ is the total thermal conductivity, and T is the absolute temperature [31]. The power factor ($S^2\sigma$) is strongly influenced by the electronic structure, particularly the band dispersion and density of states near the Fermi level. The thermoelectric transport mechanism and the dependence of performance on these parameters are schematically illustrated in Fig. 1.1(c).

Bismuth telluride (Bi_2Te_3), with a narrow band gap of approximately 0.15 eV, remains the benchmark thermoelectric material near room temperature due to its high density of states near the Fermi level [32]. PbTe, with a band gap of 0.32 eV, is widely used for mid-temperature thermoelectric applications, where band convergence engineering in PbTe–SrTe alloys significantly enhances ZT [33]. More recently, SnSe has demonstrated exceptionally high thermoelectric efficiency due to its highly anisotropic electronic structure and ultralow lattice thermal conductivity [34]. In addition, complex semiconductors such as chalcopyrites (e.g., $CuInSe_2$, $AgGaTe_2$) and oxide materials such as $SrTiO_3$ have emerged as promising candidates due to their tunable electronic properties and thermal stability [35]. For photocatalytic applications, the positions of the valence and conduction band edges relative to redox potentials are critical. TiO_2, with a band gap of 3.0–3.2 eV, is widely studied but limited to ultraviolet absorption [36]. In contrast, $BiVO_4$, with a band gap of approximately 2.4 eV, enables visible-light-driven water oxidation due to favorable band edge alignment [37].

Despite significant progress in both experimental characterization and first-principles modeling, challenges remain in achieving quantitative accuracy for complex materials, particularly those with strong electron correlations and anisotropic electronic structures. Addressing these challenges is essential for the predictive design of advanced functional materials. Furthermore, reducing dimensionality introduces additional degrees of freedom and enhanced quantum effects, enabling emergent phenomena beyond those observed in bulk systems. In two-dimensional systems, symmetry, screening, and electronic confinement

are fundamentally altered compared to their bulk counterparts. In particular, the absence of inversion symmetry and the enhanced role of spin–orbit coupling (SOC) give rise to phenomena that are weak or absent in bulk materials [38].

1.3 Engineering Two-Dimensional Materials

A defining advantage of two-dimensional (2D) materials lies in the ability to design systems with tailored properties through controlled structural modifications. Unlike bulk materials, where bonding constraints limit structural flexibility, 2D systems are typically held together by weak van der Waals (vdW) interactions. This enables the realization of a wide range of artificial structures and has established the concept of "materials by design" as a central paradigm in low-dimensional systems [13].

One of the most widely explored approaches is the vertical stacking of different monolayers to form vdW heterostructures. Owing to the weak interlayer coupling, materials with different lattice constants and electronic properties can be combined without strict lattice matching requirements. This allows precise control over band alignment, charge transfer, and interlayer coupling, leading to emergent electronic and optical properties not present in the individual layers [12]. Introducing a relative twist angle between adjacent layers further enriches this design space by generating moiré superlattices. These structures produce long-range periodic modulations that can strongly modify the electronic band structure, often resulting in flat bands and enhanced electron correlations. Such effects have been demonstrated in twisted bilayer graphene, where correlated insulating states and superconductivity emerge [39].

In addition to vertical stacking, lateral heterostructures formed by covalently bonding different materials within the same plane provide an alternative route to engineering 2D systems. These structures enable direct electronic coupling across interfaces, offering fine

control over charge transport and interface-driven phenomena, with significant potential for nanoelectronic and optoelectronic applications [40]. Beyond structural design, external tuning parameters such as strain, electric fields, and chemical doping further expand the range of achievable properties. The combination of these approaches enables continuous control over electronic, optical, and magnetic behavior, making 2D materials a versatile platform for exploring emergent quantum phenomena [41].

1.3.1 Symmetry Breaking, Spin-Orbit Coupling, and Magnetism in 2D Materials

A defining characteristic of 2D materials is their strong sensitivity to symmetry breaking and reduced dimensionality, both of which fundamentally influence their electronic and magnetic properties. In bulk crystals, inversion symmetry is often preserved due to three-dimensional periodicity, whereas in 2D systems it is naturally broken or can be readily modified by substrates, interfaces, or external perturbations. This is particularly evident in transition metal dichalcogenides (TMDCs), where the symmetry depends sensitively on the crystal phase. This is illustrated in Fig. 1.2(a), where the structural differences between H- and T-phase TMDC monolayers and their corresponding symmetry properties are shown. For H-phase TMDCs such as MoS_2 and WSe_2 intrinsically lack inversion symmetry, leading to valley-dependent spin splitting. In contrast, T-phase TMDCs generally preserve inversion symmetry in their pristine form, resulting in spin-degenerate electronic states unless symmetry is externally broken [42]. Similarly, when 2D materials are placed on heavy substrates, such as graphene on Au or W [38], interfacial symmetry breaking induces spin splitting through proximity effects as shown in Fig 1.2 (b).

SOC, particularly strong in materials containing heavy elements such as W, Pt, or Bi, plays a central role in these systems. In the presence of broken inversion symmetry, SOC lifts spin degeneracy and generates momentum-dependent spin textures, commonly de-

scribed by Rashba-type splitting, as observed in Bi/Ag surface alloys and semiconductor heterostructures [43]. Beyond modifying electronic structure, the interplay of reduced dimensionality and SOC has profound consequences for magnetism. In strictly 2D isotropic systems, long-range magnetic order is suppressed at finite temperature, as described by the Mermin-Wagner theorem [44]. However, magnetic anisotropy primarily arising from SOC can stabilize long-range magnetic order even in atomically thin systems [45]. Recent studies have confirmed intrinsic magnetism in materials such as CrI_3, $Cr_2Ge_2Te_6$, and Fe_3GeTe_2, demonstrating that stable magnetic order can persist in 2D monolayers, when sufficient anisotropy is present [46, 45, 47]. These systems highlight the crucial role of SOC driven anisotropy and reduced dimensionality in determining magnetic behavior.

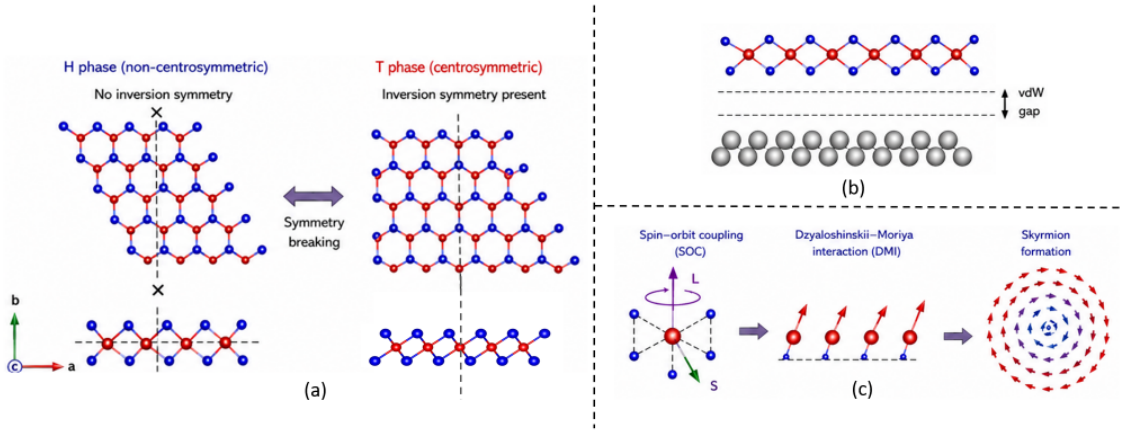

Figure 1.2: (a) H- and T-phase TMDC monolayers illustrating inversion symmetry. (b) Schematic of a TMDC/metal van der Waals heterostructure heterostructure. (c) Emergent phenomena including SOC, DMI, and skyrmions.

In addition to intrinsic magnets, magnetic properties can be engineered in thin films and heterostructures through interface effects, strain, and proximity to heavy elements. For example, Fe films grown on Ir(111) exhibit modified magnetic interactions due to strong interfacial SOC, leading to nontrivial spin configurations [48]. Such systems provide a versatile platform for tuning magnetic interactions in low-dimensional systems. The coex-

istence of broken inversion symmetry and strong SOC gives rise to antisymmetric exchange interactions, most notably the Dzyaloshinskii-Moriya interaction (DMI) [49]. Thus, in 2D systems, electronic structure, symmetry breaking, and SOC are intrinsically linked to magnetism and the emergence of complex spin textures, forming the foundation for the phenomena explored in the following sections.

1.3.2 Chiral Magnetism and Dzyaloshinskii–Moriya Interaction

In magnetic systems, the competition between different exchange interactions determines spin ordering. While the Heisenberg exchange favors collinear alignment, relativistic spin-orbit effects introduce additional interactions. In systems lacking inversion symmetry, this leads to the DMI [50, 51], which can be expressed as

$$E_{\mathrm{DMI}} = \mathbf{D}_{ij} \cdot (\mathbf{S}_i \times \mathbf{S}_j), \tag{1.2}$$

where $\mathbf{D}_{ij}$ is the DMI vector. Unlike the symmetric exchange interaction, which favors collinear spin alignment, DMI promotes canting between neighboring spins, stabilizing chiral magnetic configurations. Depending on the origin of this symmetry breaking, it can be broadly categorized into two types. In non-centrosymmetric crystal structures, such as MnSi and FeGe, DMI arises intrinsically from the lattice symmetry [52]. In contrast, in low-dimensional systems and heterostructures, DMI originates at interfaces where inversion symmetry is broken and strong SOC is introduced, as observed in systems such as Fe/Ir(111) and Co/Pt [53, 48]. This interaction stabilizes noncollinear spin textures such as spin spirals and chiral domain walls like skyrmions as shown in Fig. 1.2 (c) . Its strength depends sensitively on crystal symmetry, atomic structure, and SOC, making it tunable via material design and interface engineering [54]. In low-dimensional systems, these effects are enhanced, enabling nanoscale chiral structures.

The interplay between exchange interaction, DMI, and magnetic anisotropy determines

the magnetic ground state, including the emergence of topological spin textures [49]. Understanding and controlling DMI is therefore central to chiral magnetism in low-dimensional systems.

1.3.3 Magnetic Skyrmions

Magnetic skyrmions are topologically nontrivial spin textures characterized by a continuous rotation of spin orientations from a central core to the surrounding magnetic background. Their topology is described by the skyrmion number

$$Q = \frac{1}{4\pi} \int \mathbf{m} \cdot (\partial_x \mathbf{m} \times \partial_y \mathbf{m})\, dx\, dy, \tag{1.3}$$

which takes integer values for isolated skyrmions [55]. This topological protection distinguishes them from trivial spin configurations and underlies their stability. Skyrmions were first observed in bulk chiral magnets such as MnSi and FeGe [52], and later in ultrathin films such as Fe/Ir(111), where interfacial DMI stabilizes nanoscale skyrmions [48]. Depending on symmetry, skyrmions can adopt Bloch or Néel configurations, determined by the nature of the DMI [55].

Their nanoscale size and low current-driven mobility make skyrmions promising for spintronic applications, including racetrack memory devices [53]. Additional textures such as antiskyrmions and bimerons further enrich this field [56]. In low-dimensional systems, skyrmions can be stabilized through the interplay of DMI, magnetic anisotropy, and external fields. Their tunability via strain, electric fields, and interface engineering provides a powerful route for designing functional spintronic materials [49]. Understanding their formation and control constitutes a central theme of the present work.

1.4 Motivation and Scope of the Thesis

The preceding sections have established that the electronic structure of materials forms the foundation for understanding their transport and magnetic properties. In particular, the interplay between band structure, symmetry, and SOC plays a decisive role in determining emergent phenomena in both bulk and 2D systems. While bulk semiconductors provide a well-established framework for studying electronic and transport behavior, reducing dimensionality introduces symmetry breaking and enhanced relativistic effects, leading to new magnetic interactions such as the DMI and the stabilization of topological spin textures. While these developments have significantly advanced our understanding of electronic structure, transport, and chiral magnetism, important challenges remain in achieving quantitative accuracy in complex bulk systems and in establishing a predictive link between electronic structure and emergent magnetic interactions in 2D materials. The work presented in this thesis addresses these challenges and is divided into two main parts.

In the first part of this thesis, we focus on bulk semiconductor systems, where the relationship between electronic structure and material properties can be systematically analyzed. Particular emphasis is placed on the accurate description of electronic structure, phase stability, and thermoelectric transport in Cu- and Ag-based chalcopyrite semiconductors using advanced density functional approaches. In the second part, the focus shifts to 2D systems, where symmetry breaking and strong SOC fundamentally alter magnetic behavior. In these systems, the coexistence of broken inversion symmetry and SOC gives rise to chiral magnetic interactions such as DMI, enabling the formation of noncollinear spin textures including skyrmions. The thesis therefore investigates the microscopic origin and tunability of DMI, noncollinear magnetism, and the stabilization of skyrmionic spin textures in two-dimensional materials and vdW heterostructures. Specifically, the objectives of this thesis are summarized as follows:

- To investigate the electronic structure and phase stability of Cu- and Ag-based bulk chalcopyrite semiconductors using advanced density functional methods with improved predictive accuracy.
- To analyze the thermoelectric properties of Ag-based ternary and quaternary chalcopyrite systems, with particular emphasis on the relationship between electronic structure, carrier transport, and thermoelectric performance.
- To explore the role of reduced dimensionality, inversion symmetry breaking, and SOC in determining the magnetic properties of non-centrosymmetric 2D systems, particularly the H-phase $FeTe_2$ monolayer.
- To investigate the formation, stability, and manipulation of topological spin textures such as skyrmions using atomistic and micromagnetic approaches in vdW heterostructures, specifically T-$FeTe_2$/Pt, where interfacial symmetry breaking and strong SOC generate sizable DMI.
- To understand the microscopic origin and tunability of the Dzyaloshinskii–Moriya interaction through chemical engineering, particularly via Co and Pt doping in Ti_2Si, enabling enhanced SOC and symmetry breaking.

Through these investigations, this thesis aims to establish a unified understanding of how electronic structure governs transport phenomena in bulk systems and drives chiral magnetism in 2D materials. By connecting first-principles electronic structure calculations with emergent magnetic phenomena such as DMI and skyrmions, this work contributes to the rational design of quantum materials with tailored functionalities for future electronic and spintronic applications.

Chapter 2

Theoretical Methods

2.1 Introduction

The theoretical description of material properties requires an understanding of the underlying electronic degrees of freedom. Electrons, owing to their small mass and quantum nature, play a central role in determining the electronic, magnetic, and chemical behavior of materials, while the heavier atomic nuclei can generally be treated separately within the usual approximations. Early descriptions of electronic behavior in solids were developed from classical pictures of conduction, most notably the free-electron model introduced by Drude [57] and subsequently developed by Lorentz [58]. Although these models provided a basic description of electrical conduction, they could not account for several important properties of real materials. The development of quantum mechanics and band theory provided a more appropriate framework for describing electrons in solids and led to the classification of materials into metals, semiconductors, and insulators [59, 60].

The quantum-mechanical treatment of interacting electrons gives rise to a many-body problem whose direct solution becomes increasingly demanding with system size. A number of electronic-structure approaches, including the Hartree–Fock method, Møller–Plesset perturbation theory, and coupled-cluster methods, have therefore been developed to treat electron correlation at different levels of approximation [61, 62, 63]. While these methods can provide highly accurate results for suitable systems, their computational requirements can become prohibitive for extended materials.

Density Functional Theory (DFT), developed through the work of Hohenberg–Kohn and Kohn–Sham, provides an alternative framework for treating the electronic structure of

many-electron systems [64, 65]. The central idea is to formulate the ground-state problem in terms of the electron density rather than the full many-electron wavefunction. This reformulation makes first-principles calculations feasible for atoms, molecules, and periodic solids while retaining a practical description of the effects of electron–electron interactions [66, 67]. Within DFT, the accuracy of the calculated properties depends on the treatment of the exchange-correlation contribution. Consequently, the choice of the exchange-correlation approximation is an important consideration when calculating electronic, structural, magnetic, and related properties [64, 68].

2.2 Quantum Mechanical Description of Many-Electron Systems

The quantum-mechanical description of matter is based on the time-independent Schrödinger equation [69]. For a few simple systems, such as the hydrogen atom, this equation can be solved analytically [70]. Such a direct treatment, however, becomes impractical for systems containing many interacting electrons. The electron–electron interaction couples the motion of individual particles, making the resulting many-body problem computationally demanding [61].

For a system containing both electrons and nuclei, the time-independent Schrödinger equation can be written as an eigenvalue problem involving the total Hamiltonian $\hat{H}_T$:

$$\hat{H}_T \Psi_T = E_T \Psi_T, \tag{2.1}$$

Here, Ψ_T denotes the complete wavefunction of the system and depends on the coordinates of both electrons and nuclei, while E_T denotes the corresponding total energy. The total Hamiltonian includes the kinetic energies of the particles together with their mutual interactions. Because the nuclei are substantially heavier than the electrons, their characteristic motion occurs on a much slower time scale. This difference in mass provides the basis for

the Born–Oppenheimer approximation, which allows the nuclear and electronic degrees of freedom to be treated separately [71]. Under this approximation, the Hamiltonian, energy, and wavefunction can be written as

$$\hat{H}_T = \hat{H} + \hat{H}_n \tag{2.2}$$

$$E_T = E + E_n \tag{2.3}$$

$$\Psi_T = \Psi\Psi_n \tag{2.4}$$

where $\hat{H}$ and $\hat{H}_n$ describe the electronic and nuclear parts, respectively, and E and E_n are their corresponding energies. Likewise, the total wavefunction is represented by separate electronic (Ψ) and nuclear (Ψ_n) components. The electronic contribution constitutes the central computational problem considered in electronic-structure calculations.

Within the Born–Oppenheimer framework, the electronic problem involves N interacting electrons moving in an external potential $v_{\text{ext}}(r)$. The corresponding many-electron Schrödinger equation is

$$\left[-\frac{1}{2}\sum_{i=1}^{N}\nabla_i^2 + \sum_{i=1}^{N} v_{\text{ext}}(r_i) + \frac{1}{2}\sum_{i=1}^{N}\sum_{j\neq i}^{N}\frac{1}{|r_i - r_j|}\right]\Psi(x_1, ..., x_N) = E\Psi(x_1, ..., x_N). \tag{2.5}$$

The three terms in the Hamiltonian describe, respectively, the electronic kinetic energy, the interaction of the electrons with the external potential, and the Coulomb interaction between electron pairs. The electron–electron contribution couples the coordinates of different electrons and is a major source of difficulty in obtaining the many-body solution.

Electrons obey Fermi–Dirac statistics and are therefore fermionic particles. The corresponding many-electron wavefunction must change sign when the coordinates of any two electrons are interchanged. This antisymmetry requirement is written as

$$\Psi(x_1, ..., x_i, ..., x_j, ..., x_N) = -\Psi(x_1, ..., x_j, ..., x_i, ..., x_N), \tag{2.6}$$

where $x_i = (r_i, \sigma_i)$ contains the spatial coordinate and spin variable of the i-th electron.

The antisymmetric character of the wavefunction is directly related to the Pauli exclusion principle and places an important constraint on the allowed electronic states.

The wavefunction also provides a probabilistic description of the electronic configuration. In particular, $|\Psi|^2$ represents the corresponding probability density in the full configuration space. Consequently, the wavefunction must be normalized according to

$$\sum_{\sigma_1,\ldots,\sigma_N} \int d^3r_1 \cdots d^3r_N \, |\Psi(r\sigma, \ldots, r_N\sigma_N)|^2 = 1. \tag{2.7}$$

A more directly useful quantity for electronic-structure calculations is the electron density. The spin-resolved density is obtained by integrating out the coordinates of all electrons except one:

$$n_\sigma(r) = N \sum_{\sigma_2,\ldots,\sigma_N} \int d^3r_2 \cdots d^3r_N \, |\Psi(r\sigma, r_2\sigma_2, \ldots, r_N\sigma_N)|^2, \tag{2.8}$$

The factor N accounts for the indistinguishability of the electrons. The density is normalized such that the total number of electrons is recovered upon integration over space and summation over spin:

$$\sum_\sigma \int d^3r \, n_\sigma(r) = N. \tag{2.9}$$

The expectation value of the electronic Hamiltonian can be expressed in terms of the many-electron wavefunction as

$$\langle\Psi|\hat{H}|\Psi\rangle = \langle\Psi|\hat{T} + \hat{v}_{\text{ext}} + \hat{V}_{ee}|\Psi\rangle = T + V_{\text{ext}} + U = E_e, \tag{2.10}$$

where T, V_{ext}, and U denote the kinetic, external-potential, and electron–electron interaction contributions, respectively. These terms may be written in terms of the total electron density *n* as

$$\langle\hat{T}\rangle = -\frac{1}{2}\sum_\sigma \left\langle \Psi \left| \sum_{i=1}^{N} \nabla_i^2 \right| \Psi \right\rangle \tag{2.11}$$

$$\langle\hat{v}_{\text{ext}}\rangle = \int d^3r \, n(r) v_{\text{ext}}(r) \tag{2.12}$$

$$\langle\hat{V}_{ee}\rangle = \frac{1}{2}\int d^3r \int d^3r' \frac{n(r)n(r')}{|r - r'|}, \tag{2.13}$$

2.2.1 Wavefunction Variational Principle

The variational principle provides a practical route for obtaining the ground-state solution of a quantum-mechanical system [70]. For a normalized trial wavefunction, the expectation value of the Hamiltonian cannot fall below the exact ground-state energy. The ground state can therefore be obtained by minimizing this expectation value while enforcing the normalization constraint. This condition is expressed as

$$\delta \left\{ \langle \Psi | \hat{H} | \Psi \rangle - \mu \langle \Psi | \Psi \rangle \right\} = 0, \tag{2.14}$$

where μ acts as a Lagrange multiplier associated with the normalization of the wavefunction. Requiring the functional to be stationary with respect to variations in Ψ gives

$$(\hat{H} - \mu)|\Psi\rangle = 0, \tag{2.15}$$

which has the form of the time-independent Schrödinger equation, with μ corresponding to the associated energy eigenvalue. The variational formulation provides the underlying basis for several electronic-structure approaches, including the Hartree–Fock method and density functional theory.

2.2.2 Hartree-Fock Approximation

The Hartree-Fock (HF) approximation [72, 73] provides a mean-field treatment of the many-electron problem introduced above. Starting from the variational condition in Eq. (2.14), the many-electron state is represented in terms of N single-particle spin-orbitals. The required antisymmetry under exchange of electrons is ensured by expressing the many-electron state as a Slater determinant:

$$\Psi_{\mathrm{HF}} = \frac{1}{\sqrt{N!}} \det[\psi_1, \ldots, \psi_N], \tag{2.16}$$

or explicitly,

$$\Psi_{\text{HF}}(\vec{x}_1,\ldots,\vec{x}_N) = \frac{1}{\sqrt{N!}}\begin{vmatrix} \psi_1(\vec{x}_1) & \psi_1(\vec{x}_2) & \cdots & \psi_1(\vec{x}_N) \\ \psi_2(\vec{x}_1) & \psi_2(\vec{x}_2) & \cdots & \psi_2(\vec{x}_N) \\ \vdots & \vdots & \ddots & \vdots \\ \psi_N(\vec{x}_1) & \psi_N(\vec{x}_2) & \cdots & \psi_N(\vec{x}_N) \end{vmatrix}, \tag{2.17}$$

where ψ_i denotes the corresponding spin-orbital. The orbitals are determined by minimizing the expectation value of the electronic Hamiltonian, $\langle\Psi_{\text{HF}}|\hat{H}|\Psi_{\text{HF}}\rangle$, while maintaining their orthonormality, $\langle\psi_i|\psi_j\rangle = \delta_{ij}$. The resulting total energy within the HF approximation is

$$\begin{aligned} E_{\text{HF}} = &\sum_i \int d^3r\, \psi_i^*(\mathbf{r},\sigma)\left(-\frac{1}{2}\nabla^2\right)\psi_i(\mathbf{r},\sigma) + \int n(\mathbf{r})v_{\text{ext}}(\mathbf{r})\, d^3r \\ &+ \frac{1}{2}\int d^3r\, d^3r'\, \frac{n(\mathbf{r})n(\mathbf{r}')}{|\mathbf{r}-\mathbf{r}'|} - \frac{1}{2}\sum_{i,j}\sum_{\sigma,\sigma'}\int d^3r\, d^3r'\, \frac{\psi_i^*(\mathbf{r},\sigma)\psi_j(\mathbf{r},\sigma)\psi_j^*(\mathbf{r}',\sigma')\psi_i(\mathbf{r}',\sigma')}{|\mathbf{r}-\mathbf{r}'|}, \end{aligned} \tag{2.18}$$

The four contributions in Eq. (2.18) represent the kinetic, external-potential, Hartree, and exchange terms, respectively. The exchange contribution arises directly from the antisymmetric form of the wavefunction. For identical orbital indices, it compensates the corresponding self-interaction contribution contained in the Hartree term. Thus, within the HF description, the exchange interaction is treated exactly at the mean-field level.

Applying the variational condition to Eq. (2.18) gives the self-consistent Hartree-Fock equations:

$$\begin{aligned} &\left[-\frac{1}{2}\nabla^2 + v_{\text{ext}}(\mathbf{r}) + \int d^3r'\frac{n(\mathbf{r}')}{|\mathbf{r}-\mathbf{r}'|}\right]\psi_i(\mathbf{r},\sigma) - \sum_j \int d^3r'\frac{\psi_j^*(\mathbf{r}',\sigma')\psi_i(\mathbf{r}',\sigma')}{|\mathbf{r}-\mathbf{r}'|}\psi_j(\mathbf{r},\sigma) \\ &\qquad = \epsilon_i\psi_i(\mathbf{r},\sigma), \end{aligned} \tag{2.19}$$

where ϵ_i are the Lagrange multipliers introduced to enforce orbital orthonormality and are commonly interpreted as the corresponding orbital energies. The HF approximation pro-

vides an exact treatment of the exchange contribution within its single-determinant framework, but it does not explicitly account for electron correlation beyond this exchange description. This limitation becomes important for systems in which correlation effects play a substantial role. Methods such as configuration interaction (CI) can incorporate additional correlation effects, although their computational cost increases rapidly with system size. Density functional theory offers a more computationally practical framework in which exchange and correlation are incorporated through an exchange-correlation functional, as discussed in the following section.

2.3 Density Functional Theory

Density Functional Theory (DFT) provides a practical framework for obtaining the ground-state properties of interacting many-electron systems [64, 65]. A direct treatment of the many-electron Schrödinger equation requires the wavefunction to depend on the coordinates of all N electrons, resulting in a $3N$-dimensional spatial dependence. The associated computational effort becomes increasingly demanding as the number of electrons increases, making a direct solution unsuitable for extended materials. DFT instead takes the electron density $n(\mathbf{r})$ as the basic variable. Since the density depends only on the three spatial coordinates, the description is considerably simplified compared with the full many-electron wavefunction. This density-based formulation has made DFT a central first-principles approach for studying the structural, electronic, and magnetic properties of condensed matter systems.

2.3.1 Hohenberg-Kohn Theorems

The theoretical basis of DFT is provided by the Hohenberg-Kohn (HK) theorems [64]. These theorems establish that the ground-state electron density $n(\mathbf{r})$ contains sufficient information to characterize the ground-state properties of an interacting many-electron sys-

tem.

Theorem I: *The ground-state electron density $n(\mathbf{r})$ uniquely determines the external potential $v(\mathbf{r})$, apart from an arbitrary additive constant.* Consequently, the Hamiltonian of the system, as given in Eq. 2.5, is fixed by the ground-state density. All ground-state observables, including the total energy, can therefore be regarded as functionals of $n(\mathbf{r})$.

Theorem II: *For any trial density $\tilde{n}(\mathbf{r})$ that satisfies $\tilde{n}(\mathbf{r}) \geq 0$ and $\int \tilde{n}(\mathbf{r})d\mathbf{r} = N$, the corresponding energy functional obeys the variational condition:*

$$E[n] \leq E[\tilde{n}], \tag{2.20}$$

where $n(\mathbf{r})$ denotes the exact ground-state density. The physical density is therefore the one that minimizes the total energy among all admissible densities. The first theorem allows the total energy to be separated into a universal contribution and the interaction with the external potential:

$$E_v[n] = F_{HK}[n] + \int n(\mathbf{r})v(\mathbf{r})\, d\mathbf{r}, \tag{2.21}$$

Here, the universal Hohenberg-Kohn functional $F_{HK}[n] = T[n] + V_{ee}[n]$ contains the kinetic energy and electron–electron interaction energy. Its form does not depend explicitly on the particular external potential. The ground-state density can then be found by minimizing $E_v[n]$ while keeping the total number of electrons fixed:

$$\delta\left\{E_v[n] - \mu\left(\int n(\mathbf{r})d\mathbf{r} - N\right)\right\} = 0, \tag{2.22}$$

where μ is the Lagrange multiplier associated with the electron-number constraint $\int n(\mathbf{r})d\mathbf{r} = N$. At the stationary point, this quantity corresponds to the chemical potential of the system and gives the Euler–Lagrange equation

$$\mu = \frac{\delta E_v[n]}{\delta n(\mathbf{r})} = v(\mathbf{r}) + \frac{\delta F[n]}{\delta n(\mathbf{r})}, \tag{2.23}$$

2.3.2 Kohn-Sham (KS) Formalism

The Hohenberg–Kohn framework establishes that the ground-state density is sufficient to determine the properties of the system, but it does not provide an explicit form for the universal functional $F_{HK}[n]$. Kohn and Sham introduced a practical construction in which the original interacting many-electron problem is replaced by an auxiliary system of non-interacting electrons having the same ground-state density [65]. The electron-electron interactions are incorporated through an effective potential, reducing the problem to a set of coupled single-particle equations.

Within this formulation, the total energy is written as

$$E_v[n] = T_s[n] + \int n(\mathbf{r})v(\mathbf{r})\,d\mathbf{r} + \frac{1}{2}\int \frac{n(\mathbf{r})n(\mathbf{r}')}{|\mathbf{r}-\mathbf{r}'|}\,d^3r\,d^3r' + E_{\text{xc}}[n], \tag{2.24}$$

where $T_s[n]$ denotes the kinetic energy of the auxiliary non-interacting electrons. The second contribution describes their interaction with the external potential, while the third term represents the classical Hartree energy. The remaining many-body contributions are collected in the exchange-correlation functional $E_{\text{xc}}[n]$.

The electron density associated with the occupied KS orbitals $\{\psi_i(\mathbf{r})\}$ is obtained from

$$n(\mathbf{r}) = \sum_i |\psi_i(\mathbf{r})|^2. \tag{2.25}$$

Minimization of the total energy with respect to these orbitals, subject to their orthonormality, gives the single-particle Kohn–Sham equations:

$$\left[-\frac{1}{2}\nabla^2 + v_{\text{eff}}(\mathbf{r})\right]\psi_i(\mathbf{r}) = \epsilon_i\psi_i(\mathbf{r}), \tag{2.26}$$

where the effective potential is composed of the external, Hartree, and exchange-correlation contributions:

$$v_{\text{eff}}(\mathbf{r}) = v(\mathbf{r}) + \int \frac{n(\mathbf{r}')}{|\mathbf{r}-\mathbf{r}'|}\,d^3r' + v_{\text{xc}}(\mathbf{r}), \tag{2.27}$$

with the exchange–correlation potential defined by

$$v_{\mathrm{xc}}(\mathbf{r}) = \frac{\delta E_{\mathrm{xc}}[n]}{\delta n(\mathbf{r})}. \tag{2.28}$$

In practical calculations, the KS equations are treated through a self-consistent field (SCF) cycle. An initial electron density is first chosen and used to construct $v_{\mathrm{eff}}(\mathbf{r})$ from Eq. (2.27). The resulting KS equations in Eq. (2.26) are then solved to obtain the orbitals $\psi_i(\mathbf{r})$ and their corresponding eigenvalues ϵ_i. These orbitals are used to generate an updated density through Eq. (2.25). The updated density is subsequently used to construct a new effective potential, and the procedure is repeated until the density and total energy satisfy the chosen convergence criteria. This self-consistent procedure provides the ground-state solution within the selected approximation for $E_{\mathrm{xc}}[n]$.

The reliability of a KS calculation depends strongly on the treatment of exchange and correlation. Because the exact functional is not available in closed form, practical DFT calculations employ approximate forms of $E_{\mathrm{xc}}[n]$. The choice of this functional therefore plays an important role in determining the accuracy of calculated material properties.

2.3.3 Exchange-Correlation Functional

The exchange-correlation (XC) functional $E_{\mathrm{xc}}[n]$ contains the electronic effects that are not represented explicitly by the non-interacting kinetic-energy term and the classical Hartree contribution [74, 75]. It incorporates exchange effects associated with the fermionic nature of electrons together with correlation effects arising from their mutual Coulomb interaction [76]. Although the Kohn–Sham formulation provides an exact formal framework, the explicit dependence of $E_{\mathrm{xc}}[n]$ on the electron density is not known. Its practical treatment therefore requires an appropriate approximation.

The corresponding XC potential is obtained from the functional derivative of the XC energy, as defined in Eq. (2.28). Different approximations to $E_{\mathrm{xc}}[n]$ have been developed to

balance accuracy and computational cost. The choice of the XC functional is consequently an important part of a DFT calculation and can influence the predicted structural, electronic, and magnetic properties of a material.

Local Density Approximation (LDA)

The Local Density Approximation (LDA) provides a simple description of exchange-correlation effects by relating the XC energy at each position to the electron density at that position [75, 74]. The underlying assumption is that the electronic environment around each point can be treated locally as a homogeneous electron gas with the same density. The corresponding XC energy functional is written as

$$E_{\mathrm{xc}}^{\mathrm{LDA}}[n] = \int n(\mathbf{r})\, \epsilon_{\mathrm{xc}}(n(\mathbf{r}))\, d^3r, \tag{2.29}$$

where $\epsilon_{\mathrm{xc}}(n)$ denotes the XC energy per electron of a homogeneous electron gas characterized by the density $n(\mathbf{r})$. The associated XC potential follows from the functional derivative of the XC energy:

$$v_{\mathrm{xc}}^{\mathrm{LDA}}(\mathbf{r}) = \frac{\delta E_{\mathrm{xc}}^{\mathrm{LDA}}[n]}{\delta n(\mathbf{r})} = \epsilon_{\mathrm{xc}}(n(\mathbf{r})) + n(\mathbf{r}) \frac{\partial \epsilon_{\mathrm{xc}}(n)}{\partial n}. \tag{2.30}$$

The XC contribution can be separated into exchange and correlation components according to

$$\epsilon_{\mathrm{xc}}(n) = \epsilon_x(n) + \epsilon_c(n). \tag{2.31}$$

For the homogeneous electron gas, the exchange contribution has an analytical form [77]:

$$\epsilon_x(n) = -\frac{3}{4}\left(\frac{3}{\pi}\right)^{1/3} n^{1/3}. \tag{2.32}$$

The correlation contribution $\epsilon_c(n)$, on the other hand, is obtained from numerical calculations and represented through suitable parametrizations. Accurate quantum Monte Carlo calculations of the homogeneous electron gas provide the basis for widely used parametrizations [78, 79]. For magnetic systems, the spin dependence of the density is incorporated

through the Local Spin Density Approximation (LSDA). In this case, the total density is resolved into spin-up and spin-down components, $n_\uparrow(\mathbf{r})$ and $n_\downarrow(\mathbf{r})$, giving

$$E_{\text{xc}}^{\text{LSDA}} = \int n(\mathbf{r})\, \epsilon_{\text{xc}}(n_\uparrow(\mathbf{r}), n_\downarrow(\mathbf{r}))\, d^3r. \tag{2.33}$$

LDA is most appropriate when the electron density changes gradually over space and can provide a good description of equilibrium structural properties. Its limitations become more apparent for strongly inhomogeneous systems. In particular, LDA commonly gives overly strong binding and tends to underestimate semiconductor and insulating band gaps [80, 76, 81].

Generalized Gradient Approximation (GGA)

The Generalized Gradient Approximation (GGA) extends the LDA description by including information about how the electron density changes in space [82, 83]. Thus, in addition to the local density $n(\mathbf{r})$, the XC energy depends on its spatial gradient $\nabla n(\mathbf{r})$. This additional dependence makes GGA more suitable for systems in which the electron density is not spatially uniform. The XC energy within GGA is given by

$$E_{\text{xc}}^{\text{GGA}}[n] = \int n(\mathbf{r})\, \epsilon_{\text{xc}}(n(\mathbf{r}), \nabla n(\mathbf{r}))\, d^3r. \tag{2.34}$$

For a broad class of GGA functionals, the exchange contribution is written using an enhancement factor $F_x(s)$ applied to the LDA exchange energy:

$$E_x^{\text{GGA}}[n] = \int n(\mathbf{r})\, \epsilon_x^{\text{LDA}}(n(\mathbf{r}))\, F_x(s)\, d^3r, \tag{2.35}$$

where the dimensionless reduced density gradient s is defined as

$$s = \frac{|\nabla n(\mathbf{r})|}{2(3\pi^2)^{1/3} n(\mathbf{r})^{4/3}}. \tag{2.36}$$

The dependence on the density gradient provides GGA with greater flexibility in describing spatially varying electron densities than LDA. Among the commonly employed

GGA forms are the Perdew–Burke–Ernzerhof (PBE) [82] and Perdew–Wang (PW91) [83] functionals. In many systems, GGA gives improved structural parameters, total energies, and binding characteristics relative to LDA. Nevertheless, the description of band gaps remains a limitation, and correlation effects in strongly correlated systems may require a more sophisticated treatment.

GGA therefore offers a useful compromise between computational cost and the description of exchange-correlation effects and has consequently become a standard choice for first-principles calculations. However, the density and its first derivative are not always sufficient to describe systems with more complex electronic environments. This has motivated the development of meta-Generalized Gradient Approximation (meta-GGA) functionals, which include additional information about the electronic environment beyond $n(\mathbf{r})$ and $\nabla n(\mathbf{r})$ [84, 85].

Meta-Generalized Gradient Approximation (meta-GGA)

The meta-Generalized Gradient Approximation (meta-GGA) represents a higher level of approximation beyond GGA within density functional theory. In addition to the electron density $n(\mathbf{r})$ and its gradient $\nabla n(\mathbf{r})$, meta-GGA functionals incorporate higher-order quantities such as the kinetic energy density $\tau(\mathbf{r})$ or the Laplacian of the density, enabling a more accurate and flexible description of electronic structure [84, 85]. The kinetic energy density is defined in terms of the Kohn–Sham orbitals as

$$\tau(\mathbf{r}) = \frac{1}{2}\sum_i |\nabla\psi_i(\mathbf{r})|^2, \tag{2.37}$$

where $\psi_i(\mathbf{r})$ are the Kohn–Sham orbitals. Within this framework, the exchange–correlation energy functional is generally expressed as

$$E_{\text{xc}}^{\text{meta-GGA}}[n] = \int n(\mathbf{r})\,\epsilon_{\text{xc}}(n(\mathbf{r}), \nabla n(\mathbf{r}), \tau(\mathbf{r}))\,d^3r. \tag{2.38}$$

The inclusion of $\tau(\mathbf{r})$ allows meta-GGA functionals to distinguish between different bonding environments, thereby improving the accuracy of predicted structural and electronic properties. A key ingredient in many meta-GGA functionals, particularly SCAN-type functionals, is the dimensionless parameter α [85], defined as

$$\alpha = \frac{\tau - \tau^W}{\tau^{\text{unif}}}, \tag{2.39}$$

where $\tau^W = \frac{|\nabla n|^2}{8n}$ is the von Weizsäcker kinetic energy density [86] and $\tau^{\text{unif}} = \frac{3}{10}(3\pi^2)^{2/3}n^{5/3}$ is the kinetic energy density of a uniform electron gas. This parameter enables the functional to distinguish between different electronic environments. Among the widely used meta-GGA functionals, the strongly constrained and appropriately normed (SCAN) functional [87] satisfies all known exact constraints for a semi-local functional and provides improved accuracy for structural, energetic, and magnetic properties. A regularized version of SCAN, known as r^{2}SCAN, has been developed to improve numerical stability while retaining the accuracy of SCAN [88]. In addition to SCAN-type functionals, the revised meta-GGA for solids (rMGGAC) functional has been proposed to improve the description of exchange effects in both localized and delocalized systems [89, 90]. In this context, the Pauli kinetic energy density is defined as

$$\tau^P = \tau - \tau^W, \tag{2.40}$$

which provides a measure of electron localization. Another important class of meta-GGA functionals includes orbital-free formulations, such as the OFR2 functional, which approximate the kinetic energy density without explicit dependence on Kohn–Sham orbitals [91]. This is typically expressed as

$$\tau \approx \tau[n, \nabla n], \tag{2.41}$$

thereby eliminating the need for orbital-dependent quantities and significantly reducing computational cost. In a similar spirit, orbital-free variants of SCAN, such as SCAN-L

and its regularized form r^{2}SCAN-L, have been developed [92]. These functionals replace the explicit orbital dependence of the kinetic energy density with approximate density-based expressions, enabling computational efficiency comparable to GGA while retaining the accuracy of meta-GGA functionals. The importance of these orbital-free meta-GGA functionals lies in their ability to combine improved accuracy with reduced computational cost. By avoiding explicit orbital dependence, they are well suited for large-scale systems and high-throughput calculations. In addition, they exhibit enhanced numerical stability and reduced sensitivity to basis sets or real-space grids, making them particularly attractive for practical implementations of DFT. These meta-GGA functionals are employed in Chapter 3 for benchmarking the electronic structure and phase stability of semiconductors.

Although meta-GGA functionals are generally more computationally demanding than LDA and GGA, they offer a better balance between accuracy and efficiency compared to hybrid functionals. As a result, they are widely used in modern first-principles calculations, particularly for systems involving transition metals and complex magnetic interactions.

Beyond Semilocal Approximations: Hybrid Functionals

Semilocal functionals such as LDA, GGA, and meta-GGA describe exchange-correlation effects using local or semilocal information about the electron density. Although these approaches are computationally efficient, their treatment of exchange can lead to systematic errors in properties such as band gaps and in systems where self-interaction and long-range screening play an important role. Hybrid functionals address these limitations by combining semilocal exchange with a contribution from exact Hartree–Fock (HF) exchange.

For solid-state calculations, the Heyd–Scuseria–Ernzerhof (HSE) functional [93, 94] provides a screened hybrid approach in which the Coulomb interaction is separated into short-range (SR) and long-range (LR) parts. Exact HF exchange is incorporated only in the short-range component, while the remaining exchange and correlation terms are described

using the PBE functional. The corresponding exchange-correlation energy is

$$E_{xc}^{\mathrm{HSE}} = \alpha E_x^{\mathrm{HF,SR}}(\omega) + (1-\alpha) E_x^{\mathrm{PBE,SR}}(\omega) + E_x^{\mathrm{PBE,LR}}(\omega) + E_c^{\mathrm{PBE}}, \tag{2.42}$$

where α specifies the fraction of HF exchange and ω determines the range over which the Coulomb interaction is screened. The HSE06 parameterization uses $\alpha = 0.25$ and $\omega = 0.2\,\text{Å}^{-1}$. This screened treatment generally improves the description of band gaps and related electronic properties relative to semilocal functionals.

A limitation of HSE06 is that both α and ω are fixed parameters. Consequently, the same degree of exact exchange is applied irrespective of the dielectric response of the material. This can become important when comparing systems with substantially different screening properties, where a fixed screening prescription may not provide a uniformly accurate description.

Dielectric-dependent hybrid (DDH) functionals provide a material-dependent alternative by relating the amount of exact exchange to the dielectric screening of the system [95]. In this approach, the long-range HF contribution is weighted according to the inverse macroscopic dielectric constant, ϵ_∞^{-1}. A range-separated form of the DDH exchange-correlation energy can be written as

$$E_{xc} = (1-\alpha) E_x^{\mathrm{SR,SL}} + \alpha E_x^{\mathrm{SR,HF}} + \left(1-\epsilon_\infty^{-1}\right) E_x^{\mathrm{LR,SL}} + \epsilon_\infty^{-1} E_x^{\mathrm{LR,HF}} + E_c^{\mathrm{SL}}. \tag{2.43}$$

Here, the amount of long-range exact exchange is determined by the dielectric screening rather than being fixed universally. This provides a material-dependent treatment of exchange and can improve the transferability of hybrid calculations across systems with different dielectric responses.

The range separation is controlled by the screening parameter μ, which sets the characteristic division between short- and long-range interactions. Recent developments have introduced a first-principles determination of μ based on the compressibility sum rule, con-

necting the screening parameter with the exchange-correlation energy of the uniform electron gas [96]. The resulting methodology is employed in Chapter 4 to study high-band-gap semiconductors, for which an appropriate description of dielectric screening is important for obtaining reliable electronic properties.

Hubbard Correction: DFT+U Method

Semilocal and hybrid functionals do not always provide an adequate description of systems containing strongly localized electronic states, particularly partially filled transition-metal d orbitals and rare-earth f orbitals. For these systems, the treatment of on-site electron–electron interactions within conventional DFT can lead to excessive delocalization of localized states and consequently affect the predicted electronic and magnetic properties. The DFT+U method addresses this issue by adding an explicit on-site Coulomb interaction for the selected localized orbitals [97, 98]. The total energy is expressed as

$$E^{\mathrm{DFT}+U} = E^{\mathrm{DFT}} + E_U - E_{\mathrm{DC}}, \tag{2.44}$$

where E_U denotes the additional Hubbard interaction and E_{DC} accounts for the double counting of interactions already contained in the underlying DFT functional.

A simplified rotationally invariant formulation was introduced by Dudarev *et al.* [99]. In this approach, the correction is determined by the effective interaction parameter $U_{\mathrm{eff}} = U - J$, giving

$$E^{\mathrm{DFT}+U} = E^{\mathrm{DFT}} + \frac{U_{\mathrm{eff}}}{2} \sum_{m,\sigma} \left(n_{m\sigma} - n_{m\sigma}^2 \right), \tag{2.45}$$

where $n_{m\sigma}$ represents the occupation of a localized orbital with orbital index m and spin σ. The additional energy term favors integer occupations of the localized states and therefore provides a more appropriate treatment of their on-site Coulomb interactions. As a result, DFT+U can improve the description of electronic structures, magnetic moments, and band gaps in systems where localized electrons play an important role.

The reliability of a DFT+U calculation depends on the value assigned to the Hubbard parameter U. This parameter may be selected empirically or obtained from first-principles approaches such as linear-response and constrained DFT calculations. Compared with more computationally demanding many-body methods, DFT+U offers a relatively inexpensive way of including the dominant on-site correlation effects associated with localized orbitals.

The systems investigated in Chapters 5, 6, and 7 contain transition-metal states for which partially occupied d orbitals are important. DFT+U is therefore employed in these chapters to account for the corresponding on-site electron correlations and to obtain a more reliable description of their electronic and magnetic properties.

In this chapter, the theoretical concepts used throughout this thesis have been introduced. The discussion covered density functional theory together with the principal exchange-correlation approximations considered in the present work, ranging from semilocal functionals to hybrid and dielectric-dependent hybrid approaches. The DFT+U method was also introduced to treat systems containing localized d states. These methods form the theoretical basis for the electronic-structure calculations and subsequent analyses presented in the following chapters.

2.3.4 Pseudopotentials and Plane-Wave Basis

The explicit treatment of core and valence electrons in first-principles calculations can be computationally demanding, particularly because the wavefunctions of core electrons vary rapidly close to the atomic nuclei. A pseudopotential approach replaces the explicit core-electron contribution with an effective interaction acting on the valence electrons [100]. The resulting pseudo-wavefunctions are smoother in the region close to the nucleus and therefore require fewer basis functions for their representation. Outside a selected core radius, the pseudo-wavefunctions are constructed to reproduce the corresponding all-electron behavior.

Two commonly used approaches are norm-conserving pseudopotentials and the projector augmented wave (PAW) method. Norm-conserving constructions impose constraints on the pseudo-wavefunctions to preserve the relevant charge properties, while PAW provides a transformation between smooth pseudo-wavefunctions and the corresponding all-electron quantities [101]. The smoothness introduced by these approaches makes plane waves a convenient basis for representing electronic states in periodic systems.

For a periodic crystal, Bloch's theorem allows a Kohn–Sham state to be represented using reciprocal lattice vectors **G**:

$$\psi_{n\mathbf{k}}(\mathbf{r}) = \sum_{\mathbf{G}} C_{n,\mathbf{k}+\mathbf{G}}\, e^{i(\mathbf{k}+\mathbf{G})\cdot\mathbf{r}}, \tag{2.46}$$

where **k** denotes a wave vector within the Brillouin zone and **G** is a reciprocal lattice vector. The plane-wave basis is made finite in practical calculations by introducing a kinetic-energy cutoff E_{cut}:

$$\frac{\hbar^2|\mathbf{k}+\mathbf{G}|^2}{2m} \leq E_{\text{cut}}. \tag{2.47}$$

The cutoff determines the number of plane waves included in the calculation. Increasing E_{cut} enlarges the basis and generally improves the convergence of calculated quantities, at the expense of additional computational effort. Consequently, the cutoff is selected through convergence testing to obtain the required accuracy at a manageable computational cost.

The combination of pseudopotentials or PAW with a plane-wave basis is particularly well suited to periodic solids. It provides a convenient framework for solving the Kohn–Sham equations while allowing systematic control of basis-set convergence [102].

2.3.5 van der Waals Interactions in Density Functional Theory

Standard implementations of density functional theory, particularly within the LDA and GGA, are well suited for describing covalent and ionic bonding. However, these semi-local exchange–correlation functionals fail to capture long-range dispersion interactions,

commonly referred to as van der Waals (vdW) forces. These interactions arise from correlated charge fluctuations between spatially separated regions and are inherently non-local in nature [103, 104]. The absence of vdW interactions in conventional DFT can lead to significant inaccuracies in systems where weak interactions dominate, such as layered materials, molecular crystals, and van der Waals heterostructures. In such systems, neglecting dispersion forces results in incorrect predictions of interlayer distances, binding energies, and structural stability. To overcome this limitation, several approaches have been developed to incorporate vdW interactions within the DFT framework. One widely used class of methods is the semi-empirical dispersion correction schemes, such as the DFT-D methods, where an additional energy term is added to account for long-range interactions [105]. The total energy in such approaches can be expressed as

$$E_{\text{DFT-D}} = E_{\text{DFT}} + E_{\text{disp}}, \tag{2.48}$$

where E_{disp} represents the dispersion correction typically described by pairwise atomic interactions. Another class of methods involves non-local van der Waals density functionals (vdW-DF), which incorporate dispersion interactions directly into the XC functional through a non-local correlation term. These approaches provide a more physically grounded description of long-range interactions and have been successfully applied to a wide range of systems [104]. The inclusion of vdW interactions is particularly important in the study of low-dimensional materials and layered systems, where weak interlayer coupling plays a critical role in determining structural and electronic properties. Accurate treatment of these interactions is therefore essential for reliable prediction of material behavior.

In this thesis, van der Waals interactions are incorporated using dispersion-corrected approaches in conjunction with the DFT+U method, in order to accurately describe the structural and electronic properties of van der Waals heterostructures where both weak interlayer coupling and strong electronic correlations play an important role in Chapter 6.

2.3.6 Wannier Tight-Binding Model and Maximally Localized Wannier Functions

While first-principles calculations provide an accurate description of electronic structure, their direct use in analyzing microscopic interactions or transport properties can be computationally demanding. An efficient approach is to construct a tight-binding Hamiltonian in a localized basis, which retains the essential physics while reducing computational complexity. In this context, Wannier functions offer a convenient framework for connecting first-principles calculations with model Hamiltonians. Wannier functions are localized real-space orbitals obtained from a unitary transformation of Bloch states. For a given band n, the Wannier function centered at lattice vector $\mathbf{R}$ is defined as

$$w_n(\mathbf{R}, \mathbf{r}) = \frac{1}{N_k} \sum_{\mathbf{k}} e^{-i\mathbf{k}\cdot\mathbf{R}} \psi_{n\mathbf{k}}(\mathbf{r}), \tag{2.49}$$

where $\psi_{n\mathbf{k}}(\mathbf{r})$ are the Bloch wavefunctions. Since the Wannier representation is not unique, maximally localized Wannier functions (MLWFs) are constructed by minimizing the spatial spread of the orbitals, leading to a set of well-localized functions that closely resemble atomic-like orbitals [106, 107]. The total spread functional is given by

$$\Omega = \sum_n \left[\langle w_n | r^2 | w_n \rangle - \langle w_n | \mathbf{r} | w_n \rangle^2 \right]. \tag{2.50}$$

Using MLWFs, the Hamiltonian can be mapped onto a tight-binding form, where the matrix elements represent hopping amplitudes between localized orbitals,

$$H_{mn}(\mathbf{R}) = \langle w_m(\mathbf{0}) | \hat{H} | w_n(\mathbf{R}) \rangle. \tag{2.51}$$

This representation enables efficient interpolation of band structures and provides insight into orbital contributions and electronic interactions. In this thesis, the Wannier-based tight-binding approach is employed selectively in the analysis of electronic and magnetic properties in Chapter 5, where it is used to construct an effective low-energy Hamiltonian and to investigate microscopic origin of orbital resolved DMI.

All calculations presented in this thesis were carried out using the Vienna *ab initio* Simulation Package (VASP) [108, 109], based on density functional theory within the KS framework and employing a plane-wave basis set. Different XC approaches, including meta-GGA, hybrid functionals, and the DFT+U method, were employed as appropriate to ensure an accurate description of the electronic, transport, and magnetic properties of the systems studied. These methodologies form the foundation for the electronic structure calculations and analyses presented in the subsequent chapters.

Chapter 3

Electronic Structure and Phase Stability of Bulk Semiconductors

This chapter constitutes the first part of the thesis and focuses on the role of electronic structure in determining the properties of bulk semiconductors. In addition, the thermodynamic stability of these materials is examined through phase stability analysis, which is governed by the energetics of competing phases. The chapter also highlights the importance of XC functionals within DFT, with particular emphasis on achieving improved accuracy and computational efficiency using meta-GGA approaches. This chapter is based on the following published work:

[1] **D. Rani**, S. Jana, M. K. Niranjan, and P. Samal, *Journal of Physics: Condensed Matter*, **36**, 165502 (2024).

3.1 Introduction

In recent years, the growing demand for efficient and sustainable energy technologies has driven extensive research into semiconducting materials with tunable electronic and optical properties. Among these, ternary chalcopyrite semiconductors with the general formula $P^{I}Q^{III}R_2^{VI}$ (where P = Cu, Ag; Q = In, Ga, Al; and R = S, Se) have emerged as a promising class of materials for next-generation photovoltaic and optoelectronic applications. These compounds crystallize in a tetragonal structure derived from the zinc-blende lattice with space group $I\bar{4}2d$ [110], and their properties can be systematically tuned through chemical substitution and structural modification [111, 112, 113, 114].

A defining characteristic of chalcopyrite semiconductors is their unique crystal struc-

ture, which consists of two inequivalent cations coordinated tetrahedrally by a common anion. This leads to unequal bond lengths between cation–anion pairs, resulting in intrinsic structural distortions. Such distortions significantly influence the degree of orbital hybridization and play a crucial role in determining the electronic properties of the material. Consequently, understanding the relationship between structural parameters and electronic behavior is essential for tailoring these materials for specific applications.

Copper-based chalcopyrites, particularly Cu(In,Ga)(Se,S)$_2$ (CIGS), have attracted considerable attention due to their high efficiency and long-term stability in thin-film solar cells [115, 116, 117]. One of the key advantages of these materials is their tunable direct band gap, which can vary from 1.0 to 2.4 eV depending on composition, enabling their use in a wide range of optoelectronic applications such as solar cells, solid-state lighting, and photonic devices [118, 115, 119]. Several compounds, including $CuInSe_2$, $CuGaSe_2$, $CuGaS_2$, $CuAlSe_2$, and $CuInS_2$, have been extensively studied as efficient light absorbers due to their favorable band gaps and optical properties [120, 121, 122, 115, 116, 117, 123].

For instance, $CuInSe_2$ exhibits an optimal band gap of approximately 1.1–1.2 eV, making it highly suitable for photovoltaic applications, while $CuGaSe_2$ achieves competitive efficiencies when gallium is incorporated [124]. However, it has been observed that solar cell efficiency decreases when the band gap exceeds approximately 1.2 eV. On the other hand, wide band gap materials such as $CuAlS_2$ (3.49 eV) are suitable for light-emitting applications in the blue region of the spectrum [125]. Despite extensive experimental studies on these systems [126, 127, 128], theoretical predictions have not yet achieved comparable accuracy, primarily due to the complex nature of d-electron interactions [129].

In addition to Cu-based systems, Ag-based chalcopyrites (AIGS) have also emerged as promising materials with potential applications in optoelectronic devices, photonic sensors, and photovoltaics [130]. These materials exhibit enhanced optical properties and can improve device performance when alloyed with Cu-based compounds. For exam-

ple, Ag(In,Ga)Se_2 has been shown to enhance thin-film solar cell efficiency [131], while $AgInSe_2$ exhibits an increased band gap of 1.24 eV, improving optoelectronic performance [132, 133]. Similarly, compounds such as $AgAlS_2$, $AgAlSe_2$, $AgGaS_2$, $AgGaSe_2$, and $AgInS_2$ exhibit desirable optical and electronic properties for various applications [134, 135, 136, 137, 138].

Despite the technological importance of chalcopyrite semiconductors, accurately predicting their electronic structure remains a major theoretical challenge. The electronic properties of these materials are strongly influenced by the hybridization between transition metal d-states and chalcogen p-states, which governs the position of the valence band maximum and ultimately determines the band gap [139, 140]. These d-electron interactions are highly sensitive to the choice of computational method, making reliable theoretical modeling difficult [141, 142, 143].

DFT has been extensively employed as a first-principles approach for studying the electronic structure of materials [26]. However, conventional exchange–correlation approximations such as the LDA [144] and the GGA [145] suffer from intrinsic limitations. In particular, these semilocal functionals introduce self-interaction errors and tend to over-delocalize d-electrons, resulting in a systematic underestimation of band gaps and inaccuracies in energetic properties [141]. This limitation poses a significant challenge for accurately describing both electronic properties and thermodynamic stability. Hybrid functionals, which incorporate a fraction of exact exchange, offer improved accuracy in predicting electronic properties and band gaps [146, 147, 148, 149, 150, 151, 152]. However, their computational cost is substantially higher than that of semilocal functionals, making them impractical for large-scale or systematic investigations involving multiple materials and competing phases.

Within the framework of Density Functional Theory, meta-GGA functionals have emerged as a promising alternative [153]. By incorporating additional ingredients such as the kinetic energy density, meta-GGA functionals provide a more accurate description of electronic in-

teractions and can distinguish between different bonding environments [87, 88, 154]. These functionals offer a balance between computational efficiency and accuracy, making them particularly suitable for studying complex material systems. Although some studies have explored the use of advanced meta-GGA functionals such as SCAN and MGGAC for specific properties of chalcopyrites [155], a comprehensive and systematic investigation of their performance in describing structural properties, electronic structure, and phase stability remains lacking. In particular, understanding how these functionals capture structural distortions, p–d hybridization, band gap variations, and thermodynamic stability within a unified framework is still an open problem.

Therefore, there is a clear need to systematically investigate chalcopyrite semiconductors using advanced meta-GGA XC functionals to achieve improved accuracy without significantly increasing computational cost. Addressing this challenge forms the central motivation of the present work, which aims to provide a detailed understanding of the interplay between structural, electronic, and thermodynamic properties of bulk semiconductors.

3.2 Computational Methodology

The present study is based on first-principles calculations within the framework of DFT, as implemented in the Vienna *Ab initio* Simulation Package (VASP) [156, 108]. The interactions between core and valence electrons are described using the projector augmented wave (PAW) method [157, 109]. The XC effects are treated using both the GGA in the Perdew–Burke–Ernzerhof (PBE) form [145] and a range of advanced meta-GGA functionals. In particular, r^{2}SCAN [87, 88] and rMGGAC [89, 90] are employed to assess improvements in the prediction of structural and electronic properties. In addition, orbital-free variants such as SCAN-L, r^{2}SCAN-L [92], and OFR2 [91] are also considered to evaluate their computational efficiency and performance relative to conventional functionals. These func-

tionals provide an efficient alternative to orbital-dependent approaches while maintaining reasonable accuracy.

The Kohn–Sham wave functions are expanded in a plane-wave basis set with a kinetic energy cutoff of 520 eV. The Brillouin zone is sampled using a Γ-centered Monkhorst–Pack grid of $11 \times 11 \times 11$ for structural optimization, while a denser $15 \times 15 \times 15$ grid is used for electronic structure calculations, including density of states. All structures are fully relaxed using the primitive tetragonal unit cell corresponding to the chalcopyrite phase (space group $I\bar{4}2d$). The electronic self-consistency loop is converged to an energy tolerance of 10^{-6} eV, and the ionic relaxation is performed until the Hellmann–Feynman forces on each atom are less than 0.01 eV/Å. The visualization of crystal structures and electronic charge densities is performed using the VESTA software [158].

3.3 Results and Discussions

3.3.1 Structural Properties

Ternary chalcopyrite semiconductors with the general formula $P^{I}Q^{III}R_2$ exhibit intrinsic structural distortion due to the presence of two inequivalent cations, resulting in unequal cation–anion bond lengths [143]. The structural properties of these materials are characterized by three key parameters: the lattice constant a, the tetragonal distortion parameter $\eta = c/2a$, and the anion displacement parameter u. These parameters quantify deviations from the ideal zinc-blende structure and play a crucial role in determining the electronic properties of the system. The anion displacement parameter u is given by:

$$u = 0.25 + \frac{l_{P-R}^2 - l_{Q-R}^2}{a^2}, \tag{3.1}$$

where l_{P-R} and l_{Q-R} denote the bond lengths between the anion and the two distinct cations. In an ideal tetrahedral configuration, $u = 0.25$, while deviations from this value indicate structural distortion. Such deviations directly influence the degree of orbital hybridization

(a)

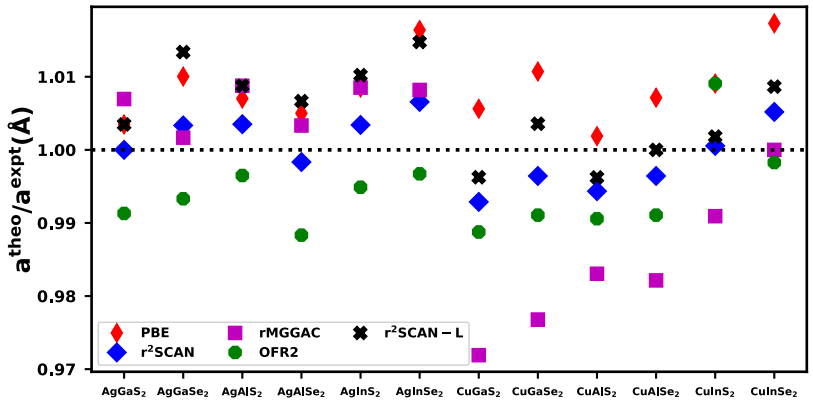

(b)

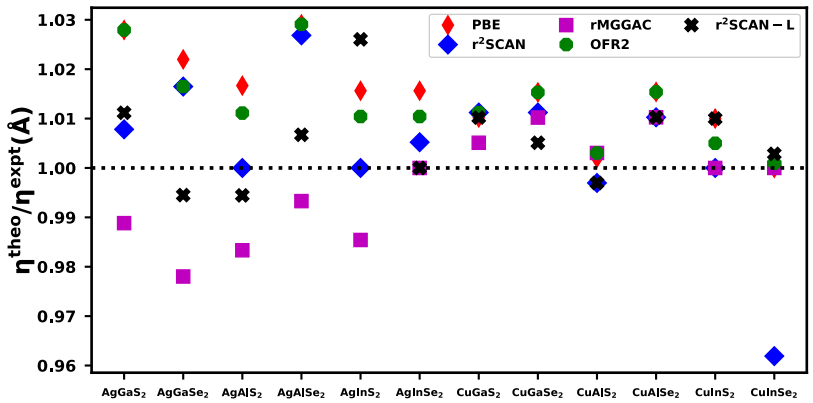

(c)

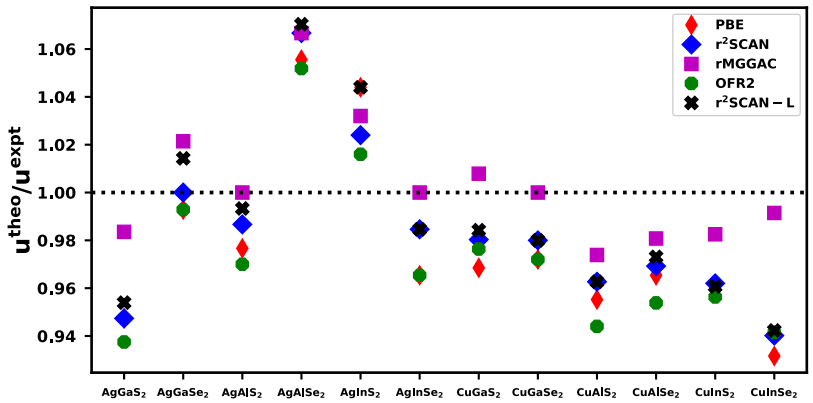

Figure 3.1: The ratio of theoretical to experimental values of (a) in-plane lattice constants 'a', (b) tetragonal ratio $\eta = c/2a$ (c) anion displacement parameter 'u' of Cu and Ag-based ternary Chalcopyrites computed using different functionals.

and are therefore closely related to the electronic properties, particularly the band gap [143]. The calculated structural parameters using different XC functionals are presented in Fig. 3.1, where the theoretical values are compared with available experimental data. Fig. 3.1(a) shows the ratio of calculated to experimental lattice constants a, while Fig. 3.1(b) and (c) illustrate the corresponding behavior of the tetragonal distortion parameter η and the anion displacement parameter u, respectively.

It is observed from Fig. 3.1(a) that the PBE-GGA functional slightly overestimates the lattice constants, with deviations typically in the range of 2–4%. This behavior arises from the known tendency of GGA to over-delocalize electron density in systems with slowly varying densities. In contrast, meta-GGA functionals provide improved predictions, with r^{2}SCAN showing particularly good agreement with experimental values across different chalcopyrite systems. he variation of the tetragonal distortion parameter η, shown in Fig. 3.1(b), indicates that orbital-free meta-GGA functionals such as r^{2}SCAN-L can capture structural distortions with reasonable accuracy while maintaining computational efficiency comparable to PBE [159, 127, 118, 160, 161, 162].

A significant improvement is observed in the prediction of the anion displacement parameter u, as shown in Fig. 3.1(c). The rMGGAC functional yields values of u that are in close agreement with experimental data, particularly for Cu-based chalcopyrites. This improvement can be attributed to the more accurate treatment of localized d-states, which directly influences the bonding characteristics and reduces errors in bond length estimation. In addition to semilocal and meta-GGA functionals, PBE+U calculations were performed to assess the role of on-site Coulomb interaction in correcting the position of localized d-states. However, the results show that the choice of U introduces system-dependent uncertainty and does not consistently improve agreement with experimental data compared to meta-GGA functionals.

Overall, the results demonstrate that while PBE provides a reasonable qualitative de-

scription of structural properties, advanced meta-GGA functionals, especially r^{2}SCAN and rMGGAC, offer significantly improved quantitative agreement with experimental observations. This highlights the importance of selecting appropriate exchange–correlation functionals for accurately describing structural distortions in chalcopyrite semiconductors.

3.3.2 Electronic Structural Properties

In this section, the electronic structure of chalcopyrite semiconductors is analyzed in terms of band structure, density of states (DOS), and band gap variations obtained using different XC functionals. A well-known limitation of conventional DFT approaches, particularly within LDA and GGA, is the presence of self-interaction error (SIE), which leads to an inaccurate description of localized d-states [139, 163]. In chalcopyrites, this limitation results in an improper treatment of p–d hybridization and the absence of derivative discontinuity in the Kohn–Sham band gap. Consequently, the band gap, is significantly underestimated compared to experimental values.

This effect is particularly evident in PBE calculations, where excessive delocalization of d-electrons enhances p–d hybridization, causing an upward shift of the valence band and, in some cases, leading to nearly vanishing band gaps. In contrast, the use of meta-GGA functionals systematically improves the band gap by providing a better balance between localized and delocalized electronic states. The performance of different functionals in predicting band gaps is summarized in Fig. 3.1(a), where the ratio of theoretical to experimental values is presented. It is evident that all meta-GGA functionals yield improved band gaps compared to PBE, with deviations ranging from 60% to 100%. Among these, the rMGGAC functional exhibits the best agreement with experimental values, with deviations as low as 1–30% [141]. The orbital-free OFR2 functional, on the other hand, closely follows PBE behavior due to its reduced sensitivity to orbital-dependent effects.

A direct comparison between rMGGAC and the hybrid HSE06 functional is shown in

(a)

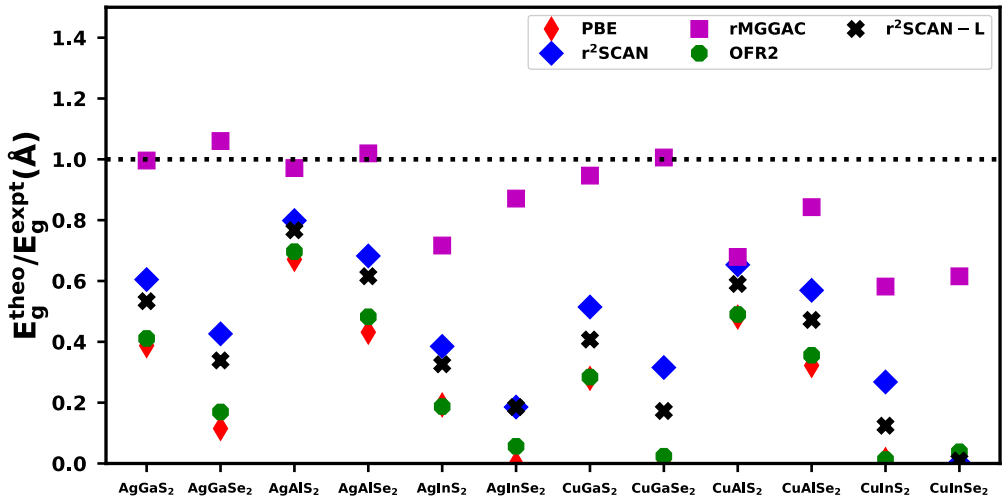

(b)

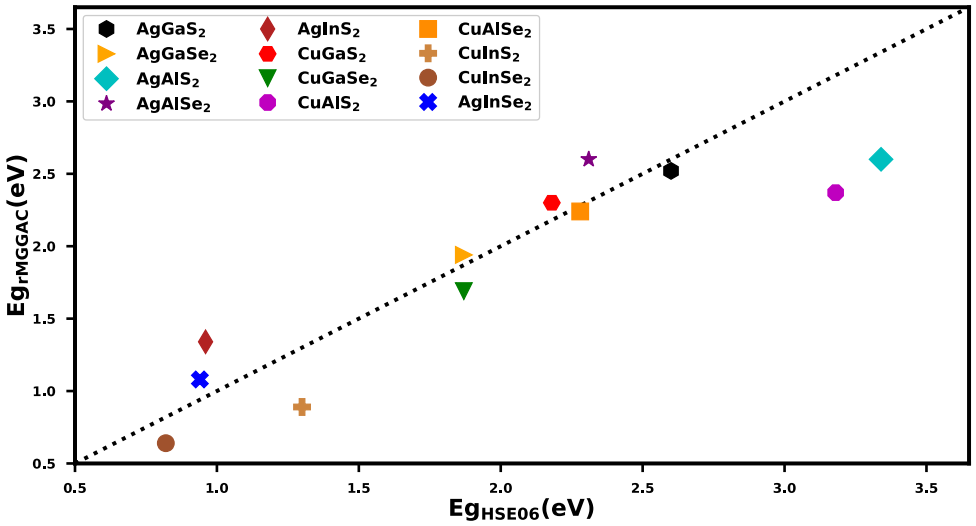

Figure 3.2: (a): The ratio of theoretical and experimental band gaps with SOC correction computed using various XC approximations and (b): Comparision of the band gaps of different chalcopyrite semiconductors computed using rMGGAC and HSE06 methods.

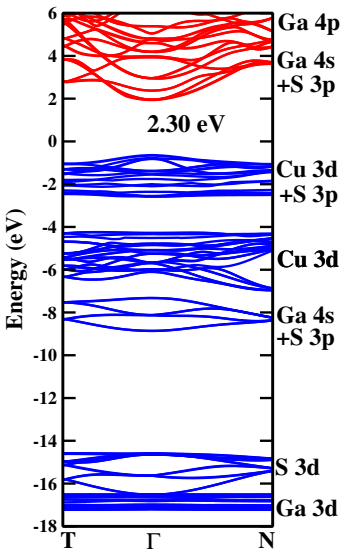

Figure 3.3: Electronic band structure of $CuGaS_2$ with SOC using the rMGGAC exchange-correlation approximation. The red lines delineate the conduction band while the blue lines represent the valence band, providing a visual representation of the material's energy levels and electronic transitions.

Fig. 3.1(b). The close agreement between the two approaches demonstrates that rMGGAC provides band gap predictions comparable to hybrid functionals, but at a significantly lower computational cost [164, 165, 166, 1, 155]. This highlights the effectiveness of meta-GGA methods for reliable electronic structure calculations. To gain deeper insight into the electronic structure, the band dispersion and density of states are analyzed for representative systems such as $CuGaS_2$. The band structure obtained using the rMGGAC functional, shown in Fig. 3.3, reveals that both the VBM and CBM are located at the Γ point, indicating a direct band gap nature. Similar behavior is observed across other chalcopyrite compounds. The projected density of states (PDOS), shown in Fig. 3.4, provides further insight into the orbital contributions. The upper valence band is predominantly formed by hybridized Cu($3d$) and S($3p$) states, while the conduction band mainly originates from antibonding combinations of Ga($4s$), Ga($3d$), and S($3s$) states. A pronounced peak in Cu d-character is observed approximately 3–4 eV below the VBM, indicating strong localization of d-states.

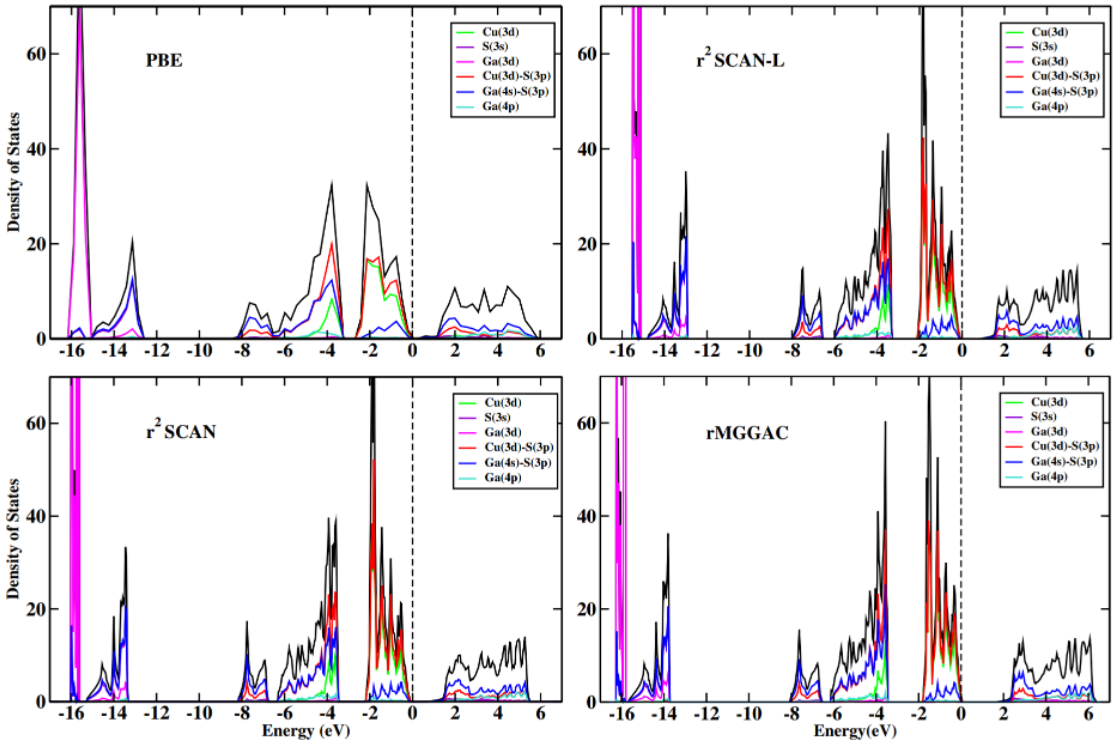

Figure 3.4: Density of States (DOS) for $CuGaS_2$ calculated using DFT-PBE and various DFT meta-GGA methods: r^{2}SCAN-L, r^{2}SCAN, and rMGGAC. The total DOS is depicted with black lines, while the projected DOS of Cu, S, and Ga are represented by green, violet, magenta, and torquoise lines respectively. The red lines correspond to Cu-S bonds, and the blue line represents Ga-S bonds. The position of the Fermi level is indicated by the dashed black line.

The strength of p–d hybridization plays a crucial role in determining the band gap. In PBE, the Cu d-states are positioned at higher energies, leading to stronger hybridization with S p-states. This interaction shifts the VBM upward, resulting in a significantly reduced band gap (0.68 eV for $CuGaS_2$), corresponding to an underestimation of about 72% compared to experiment. In contrast, meta-GGA functionals, particularly rMGGAC, shift the Cu d-states to lower energies, thereby reducing p–d hybridization. This leads to a downward shift of the valence band and a consequent increase in the band gap. For $CuGaS_2$, the rMGGAC functional predicts a band gap of 2.31 eV, which is in excellent agreement with experimen-

tal values.

The variation in band gap across different functionals can also be correlated with the structural parameter u. For functionals yielding $u < 0.25$, the anion is closer to Cu, resulting in stronger p–d overlap and enhanced repulsion in the valence band, thereby reducing the band gap. In contrast, for rMGGAC, where $u > 0.25$, the anion shifts away from Cu and toward Ga, reducing orbital overlap and weakening p–d hybridization. This leads to a widening of the band gap and improved agreement with experimental observations. A similar trend is observed across other chalcopyrite systems, where the electronic structure of the upper valence band is predominantly governed by Cu/Ag d and chalcogen p states. The increasing separation between d-states and the VBM along the sequence Al $\rightarrow$ Ga $\rightarrow$ In further reflects the role of cation chemistry in tuning the electronic structure.

Overall, the results demonstrate that accurate prediction of electronic properties in chalcopyrites requires a proper description of d-electron localization and p–d hybridization. Meta-GGA functionals, particularly rMGGAC, successfully capture these effects and provide band gap values in close agreement with experimental data, making them a reliable and computationally efficient alternative to hybrid functionals.

3.3.3 Evaluation of Phase Stability and Accuracy

After elucidating the electronic structure of the chalcopyrite semiconductors, we now focus on their thermodynamic stability through the evaluation of formation enthalpies and phase stability diagrams. This analysis is crucial not only for understanding the intrinsic stability of these compounds but also for assessing the accuracy of different exchange–correlation functionals in predicting phase stability. Such investigations are central to the broader goal of computational materials discovery [167]. In this work, the phase stability obtained using PBE and various meta-GGA functionals is systematically compared with available experimental data and hybrid functional results. Additionally, comparisons are made with data

from established materials repositories [168, 169, 170] to identify consistent trends across different computational approaches.

Gibbs Free Energies of Chalcopyrites and Competing Phases

At thermodynamic equilibrium, the Gibbs free energy of the chalcopyrite compound PQR_2 is given by:

$$G_{PQR_2} = \mu_P + \mu_Q + 2\mu_R \tag{3.2}$$

which can be rewritten in terms of chemical potential differences as:

$$\Delta G_{PQR_2} = \Delta\mu_P + \Delta\mu_Q + 2\Delta\mu_R \tag{3.3}$$

Here, $\Delta\mu_i = \mu_i - \mu_i^0$ represents the deviation of the chemical potential from its elemental reference state. The thermodynamic stability condition to prevent elemental precipitation requires:

$$\Delta\mu_i \leq 0 \tag{3.4}$$

The Gibbs free energy can be expressed as:

$$G = E_{\text{DFT}} + F_{\text{vib}} + PV \tag{3.5}$$

where E_{DFT} is the total energy, F_{vib} is the vibrational contribution, and PV accounts for pressure–volume effects. In this work, entropy and pressure contributions are neglected, leading to:

$$\Delta G_{PQR_2} = E^{DFT}_{PQR_2} - E^{DFT}_P - E^{DFT}_Q - 2E^{DFT}_R \tag{3.6}$$

A negative ΔG confirms thermodynamic stability. The calculated formation enthalpies for all chalcopyrites are summarized in Table 3.1. A clear trend emerges: the PBE functional significantly underestimates formation enthalpies by approximately 25–42%, consistent with its known underbinding behavior [171]. In contrast, meta-GGA functionals provide systematic improvement. SCAN and r^{2}SCAN reduce the error to about 12–35%,

Table 3.1: Calculated enthalpy of formation of PQR_2 (eV per formula unit).

Compound	PBE	SCAN	r^{2}SCAN	MGGAC	rMGGAC	SCANL	r^{2}SCANL	OFR2	Ref
$CuInSe_2$	-1.78	-2.05	-2.15	-2.36	-2.37	-1.80	-2.05	-1.91	-2.77[a]
$AgInSe_2$	-1.71	-1.93	-1.53	-2.46	-2.53	-1.80	-2.06	-1.85	-2.51[a]
$CuGaS_2$	-2.41	-2.79	-2.89	-3.16	-3.30	-2.60	-2.79	-2.67	-2.99[b]
$AgGaS_2$	-2.13	-2.39	-2.54	-2.96	-2.98	-2.11	-2.43	-2.31	–
$CuAlS_2$	-3.35	-3.97	-3.93	-4.28	-4.17	-3.76	-3.83	-3.59	-4.50[c]
$AgAlS_2$	-3.09	-3.66	-3.67	-4.17	-3.92	-3.44	-3.56	-3.31	–
$CuGaSe_2$	-1.94	-2.12	-2.33	-2.39	-2.57	-1.97	-2.18	-2.70	-3.27[d]
$AgGaSe_2$	-1.84	-1.91	-2.17	-2.38	-2.44	-1.68	-2.01	-1.88	–
$CuAlSe_2$	-2.54	-2.82	-3.05	-3.31	-3.24	-2.73	-2.89	-2.70	-4.24[e]
$AgAlSe_2$	-2.51	-2.83	-2.97	-3.37	-3.18	-2.54	-2.80	-2.59	-3.24[f]
$CuInS_2$	-2.05	-2.55	-2.60	-2.90	-3.06	-2.48	-2.60	-2.42	-3.30[g]
$AgInS_2$	-1.68	-2.15	-2.25	-2.51	-2.55	-1.98	-2.18	-2.00	–

[a][170] [b][172] [c][173] [d][174] [e][175] [f][176] [g][122]

while orbital-free functionals (OFR2, SCAN-L, r^{2}SCAN-L) show moderate improvement with comparable computational cost. Among all approaches, MGGAC and rMGGAC exhibit the highest accuracy. For instance, in $AgInSe_2$ and $CuAlS_2$, the deviation is nearly negligible ($\sim$0.01%), indicating performance comparable to hybrid functionals. This highlights the capability of these functionals in accurately describing formation energetics. A comprehensive comparison of formation enthalpies of chalcopyrites and their competing binary phases is presented in Fig. 3.5. The competing phases are selected based on experimentally known stable binaries, including Cu–Se, Ag–Se, Ga–S, In–Se, and related systems. From Fig. 3.5, several important trends are observed. First, PBE consistently predicts underbinding for both chalcopyrites and binary phases. Second, meta-GGA functionals significantly improve the relative energetics. A notable feature of rMGGAC is its systematic behavior: it slightly underestimates formation enthalpies for P–R binaries while overestimating those for Q–R binaries. Despite this asymmetry, it remains highly accurate for the primary chalcopyrite compounds.

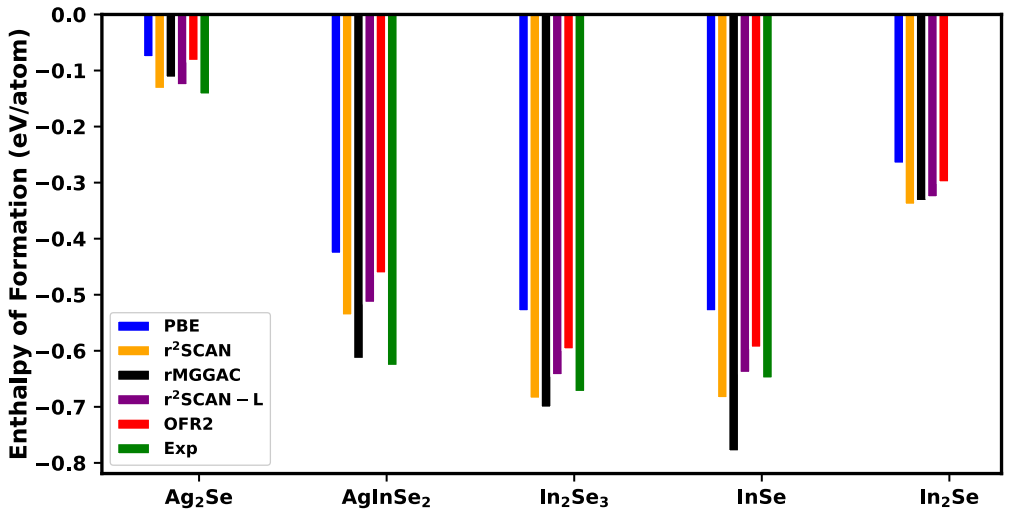

Figure 3.5: Comparisons of absolute values of formation enthalpies in eV per atom of the chalcopyrite and the binaries calculated by PBE and meta-GGA with reference data for $AgInSe_2$ [1], In−Se binaries [2] and Ag−Se binary [3]

.

Phase Stability Diagrams

To further evaluate stability, phase diagrams are constructed using chemical potential constraints. For example, for $AgInSe_2$:

$$\Delta\mu_{Ag} + \Delta\mu_{In} + 2\Delta\mu_{Se} = \Delta G_{AgInSe_2} \tag{3.7}$$

with the constraints:

$$\Delta\mu_i \leq 0 \tag{3.8}$$

The phase stability diagrams obtained using different functionals are shown in Fig. 3.6. Each point in the diagram corresponds to a set of chemical potentials satisfying thermodynamic equilibrium. The shaded region represents the stability window where the chalcopyrite phase is stable against decomposition into competing binaries. The boundaries of this region are determined by competing phases such as Ag_2Se and In_2Se_3, leading to conditions

such as:

$$2\Delta\mu_{Ag} + \Delta\mu_{Se} \leq \Delta H_{Ag_2Se} \tag{3.9}$$

$$2\Delta\mu_{In} + 3\Delta\mu_{Se} \leq \Delta H_{In_2Se_3} \tag{3.10}$$

A strong dependence on the choice of functional is observed. PBE yields smaller stability

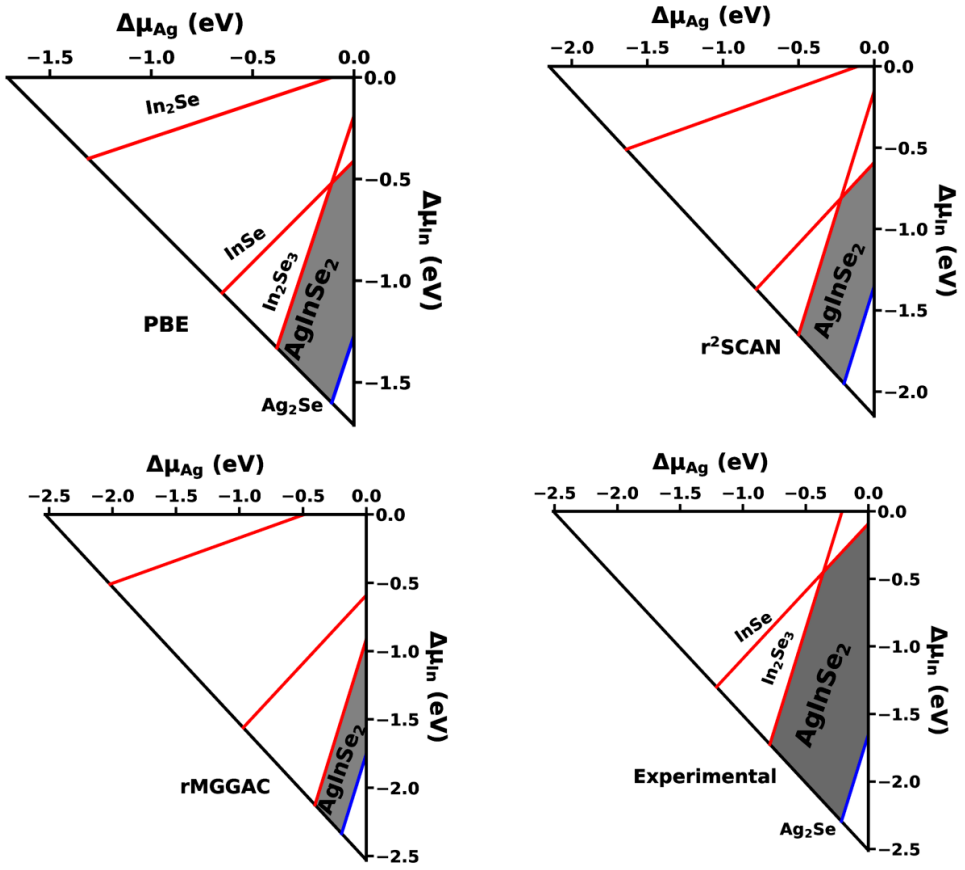

Figure 3.6: Phase stability diagrams of $AgInSe_2$ obtained using different XC functionals (PBE, r^{2}SCAN, r^{2}SCANL, rMGGAC, and OFR2), compared with experimental results from Kim *et al.* [1]. The shaded region represents the thermodynamically stable chemical potential range of $AgInSe_2$, while regions below the blue lines and above the red lines indicate instability toward Ag–Se and In–Se competing phases, respectively.

regions due to underestimation of formation enthalpies. The OFR2 functional is included primarily for benchmarking purposes due to its computational efficiency. However, as its

behavior closely resembles that of the GGA-PBE approximation, detailed analyses such as density of states and phase stability diagrams are presented only for the more accurate meta-GGA functionals. In contrast, r^{2}SCAN produces larger stability regions and shows good agreement with hybrid functional (HSE06) results. Although rMGGAC accurately predicts formation enthalpies, its deviations in certain competing phases (e.g., In_2Se_3) lead to inconsistencies in the predicted stability region, occasionally resulting in apparent instability.

Overall, these results highlight that accurate prediction of phase stability requires a balanced description of both chalcopyrite compounds and competing phases. While rMGGAC provides highly accurate formation enthalpies, r^{2}SCAN offers more consistent phase stability predictions, making it a reliable choice for materials design.

3.4 Conclusion

In this chapter, a detailed first-principles study of Cu- and Ag-based chalcopyrite semiconductors has been carried out to understand the interplay between structural parameters, electronic structure, and thermodynamic stability within density functional theory. Particular emphasis has been placed on the role of exchange–correlation functionals in capturing the underlying physics of these materials.

The structural properties reveal that small variations in the anion displacement parameter (u) and tetragonal distortion (η) play a decisive role in determining the electronic structure. In particular, deviations of u from the ideal value directly modify the cation–anion bond lengths, thereby controlling the extent of p–d hybridization between Cu/Ag d-states and chalcogen p-states. This hybridization is the key microscopic mechanism governing the position of the valence band maximum. Within the PBE approximation, the overdelocalization of d-electrons leads to an enhanced p–d repulsion, resulting in an upward

shift of the valence band and a severe underestimation of the band gap. In contrast, meta-GGA functionals reduce this self-interaction error and provide a more accurate localization of d-states. Among them, the rMGGAC functional yields band gaps in close agreement with experimental values, indicating that it captures the balance between localization and hybridization more effectively. A comparison with hybrid functionals such as HSE06 shows that, although hybrid approaches improve band gap prediction through partial inclusion of exact exchange, they may overestimate gaps in certain systems. In contrast, rMGGAC achieves comparable accuracy without introducing empirical parameters, highlighting its efficiency and predictive capability.

The thermodynamic stability of these materials has been analyzed through formation enthalpies and chemical potential phase diagrams. From a physical perspective, phase stability is governed by the relative energetics of competing bonding environments in ternary and binary phases. While rMGGAC provides highly accurate formation energies for ternary compounds, its description of binary phases is less balanced, leading to inconsistencies in the stability regions. On the other hand, the r^{2}SCAN functional provides a more uniform description of bonding across different chemical environments, resulting in reliable prediction of phase stability. The calculated stability regions for experimentally known compounds, such as $CuInSe_2$, $CuGaS_2$, and $CuInS_2$, show good agreement with experimental observations, confirming the robustness of this approach.

Overall, this study highlights that an accurate description of chalcopyrite semiconductors requires a delicate balance between d-state localization and p–d hybridization, as well as a consistent treatment of competing phases using semilocal XC approximations. These insights provide a fundamental understanding of the electronic and thermodynamic behavior of chalcopyrites and establish a reliable framework for exploring more complex low-dimensional systems in subsequent chapters.

Chapter 4

Thermoelectric Transport of Silver-Based Chalcopyrite Semiconductors

This chapter extends the study of bulk chalcopyrite semiconductors from electronic structure to thermoelectric transport properties. While the previous chapter established the role of electronic structure in determining band gaps and stability, here we focus on how these features influence charge and heat transport. The thermoelectric performance is evaluated in terms of the Seebeck coefficient, electrical conductivity, and thermal conductivity, which together determine the figure of merit (ZT). These properties are calculated using Boltzmann transport theory combined with first-principles electronic structure calculations. To achieve accurate band gap and transport predictions, a nonempirical dielectric-dependent hybrid (DDH) functional is employed. Additionally, carrier scattering effects are incorporated through deformation potential theory, enabling realistic estimation of relaxation times.

This chapter is based on the following published work:

[2] **D. Rani**, S. Jana, M. K. Niranjan, and P. Samal, *J. Phys. Chem. C*, **129**, 3784 (2025).

4.1 Introduction

Thermoelectric (TE) materials have captured significant attention, particularly over the past two decades, due to their unique ability to directly convert heat into electricity without relying on moving components [177, 178]. These materials are considered crucial for the development of sustainable energy technologies, with promising applications ranging from waste heat recovery to power generation in wearable electronic devices and systems de-

signed for disaster mitigation [179, 180, 181]. Despite these advantages, the widespread deployment of thermoelectric devices is limited by their relatively low energy conversion efficiency. The performance of TE materials is quantified by the dimensionless figure of merit,

$$ZT = \frac{\sigma S^2 T}{\kappa}, \tag{4.1}$$

where S is the Seebeck coefficient, σ is the electrical conductivity, T is the absolute temperature, and κ is the total thermal conductivity, which includes both electronic and lattice contributions. Achieving high ZT requires a careful balance between these interdependent transport parameters, making the design of efficient thermoelectric materials a challenging task [182, 183].

Conventional thermoelectric materials such as Bi_2Te_3 are widely used in commercial cooling applications [184], while PbTe is commonly employed for high-temperature thermoelectric applications [185]. Other materials, including NiTiSn and ZrNiSn, have also been explored due to their potential for thermoelectric applications [186]. The performance of these materials is typically associated with achieving ZT values close to unity, either through enhancement of the power factor ($S^2\sigma$) or reduction in thermal conductivity. However, the toxicity of lead-based compounds and the high cost of tellurium pose significant challenges for their large-scale application.

In recent years, attention has shifted toward Ag-based chalcopyrites, which have emerged as promising alternatives due to their structural versatility and tunable electronic properties [187, 188, 189, 190]. These materials include ternary systems of the form $AgXY_2$ (X = Ga, In; Y = S, Se, Te) and quaternary compounds Ag_2PQR_4 (P = Mg, Mn, Fe, Zn, Cd, Hg; Q = Si, Ge, Sn; R = S, Se, Te), which crystallize in diamond-like structures. Their compositional flexibility allows for fine-tuning of electronic structure and transport properties, making them attractive candidates for thermoelectric applications. Experimental and the-

oretical studies have demonstrated that compounds such as $AgGaTe_2$ and $AgInTe_2$ exhibit low thermal conductivity, with values of 1.94 and 2.05 W m^{-1} K^{-1}, respectively, at room temperature [191]. Such low thermal conductivity is highly desirable for enhancing thermoelectric performance. Further investigations by Sharma *et al.* [192] have explored the thermal properties of $AgGaTe_2$, including its Debye temperature, entropy, and heat capacity under varying pressure and temperature conditions.

Understanding the interplay between transport properties, temperature, and carrier concentration is essential for optimizing thermoelectric performance. In particular, identifying the optimal doping concentration is crucial for maximizing ZT. For example, $AgGaTe_2$ has been identified as a promising p-type thermoelectric material with an optimal carrier concentration in the range of 10^{19} to 10^{20} cm^{-3} [188, 193]. Previous theoretical studies based on the PBE+U approach [194] have reported ZT values of 1.38 and 0.91 at 800 K for p-type $AgGaTe_2$ (AGT) and $AgInTe_2$ (AIT), respectively.

In addition to ternary compounds, quaternary materials such as Ag_2ZnSnS_4 (AZTS) and $Ag_2ZnSnSe_4$ (AZTSe) have also attracted attention due to their suitable band gaps and high absorption coefficients, which are advantageous for optoelectronic applications [195, 196, 197]. Experimental studies have reported band gaps of 1.20 eV and 1.40 eV for AZTS and AZTSe, respectively. Furthermore, AZTS has demonstrated significant potential in solar cell applications, achieving efficiencies of up to 10.7% [198]. These materials have also been explored for photocatalytic [195] and photoelectrochemical applications [199]. Comparisons with Cu_2ZnSnS_4 (CZTS) reveal similarities in structural and phase stability, along with differences in electrical conductivity [200, 197]. Information on related compounds such as Ag_2ZnGeS_4 (AZGS) is available in the literature [201], while $Ag_2ZnGeSe_4$ (AZGSe) has been theoretically investigated using the mbj-GGA approach, showing enhanced carrier concentration and absorption properties [202]. These results highlight the potential of quaternary chalcopyrites for improving thermoelectric and optoelectronic per-

formance.

Despite these promising developments, the thermoelectric properties of Ag-based quaternary chalcopyrites remain relatively unexplored. Optimization of key parameters such as carrier concentration, effective mass, and band gap is essential for achieving high ZT, as emphasized by Snyder *et al.* [35]. In this chapter, we employ the multiband Boltzmann transport equation (BTE) framework to investigate the thermoelectric transport properties of selected Ag-based chalcopyrites. The electronic structure parameters, including band gap and effective mass, are obtained from first-principles calculations and used as inputs for transport calculations. The relaxation time approximation (RTA), based on the multiband carrier transport model [203], is incorporated to account for carrier scattering effects.

The thermoelectric properties of AGT, AIT, AZTS, AZTSe, AZGS, and AZGSe are systematically analyzed. Based on these results, optimal carrier concentrations are identified to maximize the figure of merit (ZT). The methodology presented here provides a comprehensive framework for understanding and designing high-performance thermoelectric materials and can be extended to other Ag-based systems [204].

4.2 Methods and Technical Details

4.2.1 Method

All calculations are performed within the framework of density functional theory using the screened dielectric-dependent hybrid (DDH) functional, implemented within the generalized Kohn–Sham (gKS) scheme. The exchange–correlation potential in the DDH approach is expressed as [205]:

$$\begin{aligned} \boldsymbol{V}_{xc}^{DDH}(1,\epsilon_\infty^{-1};\mu) &= \left[1-(1-\epsilon_\infty^{-1})\,\mathbf{Erf}(\mu r)\right]\boldsymbol{V}_x^{Fock} \\ &- (1-\epsilon_\infty^{-1})\boldsymbol{V}_x^{\text{sl-sr},\mu} + (1-\epsilon_\infty^{-1})\boldsymbol{V}_x^{\text{sl}} + \boldsymbol{V}_c^{\text{sl}}\,. \end{aligned} \tag{4.2}$$

The choice of exchange–correlation functional depends on the physical properties of interest. In the previous chapter, meta-GGA functionals were employed as they provide a balanced and computationally efficient description of structural properties, band gaps, and phase stability. These functionals successfully capture the essential physics of p–d hybridization and significantly improve upon GGA. However, thermoelectric transport properties are highly sensitive to the details of the electronic structure near the Fermi level, particularly the band gap and band curvature. Even small inaccuracies in band gap can lead to significant errors in the Seebeck coefficient and electrical conductivity. Therefore, a more accurate description of the electronic structure is required. While hybrid functionals such as HSE06 [146, 147] improve band gap predictions, they employ a fixed fraction of exact exchange, which is not material-dependent and may not provide consistent accuracy across different systems.

In contrast, the DDH functional determines the fraction of exact exchange from the macroscopic dielectric constant, making it a nonempirical and system-specific approach. Thus, DDH offers a better balance between accuracy and transferability compared to meta-GGA and fixed hybrid functionals, making it particularly suitable for reliable prediction of thermoelectric transport properties. The DDH approach is inspired by the static limit of the GW approximation, particularly the COH-SEX formalism, where the Coulomb hole (COH) is described using semilocal approximations and the screened exchange (SEX) is captured through the Fock term [206].

A crucial aspect of the DDH method is the determination of the macroscopic high-frequency dielectric constant (ϵ_∞) and the screening parameter (μ). While ϵ_∞ obtained from PBE often provides a reasonable starting point, a self-consistent evaluation within the DDH framework is more reliable, particularly in cases where PBE incorrectly predicts metallic behavior [207]. The screening parameter μ is evaluated using the μ_{eff}^{fit} approach proposed in Ref. [208], which is based on the compressibility sum rule combined with linear-response

time-dependent DFT (LR-TDDFT).

4.2.2 Technical Details of Calculation Procedures

Structural optimization and electronic structure calculations are performed using the Vienna *Ab initio* Simulation Package (VASP) [108, 156]. The exchange–correlation energy within the semilocal framework is described using the PBE functional [145]. Due to the presence of localized Ag-d electrons, which are not accurately described within standard GGA, the DDH approach is employed [208, 207]. This approach significantly improves the description of band gaps and electronic properties in chalcopyrites. A plane-wave kinetic energy cutoff of 400 eV is used for all calculations. The Brillouin zone is sampled using a Γ-centered Monkhorst–Pack $8\times8\times8$ **k**-point grid. The electronic self-consistency is achieved with an energy convergence criterion of 10^{-6} eV. Structural relaxations are performed until the Hellmann–Feynman forces on each atom are less than 0.01 eV/Å. PAW pseudopotentials are used to describe the interaction between core and valence electrons [109, 157]. SOC is included in all calculations due to its significant influence on the electronic structure and effective mass, even in systems with relatively lighter elements [209]. Elastic constants (C_{ij}) are calculated using the strain–stress method, applying strains up to 15% in increments of 5%. The macroscopic elastic properties, including bulk modulus (B) and shear modulus (G), are evaluated using the Voigt–Reuss–Hill (VRH) approximation [210], which is known to provide good agreement with experimental data. The DDH self-consistent procedure is carried out as follows: (i) The screening parameter μ_{eff}^{fit} is calculated using LDA orbitals, (ii) The initial dielectric constant ϵ_∞ is obtained from PBE (RPA@PBE) and used in Eq. 4.2, (iii) the DDH calculation is performed, and ϵ_∞ is updated using RPA@DDH. This process is iterated until self-consistency in ϵ_∞ is achieved. The final values of ϵ_∞ and μ for all studied materials are listed in Table 4.1.

Table 4.1: High-frequency macroscopic dielectric constants (ϵ_∞) obtained from RPA@PBE and RPA@DDH, along with screening parameters μ (in Å^{-1}).

Material	ϵ_∞ (RPA@PBE)	ϵ_∞ (RPA@DDH)	μ (Å^{-1})
AGT	15.39	7.99	1.49
AIT	11.80	7.69	1.33
AZTS	17.60	5.37	1.43
AZTSe	11.85	6.38	1.36
AZGS	7.02	5.35	1.39
AZGSe	8.45	6.55	1.47

4.3 Results and Discussion

4.3.1 Details of Crystal Structure

The crystal structures of the studied Ag-based chalcopyrites exhibit tetragonal symmetry with slight variations depending on composition. The ternary compounds AXT (X = Ga, In) crystallize in the $I\bar{4}2d$ space group [211], whereas the quaternary compounds AZSQ and AZGQ (Q = S/Se) adopt $I\bar{4}2m$ [212] and $I\bar{4}$ space groups, respectively.

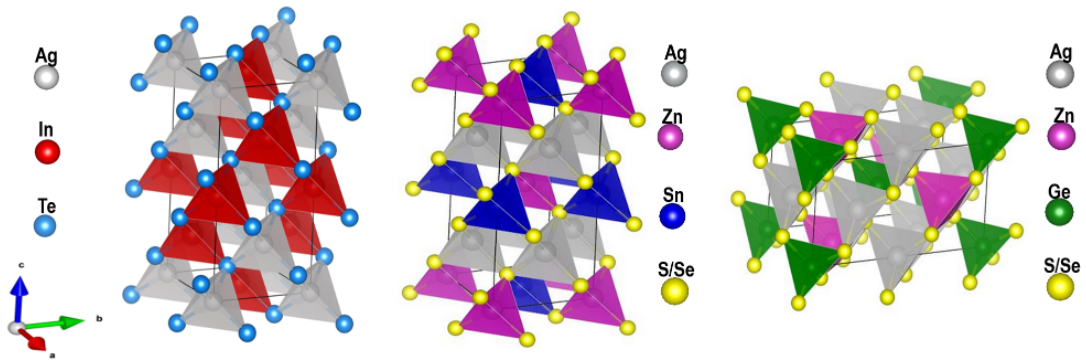

Figure 4.1: The PBE method was used to optimize the crystal structures of (a) tetragonal AXT (X = Ga/In) with Te atoms in sky blue, Ga/In atoms in red, and Ag atoms in grey. (b) The crystal structure of AZTQ (Q = S/Se) showing S/Se atoms in yellow, Zn in magenta, Ag in grey, and Sn in blue. (c) The structure of AZGQ (Q = S/Se), where S/Se atoms are bonded with Ge atoms (green), along with Zn (magenta) and Ag (grey).

Fig. 4.1 illustrates the optimized crystal structures of both ternary (AXT) and quater-

nary (AZPQ and AZGQ) systems. The structures exhibit tetragonal symmetry, where the deviation of the c-axis from ideal cubic symmetry gives rise to tetragonal distortion. This structural anisotropy is a characteristic feature of chalcopyrite systems and plays an important role in determining their electronic and transport properties. The optimized lattice parameters ($a = b \neq c$) and the tetragonal distortion parameter $\eta = c/2a$ are obtained using the PBE functional and are summarized in Table 4.2, along with available experimental values. The overall agreement between calculated and experimental values confirms the reliability of the structural optimization. The atomic configurations used in the PAW pseudopotentials include Ag($4d^{10}5s^1$), Zn($3d^{10}4p^2$), Sn($4d^{10}5s^25p^2$), S($3s^23p^4$), Se($4s^24p^4$), Ga($3d^{10}4s^24p^1$), Ge($3d^{10}4s^24p^2$), In($4d^{10}5s^25p^1$), and Te($5s^25p^4$).

Table 4.2: PBE optimized lattice constants (a, c), distortion parameter $\eta = c/2a$, and Ag–chalcogen bond lengths for AXT (X = Ga, In), AZTY, and AZGY (Y = S, Se), compared with experimental values where available. Percent deviations are shown in parentheses.

	a (Å)		c (Å)		η		$d_{\text{Ag-y}}$ (Å)	
	PBE	Exp.	PBE	Exp.	PBE	Exp.	PBE	Exp.
AGT	6.40 (1.78)	6.288[1]	12.32 (3.1)	11.940[1]	0.9625 (1.4)	0.949[1]	2.799 (1.41)	2.76[4]
AIT	6.56 (1.43)	6.467[1]	13.00 (2.9)	12.633[1]	0.9908 (1.41)	0.977[1]	2.811 (1.07)	2.78[4]
AZTS	5.562 (2.30)	5.693[2]	12.15 (7.12)	11.342[2]	1.092 (9.63)	0.996[2]	2.561 (-0.3)	2.57[5]
AZTSe	5.873 (1.95)	5.99[3]	12.606 (9.76)	11.47[3]	1.07 (11.45)	0.960[3]	2.656 (-0.22)	2.65[6]
AZGS	5.76	–	10.633	–	0.24	–	2.578	–
AZGSe	6.03	–	11.25	–	0.24	–	2.678	–

[1] Ref. [213], [2] Ref. [214], [3] Ref. [215], [4] Ref. [187], [5] Ref. [216] and [6] Ref. [217]

In addition to lattice distortion, an important structural feature is the variation in bond lengths arising from differences in atomic radii between Ag and the chalcogen atoms (Te,

S, Se). This size mismatch leads to local lattice distortions, particularly affecting the Ag–chalcogen bond lengths ($d_{\text{Ag-y}}$), as listed in Table 4.2. These local distortions are not merely structural in nature but have significant physical implications. The variation in bond lengths modifies the interatomic force constants and introduces lattice anharmonicity, which enhances phonon scattering. As a result, the lattice thermal conductivity is reduced, a behavior that is highly desirable for thermoelectric applications.

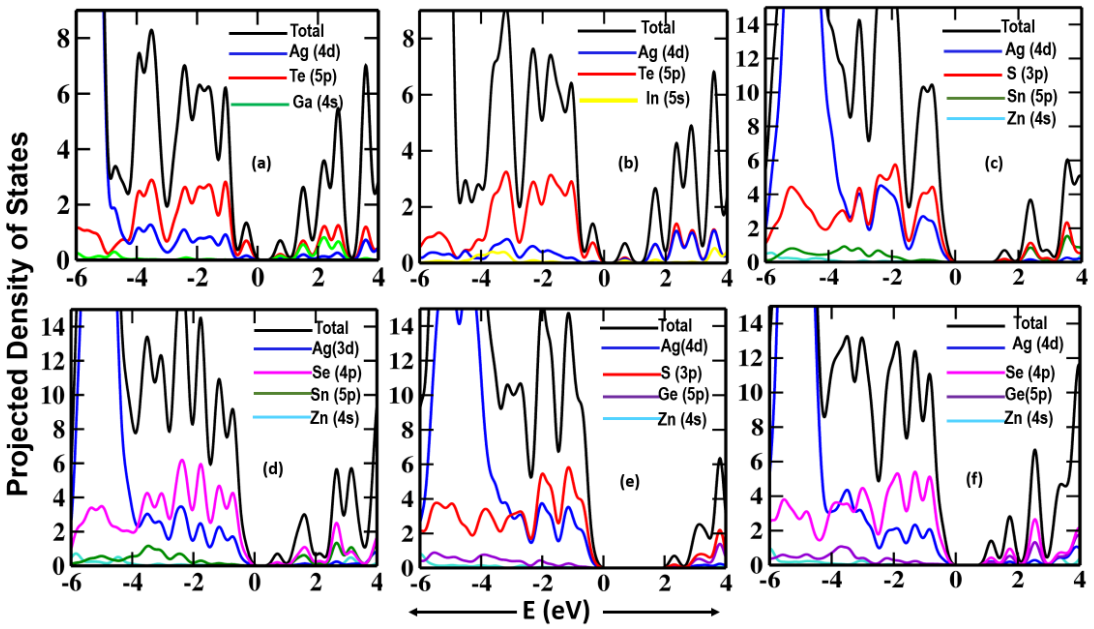

Figure 4.2: Projected density of states (PDOS) for (a) $AgGaTe_2$, (b) $AgInTe_2$, (c) Ag_2ZnSnS_4, (d) $Ag_2ZnSnSe_4$, (e) Ag_2ZnGeS_4, and (f) $Ag_2ZnGeSe_4$ in the energy range from -6 to 4 eV.

The influence of crystal structure on the electronic properties is further illustrated through the projected density of states (PDOS) shown in Fig. 4.2. The PDOS highlights the contribution of individual atomic orbitals to the electronic states, providing insight into how different elements participate in the formation of the valence and conduction bands. These electronic features are closely linked to transport properties, particularly the effective mass and carrier scattering mechanisms, which are discussed in subsequent sections.

4.3.2 Band Structures

We investigated the electronic band structures of AXT (X = Ga, In) and AZPQ (P = Ge/Sn and Q = S/Se) using density functional theory within the dielectric-dependent hybrid (DDH) framework. All studied compounds exhibit direct band gaps located at the Γ point. The calculated band gaps, both with and without spin–orbit coupling (SOC), are summarized in Table 4.3. The inclusion of SOC leads to a noticeable reduction in the band gap, as observed for $AgGaTe_2$ and $AgInTe_2$, where the band gap decreases from 1.25 eV to 1.06 eV and from 1.17 eV to 0.94 eV, respectively. This reduction originates from the strong SOC associated with the heavy Te atoms.

Table 4.3: Calculated band gap with SOC (E_g^{SOC}), without SOC (E_g^{wSOC}), and experimental band gap (E_g^{exp}), along with the valence band maxima (VBM) for the three highest valence bands. Effective masses (m^*) are given for the lowest conduction band (e) and the three highest valence bands (h_1, h_2, h_3), both perpendicular ($\perp$) and parallel ($\parallel$) to the axis in AXT, AZTY, and AZGY using the DDH method. All values are in eV and m_0 (free electron mass).

	AGT	AIT	AZTS	AZTSe	AZGS	AZGSe
E_g^{SOC} (eV)	1.06	0.94	1.80	0.86	2.55	1.40
E_g^{wSOC} (eV)	1.25	1.17	1.82	0.94	2.56	1.45
E_g^{exp} (eV)	1.20[1]	1.04[2]	2.01[3]	1.40[4]	–	–
$VBM_{1,h}$ (eV)	0.00	0.00	0.00	0.00	0.00	0.00
$VBM_{2,h}$ (eV)	-0.002	-0.017	-0.012	-0.0078	-0.006	-0.0051
$VBM_{3,h}$ (eV)	-0.105	-0.077	-0.101	-0.018	-0.166	-0.172
$m^*_{1,e\perp}$	0.091	0.083	0.191	0.116	0.210	0.117
$m^*_{1,e\parallel}$	0.077	0.073	0.186	0.081	0.177	0.107
$m^*_{1,h\perp}$	0.256	0.445	0.679	0.625	0.765	0.525
$m^*_{1,h\parallel}$	0.085	0.083	0.770	0.172	0.215	0.123
$m^*_{2,h\perp}$	0.466	0.387	0.661	0.625	0.781	0.448
$m^*_{2,h\parallel}$	0.086	0.084	0.620	0.155	0.821	0.124
$m^*_{3,h\perp}$	0.138	0.105	0.644	0.355	0.681	0.208
$m^*_{3,h\parallel}$	0.389	0.311	0.611	0.179	0.530	0.563

References for experimental band gaps: [1] [218], [2] [213], [3] [195], and [4] [196].

The band structures of $AgGaTe_2$ and $AgInTe_2$ are shown in Fig. 4.3. The valence band region is primarily dominated by hybridized Ag-d and Te-p orbitals. Due to the large atomic number of Te, its p orbitals contribute significantly to the valence band, leading to pronounced SOC-induced splitting. Specifically, the third valence band shifts to lower energy, while the top two valence bands remain nearly degenerate at the Γ point. In contrast, the SOC contributions from Ag, Ga, and In are comparatively weaker due to their lower atomic masses and reduced orbital contribution near the valence band maximum. This behavior is consistent across both ternary systems. An important observation is the presence of the third valence band ($VBM_{3,h}$), which lies slightly below the topmost valence band. Its energy position is found to be -0.105 eV for $AgGaTe_2$ and -0.077 eV for $AgInTe_2$.

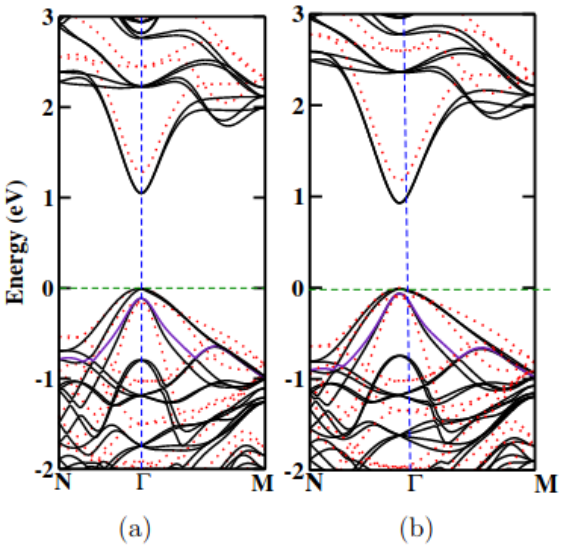

Figure 4.3: Calculated band structures of (a) AGT and (b) AIT using the DDH functional. Bands without SOC are shown as dashed red lines, while those with SOC are shown as solid black lines. The third valence band maximum ($VBM_{3,h}$) is highlighted in purple.

The proximity of this band to the valence band maximum plays a crucial role in determining thermoelectric properties. A lower-lying band reduces carrier excitation, which in turn affects electrical conductivity, Seebeck coefficient, and electronic thermal conductivity [219, 220]. Therefore, it is essential to include all three valence bands in hole transport

calculations to accurately capture carrier contributions.

For quaternary chalcopyrites, the experimental band gaps of AZTS and AZTSe are reported as 2.01 eV and 1.40 eV, respectively [195]. Experimental data for AZGS and AZGSe are not yet available. The calculated band gaps using the DDH functional show that SOC induces relatively small changes in sulfide systems (AZTS and AZGS), whereas more significant changes are observed in selenide systems (AZTSe and AZGSe). Specifically, the band gaps decrease from 1.82 eV to 1.80 eV (AZTS), 0.94 eV to 0.86 eV (AZTSe), 2.56 eV to 2.55 eV (AZGS), and 1.45 eV to 1.40 eV (AZGSe) upon inclusion of SOC. This trend

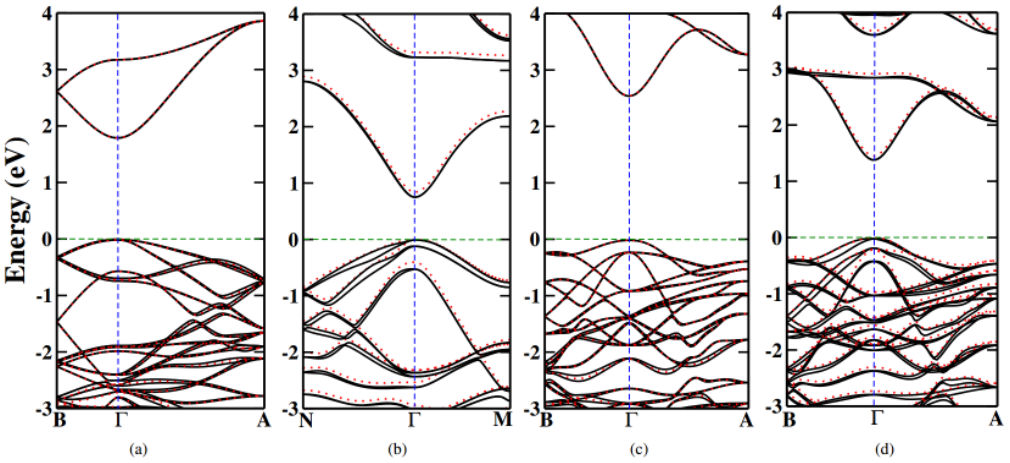

Figure 4.4: Calculated band structures of quaternary chalcopyrites: (a) AZTS, (b) AZTSe, (c) AZGS, and (d) AZGSe. Solid black lines represent calculations including SOC, while red dashed lines correspond to results without SOC.

can be understood from the atomic mass of the chalcogen atoms. Sulfur, being lighter, contributes weaker SOC effects, whereas selenium leads to stronger SOC-induced splitting. Additionally, the difference between Sn and Ge contributes to variations in SOC strength, with Sn exhibiting stronger SOC effects. These effects are clearly visible in Fig. 4.4, where the top valence bands show minimal splitting in sulfide systems but noticeable splitting in selenide systems. In particular, the third valence band exhibits a more pronounced shift compared to the top two bands. Overall, the presence of closely spaced multiple valence

bands is a key feature of these materials and plays a significant role in hole transport. The inclusion of these bands is therefore essential for accurate thermoelectric modeling.

4.3.3 Effective Mass

The effective mass (m^*) of charge carriers, such as electrons and holes in semiconductors, plays a crucial role in determining their transport properties. Physically, it describes the response of carriers to external forces, analogous to their inertia in a periodic potential. A lower effective mass corresponds to higher carrier mobility, enabling faster transport under an applied electric field and resulting in enhanced electrical conductivity. In contrast, a higher effective mass reduces carrier mobility but can increase the density of states near the band edges, which is beneficial for enhancing the Seebeck coefficient [221]. Therefore, an optimal balance between light and heavy effective masses is essential for achieving high thermoelectric performance. The effective mass tensor for electrons and holes is obtained from the curvature of the electronic band structure and is defined as:

$$m^* = \frac{\hbar^2}{\frac{\partial^2 E(\mathbf{k})}{\partial k^2}} ,$$

where $E(\mathbf{k})$ is the energy dispersion relation as a function of the wavevector $\mathbf{k}$. In anisotropic systems, the effective mass is represented as a tensor:

$$\mathbf{M} = \begin{pmatrix} m_{11} & m_{12} & m_{13} \\ m_{12} & m_{22} & m_{23} \\ m_{13} & m_{23} & m_{33} \end{pmatrix} .$$

For the tetragonal chalcopyrite systems considered here, the effective mass tensor can be approximated as diagonal, with m_{11} and m_{22} corresponding to the transverse directions (a and b axes), denoted as $m^*_{i,j\parallel}$, and m_{33} corresponding to the longitudinal direction (c axis), denoted as $m^*_{i,j\perp}$ [222]. The effective masses of electrons in the conduction band and holes in the three highest valence bands are calculated along both longitudinal and transverse directions for all six materials, as summarized in Table 4.3. These values are obtained by fitting

the band dispersion near the Γ point, where the band extrema are located. A clear trend emerges from the calculated results: both electron and hole effective masses are generally smaller in ternary compounds (AGT and AIT) compared to quaternary compounds (AZTS, AZTSe, AZGS, and AZGSe). This can be attributed to the relatively more dispersive bands in ternary systems, indicating stronger band curvature and higher carrier mobility.

In quaternary chalcopyrites, the increased structural complexity and enhanced orbital interactions lead to flatter bands, resulting in larger effective masses. For instance, the heaviest electron effective mass is found to be 0.191 m_0 ($\perp$ direction) in AZTS, while the heaviest hole effective mass reaches 0.821 m_0 ($\parallel$ direction) in quaternary systems, which is significantly larger than the maximum hole effective mass of 0.466 m_0 observed in ternary compounds. As evident from Figs. 4.3 and 4.4, multiple valence bands are present near the valence band maximum in both ternary and quaternary compounds. However, the bands are more closely spaced in the quaternary systems, indicating stronger band convergence. This enhanced band convergence increases the density of states near the valence band maximum, leading to a higher effective mass and improved Seebeck coefficient. Thus, the observed variation in effective mass reflects a trade-off between carrier mobility and density of states. While ternary compounds exhibit higher mobility due to lighter effective masses, quaternary compounds benefit from enhanced Seebeck coefficients owing to stronger band convergence.

In the following section, we analyze how these effective mass characteristics influence the thermoelectric transport properties, including electrical conductivity, Seebeck coefficient, and the overall figure of merit.

4.3.4 Electron Transport Properties

To analyze electronic transport properties, we employ the semi-classical Boltzmann transport equation (BTE) within the relaxation time approximation (RTA) [203], using the Boltz-

TraP2 (BTP2) code [223]. Our calculations spanned the temperature range from 600 to 800 K, with 100 K increments, and encompassed hole carrier concentrations up to 10^{23} cm^{-3}. Within the BTE framework, we determine the Seebeck coefficient (S), electrical conductivity (σ), and electronic contribution to thermal conductivity (κ_e) through the Onsager coefficients, as defined below:

$$S = \frac{1}{qT} \cdot \frac{L^1_{x,y}}{L^0_{x,y}}, \tag{4.3}$$

$$\sigma = L^0_{x,y}, \tag{4.4}$$

$$\kappa_e = \frac{1}{q^2 T} \left(L^2_{x,y} - \frac{(L^1_{x,y})^2}{L^0_{x,y}} \right), \tag{4.5}$$

where q represents the elementary charge, and $L^i_{x,y}$ denotes the kernel of the generalized transport coefficient at temperature T, expressed as [224]:

$$L^i_{x,y} = q^2 \sum_{x,y} \tau_{x,y} v^2_{x,y} \left(\varepsilon_{x,y} - \mu\right)^i \left(-\frac{\partial f_{x,y}}{\partial \varepsilon_{x,y}} \right), \tag{4.6}$$

Here, $\tau_{x,y}$, $v_{x,y}$, $\varepsilon_{x,y}$, and $f_{x,y}$ respectively represent the electronic relaxation time, group velocity, energy, and Fermi–Dirac distribution function of the xth band at wave vector y. From Eqs. 4.4, 4.5, and 4.6, it is evident that the electrical conductivity (σ) and electronic thermal conductivity (κ_e) depend explicitly on the relaxation time τ, making its accurate determination essential for reliable transport predictions. A commonly adopted approach within the BTE framework is the constant relaxation time approximation (CRTA), where $\tau = \tau_0$ is assumed to be constant [225, 226, 227]. Within this approximation, the BTP2 code provides reduced transport coefficients, $\sigma_0 = \sigma/\tau_0$ and $\kappa_{e,0} = \kappa_e/\tau_0$, which depend on the electronic structure, temperature, and carrier concentration, but are independent of the actual value of τ_0. While CRTA simplifies the computational procedure and captures qualitative trends, it neglects the energy and temperature dependence of carrier scattering processes. As a result, it limits the accuracy of quantitative transport predictions.

To overcome this limitation and obtain a more realistic estimate of transport properties, the relaxation time τ is calculated explicitly using deformation potential theory [228, 229] is utilized within the single parabolic band (SPB) model. The relaxation time for a three-dimensional system is expressed as [230, 231]:

$$\tau = \frac{1}{3} \times 2\sqrt{2\pi} \cdot \frac{C\overline{h}^4}{(k_B T m^*_{\text{dos}})^{3/2}} \left(\frac{1}{D}\right)^2 . \tag{4.7}$$

Here, $\overline{h}$ is the reduced Planck constant, C denotes the elastic constant, k_B is the Boltzmann constant, m^*_{dos} is the density-of-states effective mass (for p-type systems, hole effective mass is considered), and D represents the deformation potential. The calculated elastic constants,

Table 4.4: The calculated single-crystal elastic constants C_{ij} (in GPa), deformation potentials for both electrons D(e) and holes D(h) (in eV), longitudinal (v_L; in m/s), transverse (v_T; in m/s), average sound velocity ($\bar{v}$; in m/s), and Debye temperature (Θ_D; in K) for materials AXT, AZTY, and AZGY (where X = G, I; Y = S, Se) using the Dielectric Dependent Hybrid approach.

Property	AGT	AIT	AZTS	AZTSe	AZGS	AZGSe
C_{11} (GPa)	53.90	49.55	72.11	55.99	83.27	75.97
C_{12} (GPa)	30.99	31.47	58.26	43.28	51.75	48.04
C_{13} (GPa)	33.82	30.94	37.45	41.06	60.99	47.14
C_{33} (GPa)	52.72	48.24	68.01	71.26	83.22	75.97
C_{44} (GPa)	41.38	35.23	25.81	41.14	51.71	47.27
C_{66} (GPa)	36.60	34.24	59.24	46.70	51.50	46.28
D(e) (eV)	5.31	9.08	11.23	9.22	14.19	8.09
D(h) (eV)	4.49	8.61	8.82	7.79	10.35	6.88
v_L (m/s)	3527.86	3373.97	3845.77	4222.68	5217.12	4117.47
v_T (m/s)	2020.93	1899.99	3895.31	2605.64	3253.21	2248.92
$\bar{v}$ (m/s)	2245.14	2113.82	3878.51	2874.30	3584.63	2508.03
Θ_D (K)	211.3	192.2	403.20	284.6	380.4	253.3

deformation potentials, and related parameters are listed in Table 4.4. All materials satisfy

the mechanical stability criteria for tetragonal systems:

$$C_{11} > C_{12}, \tag{4.8}$$

$$2C_{13}^2 < C_{33}(C_{11} + C_{12}), \tag{4.9}$$

$$C_{44} > 0, \tag{4.10}$$

$$C_{66} > 0. \tag{4.11}$$

The relaxation time calculated using Eq. 4.7 is plotted in Fig. 4.5. It is observed that τ decreases with increasing temperature due to enhanced phonon scattering. Among the studied materials, AZGSe exhibits the highest relaxation time, while AIT shows the lowest. At 800 K, τ values for AGT and AIT are 0.98×10^{-14} s and 0.44×10^{-14} s, respectively, whereas quaternary systems show comparatively larger values. This indicates that quaternary chalcopyrites experience relatively weaker scattering interactions, resulting in longer relaxation times. Although deformation potential theory may overestimate τ due to neglect of additional scattering mechanisms, the relative trends remain reliable.

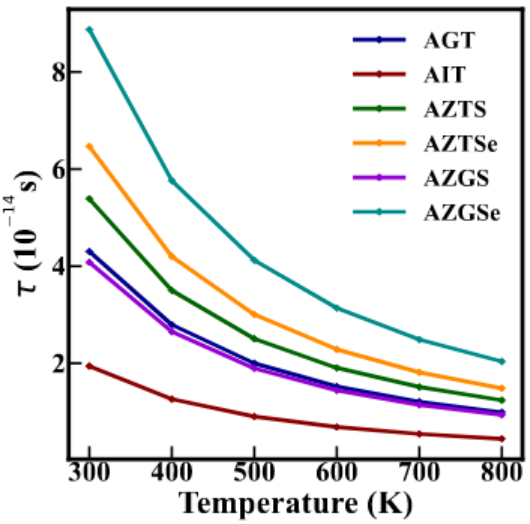

Figure 4.5: Calculated values of relaxation time τ using deformation potential theory over the temperature range of 300–800 K.

Transport Properties of AXT Systems

Using the calculated relaxation time and band structure (Fig. 4.3), transport coefficients are computed using BTE-RTA. Fig. 4.6 shows that the Seebeck coefficient decreases with increasing carrier concentration, whereas electrical conductivity increases. This interplay leads to an optimal power factor ($S^2\sigma$) at intermediate carrier concentrations. At low carrier concentration and high temperature, a weak bipolar effect is observed in κ_e, arising from thermally excited minority carriers. However, the absence of sign reversal in the absence of sign reversal in the Seebeck coefficient indicates that hole carriers remain dominant, confirming a weak bipolar contribution at high temperatures. The maximum power factor for AGT reaches 27.7 μW/cmK^2 at 800 K, whereas AIT exhibits a lower value of 13.53 μW/cmK^2.

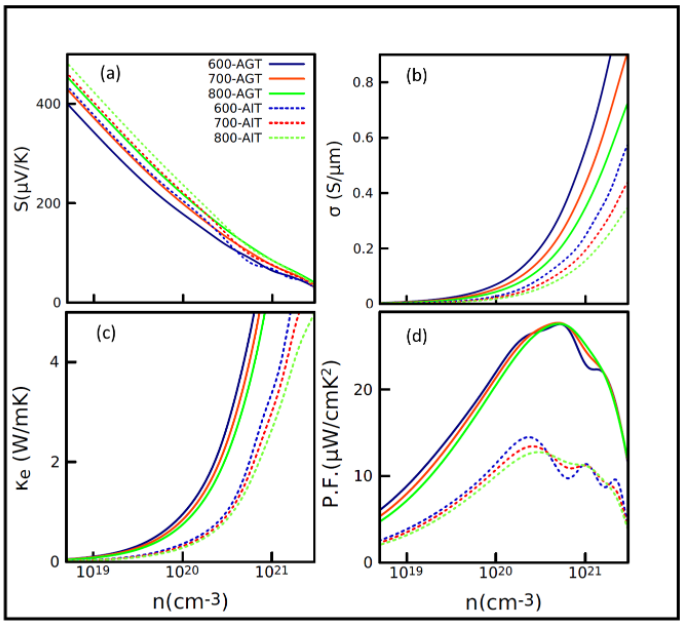

Figure 4.6: Seebeck coefficient, electrical conductivity, electronic thermal conductivity, and power factor as a function of carrier concentration for AGT and AIT at different temperatures.

Transport Properties of AZPQ Systems

Comprehending the transport properties of quaternary chalcopyrites presents a more intricate task compared to their ternary counterparts. This complexity stems from the introduction of an additional element and the resulting intricate interactions within the material [195]. Through the analysis of the scattering time (τ), we can extract valuable insights into the mechanisms governing heat and charge transport within these materials [226]. In AZPQ-type compositions, the incorporation of an additional element relative to ternary chalcopyrites provides greater control over several crucial properties, including the band gap, carrier concentration, and scattering mechanisms influencing transport. This enhanced tunability is beneficial for optimizing thermoelectric performance. The Seebeck coefficient (S), a crucial parameter in thermoelectric materials, shows a notable enhancement for AZPQ systems, as shown in Fig. 4.7(a) and (e), compared to their AXT counterparts within the same range of hole doping concentration (Fig. 4.6).

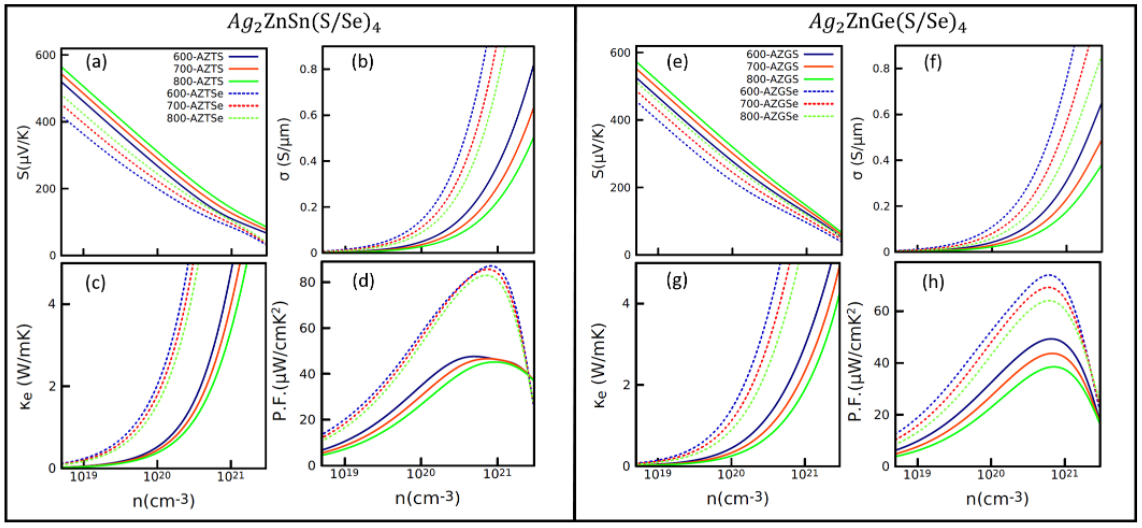

Figure 4.7: Transport coefficients as a function of carrier concentration for quaternary chalcopyrites at different temperatures.

This enhancement originates from stronger band convergence near the valence band

maximum (Fig. 4.4), which increases the density of states (Fig. 5.3(c)-(f)) and the corresponding density-of-states effective mass, as summarized in Table 4.1. This combined effect leads to an improved Seebeck response.

In addition, AZPQ materials exhibit relatively high electrical conductivity (σ) compared to AXT systems (Fig. 4.7(b) and (f)), indicating that the increase in effective mass does not significantly degrade carrier transport. The simultaneous presence of enhanced Seebeck coefficient and high electrical conductivity results in significantly improved power factors. As shown in Fig. 4.7(d), the optimal power factor ($S^2\sigma$) for AZTSe reaches 87.5 μW/cmK^2 at a hole doping concentration of 8.2×10^{20} cm^{-3}, which is significantly higher than that of AZTS, which exhibits a PF of 47.7 μW/cmK^2 at a lower carrier concentration of 5.4×10^{20} cm^{-3}. On the other hand, AZGSe and AZGS, both Ge-based materials, exhibit PF values of 74.7 μW/cmK^2 and 49.4 μW/cmK^2, respectively, at a hole doping level of 6.2×10^{20} cm^{-3} (Fig. 4.7(h)). A comparison between Sn- and Ge-based systems indicates that Se-based compounds consistently show higher PF than their S-based counterparts.

If the total thermal conductivity ($\kappa = \kappa_e + \kappa_l$) follows a similar trend, this could limit the overall thermoelectric performance of Se-based materials. A higher thermal conductivity enhances heat flow across the material, reducing the temperature gradient and thereby lowering the Seebeck voltage. Therefore, although Se-based materials exhibit superior power factors, their overall efficiency depends on achieving an optimal balance between electrical transport and thermal conductivity. Maximizing the thermoelectric figure of merit (ZT) requires careful optimization of these competing factors.

4.3.5 Lattice thermal transport

Optimization of the thermoelectric figure of merit (ZT) requires careful consideration of the total thermal conductivity (κ), which consists of both electronic (κ_e) and lattice (κ_l) contributions. While κ_e can be obtained from the Boltzmann transport equation (Eq. 4.5),

the direct calculation of κ_l using the full phonon BTE is computationally demanding due to the complexity of phonon interactions [232, 233]. To overcome this limitation, we employ Slack's model, which provides an efficient and reliable estimate of lattice thermal conductivity based on macroscopic material parameters [234, 235]. The lattice thermal conductivity is expressed as:

$$\kappa_l = A\frac{\delta\,\overline{M}\,\Theta^3}{\gamma^2\,n^{2/3}\,T}, \tag{4.12}$$

where δ^3, $\overline{M}$, Θ, γ, n, and T represent the volume per atom, average atomic mass, acoustic Debye temperature, Grüneisen parameter, number of atoms in the primitive unit cell, and temperature, respectively. The constant A is given by:

$$A = \frac{2.43\times10^{-8}}{1-\frac{0.514}{\gamma}+\frac{0.228}{\gamma^2}}. \tag{4.13}$$

From Eq. 4.12, it is evident that the evaluation of lattice thermal conductivity requires the determination of two key quantities: the acoustic Debye temperature (Θ) and the Grüneisen parameter (γ), which describe the phonon spectrum and lattice anharmonicity, respectively. In this work, the Grüneisen parameter is estimated using elastic properties following the approach proposed by Xiao *et al.* [236]. This method relates lattice anharmonicity to the elastic response of the material through Poisson's ratio, thereby avoiding computationally expensive phonon calculations. The Grüneisen parameter is given by:

$$\gamma = \frac{3}{2}\left(\frac{1+\nu}{2-3\nu}\right). \tag{4.14}$$

Here, Poisson's ratio (ν) acts as an intermediate parameter linking the elastic response to lattice anharmonicity. It is expressed in terms of longitudinal (v_L) and transverse (v_S) sound velocities as:

$$\nu = \frac{1-2\left(\frac{v_S}{v_L}\right)^2}{2-2\left(\frac{v_S}{v_L}\right)^2}. \tag{4.15}$$

The sound velocities are obtained from the elastic constants and density of the material as:

$$v_L = \sqrt{\frac{B + \frac{4}{3}G}{\rho}}, \quad v_S = \sqrt{\frac{G}{\rho}}, \tag{4.16}$$

and the average sound velocity ($\overline{v}$) is given by:

$$\overline{v} = \left[\frac{1}{3}\left(\frac{1}{v_L^3} + \frac{2}{v_S^3}\right)\right]^{-1/3}. \tag{4.17}$$

Using the average sound velocity, the acoustic Debye temperature is calculated as:

$$\Theta = \frac{h}{k_B}\left(\frac{3m}{4\pi}\right)^{1/3} \overline{v}\, n^{-1/3}. \tag{4.18}$$

Table 4.5: The calculated Voigt, Reuss, and Hill moduli: bulk modulus (B), shear modulus (G), Young's modulus (E), Poisson's ratio (η_p), and the ratio of bulk to shear modulus (B/G) for AXT (X = Ga, In), AZTY, and AZGY (Y = S, Se). Values for moduli are in GPa, while ratios are dimensionless.

Material	Bulk Modulus (B)			Shear Modulus (G)			Young's Modulus (E)			Poisson's Ratio (η_p)			B/G Ratio		
	Voigt	Reuss	Hill	Voigt	Reuss	Hill	Voigt	Reuss	Hill	Voigt	Reuss	Hill	Voigt	Reuss	Hill
AGT	39.76	39.75	39.76	28.00	18.38	23.19	68.03	47.78	58.25	0.21	0.30	0.26	1.42	2.16	1.71
AIT	37.12	37.10	37.11	24.56	16.22	20.39	60.37	42.47	51.70	0.23	0.30	0.27	1.51	2.28	1.82
AZTS	55.01	51.50	52.35	23.44	19.05	20.43	56.7	49.99	52.87	0.27	0.33	0.31	2.34	2.70	2.56
AZTSe	48.23	47.74	47.98	56.97	17.26	13.11	122.63	46.20	88.52	0.08	0.33	0.19	0.85	2.76	1.29
AZGS	59.41	59.31	59.36	18.10	77.76	47.93	49.29	162.35	113.30	0.36	0.04	0.18	3.28	0.76	1.23
AZGSe	55.69	55.09	55.38	33.93	20.94	27.43	84.61	55.76	70.64	0.25	0.33	0.28	1.64	2.63	4.31

Thus, the lattice thermal conductivity is evaluated through a sequential procedure: elastic constants (B, G) are first used to determine sound velocities (v_L, v_S), which yield Poisson's ratio (ν), and subsequently the Grüneisen parameter (γ). The sound velocities also provide the Debye temperature (Θ), and these quantities (given in Table 4.4) are finally substituted into Eq. 4.12 to obtain κ_l. The required elastic properties, including bulk modulus (B), shear modulus (G), and Young's modulus (E), are derived from the elastic constants tensor [237]. The Voigt–Reuss–Hill approximation [238, 239] is employed to evaluate B, G, and Poisson's ratio, as summarized in Table 4.5. The B/G ratio is used to assess the mechanical nature of the material, where values below 2 indicate ductile behavior. Once

all parameters are determined, the lattice thermal conductivity is calculated using Eq. 4.12 and plotted as a function of temperature, as shown in Fig. 4.8. A decreasing trend in κ_l with increasing temperature is observed, which can be attributed to enhanced phonon–phonon scattering at elevated temperatures.

To validate the accuracy of this approach, the calculated values for AGT and AIT are compared with experimental results of 1.7 W/mK and 0.94 W/mK at 300 K, respectively [240, 241]. Among all materials, AZTS exhibits the highest lattice thermal conductivity, while AZTSe shows the lowest, highlighting the role of atomic mass and lattice anharmonicity in governing phonon transport. The optimized values of κ_l at 800 K are found to be 0.52, 0.67, 0.71, 0.45, 0.46, and 0.54 W/mK for AGT, AIT, AZTS, AZTSe, AZGS, and AZGSe, respectively.

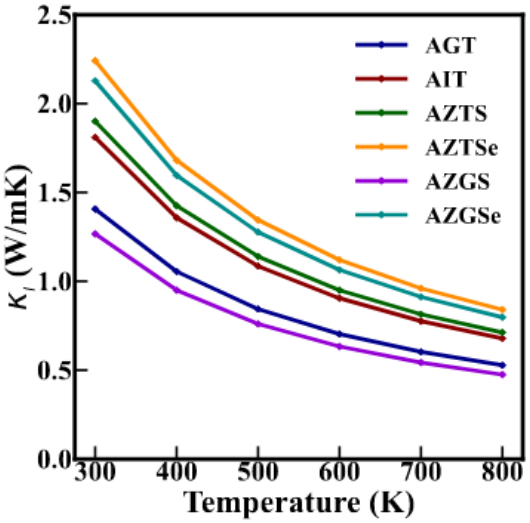

Figure 4.8: The computed lattice thermal conductivity obtained through Eq. 4.12, covering the temperature range from 300K to 800K.

4.3.6 Figure of merit

An accurate estimation of the thermoelectric figure of merit (ZT) requires reliable evaluation of both the electron relaxation time (τ) and lattice thermal conductivity (κ_l). The in-

herent structural complexity of ternary and quaternary chalcopyrites, characterized by low symmetry and large unit cells, poses a significant challenge for many-body calculations of τ. To address this, we employ the deformation potential (DP) method, which accounts for the interaction between charge carriers and acoustic phonons, as originally proposed by Bardeen and Shockley, as described in Section 4.3.4. Although the DP approach neglects Coulombic scattering from polar optical phonons, it has proven to be a reasonably accurate and efficient approximation for thermoelectric materials.

According to the Fröhlich model [242], the Coulombic interaction associated with electron–polar optical phonon scattering can be effectively screened in materials with large dielectric constants (ϵ_∞ and ϵ_s). As reported in previous studies [243], large dielectric constants are a desirable characteristic of efficient thermoelectric materials, thereby justifying the use of the DP approximation for estimating τ in the present systems. Using the calculated relaxation time and lattice thermal conductivity, the figure of merit ZT is evaluated for all compounds, as shown in Fig. 4.9. The relaxation time decreases with increasing temperature, approximately following a $T^{-3/2}$ dependence as given in Eq. 4.7. Consequently, the variation of ZT with temperature exhibits a dome-like behavior, with a maximum around 800 K. Therefore, ZT is analyzed in the temperature range of 600–800 K.

For p-type thermoelectric materials, thermal excitation of minority carriers becomes more prominent at low hole concentrations and high temperatures. As shown in Fig. 4.9(a–c), at lower hole concentrations the variation in ZT with temperature is relatively small due to this thermal excitation effect. Overall, ZT strongly depends on both carrier concentration and temperature. There are limited reports on the thermoelectric performance of AGT and AIT in the literature [244, 188, 245]. As shown in Fig. 4.9(a), AGT exhibits nearly isotropic ZT values of 1.14 and 1.40 at 700 K and 800 K, respectively, at a hole carrier concentration of 4.88×10^{19} cm^{-3}. These values indicate efficient heat-to-electricity conversion, making AGT a promising candidate for high-temperature thermoelectric applications. In contrast,

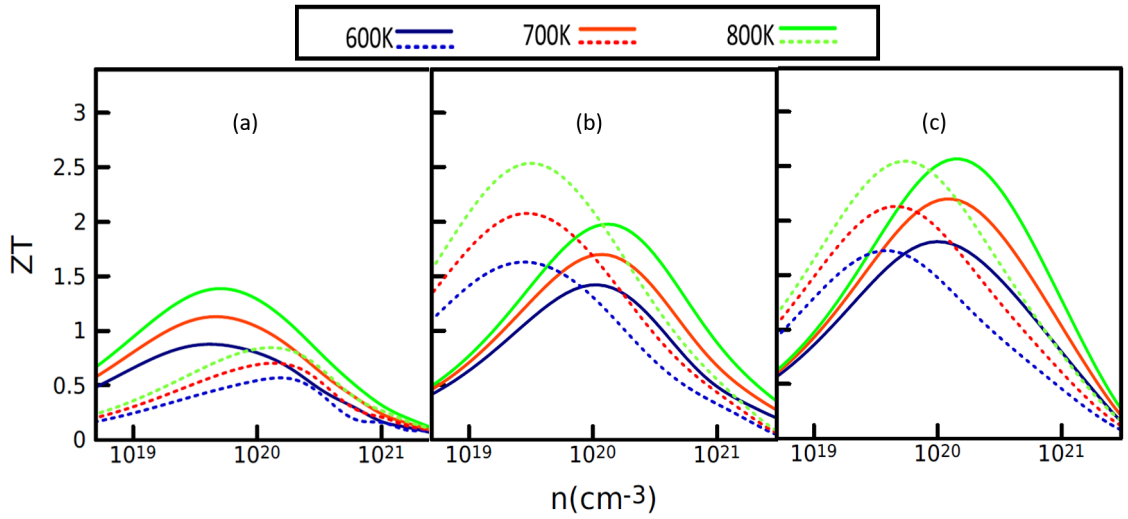

Figure 4.9: The computed thermoelectric figure of merit ZT as a function of carrier concentration at temperatures of 600 K, 700 K, and 800 K for various compounds: (a) AGT (solid lines) and AIT (dotted lines), (b) AZTS (solid lines) and AZTSe (dotted lines), and (c) AZGS (solid lines) and AZGSe (dotted lines).

AIT exhibits a maximum ZT of 0.86 at a hole concentration of 1.29×10^{20} cm^{-3}, suggesting comparatively weaker transport performance. The inability to achieve $ZT > 1$ indicates limited thermoelectric efficiency in comparison to AGT. Furthermore, at 600 K, AGT shows a ZT value of 0.90 at a hole concentration of 10^{19} cm^{-3}, indicating reduced performance at lower temperatures.

For quaternary chalcopyrites, experimental validation for the proposed Ag-based systems is currently lacking. Based on the power factor comparison shown in Fig. 4.7(d) and (h), Se-based quaternary compounds are expected to exhibit superior thermoelectric performance compared to S-based counterparts. For AZTS, a maximum ZT of 1.98 at 800 K is achieved at a hole concentration of 1.34×10^{20} cm^{-3}, whereas AZTSe reaches a higher ZT of 2.53 at 800 K at a lower hole concentration of 3.25×10^{19} cm^{-3}. These results indicate excellent thermoelectric performance in quaternary systems. It is important to note that AZGS, like many quaternary chalcogenides with cation-substituted tetrahedral (CST)

networks, exhibits a quasi-linear conduction band, resulting in negligible n-type thermoelectric behavior. AZGSe also behaves as a p-type material, achieving ZT values of 1.72, 2.13, and 2.55 at 600 K, 700 K, and 800 K, respectively, at corresponding hole concentrations of 4.9×10^{19}, 5.8×10^{19}, and 7×10^{19} cm^{-3}. An interesting observation is that although AZGSe exhibits a higher power factor than AZGS (Fig. 4.7(h)), the ZT of AZGS is higher. This difference arises from the lower lattice thermal conductivity (κ_l) of AZGS compared to AZGSe, as shown in Fig. 4.8. This highlights the critical role of lattice thermal conductivity in determining the overall thermoelectric performance.

Among the six materials studied, all compounds except AGT and AIT exhibit $ZT > 1$ at high carrier concentrations (10^{19}–10^{21} cm^{-3}) up to 700 K, indicating strong potential for thermoelectric applications. At higher temperatures (800 K), AGT also achieves $ZT > 1$, making it a promising candidate for high-temperature operation. These results demonstrate the potential of these materials for efficient waste heat conversion. However, it is important to note that real materials may exhibit additional scattering mechanisms not captured in density functional theory (DFT) calculations. Therefore, experimental validation is essential to confirm the predicted performance. In addition to a high figure of merit, practical thermoelectric materials must also exhibit good dopability. Diamond-like chalcogenides are known for their excellent p-type dopability, allowing effective tuning of electronic properties. This characteristic is crucial for optimizing thermoelectric performance and advancing practical energy conversion technologies.

4.4 Conclusions

We have performed first-principles calculations utilizing the non-empirical range-separated DDH approach to investigate the TE properties of ternary and quaternary Ag-based chalcopyrites. The DDH method enables an accurate description of the electronic band struc-

ture, which is essential for reliable prediction of thermoelectric properties.

Among the studied materials, AZGS exhibits the largest band gap of 2.52 eV, along with noticeable SOC effects arising primarily from the chalcogen atoms. These features play an important role in determining the electronic transport behavior. To describe charge carrier scattering, the deformation potential (DP) theory has been employed to calculate the relaxation time, capturing the interaction between charge carriers and acoustic phonons. The obtained values are in good agreement with available experimental data, thereby supporting the validity of the theoretical approach. The lattice thermal conductivity (κ_L) has been estimated using Slack's model, which provides an efficient alternative to computationally intensive phonon calculations. This approach is well suited for semiconductors where phonon–phonon scattering dominates, and the obtained results follow trends consistent with experimental observations, confirming its reliability within the considered temperature range.

Our results demonstrate that AZGS is the most promising thermoelectric material among the studied systems, achieving a maximum ZT of 2.57 at 800 K. In addition, AZGSe and AZTSe also exhibit excellent thermoelectric performance, with ZT values of 2.55 and 2.53 at 800 K, respectively. AZTS further shows competitive behavior with a ZT of 1.98 at 800 K. Overall, the quaternary chalcopyrites display superior thermoelectric performance in the temperature range of 600–800 K. While AGT exhibits promising performance at higher temperatures, its efficiency decreases at lower temperatures. These findings highlight the strong potential of quaternary Ag-based chalcopyrites for high-temperature thermoelectric applications. The combination of accurate electronic structure from the DDH functional and efficient transport modeling establishes a reliable framework for predicting thermoelectric performance. This work provides valuable insights and a solid foundation for further theoretical and experimental investigations toward the development of efficient thermoelectric materials for sustainable energy conversion.

Chapter 5

Noncollinear Magnetism in Pristine Two-Dimensional Systems

This chapter constitutes the second part of the thesis and focuses on the emergence of spin-dependent phenomena in 2D materials. Reduced dimensionality leads to broken inversion symmetry and enhanced SOC, giving rise to novel magnetic interactions. In this work, we investigate the Heisenberg exchange interaction, magnetic anisotropy energy (MAE), and the DMI. These interactions determine the magnetic ground state, the preferred spin orientation, and the emergence of chiral spin textures, respectively. Unlike conventional approaches relying on external engineering, we focus on pristine 2D systems where these effects arise intrinsically. The role of strain and electronic correlations in tuning these interactions is also explored.

This chapter is based on the following published work:

[1] **D. Rani**, B. R. K. Nanda, and P. Samal, *Physical Review B*, **112**, 174401 (2025).

5.1 Introduction

Following the investigation of bulk chalcopyrite semiconductors and their thermoelectric transport in the previous Chapters 3, 4, we now turn our attention to low-dimensional systems, where reduced dimensionality gives rise to fundamentally different physical phenomena. In particular, two-dimensional 2D materials exhibit broken inversion symmetry, reduced coordination, and enhanced quantum confinement, which significantly amplify the role of SOC.

SOC is a fundamental mechanism driving various spin-dependent interactions in low-

dimensional systems. In 2D materials, SOC leads to phenomena such as the DMI, magnetic anisotropy energy (MAE), and Rashba spin splitting, all of which are crucial for controlling spin textures and magnetic anisotropies [246, 247]. These effects become particularly prominent in systems with broken inversion symmetry and strong electronic correlations, offering opportunities to engineer spintronic functionalities directly within atomic layers [45, 248].

Recent studies have identified 2D TMDCs of the form MX_2 as promising platforms for spintronic applications due to their intrinsic magnetic and electronic properties [249, 250]. TMDCs consist of transition metals (M = Mn, Fe, Ni, V, Cr, Sc, Ti) and chalcogen atoms (X = S, Se, Te), forming layered structures held together by van der Waals forces. This structural feature allows these materials to be exfoliated into atomically thin monolayers, enabling quantum confinement effects and enhanced interfacial interactions. TMDCs exhibit a rich diversity of physical behaviors, ranging from semiconducting to metallic and superconducting phases, driven by their tunable band gaps and diverse crystal symmetries [251]. Importantly, the presence of heavy transition metals results in strong SOC, a critical ingredient in determining magnetic anisotropy and DMI. TMDCs with magnetic elements such as Fe, Cr, and Mn show robust magnetism even at the monolayer level [13, 41]. Furthermore, the DMI in these systems can be effectively tuned via external strain, magnetic fields, or interface engineering with high-SOC materials [252, 49], making them attractive candidates for the development of next-generation spintronic technologies [253].

The DMI arises in systems with strong SOC and broken inversion symmetry, often occurring at interfaces between magnetic and non-magnetic layers or in bulk non-centrosymmetric crystals [254, 255, 256]. This antisymmetric exchange interaction is expressed as $\sum_{\langle i,j \rangle} \mathbf{d}_{ij} \cdot (\mathbf{S}_i \times \mathbf{S}_j)$, where $\mathbf{d}_{ij}$ represents the DMI vector between neighboring spins $\mathbf{S}_i$ and $\mathbf{S}_j$. Unlike the conventional Heisenberg exchange interaction, which favors collinear spin alignment, DMI stabilizes noncollinear and chiral magnetic configurations [257]. In magnetic multi-

layer systems, DMI is typically interfacial, arising from the interaction between ferromagnetic layers (such as Co, Fe, or Ni) and heavy non-magnetic layers with strong SOC (such as Pt, Ir, or W) [252]. The SOC of the non-magnetic layer induces a torque on neighboring spins, leading to a preferred rotational alignment and stabilizing chiral spin textures such as spin spirals and skyrmions [258, 259]. The interplay between DMI, perpendicular magnetic anisotropy (PMA), and Heisenberg exchange governs the stability, symmetry, and dynamics of magnetic textures [49, 260, 261]. This competition often leads to the emergence of noncollinear spin configurations and plays a central role in spin dynamics at the nanoscale [262].

Magnetic ordering has been extensively studied in a wide range of materials, including non-centrosymmetric bulk compounds such as MnSi, FeGe, CoGe, and GdFeCo [263, 264, 265, 266]. In addition, interfacial multilayer systems like Pt/Co/Ir, Pt/CoFe/MgO, Ta/CoFe/MgO, and Ir(111)/Fe exhibit rich magnetic behavior driven by strong SOC and broken inversion symmetry [252, 267, 48]. With the advent of low-dimensional magnetism, recent studies have focused on intrinsic two-dimensional magnetic systems such as $MnBi_2Te_4$ [268], Fe_nGeTe_2 ($n = 3, 4, 5$) [269], CrI_3 [46], $CrGeTe_3$ [270], and VSe_2 [271]. These materials provide ideal platforms for exploring magneto-optical and magnetoelectric effects at the atomic scale. Furthermore, Janus monolayers such as $Cr_2X_3Y_3$ (X, Y = Cl, Br, I; X $\neq$ Y) [272], MnXY (X, Y = S, Se, Te; X $\neq$ Y) [273], and CrXTe (X = S, Se) [274] introduce additional symmetry breaking, enabling enhanced DMI and novel magnetic interactions.

Motivated by these developments, we focus on the pristine $FeTe_2$ monolayer, which has been identified as a promising candidate for spintronic applications [249, 250]. Despite its potential, there are very limited studies addressing the role of DMI in this system. We consider the H-phase $FeTe_2$ structure (point group D_{3h}), which inherently lacks inversion symmetry and contains heavy Te atoms, making it suitable for strong SOC-driven interac-

tions [275]. To investigate its magnetic properties, we systematically apply biaxial strain ranging from -6% to 6%, ensuring structural stability through phonon dispersion analysis. Our results show that both strain and electronic correlation significantly influence the magnetic anisotropy energy (MAE), including a sign reversal that enables switching of the magnetic easy axis from in-plane to out-of-plane. A large variation in MAE, from -6 to 5.3 meV, is observed due to the redistribution of spin-polarized electronic states. Additionally, the competition between exchange interactions (including direct and superexchange mechanisms) and DMI leads to complex noncollinear magnetic behavior in $FeTe_2$. These findings demonstrate that pristine 2D TMDC can host strong and tunable spin-dependent interactions intrinsically, without the need for external engineering. Our study provides fundamental insights into the design of 2D magnetic materials for next-generation spintronic applications.

5.2 Structural & Computational Details

Fig. 5.1(a) presents the top and side views of the monolayer H-phase $FeTe_2$, which crystallizes in a hexagonal structure with point group D_{3h}. In this configuration, a layer of Fe atoms is sandwiched between two layers of Te atoms. The Fe atoms are coordinated by Te atoms in a trigonal prismatic geometry, a characteristic feature of transition metal dichalcogenides. This structural arrangement governs the splitting of Fe d-orbitals, thereby influencing the electronic and magnetic properties of the system. Moreover, the absence of inversion symmetry combined with the presence of heavy Te atoms makes this system an ideal platform to investigate SOC-driven effects such as magnetic anisotropy and the DMI [250].

The first-principles calculations for the $FeTe_2$ monolayer are performed within the framework of DFT using the Vienna *Ab initio* Simulation Package (VASP) [156]. The electron–

ion interactions are described using the PAW method [108, 109], while the exchange–correlation effects are treated using the PBE functional within the GGA [145]. To properly account for the strong correlation effects associated with Fe $3d$ electrons, the DFT+U approach is employed [250, 276]. The Kohn–Sham wave functions are expanded in a plane-wave basis with a kinetic energy cutoff of 480 eV. The Brillouin zone is sampled using a Γ-centered $18 \times 18 \times 1$ Monkhorst–Pack k-point grid. To accurately evaluate the magnetic exchange interactions (J_1, J_2, and J_3), a 4×4 supercell is used, which allows inclusion of first-, second-, and third-nearest-neighbor interactions essential for describing the Heisenberg exchange.

For the calculation of DMI, a 4×1 supercell is employed, where the spin orientation of Fe atoms is rotated in both clockwise and anticlockwise directions. This approach enables the extraction of chiral asymmetry in the system, which is necessary for determining the DMI vector and its influence on the magnetic properties. Phonon dispersion calculations are carried out using the PHONOPY package [277] to confirm the dynamical stability of the structures. To evaluate the DMI vectors ($\mathbf{d}_{ij}$), the calculations are performed in three stages. First, the atomic structures are fully relaxed until the total energy and force converge below 10^{-6} eV and 0.001 eV/Å, respectively. Subsequently, the Kohn–Sham equations are solved without SOC to obtain the ground-state charge density. In the final step, SOC is included, and the total energy is computed self-consistently as a function of the spin orientation using the constrained magnetic moment method implemented in VASP. This approach, previously applied to bulk frustrated systems and insulating chiral magnets [278], is adapted here to analyze the DMI in the $FeTe_2$ monolayer.

5.3 Results and Discussion

5.3.1 Structural Stability & Strain

Biaxial strain (ϵ) is applied by uniformly varying the in-plane lattice constants ($a = b$) from -6% to $+6\%$ in steps of 2%, as shown in Fig. 5.1(e). The dynamical stability of both unstrained and strained structures is examined through phonon spectra calculated using a 4×4 supercell (Figs. 5.1(b)–5.1(d)). The absence of imaginary phonon modes confirms that the H-$FeTe_2$ monolayer remains dynamically stable within this strain range, while instability appears beyond 6% strain.

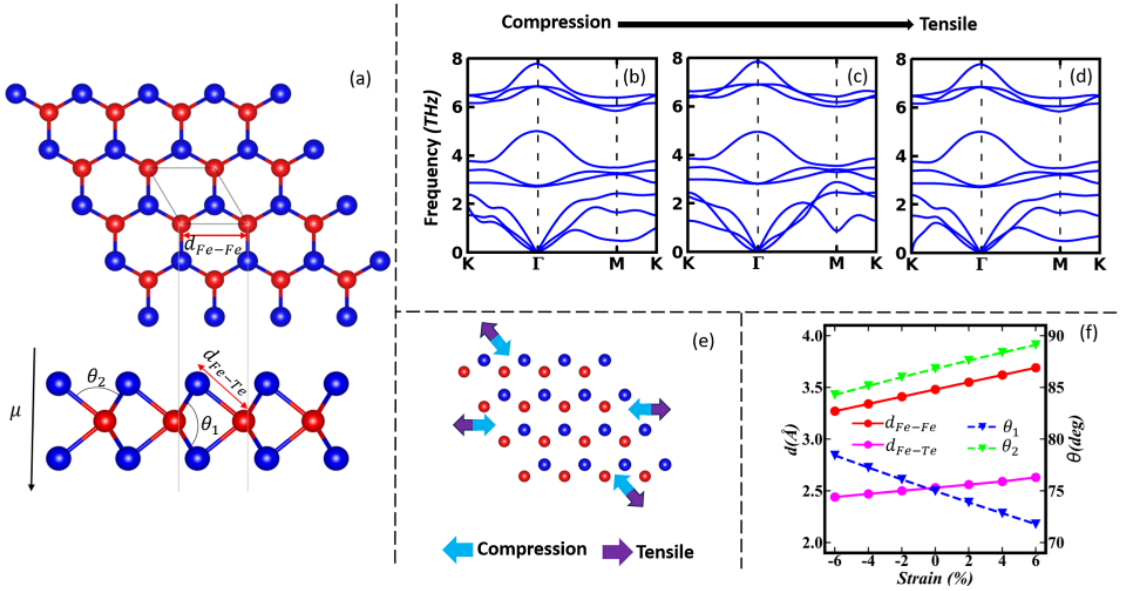

Figure 5.1: **Structure of $FeTe_2$ monolayer under strain.** (a) Top and side views of the 2H phase of the $FeTe_2$ monolayer. In the top view, the atomic arrangement is shown with Fe atoms (red spheres) and Te atoms (blue spheres), where $d_{\text{Fe–Fe}}$ denotes the in-plane lattice constant. The side view illustrates the bond lengths $d_{\text{Fe–Te}}$ and the bond angles θ_1 and θ_2. (b)-(d) Phonon band structure of the $FeTe_2$ monolayer at -6, 0 and 6 % strain, confirming its dynamic stability. (e) Schematic diagram showing the application of biaxial strain on the top surface of the $FeTe_2$ monolayer. (f) Variation of bond lengths ($d_{\text{Fe–Te}}$) and bond angles (θ_1, θ_2) as a function of applied biaxial strain (%).

The H-$FeTe_2$ structure lacks inversion symmetry, leading to an asymmetric local en-

vironment around Fe atoms. Although the Fe–Te bond lengths are equal, the bond angles differ ($\theta_1 \neq \theta_2$), resulting in local symmetry breaking. According to Moriya's theory [256], such asymmetry in the presence of SOC allows the emergence of DMI. For hexagonal symmetry, the DMI vector lies in-plane and is perpendicular to the spin direction. Strain significantly modifies both structural and magnetic properties. The Fe–Te bond length ($d_{\text{Fe–Te}}$) increases under tensile strain, while θ_1 decreases and θ_2 increases, as shown in Fig. 5.1(f). The magnetic moment of Fe (μ) also increases with tensile strain (Table 5.1). Additionally, Te atoms contribute more strongly to SOC compared to Fe, with $E_{\text{SOC}}^{\text{Te}} \gg E_{\text{SOC}}^{\text{Fe}}$.

Table 5.1: Optimized bond lengths ($d_{\text{Fe-Fe}}$ and $d_{\text{Fe-Te}}$), bond angles (θ_1 and θ_2), magnetic moment (μ) of Fe atom, and Fe and Te resolved SOC contributions ($E_{\text{SOC}}^{\text{Fe}}$ and $E_{\text{SOC}}^{\text{Te}}$) to the energy in $FeTe_2$ monolayer under different strains.

Strain (%)	$d_{\text{Fe–Fe}}$ (Å)	$d_{\text{Fe–Te}}$ (Å)	θ_1 (deg)	θ_2 (deg)	μ (μ_B)	$E_{\text{SOC}}^{\text{Fe}}$ (meV)	$E_{\text{SOC}}^{\text{Te}}$ (meV)
-6	3.27	2.44	78.43	84.28	2.020	-9.15	-209.81
-4	3.34	2.47	77.25	85.15	2.030	-9.27	-211.03
-2	3.41	2.50	76.10	85.99	2.046	-9.30	-213.22
0	3.48	2.53	74.98	86.81	2.067	-9.38	-215.07
2	3.55	2.56	73.88	87.60	2.071	-9.66	-215.55
4	3.62	2.59	72.83	88.37	2.081	-10.16	-215.60
6	3.69	2.63	71.78	89.11	2.089	-10.42	-215.64

5.3.2 Effect of Electron Correlation

Due to the localized nature of Fe d-electrons, electron correlation plays an important role in determining the electronic and magnetic properties of $FeTe_2$. To account for this, the PBE+U method is employed [279]. The effective Hubbard parameter U is calculated using the linear response approach [280], yielding a self-consistent value of $U = 3.20$ eV (Fig. 5.2(a)). In this method, U is obtained from the difference between the inverse interacting and non-interacting response functions:

$$U = \chi_0^{-1} - \chi^{-1} = \left(\frac{\partial n_i^{\text{Scf}}}{\partial \alpha_i}\right)^{-1} - \left(\frac{\partial n_i^{\text{Nscf}}}{\partial \alpha_i}\right)^{-1}, \tag{5.1}$$

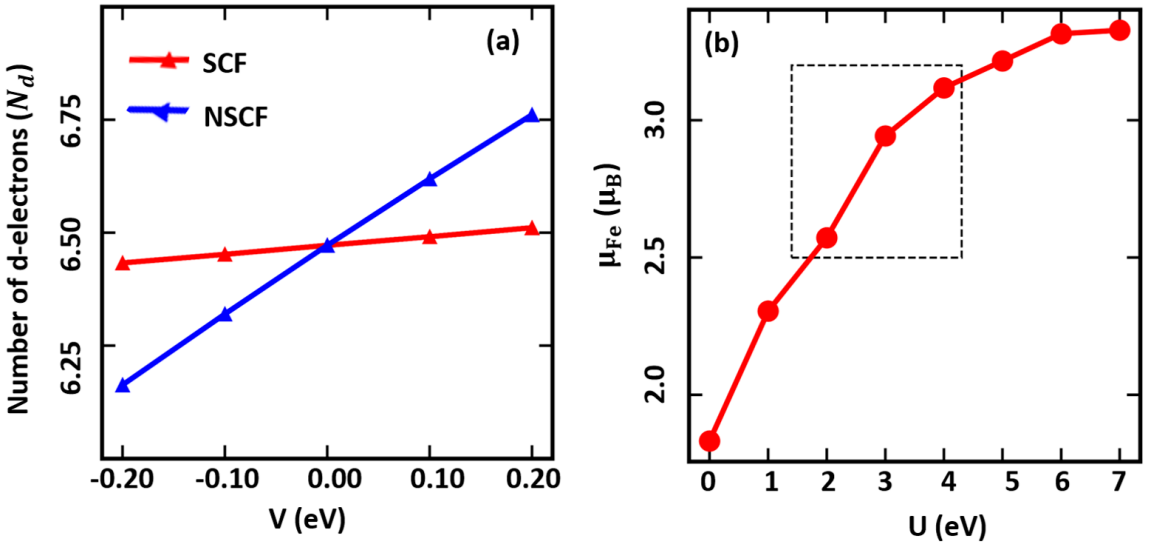

Figure 5.2: (a) Computation of the on-site Hubbard U parameter using linear response theory: the number of Fe d-electrons (N_d) is plotted as a function of the applied on-site potential shift V, using both self-consistent (SCF) and non-self-consistent (NSCF) approaches. The difference in the slopes of these lines yields the U value. (b) Variation of the magnetic moment of Fe atoms (μ_{Fe}) as a function of the Hubbard U parameter. The dotted box highlights the region where the magnetic moment exhibits the maximum change with increasing U.

where α_i is a small perturbation applied to site i, and n_i^{Scf} and n_i^{Nscf} are the corresponding occupations from SCF and NSCF calculations. Previous studies [250, 276] typically use $U = 2$ eV. To examine the role of correlation, we calculate the Fe magnetic moment (μ_{Fe}) as a function of U (0–7 eV). As shown in Fig. 5.2(b), μ_{Fe} increases with U, with a rapid change in the range 2–4 eV, followed by a slower increase at higher U, indicating saturation toward a high-spin state. Based on this behavior, we focus on the range $U = 2$–4 eV, where correlation effects most strongly influence the magnetic properties of $FeTe_2$.

5.3.3 Electronic Structure

To understand the combined effect of electronic correlation and lattice strain on the electronic and magnetic properties of the $FeTe_2$ monolayer, we analyze the spin-resolved orbital-projected density of states (PDOS), as shown in Fig. 5.3. The rows correspond to increasing

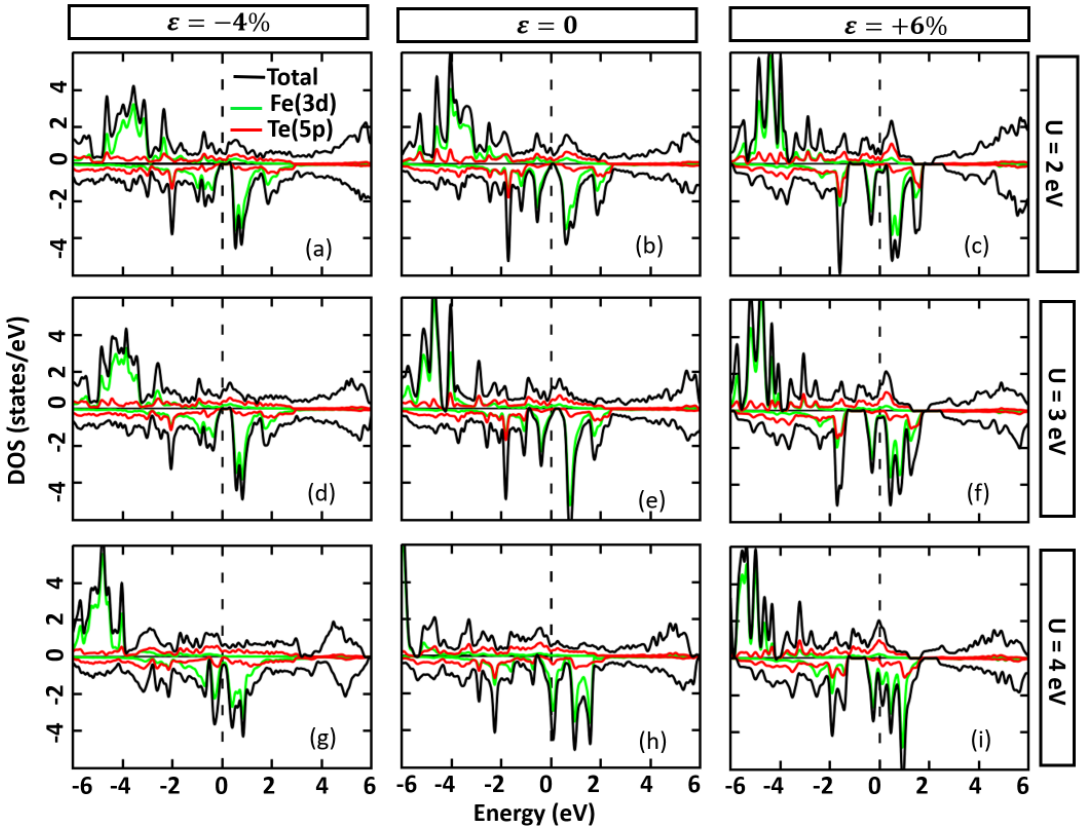

Figure 5.3: **Evolution of electronic structure of $FeTe_2$ as a function of Strain and correlation.** Total and orbital projected resolved density of states of the $FeTe_2$ monolayer under three different strain conditions: $\varepsilon = -4\%$, 0%, and $+6\%$ (left to right columns), and for varying U (2 - 4 eV). The Fermi level (E_F) is set to 0.

on-site Coulomb interaction ($U = 2$–4 eV), while the columns represent biaxial strain values of $\varepsilon = -4\%$, 0%, and $+6\%$. Across all cases, the system remains metallic in the spin-up channel. In contrast, the spin-down channel exhibits a finite gap near the Fermi level (E_F) under compressive strain and weak correlation. As the strain becomes tensile and the value of U increases, the Fe-d spin-down states shift toward E_F, leading to a metallic character in both spin channels. Additionally, with increasing correlation strength, the Fe-d states in the spin-up channel shift to lower energies, indicating enhanced localization. The combined influence of strain and electronic correlation also induces noticeable modifications

in the Te-p states. As shown in Fig. 5.7, the p_z states exhibit a more pronounced variation compared to the nearly degenerate p_x and p_y states, reflecting the anisotropic response of the electronic structure to external perturbations.

Overall, the evolution of the electronic structure suggests a strain-driven crossover from a relatively itinerant electronic character under compressive strain to a more localized behavior under tensile strain. Furthermore, the increasing asymmetry between spin-up and spin-down spectral weights with higher U and tensile strain indicates an imbalance in spin occupation. This redistribution of electronic states plays a crucial role in determining the magnetic interactions, including Heisenberg exchange interactions (J), Dzyaloshinskii–Moriya interaction (DMI, d), and magnetic anisotropy (K), which are discussed in the following sections. In particular, the influence of these electronic changes on MAE will be examined in Section 5.3.5.

5.3.4 Magnetic Interactions

The magnetic interactions in the system are described using the following spin Hamiltonian:

$$H = \frac{1}{2}\sum_{i,j} J_{ij}\mathbf{S}_i \cdot \mathbf{S}_j + K_u \sum_i (S_i^z)^2 + \frac{1}{2}\sum_{i,j} \mathbf{d}_{ij} \cdot (\mathbf{S}_i \times \mathbf{S}_j) + \mu B \sum_i S_i^z, \tag{5.2}$$

where J_{ij} represents the Heisenberg exchange interaction between spins at sites i and j. The second term describes the magnetic anisotropy, with K_u being the single-ion anisotropy constant. A positive K_u favors out-of-plane spin alignment, while a negative value favors in-plane alignment. The third term corresponds to the Dzyaloshinskii–Moriya interaction (DMI), where $\mathbf{d}_{ij}$ is the DMI vector responsible for stabilizing noncollinear and chiral spin configurations. The last term represents the Zeeman interaction, which aligns spins along the external magnetic field B.

To extract the exchange interaction parameters J_{ij} from DFT calculations, we employ Noodleman's broken symmetry approach [281], where the energy difference between high-

spin (HS) and broken-symmetry (BS) configurations is given by:

$$E_{\mathrm{HS}} - E_{\mathrm{BS}} = \frac{1}{2} S_{\mathrm{max}}^2 J. \tag{5.3}$$

In the present study, exchange interactions up to third nearest neighbors (J_1, J_2, and J_3) are considered. To determine these parameters, four magnetic configurations are examined: ferromagnetic (FM), Néel-type antiferromagnetic (AFM), stripy AFM, and zigzag AFM (see Fig. 5.4). The total energies obtained from DFT for these configurations are mapped onto the Heisenberg model, resulting in the following set of linear equations:

$$E_{\mathrm{FM}} = S^2 \left(6J_1 + 6J_2 + 6J_3\right) + E_0, \tag{5.4a}$$

$$E_{\mathrm{Néel}} = S^2 \left(-2J_1 + 2J_2 - 2J_3\right) + E_0, \tag{5.4b}$$

$$E_{\mathrm{Stripy}} = S^2 \left(-2J_1 - 2J_2 + 6J_3\right) + E_0, \tag{5.4c}$$

$$E_{\mathrm{Zigzag}} = S^2 \left(2J_1 - 2J_2 - 2J_3\right) + E_0. \tag{5.4d}$$

Here, S is the spin moment of the magnetic atom and E_0 is the non-magnetic reference energy. Solving these equations yields the exchange interaction parameters J_1, J_2, and J_3, which are presented in Fig. 5.4(f)–(h) as a function of strain and correlation strength, with numerical values summarized in Table 5.2.

Table 5.2: Magnetic exchange interactions (J_1, J_2, J_3) and single-ion anisotropy (K_u) for $U = 2$–4 eV as a function of strain (-6% to 6%). All values are in meV.

	$U = 2$ eV				$U = 3$ eV				$U = 4$ eV			
Strain (%)	J_1	J_2	J_3	K_u	J_1	J_2	J_3	K_u	J_1	J_2	J_3	K_u
-6	-7.87	5.13	-8.71	-3.01	-7.67	6.12	-6.00	-1.68	-5.44	5.85	-3.93	-1.32
-4	-9.02	4.09	-8.56	-4.89	-8.88	5.70	-5.19	-1.99	-6.63	4.22	-3.41	-1.54
-2	-11.88	3.28	-4.77	-6.47	-6.92	4.03	-3.40	-2.73	-4.58	3.93	-2.39	-4.68
0	-9.40	3.33	-4.02	-6.54	-5.05	3.17	-2.84	-4.80	-4.21	2.96	-2.16	2.68
2	-7.51	3.15	-3.37	1.18	-4.40	-1.88	-2.55	3.38	-3.45	-2.40	-1.43	4.72
4	-5.81	2.64	-3.28	2.89	-3.47	-2.74	-1.80	4.17	-2.96	-3.13	-1.18	4.91
6	-2.49	2.06	-2.34	4.50	-1.49	-2.78	-1.03	4.98	-1.59	-3.89	-0.96	5.30

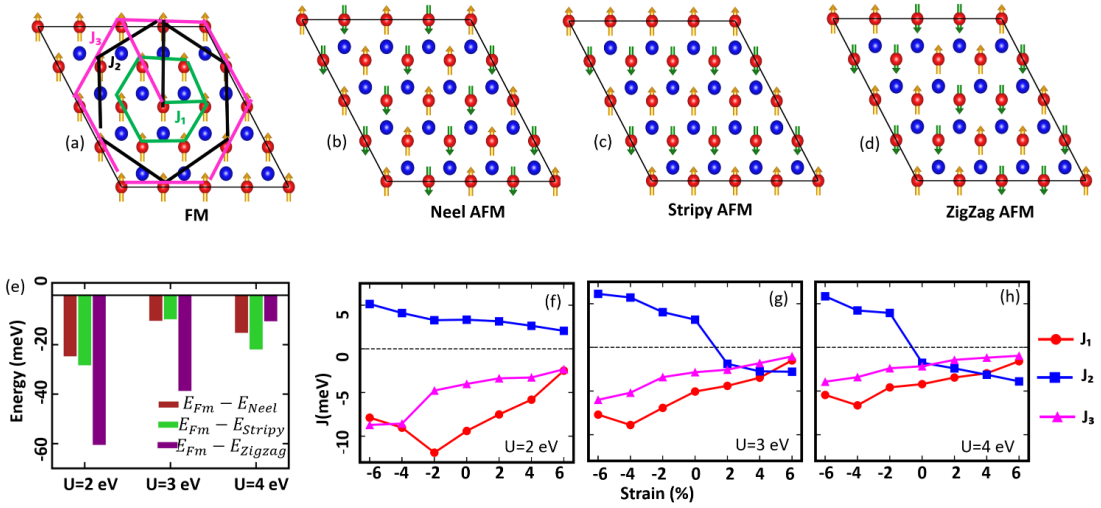

Figure 5.4: **Strain and correlation tunable magnetic exchange interactions.** Top view of the $FeTe_2$ monolayer: (a) FM spin configuration along with a schematic representation of the lattice showing Heisenberg exchange interactions J_1, J_2, and J_3; (b)–(d) Different types of AFM spin configurations: Néel-type, stripy, and zigzag patterns, respectively; (e) Energy differences between the four spin configurations (FM, Néel, stripy, and zigzag) for unstrained $FeTe_2$ as a function of U; (f)–(h) Variation of Heisenberg exchange interactions J_1, J_2, and J_3 as a function of strain (%) for $U = 2$, 3, and 4 eV, respectively.

The calculated exchange interactions exhibit a non-monotonic dependence on strain. Under compressive strain ($\varepsilon < 0$), $|J_1|$ and $|J_3|$ are relatively large, indicating strong ferromagnetic interactions, particularly around $\varepsilon = -2\%$. As the strain becomes tensile, J_1 decreases in magnitude and approaches zero, while J_2 changes sign and becomes ferromagnetic for $U > 2$ eV. Increasing electronic correlation weakens the strength of J_1 and J_3. These trends reflect a strain-driven modification of magnetic interaction pathways, originating from changes in bond lengths ($d_{\text{Fe–Fe}}$, $d_{\text{Fe–Te}}$) and bond angles (θ_1, θ_2), which affect both direct exchange and superexchange mechanisms. To determine the magnetic ground state, the energy differences of AFM configurations relative to the FM state are shown in Fig. 5.4(e). The FM configuration consistently exhibits the lowest energy across all considered U values, confirming it as the ground state. The combined effect of strain and electronic correlation provides an effective route for tuning magnetic interactions in $FeTe_2$

monolayers. Under compressive strain and low U, competing exchange interactions can lead to magnetic frustration, potentially stabilizing noncollinear spin configurations. In contrast, tensile strain and higher U favor stronger ferromagnetic interactions, resulting in a more stable magnetic order.

5.3.5 Magnetic Anisotropy Energy

The second term in the Hamiltonian [Eq. 5.2] represents the single-ion magnetic anisotropy. In $FeTe_2$ monolayers, strong spin–orbit coupling (SOC), primarily originating from the heavy Te atoms, introduces significant spin-dependent energy shifts, thereby enhancing the magnetic anisotropy. This anisotropy can be effectively tuned by lattice strain and electronic correlation. The magnetic anisotropy energy (MAE) is evaluated as the energy difference between in-plane and out-of-plane magnetization directions:

$$K_u = E_{[100]} - E_{[001]} = E^x - E^z,$$

where $K_u > 0$ corresponds to out-of-plane magnetic anisotropy (OPMA), while $K_u < 0$ indicates in-plane magnetic anisotropy (IPMA).

The strain-dependent variation of K_u for different U values is shown in Fig. 5.5 (a) and summarized in Table 5.2. Under compressive strain (-6% to -2%), K_u remains negative for all U, indicating IPMA. As the strain becomes tensile, K_u changes sign, marking a transition to OPMA. This crossover is further enhanced with increasing U, reflecting stronger electron localization and enhanced SOC effects. For $U = 2$ eV, the unstrained system exhibits a strong in-plane anisotropy with $K_u = -6.54$ meV, consistent with previous studies [250]. Under tensile strain, K_u increases significantly, reaching 5.30 meV at 6% strain for $U = 4$ eV. This enhancement originates from strain-induced modifications in bond angles and crystal field, which alter orbital overlaps and strengthen anisotropic SOC contributions, particularly between Te p and Fe d orbitals. Fig. 5.5 (b) shows the atom-

resolved MAE contributions from Fe and Te atoms. In all cases, Te atoms dominate the MAE, highlighting the crucial role of Te-driven SOC. At $U = 2$ eV and $\varepsilon = -2\%$, Te contributes to IPMA, while at $U = 4$ eV and $\varepsilon = 2\%$, the contribution becomes positive, indicating a transition to OPMA. The contribution from Fe atoms remains comparatively small.

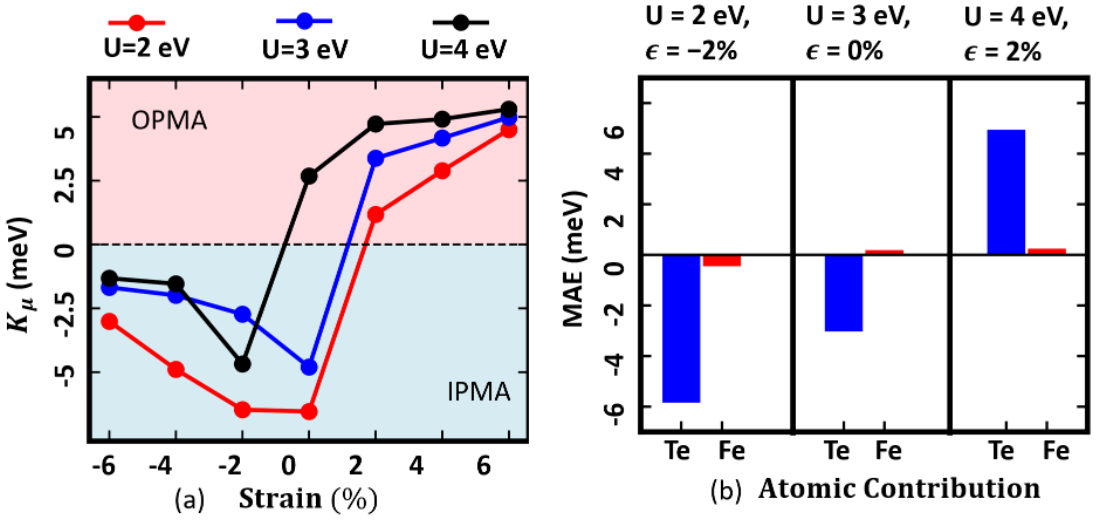

Figure 5.5: (a) Single-ion magnetic anisotropy energy K_u as a function of biaxial strain for different U values. The pink and blue shaded regions denote out-of-plane and in-plane magnetic anisotropy, respectively. (b)Atom-resolved MAE for $FeTe_2$ under varying U and biaxial strain. The panels correspond to ($U = 2$ eV, $\varepsilon = -2\%$), ($U = 3$ eV, $\varepsilon = 0\%$), and ($U = 4$ eV, $\varepsilon = 2\%$).

To gain microscopic insight into the origin of MAE, we analyze orbital-resolved hybridization contributions based on second-order perturbation theory [282]. The MAE can be expressed as:

$$\Delta E^{\downarrow\downarrow} = \lambda^2 \sum_{o^\downarrow, u^\downarrow} \frac{|\langle o^\downarrow|L_z|u^\downarrow\rangle|^2 - |\langle o^\downarrow|L_x|u^\downarrow\rangle|^2}{\varepsilon_{u^\downarrow} - \varepsilon_{o^\downarrow}}, \tag{5.5a}$$

$$\Delta E^{\uparrow\downarrow} = -\lambda^2 \sum_{o^\uparrow, u^\downarrow} \frac{|\langle o^\uparrow|L_z|u^\downarrow\rangle|^2 - |\langle o^\uparrow|L_x|u^\downarrow\rangle|^2}{\varepsilon_{u^\downarrow} - \varepsilon_{o^\uparrow}}, \tag{5.5b}$$

$$\text{MAE} = \Delta E^{\downarrow\downarrow} + \Delta E^{\uparrow\downarrow}, \tag{5.5c}$$

where λ is the SOC strength, and o and u denote occupied and unoccupied states, respectively. The MAE depends on both the angular momentum matrix elements and the energy separation between states.

Table 5.3: Matrix element differences between magnetization directions for Te p orbitals.

	$o^{\downarrow}$			$o^{\uparrow}$		
$u^{\downarrow}$	p_x	p_y	p_z	p_x	p_y	p_z
p_x	0	-1	0	0	1	0
p_y	-1	0	1	1	0	-1
p_z	0	1	0	0	-1	0

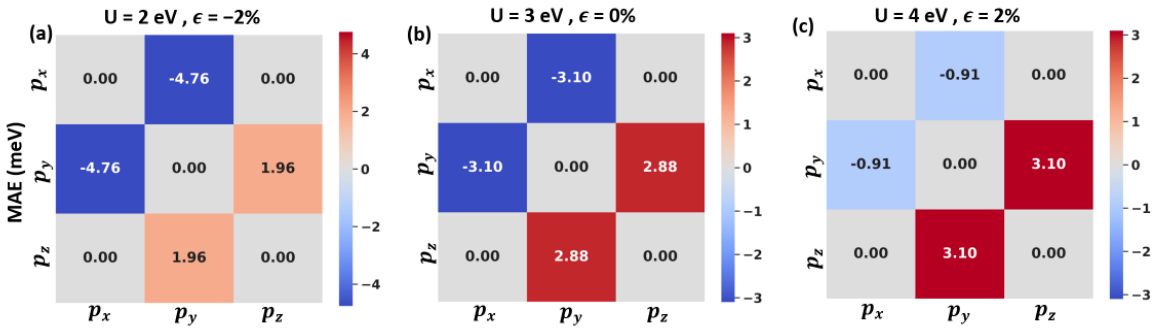

Figure 5.6: MAE contribution from 5p orbital hybridization in of Te atoms in the $FeTe_2$ monolayer under different conditions: (a) $U = 2$ eV, $\epsilon = -2\%$ (compressive strain), (b) $U = 3$ eV, $\epsilon = 0\%$ (unstrained), and (c) $U = 4$ eV, $\epsilon = +2\%$ (tensile strain).

Equations 5.5a and 5.5b indicate that states near the Fermi level dominate the MAE. Both intra-spin and inter-spin transitions contribute. The orbital-resolved contributions for different strain and U values are shown in Fig. 5.6(a)–(c).

The p_x–p_y matrix element difference is negative, favoring IPMA, while the p_y–p_z contribution is positive, favoring OPMA. From the PDOS (Fig. 5.7), the energy separation between $p_y^{u\downarrow}$ and p_z^o decreases with increasing strain and U, enhancing the p_y–p_z contribution and promoting OPMA. At $U = 4$ eV and $+2\%$ strain, the p_z state crosses the Fermi level, further strengthening this effect. In contrast, the p_x–p_y contribution weakens due to

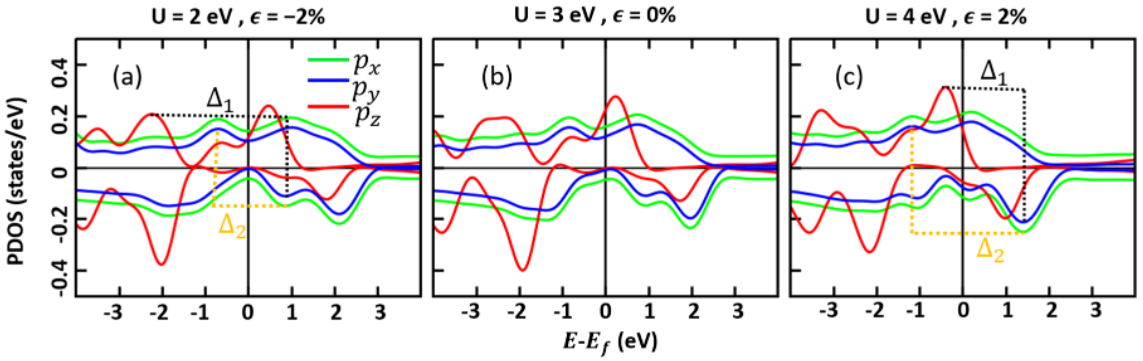

Figure 5.7: Orbital resolved projected density of states (PDOS) for the Te p orbitals (p_x: green, p_y: blue, p_z: red) in the $FeTe_2$ monolayer under different conditions: (a) $U = 2$ eV, $\varepsilon = -2\%$ (compressive strain), (b) $U = 3$ eV, $\varepsilon = 0\%$ (unstrained), and (c) $U = 4$ eV, $\varepsilon = +2\%$ (tensile strain). The Fermi level is set at $E - E_F = 0$ eV and marked by the vertical black line.

increased energy separation caused by the shift of p_x states below the Fermi level. As a result, OPMA dominates under tensile strain and strong correlation.

Overall, the enhancement of MAE arises from increased out-of-plane orbital hybridization driven by strain and electronic correlation. This analysis clearly demonstrates that Te p-orbitals and their hybridization dynamics play a decisive role in determining the magnetic easy axis in $FeTe_2$ monolayers.

5.3.6 Dzyaloshinskii–Moriya Interaction

The DMI originates from SOC in systems lacking inversion symmetry and plays a key role in stabilizing non-collinear magnetic textures such as spin spirals and skyrmions [283]. In the $FeTe_2$ monolayer, inversion symmetry is broken due to the asymmetric positioning of Te atoms with respect to the Fe layer, allowing for a finite DMI.

According to Moriya's symmetry rules [255, 256], the DMI vector between two neighboring spins can be expressed as

$$\mathbf{d}_{ij} = d_{\parallel}(\hat{z} \times \hat{u}_{ij}) + d_{\perp}\hat{z}, \tag{5.6}$$

where $\hat{u}_{ij}$ is the unit vector connecting sites i and j, and $d_{\parallel}$ and $d_{\perp}$ denote the in-plane and out-of-plane components of the DMI vector, respectively.

Derivation of DMI from total energy differences

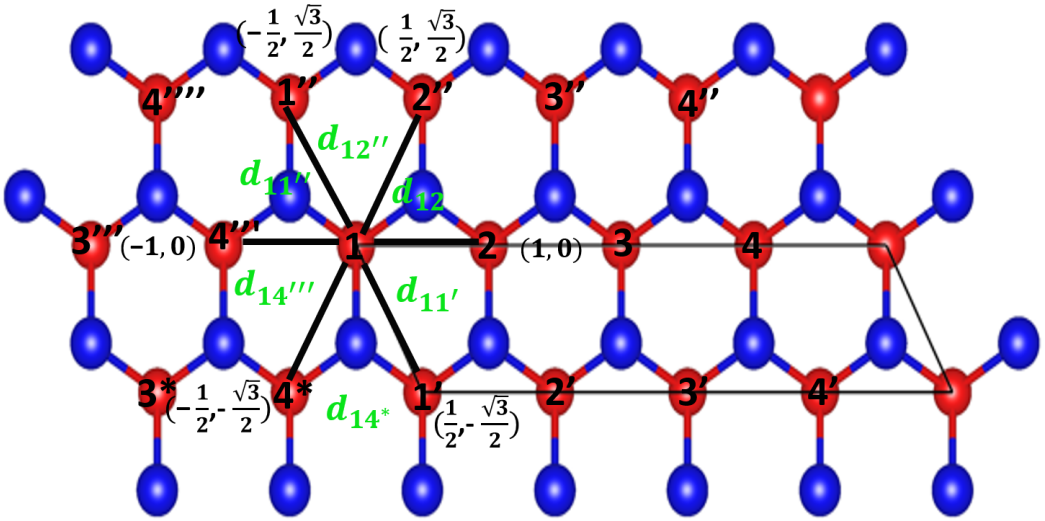

Figure 5.8: Top view of the $4 \times 1 \times 1$ $FeTe_2$ monolayer (Fe atoms in red and Te atoms in blue) showing the spin configurations used for calculating the DMI.

To extract the DMI strength from first-principles calculations, we consider the antisymmetric exchange term:

$$H_{\mathrm{DMI}} = \sum_{\langle i,j \rangle} \mathbf{d}_{ij} \cdot (\mathbf{S}_i \times \mathbf{S}_j). \tag{5.7}$$

Two spin configurations, clockwise (CW) and anticlockwise (ACW), are constructed. Since the symmetric Heisenberg exchange remains unchanged under reversal of chirality, the energy difference arises solely from the DMI term:

$$d^{\mathrm{tot}} = \frac{E_{\mathrm{CW}} - E_{\mathrm{ACW}}}{m}. \tag{5.8}$$

The constant m depends on the crystal structure and the magnetic supercell. The spin interaction energy for atom 1 from Fig. 5.8, including exchange, anisotropy, DMI, and Zeeman contributions, is written as:

$$\begin{aligned} E^1 =& \frac{1}{2}\Bigg[J_1\Big(S_1\cdot S_{4'''} + S_1\cdot S_2 + S_1\cdot S_{1'} + S_1\cdot S_{1''} + S_1\cdot S_{2''} + S_1\cdot S_{4^*}\Big) \\ &+ J_2\Big(S_1\cdot S_{2'} + S_1\cdot S_{3''} + S_1\cdot S_{4''''} + S_1\cdot S_{3^*}\Big) \\ &+ J_3\Big(S_1\cdot S_3 + S_1\cdot S_{3'''}\Big)\Bigg] + A_\mu\left(S_1^z\right)^2 + \frac{1}{2}\sum \mathbf{d}_{ij}\cdot(S_1\times S_j) + \mu\nu B S_1^z. \end{aligned} \tag{5.9}$$

The factor $1/2$ accounts for double counting of bonds. Spins $1'$ and $1''$ are parallel and antiparallel to $\mathbf{S}_1$, respectively. For the in-plane DMI component, the expression reduces to:

$$\begin{aligned} E^1 =& \frac{1}{2}\left[J_1(2) + J_2(0) + J_3(0)\right] + A_\mu\left(S_1^z\right)^2 \\ &+ \frac{1}{2}\left[d^x_{12} - d^x_{14'''} - d^x_{14^*} + d^x_{12''}\right] + \mu\nu B S_1^z. \end{aligned} \tag{5.10}$$

Using Moriya's symmetry rules, $\mathbf{d}_{ij} \propto \hat{z}\times\hat{u}_{ij}$, the DMI contribution becomes:

$$E^{(1)} = \frac{1}{2}[2J_1] + A_\mu\left(S_1^z\right)^2 + \frac{1}{2}d_\parallel\left[\cos(0^\circ) - \cos(180^\circ) - \cos(240^\circ) + \cos(60^\circ)\right] + \mu\nu B S_1^z. \tag{5.11}$$

which leads to:

$$E^1_{CW} = \frac{1}{2}[2J_1] + A_\mu\left(S_1^z\right)^2 + \frac{1}{2}[3d_\parallel] + \mu\nu B S_1^z, \tag{5.12}$$

$$E^1_{ACW} = \frac{1}{2}[2J_1] + A_\mu\left(S_1^z\right)^2 - \frac{1}{2}[3d_\parallel] + \mu\nu B S_1^z. \tag{5.13}$$

By solving Eqns. 5.12 and 5.13

$$d_\parallel = \frac{E^1_{CW} - E^1_{ACW}}{3}. \tag{5.14}$$

For the full supercell:

$$d_\parallel = \frac{E_{CW} - E_{ACW}}{12}. \tag{5.15}$$

Similarly,

$$d_\perp = \frac{E_{CW} - E_{ACW}}{16}. \tag{5.16}$$

Micromagnetic DMI

In the continuum limit, the spins are represented by a smooth magnetization field $\mathbf{m}(\mathbf{r})$. Using a Taylor expansion:

$$\mathbf{m}(\mathbf{r}_j) \simeq \mathbf{m}(\mathbf{r}_i) + ru_{ij}^{x}\frac{\partial \mathbf{m}}{\partial x} + ru_{ij}^{y}\frac{\partial \mathbf{m}}{\partial y}. \tag{5.17}$$

The DMI energy for atom i interacting with six nearest neighbors is:

$$E_{i,\mathrm{DMI}} = \frac{1}{2}rd_{\parallel}\sum_{n=1}^{6}(\hat{z}\times\hat{u}_n)\cdot\left[\mathbf{m}(\mathbf{r}_i)\times\frac{\partial \mathbf{m}}{\partial u_n}\right]. \tag{5.18}$$

Using Lifshitz invariants:

$$L_{pq}^{(u)} = m_p\frac{\partial m_q}{\partial u} - m_q\frac{\partial m_p}{\partial u}, \tag{5.19}$$

where p, q represent arbitrary Cartesian coordinates, such as x and y. As per figure 5.8, the energy value for 6 nearest neigbouring astoms can be calculating by subsitituing u into equation B.16 where

$$E_{i,\mathrm{DMI}} = \epsilon_{2''} + \epsilon_2 + \epsilon_{1'} + \epsilon_{4^*} + \epsilon_{4'''} + \epsilon_{1''}, \tag{5.20}$$

$$= \frac{1}{2}rd_{\parallel}\left[\frac{1}{4}L_{zx}^{(x)} + \frac{3}{4}L_{zy}^{(y)} + L_{zx}^{(x)} + \frac{1}{4}L_{zx}^{(x)} + \frac{3}{4}L_{zy}^{(y)} + \frac{1}{4}L_{zx}^{(x)} + \frac{3}{4}L_{zy}^{(y)} + L_{zx}^{(x)} + \frac{1}{4}L_{zx}^{(x)} + \frac{3}{4}L_{zy}^{(y)}\right], \tag{5.21}$$

$$= \frac{1}{2}rd_{\parallel}\left[3L_{zx}^{(x)} + 3L_{zy}^{(y)}\right], \tag{5.22}$$

$$= \frac{3}{2}rd_{\parallel}\left[L_{zx}^{(x)} + L_{zy}^{(y)}\right]. \tag{5.23}$$

The above expression for $E_{i,\mathrm{DMI}}$ is written in terms of discrete spin interactions and their spatial variations. To establish a connection with the continuum description, the discrete summation over neighboring spins is mapped onto a continuous magnetization field $\mathbf{m}(\mathbf{r})$. In this framework, the Lifshitz invariants $L_{pq}^{(u)}$ represent the lowest-order terms capturing chiral spin variations arising from SOC. By comparing the atomistic DMI energy with the

standard micromagnetic form of the DMI energy density,

$$E = D\left[m_z \frac{dm_x}{dx} - m_x \frac{dm_z}{dx}\right] + id(x \leftrightarrow y), \tag{5.24}$$

one can directly identify the coefficient of the Lifshitz invariants with the micromagnetic DMI constant D. we can evaluate dmi strength D normalized by number of magnetic atoms N in the unit cell and volume corresponding to a Fe atom in the magnetic film, where V = $\frac{\sqrt{3}a^2}{2}\cdot$ t where $\frac{\sqrt{3}a^2}{4}$ is the atomic surface area for a hexagonal lattice and t is the thickness of the magnetic layer :

$$D = \frac{\sqrt{3}d_{\parallel}N}{a \cdot t}. \tag{5.25}$$

5.3.7 Deviation of DMI as a function of strain and correlation

The data in Table 5.4 show that the out-of-plane DMI component $d_{\perp}$ remains negligible across all considered strain values and Hubbard U parameters, indicating that it plays only a minor role in the magnetic interaction landscape of the system. In contrast, the in-plane component $d_{\parallel}$ exhibits a strong and non-monotonic dependence on strain.

Table 5.4: Nearest-neighbor (NN) in-plane and out-of-plane DMI constants ($d_{\parallel}$ and $d_{\perp}$) and micromagnetic DMI strength (D) as a function of strain (-6% to 6%), calculated using PBE+U with $U = 2, 3, 4$ eV. The units of $d_{\parallel}$ and $d_{\perp}$ are meV, while D is in mJ/m^2.

	$U=2$			$U=3$			$U=4$		
Strain (%)	$d_{\parallel}$	$d_{\perp}$	D	$d_{\parallel}$	$d_{\perp}$	D	$d_{\parallel}$	$d_{\perp}$	D
-6	0.36	0.01	0.99	0.48	0.11	1.32	0.99	0.13	2.72
-4	0.27	-0.05	0.73	0.33	0.03	0.88	0.57	0.09	1.53
-2	-0.15	-0.07	-0.40	0.19	-0.05	0.50	-0.41	0.02	-1.08
0	-0.17	-0.08	-0.44	-0.39	-0.04	-1.00	-0.27	-0.08	-0.70
2	-0.56	-0.08	-1.41	-0.85	-0.09	-2.15	-1.21	-0.03	-3.06
4	-0.29	0.05	-0.72	0.22	0.01	0.54	0.59	0.13	1.46
6	0.25	0.04	0.61	0.54	0.03	1.31	0.95	0.13	2.31

As shown in Fig. 5.9(c), $d_{\parallel}$ changes sign with strain, corresponding to a switching of the preferred spin spiral configuration from anticlockwise (ACW) to clockwise (CW), and then

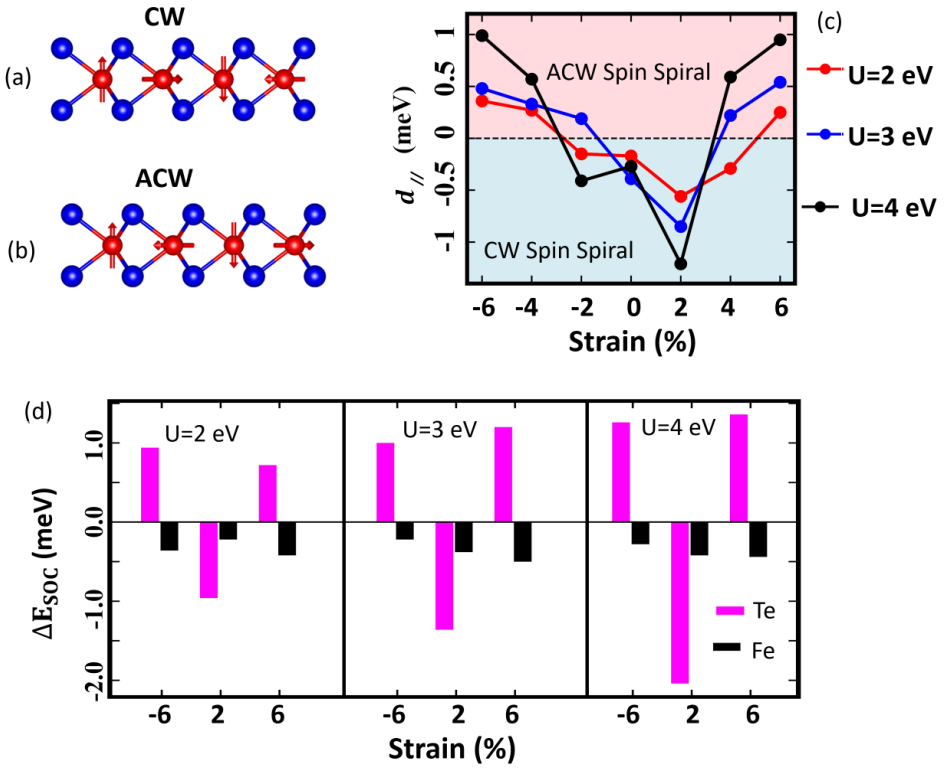

Figure 5.9: (a)–(b) Representation of the Clockwise and Anticlockwise spin configurations in a 4×1 $FeTe_2$ monolayer. Red arrows indicate the directions of the magnetic moments, (c) In-plane DMI component ($d_{\parallel}$) versus strain; positive values favor ACW and negative values favor CW spirals. (d) Contribution to ΔE_{SOC} by Fe and Te, calculated for opposite chiralities at $\varepsilon = -6\%$, 2%, and 6% for $U = 2$, 3, and 4 eV.

back to ACW. This behavior reflects a strain-driven modulation of the chiral magnetic interactions and originates from changes in spin–orbit coupling (SOC), orbital hybridization, and local crystal symmetry. In particular, the increase in $d_{\parallel}$ beyond 2% tensile strain can be attributed to enhanced SOC effects arising from modified hybridization between Fe d-orbitals and Te p-orbitals. As strain alters the structural parameters, such as the Fe–Te bond length ($d_{\mathrm{Fe–Te}}$) and bond angles (θ_1, θ_2), the resulting changes in orbital overlap strengthen the asymmetric exchange interactions responsible for DMI. The inversion asymmetry of the

system is also enhanced under strain, further contributing to the increase in DMI strength. For example, at $U = 2$ eV, $d_{\parallel}$ is approximately -0.17 meV at -2% strain, and increases with tensile strain, reaching 0.25 meV at 6%. This evolution is accompanied by a change in chirality from CW to ACW, consistent with the observed sign reversal.

To gain insight into the microscopic origin of DMI, we analyze the atom-resolved SOC energy difference between CW and ACW spin configurations, defined as

$$\Delta E_{\mathrm{SOC}} = E_{\mathrm{SOC}}^{\mathrm{CW}} - E_{\mathrm{SOC}}^{\mathrm{ACW}},$$

for selected strain values (-6%, 2%, and 6%) and $U = 2$, 3, and 4 eV, as shown in Fig. 5.9(d). The decomposition of ΔE_{SOC} into contributions from Fe and Te atoms reveals that Te consistently dominates the SOC response. This is primarily due to its larger atomic number, which enhances relativistic effects and strengthens the SOC-driven anisotropic exchange responsible for DMI. Interestingly, the relative contributions from Fe and Te vary with strain. At -6% strain, the contributions have opposite signs (Fe positive and Te negative), indicating a competing interplay that reduces the net DMI and favors ACW spin orientation. At 2% strain, both contributions become positive, suggesting a cooperative enhancement of the CW spin spiral state. At 6% strain, the behavior again resembles the compressive case, with opposing contributions that stabilize the ACW configuration. While the sign of ΔE_{SOC} remains unchanged for all values of U, its magnitude varies significantly. This trend is consistent with the strain-induced evolution of $d_{\parallel}$ shown in Fig. 5.9(c), confirming that the DMI is directly governed by SOC modifications arising from changes in crystal symmetry, bonding environment, and orbital hybridization.

As shown in Table 5.4, the micromagnetic DMI constant D follows the same trend as $d_{\parallel}$. For each value of U, D increases under both compressive (-6%) and tensile (6%) strain, reaching maximum values of 2.72 mJ/m^2 and 2.31 mJ/m^2, respectively, for $U = 4$ eV. This indicates that extreme strain conditions enhance the asymmetric exchange interactions re-

sponsible for DMI. In contrast, near-zero strain regimes (particularly around 2%) exhibit a sign reversal of D, reaching large negative values (up to -3.06 mJ/m^2 at $U = 4$ eV), corresponding to a CW spin spiral orientation. This chirality switching arises from strain-induced modifications in Fe–Te bond geometry and the electronic structure, which alter the magnitude and direction of SOC contributions. Furthermore, increasing U enhances the magnitude of D, especially under strain. This behavior originates from increased localization of Fe d-electrons, which strengthens SOC-mediated exchange interactions. Overall, the micromagnetic DMI constant D emerges as a highly tunable parameter, controlled by both strain and electronic correlation. This tunability provides an effective route for engineering chiral spin textures in $FeTe_2$ and related two-dimensional magnetic systems.

5.4 Conclusions

In summary, we have systematically investigated the effects of biaxial strain and electronic correlation on the MAE and DMI in a pristine $FeTe_2$ monolayer using DFT+U calculations including SOC. Our results demonstrate that both strain and correlation play a crucial role in determining the magnetic properties of the system. In particular, tensile strain induces a transition of the magnetic easy axis from in-plane to out-of-plane, with the MAE varying significantly from approximately -6 to $+5.3$ meV. This large modulation originates from the strain-induced redistribution of spin-polarized occupied and unoccupied states near the Fermi level. The underlying mechanism is associated with changes in electron hopping strengths, driven by variations in bond lengths and local crystal field under strain. Simultaneously, the in-plane DMI component ($d_{\parallel}$), which governs the twisting of spin configurations, exhibits a strong dependence on strain, with both its magnitude and sign undergoing significant changes. This behavior arises from strain-induced modifications in SOC strength, orbital hybridization, and symmetry. As a consequence, the micromagnetic

DMI constant (D) reaches values as high as 3.06 mJ/m^2 under optimal conditions. In contrast, the out-of-plane component ($d_\perp$) remains negligible across all strain and correlation regimes, confirming that the DMI in this system is predominantly of the Néel type, driven by in-plane inversion symmetry breaking.

Overall, our findings establish that both MAE and DMI can be effectively tuned in a pristine two-dimensional material without relying on conventional approaches such as chemical doping or heterostructure engineering. This highlights $FeTe_2$ as a promising platform for exploring complex magnetic interactions and designing tunable chiral spin textures in low-dimensional systems.

Chapter 6

Exploring Skyrmion Stability in Centrosymmetric Monolayers

In the previous chapter, we showed that DMI and MAE arise intrinsically in H-$FeTe_2$ due to broken inversion symmetry and strong SOC. In contrast, centrosymmetric systems such as T-$FeTe_2$ lack DMI, limiting the formation of non-collinear spin textures. To address this, we construct a van der Waals heterostructure of $FeTe_2$ with Pt, which breaks inversion symmetry and enhances SOC. We then investigate how the interplay of exchange interactions, MAE, and DMI stabilizes skyrmions using micromagnetic simulations based on first-principles parameters.

This chapter is based on the following work:

[1] **D. Rani**, B. R. K. Nanda, and P. Samal, *To be submitted*.

6.1 Introduction

Chiral topological magnetic textures, particularly skyrmions [284], have attracted significant attention due to their nanoscale size, topological stability, and low current-driven mobility. These properties make them promising candidates for next-generation spintronic devices, including racetrack memories and logic architectures [285, 286, 287, 288]. Unlike conventional domain walls, skyrmions behave as particle-like objects and can be manipulated with extremely low current densities, enabling energy-efficient information storage and processing [289, 290, 291].

The stabilization of skyrmions is primarily governed by the competition between symmetric exchange interaction, magnetic anisotropy, and the antisymmetric DMI [292, 293].

In systems with sufficiently strong DMI, the balance between these interactions favors chiral spin configurations such as spin spirals and skyrmions. However, in many materials, especially those based on $3d$ transition metals, the intrinsic DMI remains relatively weak [294], making the stabilization of skyrmions challenging under realistic conditions.

To overcome this limitation, extensive efforts have been devoted to engineering DMI through interface design. In particular, ferromagnet/heavy metal (FM/HM) heterostructures have emerged as an effective platform, where strong SOC from heavy elements and interfacial inversion symmetry breaking significantly enhance DMI. A notable example is the observation of atomic-scale skyrmions in Fe/Ir(111) systems [295]. Subsequently, room-temperature skyrmions have been realized in FM/HM heterostructures such as Ir/Co/Pt and Ir/Fe/Co/Pt, where asymmetric stacking maximizes SOC and DMI [296, 297]. These studies highlight the crucial role of interfacial engineering in stabilizing chiral magnetic textures.

Despite these advances, realizing skyrmions in centrosymmetric 2D materials remains a significant challenge. In such systems, inversion symmetry suppresses the intrinsic DMI, preventing the formation of chiral spin textures. 2D TMDCs, including $FeTe_2$, offer a versatile platform for exploring low-dimensional magnetism [298]; however, their centrosymmetric phases (T-$FeTe_2$) do not naturally host DMI. A promising route to overcome this limitation is through vdW heterostructure engineering. By interfacing a magnetic monolayer with a HM, inversion symmetry can be broken at the interface, while strong SOC enhances the DMI [288]. Recent studies have demonstrated that such heterostructures can host chiral spin textures even at low or zero external magnetic fields, making them attractive for practical applications [295, 296, 297, 299]. In this work, we focus on $FeTe_2$/Pt vdW heterostructures based on the centrosymmetric 1T phase of $FeTe_2$. While pristine 1T-$FeTe_2$ lacks intrinsic DMI, interfacing it with Pt induces strong interfacial SOC and symmetry breaking, leading to a finite DMI. By systematically investigating different stacking configurations and varying the number of Pt layers, we analyze how interfacial structure,

orbital hybridization, and magnetic anisotropy influence the magnitude and orientation of DMI. Using DMI parameters extracted from first-principles calculations, we perform micromagnetic simulations to explore the stability of skyrmions in these heterostructures. Our results demonstrate that $FeTe_2$/Pt systems can host stable skyrmions under experimentally accessible conditions, providing a viable pathway for designing ultrathin spintronic devices based on chiral magnetic textures.

6.2 Computational Methods

First-principles calculations for the 2D vdW heterostructure $FeTe_2$/Pt(111) were performed using DFT, as implemented in the Vienna *Ab initio* Simulation Package (VASP) [156]. The electron–ion interactions were treated using the PAW method [108, 109], and the exchange–correlation functional was described within the PBE generalized gradient approximation (GGA) [145]. To account for the localized nature of Fe $3d$ electrons, the DFT+U method was employed [250, 276], with an effective Hubbard parameter $U_{\text{eff}} = 3.00$ eV [298]. The Kohn–Sham orbitals were expanded in a plane-wave basis set with a kinetic energy cutoff of 520 eV. Brillouin-zone integrations were performed using a Γ-centered $12 \times 12 \times 1$ Monkhorst-Pack k-point mesh. A vacuum spacing of 25 Å was introduced along the out-of-plane direction to avoid spurious interactions between periodic images. To accurately describe the weak interlayer interactions in the vdW heterostructure, dispersion corrections were included using the DFT-D3 method with Becke–Johnson damping [300, 301]. All structures were fully relaxed until the total energy converged within 10^{-6} eV and the Hellmann–Feynman forces were below 0.001 eV/Å. The dynamical stability of the optimized structures was verified by calculating the phonon spectra using the finite-displacement method as implemented in the PHONOPY package [277]. The DMI was calculated using the supercell approach, following the procedure described in Section 5.2

of Chapter **??**. In brief, the DMI is obtained from the total energy difference between CW and ACW spin configurations in the presence of SOC [302, 303]. Finally, the micromagnetic simulations were performed using the MUMAX3 package [304], where parameters such as exchange interaction, magnetic anisotropy, and DMI obtained from first-principles calculations were used to investigate the stability and evolution of skyrmion spin textures.

6.3 Result and Discussions

6.3.1 Geometric Properties of the Heterostructures

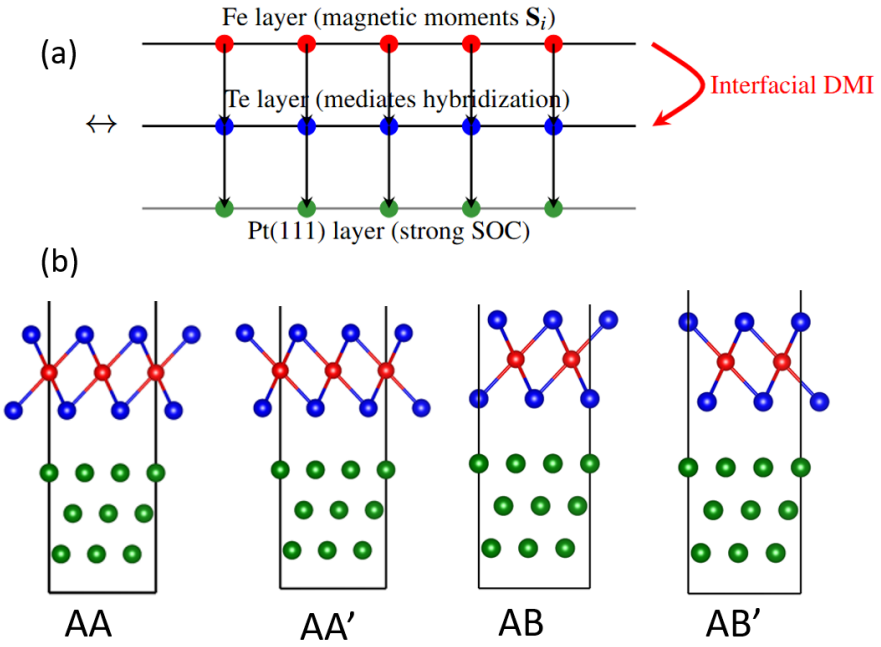

Figure 6.1: **Schematic illustration and stacking configurations of $FeTe_2$/Pt(111) heterostructures.** (a) Layer-resolved view showing Fe magnetic moments, Te-mediated hybridization, and the Pt(111) substrate with strong SOC. (b) Side views of different stacking configurations (AA, AA′, AB, AB′) illustrating distinct atomic registries between $FeTe_2$ and Pt.

Constructing vdW heterostructures provides an effective route for tailoring the elec-

tronic and magnetic properties of 2D materials through interlayer coupling, charge redistribution, and symmetry engineering. In the case of $FeTe_2$, the 1T (tetragonal) polymorph exhibits metallic behavior, which facilitates efficient charge transfer across the interface. Such charge transfer can significantly modify the local crystal-field environment of Fe atoms, thereby influencing the exchange interactions and the SOC landscape within the heterostructure [42, 305]. Motivated by these considerations, we construct vdW heterostructures by interfacing monolayer 1T-$FeTe_2$ (with in-plane lattice parameter $a = 3.48$ Å [42]) with a Pt overlayer ($a = 2.50$ Å [306]). Pt is chosen due to its strong intrinsic SOC and its ability to enhance interfacial SOC interactions through inversion symmetry breaking at the interface. A schematic representation of the heterostructure is shown in Fig. 6.1(a), where the Fe layer hosts magnetic moments and the intermediate Te layer mediates hybridization with the underlying Pt(111) substrate. Since $FeTe_2$ and Pt possess significantly different lattice constants, constructing a commensurate interface requires careful supercell design. To minimize lattice mismatch, a 2×2 supercell of $FeTe_2$ is matched with a 3×3 supercell of the Pt(111) surface, resulting in a mismatch below 5%.

This approach preserves the intrinsic structural characteristics of both materials while avoiding artificial strain effects that could obscure the underlying magnetic interactions. Furthermore, multiple stacking configurations are considered, as illustrated in Fig. 6.1(b), including AA, AA′, AB, and AB′ arrangements. These configurations correspond to different atomic registries between $FeTe_2$ and the Pt substrate, leading to variations in interfacial hybridization and local symmetry. In particular, the AB stacking, corresponding to a lateral shift of $(1/3,\ 1/3)$, breaks the local inversion symmetry more effectively and enhances the orbital hybridization between Te/Fe and Pt atoms. As a result, such configurations are expected to exhibit stronger interfacial coupling compared to other stacking arrangements. As shown in Table 6.1, the AA configuration is the most stable, whereas AB and AB′ are nearly degenerate and only slightly higher in energy. This small energy difference suggests

that different stacking arrangements can be experimentally accessible and may coexist.

Table 6.1: Relative total energies of different stacking configurations of the T-$FeTe_2$/Pt(111) heterostructure. Energies are given in meV per atom with respect to the most stable configuration (AA).

Configuration	**AA**	**AA′**	**AB**	**AB′**
Energy (meV/atom)	0.0	35.0	1.6	2.0

As shown in Fig. 6.2, the AB′ configuration exhibits imaginary phonon modes, indicating its dynamical instability. Therefore, in the following analysis, we focus only on the dynamically stable AA and AB stacking configurations.

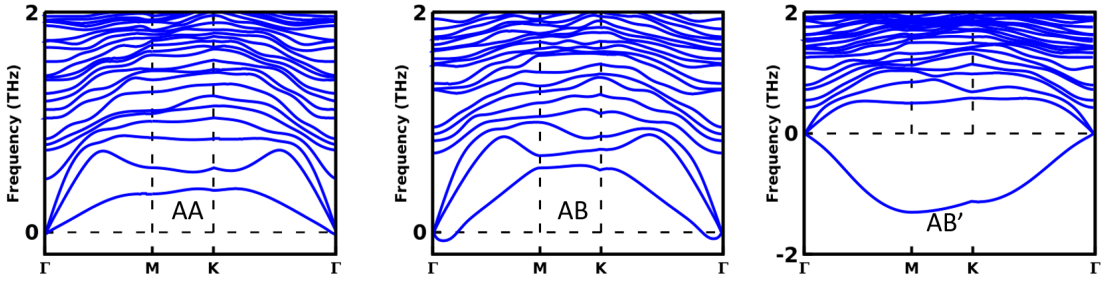

Figure 6.2: **Phonon dispersion of different stacking configurations of $FeTe_2$/Pt(111) heterostructures.** Phonon spectra along the high-symmetry path are shown for (a) AA, (b) AB, and (c) AB′ configurations.

6.3.2 Charge density distribution

To further understand the nature of interfacial interactions, we analyze the charge density difference ($\Delta\rho$) of the $FeTe_2$/Pt(111) heterostructures, as shown in Fig. 6.3. The charge density difference is defined as

$$\Delta\rho = \rho_{FeTe_2/Pt(111)} - \rho_{FeTe_2} - \rho_{Pt(111)},$$

where $\rho_{FeTe_2/Pt(111)}$, ρ_{FeTe_2}, and $\rho_{Pt(111)}$ represent the charge densities of the heterostructure, isolated $FeTe_2$ layer, and Pt (111) substrate, respectively.

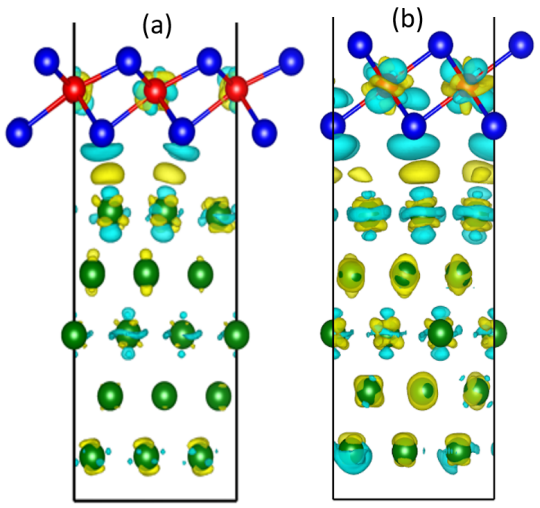

Figure 6.3: **Charge density difference in $FeTe_2$/Pt(111) heterostructures.** Charge density difference plots for (a) AA and (b) AB configurations, where yellow and cyan denote charge accumulation and depletion, respectively. The redistribution of charge near the Te and Pt atoms indicates strong interfacial hybridization and charge transfer across the interface.

In the plots, the yellow and cyan isosurfaces correspond to charge accumulation and depletion, respectively. A pronounced redistribution of charge is observed at the $FeTe_2$/Pt interface, indicating strong interlayer interaction. In particular, significant charge accumulation is visible around the Te atoms and the topmost Pt layer, while depletion regions appear near the Fe atoms. This suggests that electrons are transferred from the Fe layer toward the Te–Pt interface, leading to a modified electronic environment around the magnetic Fe sites. The observed charge redistribution highlights strong hybridization between Te p orbitals and Pt d orbitals, which acts as a bridge for electronic coupling between the Fe layer and the HM substrate. This hybridization plays a key role in modifying the local crystal field and enhancing SOC effects at the interface.

Comparing the two stacking configurations, the AB stacking exhibits a more pronounced and spatially extended charge redistribution compared to the AA configuration. This behavior originates from the lateral $(1/3,\ 1/3)$ shift in the AB configuration, which leads to

enhanced orbital overlap between Te/Fe and Pt atoms. As a result, the interfacial hybridization is stronger in AB, which is expected to have a significant impact on the electronic and magnetic properties of the heterostructure. Overall, the charge density difference analysis confirms that the $FeTe_2$/Pt interface is characterized by substantial charge transfer and orbital hybridization, which are essential for tuning the interfacial electronic structure and related physical properties.

6.3.3 Spin model and magnetic parameters

To quantitatively describe the magnetic interactions in the $FeTe_2$/Pt(111) heterostructure, we map the first-principles results onto an effective spin Hamiltonian defined on the Fe sublattice.

$$H = \frac{1}{2}\sum_{i,j} J_{ij}\,\mathbf{S}_i \cdot \mathbf{S}_j - K_\mu \sum_i \left(S_i^z\right)^2 + \frac{1}{2}\sum_{i,j} \mathbf{d}_{ij} \cdot \left(\mathbf{S}_i \times \mathbf{S}_j\right) \ , \tag{6.1}$$

The Hamiltonian includes isotropic Heisenberg exchange interactions up to third nearest neighbors (J_1, J_2, J_3), uniaxial magnetic anisotropy (K_u), and the DMI, which arises due to broken inversion symmetry at the interface combined with strong SOC. The extracted magnetic parameters as a function of Pt thickness are summarized in Table 6.2, and their evolution is illustrated in Fig. 6.4. These results reveal a complex interplay between exchange interaction, interfacial hybridization, and SOC, all of which are strongly modulated by the thickness of the Pt substrate and stacking geometry.

Magnetic moment and electronic reconstruction

The magnetic moment of Fe given in Table 6.2 shows a noticeable dependence on Pt thickness, particularly in the AA stacking where it decreases significantly from 3.55 μ_B at 1 ML to $\sim$2.3 μ_B at 2 ML, followed by a gradual stabilization. This reduction is a direct consequence of enhanced hybridization between Fe d states and Te p states, which further couple

to Pt d orbitals, as already indicated by the charge density redistribution. The delocalization of Fe d electrons reduces the local magnetic moment and modifies the exchange pathways. In contrast, the AB stacking exhibits a relatively stable magnetic moment across thickness, suggesting a different hybridization environment due to its shifted atomic registry.

Table 6.2: Magnetic moment (μ), exchange interactions (J_1, J_2, J_3), magnetic anisotropy (K_u), DMI ($d_\parallel$), and micromagnetic DMI (D).

Pt layers (ML)	μ (μ_B)	J_1	J_2	J_3	K_u	$d_\parallel$	D (mJ m^{-2})
AA stacking							
1	3.55	-6.10	-3.13	-1.08	-2.30	0.14	0.38
2	2.30	-5.15	-2.89	-0.89	2.28	0.32	0.86
3	2.91	-4.54	-2.10	-0.60	3.13	0.80	2.11
4	2.97	-3.87	-2.32	0.13	2.90	0.50	1.29
5	2.89	4.90	-1.40	0.22	2.12	0.33	0.84
AB′ stacking							
1	2.71	-4.50	-2.96	-0.93	-1.86	0.26	0.71
2	2.74	-2.35	-1.16	-0.71	2.96	0.56	1.50
3	2.75	-3.06	-2.05	-0.43	3.21	1.75	4.50
4	3.32	-2.90	-1.68	-0.32	3.39	0.81	2.09
5	3.51	2.33	-1.08	0.50	3.01	0.22	0.55

Exchange interactions

By solving the total energy expressions given in Chapter 5, we extract the exchange parameters J_1, J_2, and J_3 for the AA and AB stacking configurations. The calculated values are summarized in Table 6.2, and their variation with Pt thickness is shown in Figs. 6.4(a) and (b). Among the three interactions, the nearest-neighbor exchange J_1 is clearly dominant, while J_2 and J_3 remain comparatively weaker across all Pt thicknesses. The dominance of J_1 originates from its direct Fe–Fe exchange nature, which involves strong overlap between neighboring Fe d orbitals. As a result, J_1 primarily determines the magnetic ground state of the system. At low Pt thickness (1–3 ML), J_1 is negative, indicating FM coupling

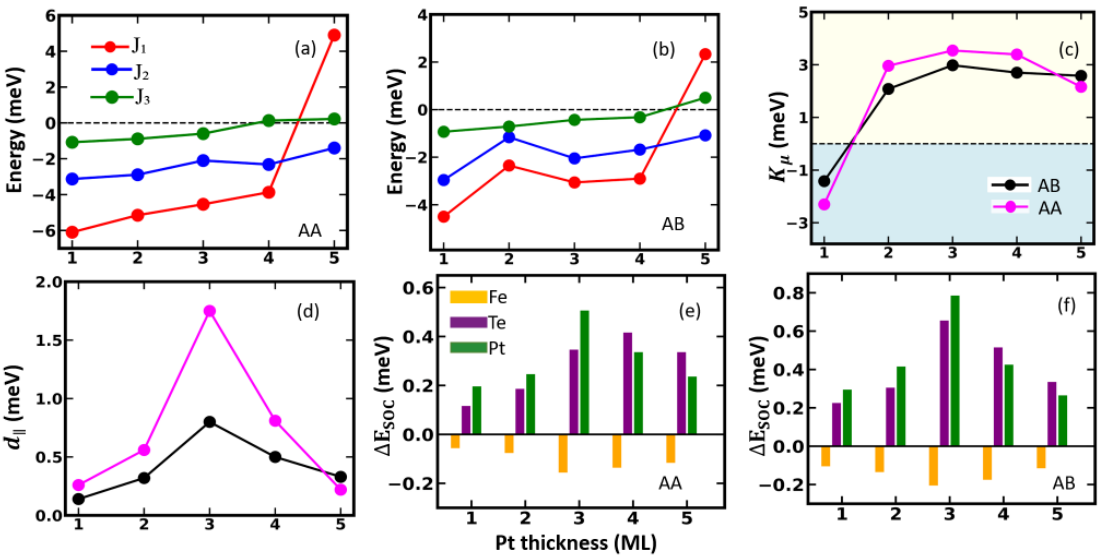

Figure 6.4: Variation of magnetic interactions and spin–orbit coupling contributions in $FeTe_2$/Pt heterostructures as a function of Pt thickness (ML). (a,b) Evolution of the nearest- (J_1), next-nearest- (J_2), and third-nearest-neighbor (J_3) exchange interactions for (a) AA and (b) AB stackings. (c) K_u for both stackings. The blue-shaded region ($K_u < 0$) corresponds to in-plane magnetic anisotropy, while the yellow-shaded region ($K_u > 0$) indicates out-of-plane magnetic anisotropy. (d) In-plane DMI $d_{||}$ as a function of Pt thickness for AA and AB configurations. (e,f) Atom-resolved SOC energy contributions (ΔE_{SOC}) from Fe, Te, and Pt atoms for AA and AB stackings.

between Fe spins. In this regime, the Fe d electrons are relatively localized, and the direct exchange interaction favors parallel spin alignment. However, with increasing Pt thickness, a significant modification of J_1 is observed. In particular, J_1 increases in magnitude and eventually changes sign at larger thickness (around 5 ML), indicating a transition from FM to AFM. This behavior is consistent with the charge density redistribution discussed earlier in Fig. 6.3, where increased delocalization of Fe d electrons toward the Te–Pt interface modifies the strength of direct exchange and enhances substrate-mediated interactions. This sign reversal of J_1 can be attributed to the gradual delocalization of Fe d electrons due to hybridization with Te p and Pt d orbitals. As the electronic states become more itinerant, the balance between exchange mechanisms changes, weakening the ferromagnetic

direct exchange and allowing antiferromagnetic contributions to dominate. This behavior reflects the strong influence of the metallic Pt substrate on the magnetic interactions within the $FeTe_2$ layer.

The next-nearest neighbor interaction J_2 is mediated via Te atoms through a Fe–Te–Fe superexchange pathway. As shown in Fig. 6.4 (a)-(b), this interaction depends sensitively on the Fe–Te–Fe bond geometry and orbital overlap. The consistently negative and relatively small magnitude of J_2 suggests that the superexchange interaction favors weak FM coupling but does not compete strongly with J_1 for both the stackings. The third-nearest neighbor interaction J_3 originates from a longer-range exchange mechanism, which can be associated with an RKKY-like interaction mediated by the conduction electrons of the Pt substrate. This interaction is relatively weak but shows a noticeable dependence on Pt thickness, reflecting the increasing role of itinerant electrons at the interface. The small magnitude of J_3 indicates that long-range exchange interactions play a secondary role in determining the magnetic ground state.

In AA stacking, the $FeTe_2$ monolayer is placed directly on the Pt(111) surface, aligning Fe atoms directly above Pt atoms. This direct alignment maximizes the Fe–Pt orbital overlap, making all exchange interactions strongly sensitive to Pt thickness. In AB stacking, the $FeTe_2$ monolayer is laterally shifted by $(1/3, 1/3)$ relative to the Pt surface, displacing Fe atoms away from the direct Pt atop site. This reduces the Fe–Pt orbital overlap and weakens the substrate-induced delocalization of Fe d electrons, resulting in smaller overall magnitudes of J_1, J_2, and J_3 compared to AA across all Pt thicknesses.

Overall, the exchange interactions in the $FeTe_2$/Pt(111) heterostructure arise from a combination of direct Fe–Fe exchange (J_1), Te-mediated superexchange (J_2), and longer-range interactions (J_3) influenced by the metallic substrate. While J_1 provides the dominant contribution, the finite magnitude of J_2 and J_3 indicates the presence of additional exchange pathways that can modify the magnetic interactions beyond nearest neighbors. The inclu-

sion of these interactions is therefore essential for accurately describing the magnetic energetics and capturing possible deviations from simple collinear ordering. In particular, the interplay among J_1, J_2, and J_3 can influence the stability of competing magnetic configurations and plays an important role in determining the spin textures discussed in the following sections.

Magnetic Anisotropy Energy

The Single-ion anisotropy energy (SIA) is defined as the total energy difference between out-of-plane and in-plane magnetization directions,

$$K_u = E_{\parallel} - E_{\perp}, \tag{6.2}$$

where $E_{\parallel}$ and $E_{\perp}$ correspond to the total energies with magnetization oriented in-plane and out-of-plane, respectively. A positive (negative) value of K_u indicates out-of-plane (in-plane) magnetic anisotropy. As shown in Fig. 6.4(c), K_u changes from negative to positive with increasing Pt thickness, indicating a transition from in-plane to out-of-plane anisotropy. This behavior arises from enhanced SOC at the $FeTe_2$/Pt interface due to increased hybridization with Pt d states. Both AA and AB stacking configurations exhibit a similar trend, with maximum K_u at intermediate thickness, while differences between them remain small and originate from stacking-dependent hybridization. It is worth noting that, although the AA configuration shows a slightly larger exchange interaction compared to AB, the SIA exhibits the opposite trend. This difference arises because exchange interactions and magnetic anisotropy originate from distinct microscopic mechanisms. While the exchange interaction is primarily governed by direct Fe–Fe overlap, the SIA is dominated by spin–orbit coupling and its sensitivity to interfacial hybridization. As a result, the enhanced Fe–Te–Pt hybridization in the AB configuration has a stronger impact on SOC-driven anisotropy than on direct exchange, leading to a comparatively larger anistropy despite a similar or smaller exchange interaction.

Dzyaloshinskii–Moriya interaction.

We begin by analyzing the DMI, which plays a central role in stabilizing chiral magnetic textures in this system. According to Moriya's symmetry rules [293], the $FeTe_2$/Pt(111) interface lacks inversion symmetry between adjacent Fe sites but preserves vertical mirror planes passing through each Fe–Fe bond. This symmetry constrains the DMI vector $\mathbf{D}_{ij}$ to lie within the mirror plane and be perpendicular to the Fe–Fe bond direction. Accordingly, the DMI vector can be expressed as

$$\mathbf{D}_{ij} = d_{\parallel}\,(\hat{\mathbf{v}}_{ij} \times \hat{\mathbf{z}}) + d_{\perp}\,\hat{\mathbf{z}}, \tag{6.3}$$

where $\hat{\mathbf{v}}_{ij}$ is the unit vector connecting sites i and j, and $\hat{\mathbf{z}}$ is the out-of-plane direction. The in-plane component $d_{\parallel}$ originates from interfacial SOC and is primarily responsible for stabilizing chiral spin textures. Although the out-of-plane component $d_{\perp}$ is symmetry-allowed, it is significantly smaller and does not contribute appreciably to chiral stabilization; hence, it is neglected in the following analysis. The dominant in-plane DMI component $d_{\parallel}$ is extracted from first-principles calculations using the chirality-dependent total-energy difference method [274, 272, 307, 261]. In this approach, clockwise (CW) and Anticlockwise (ACW) spin configurations are imposed on a 2×1 supercell, defined as

$$\begin{aligned}
\text{CW:}\quad & (\mathbf{S}_1,\,\mathbf{S}_2) = \big[(0,0,S),\,(S,0,0)\big],\\
& (\mathbf{S}_3,\,\mathbf{S}_4) = \big[(0,0,-S),\,(-S,0,0)\big];\\
\text{ACW:}\quad & (\mathbf{S}_1,\,\mathbf{S}_2) = \big[(0,0,S),\,(-S,0,0)\big],\\
& (\mathbf{S}_3,\,\mathbf{S}_4) = \big[(0,0,-S),\,(S,0,0)\big].
\end{aligned} \tag{6.4}$$

The energy difference between these two chiral states yields the DMI strength,

$$d_{\parallel} = \frac{E_{\text{CW}} - E_{\text{ACW}}}{12}, \tag{6.5}$$

as derived in Section 5.3.6 of chapter 5. The sign of $d_{\parallel}$ determines the preferred chirality: $d_{\parallel} > 0$ ($d_{\parallel} < 0$) favors anticlockwise (clockwise) spin rotation.

The calculated values of $d_{\parallel}$ for different stacking configurations and Pt thicknesses are summarized in Table 6.2 and plotted in Fig. 6.4 (d). Among all cases, the AB stacking at 3 ML Pt exhibits the largest DMI, reaching 1.75 meV. This value is significantly higher than those reported for several other vdW magnetic systems, such as Co/graphene bilayers (1.14 meV) [308], $CrTe_2/PtS_2$ (1.02 meV) [302], Pt/CrI_2 (0.28 meV) [309], and Janus monolayers including VBrS (0.15 meV), VIS (0.10 meV), and VISe (0.18 meV) [310]. In both the stackings, $d_{\parallel}$ exhibits a non-monotonic behavior, increasing with Pt thickness and reaching a maximum at intermediate thickness (around 3 ML), followed by a decrease at larger thickness. This trend reflects the competition between interfacial SOC and hybridization effects. At low Pt thickness, the SOC contribution is relatively weak, resulting in small DMI. As the thickness increases, enhanced hybridization between Fe d, Te p, and Pt d orbitals strengthens the SOC-induced asymmetric exchange, leading to a larger DMI. However, at higher thickness, the additional Pt layers behave more bulk-like, reducing the effective interfacial asymmetry and thereby weakening the DMI. Furthermore, the AB stacking consistently shows a larger DMI compared to AA, which can be attributed to the lateral shift that enhances inversion symmetry breaking and interfacial hybridization. This results in a stronger SOC-driven chiral interaction in the AB configuration.

To further understand the microscopic origin of DMI, we analyze the atom-resolved SOC energy difference

$$\Delta E_{\mathrm{SOC}} = E_{\mathrm{SOC}}^{\mathrm{CW}} - E_{\mathrm{SOC}}^{\mathrm{ACW}}, \tag{6.6}$$

as shown in Fig. 6.4(e) and (f). The results indicate that the dominant contribution to ΔE_{SOC} originates from the interfacial Pt atoms, followed by Te, while the contribution from Fe is comparatively small and, in some cases, opposite in sign. This confirms that the HM substrate acts as the primary source of SOC, whereas Te atoms mediate the transfer of this SOC to the magnetic Fe layer via hybridization. Interestingly, a careful analysis of

Fig. 6.4(e) and (f) reveals that, beyond 3 ML Pt thickness, the relative contribution of Te to ΔE_{SOC} becomes comparable to or even larger than that of Pt. This indicates that, although Pt remains the primary source of strong SOC, enhanced hybridization at larger thickness enables Te atoms to play a more active role in mediating the chiral interaction. This behavior reflects a redistribution of SOC effects across the interface, where the SOC influence of Pt is effectively transferred to Te through electronic delocalization. These observations are consistent with the Fert–Levy mechanism of DMI [311, 293], in which heavy atoms act as spin-orbit active scattering centers. In this framework, the strong SOC of Pt induces spin-dependent scattering, which is transmitted to the Fe layer via Te-mediated hybridization. Therefore, the DMI in the $FeTe_2$/Pt(111) heterostructure arises from a cooperative multi-site interaction involving Pt, Te, and Fe atoms, rather than a purely localized interfacial effect.

6.3.4 Spin textures from micromagnetic simulations

After extracting the magnetic interaction parameters of the spin Hamiltonian from first-principles calculations, we perform micromagnetic simulations to investigate the magnetic ordering and spin textures of the $FeTe_2$/Pt(111) vdW heterostructures using MUMAX3 [304]. A key quantity governing the emergence of chiral magnetic states is the ratio between the DMI and the isotropic exchange, $|d_{\parallel}/J|$. For the AA stacking, $|d_{\parallel}/J|$, where $J = J_1 + J_2 + J_3$, increases from ~ 0.01 at 1 ML to ~ 0.11 at 3 ML, and then decreases at larger thickness. In contrast, for the AB stacking, $|d_{\parallel}/J|$ reaches significantly larger values, attaining ~ 0.13 at 2 ML and ~ 0.27 at 3 ML, before decreasing at higher thickness. These values fall within or exceed the typical range of 0.1–0.2 observed in skyrmionic systems [53], indicating favorable conditions for the stabilization of chiral spin textures, particularly in the AB′ stacking at intermediate Pt thickness.

The stability and evolution of chiral magnetic textures were investigated using micro-

magnetic simulations within the continuum framework. In the presence of an external magnetic field $\mathbf{H}(\mathbf{r}) = \mathbf{H}_0$, the total magnetic energy of the system can be written in terms of the local magnetization vector $\mathbf{M}(\mathbf{r})$ as

$$E = E_{\text{DMI}}[\mathbf{M}(\mathbf{r})] + E_{\text{ex}}[\mathbf{M}(\mathbf{r})] + E_{\text{ani}}[\mathbf{M}(\mathbf{r})] + E_{\text{dem}}[\mathbf{M}(\mathbf{r})] + E_{\text{Zeeman}}[\mathbf{M}(\mathbf{r}), \mathbf{H}(\mathbf{r})], \quad (6.7)$$

where $\mathbf{M}(\mathbf{r})$ denotes the unit local magnetization vector at position $\mathbf{r}$, and the different contributions correspond to the DMI, exchange interaction, magnetic anisotropy, demagnetization energy, and Zeeman interaction, respectively. The individual energy-density terms are given by

$$\epsilon_{\text{DMI}}(\mathbf{r}) = D\left[M_z(\nabla \cdot \mathbf{M}) - (\mathbf{M} \cdot \nabla)M_z\right], \quad (6.8)$$

$$\epsilon_{\text{ex}}(\mathbf{r}) = A(\nabla \mathbf{M})^2, \quad (6.9)$$

$$\epsilon_{\text{ani}}(\mathbf{r}) = -K_u(M_z)^2, \quad (6.10)$$

$$\epsilon_{\text{dem}}(\mathbf{r}) = -\frac{1}{2}M_s\mathbf{M} \cdot \mathbf{B}_{\text{dem}}, \quad (6.11)$$

$$\epsilon_{\text{Zeeman}}(\mathbf{r}) = -M_s\mathbf{M} \cdot \mathbf{H}, \quad (6.12)$$

where A denotes the exchange stiffness, D represents the micromagnetic DMI constant, K_u is the uniaxial magnetic anisotropy constant, and M_s is the saturation magnetization. The demagnetization field $\mathbf{B}_{\text{dem}}$ accounts for long-range dipolar interactions in the system. The continuum parameters were obtained by mapping the atomistic spin Hamiltonian onto the micromagnetic model as derived in detail in Appendix A are given by:

$$D = \frac{\sqrt{3}d_{\parallel}}{at}, \qquad A = \frac{\sqrt{3}(J_1 + J_2 + J_3)}{2t}, \qquad K = \frac{2K_{\mu}}{\sqrt{3}a^2t}, \qquad M_s = \frac{2m}{\sqrt{3}a^2t}, \quad (6.13)$$

where a is the lattice constant, t corresponds to the effective monolayer thickness, and m denotes the magnetic moment per magnetic atom. The simulations were performed on a $256 \times 256 \times 1$ computational grid with periodic boundary conditions applied along the in-plane directions to suppress finite-size effects. A cell size of $1\,\text{nm} \times 1\,\text{nm} \times t$ was used

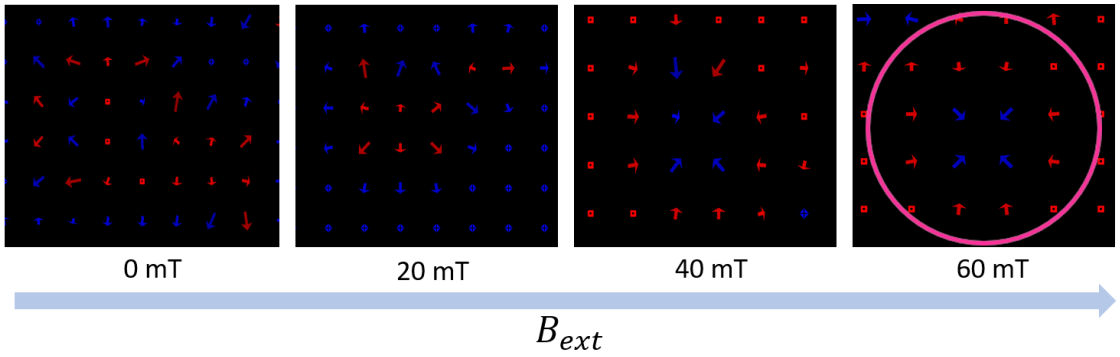

Figure 6.5: Evolution of the magnetic texture in AB stacked $FeTe_2$/Pt(111) with three Pt monolayers under increasing external magnetic field. The system evolves from a disordered noncollinear spin configuration at zero field to a stabilized isolated Néel-type skyrmion at 60 mT.

throughout the calculations. Random spin configurations were used as initial states, and the system was subsequently relaxed through energy minimization to obtain stable equilibrium magnetic textures.

Figure 6.5 shows the evolution of the magnetic texture in AB stacked $FeTe_2$/Pt(111) with three Pt monolayers under increasing external magnetic field (B_{ext}). At zero magnetic field, the system exhibits a disordered noncollinear spin configuration without a distinct topological structure, arising from the competition between exchange interaction and interfacial DMI. As B_{ext} increases to 20 mT, the background magnetization progressively aligns along the field direction, while localized chiral spin canting remains preserved. Upon further increasing B_{ext} to 40 mT, a localized skyrmion-like texture emerges, characterized by a core magnetization opposite to the surrounding ferromagnetic background and a continuous radial rotation of the intermediate spins. At $B_{\text{ext}} = 60$ mT, the skyrmionic texture becomes fully stabilized, resulting in an isolated Néel-type skyrmion embedded within a nearly uniform ferromagnetic background. The stabilized skyrmions possess a characteristic radius (r_{sk}) of approximately 5.1 nm under an external magnetic field of 60 mT. The stabilization of the skyrmion originates from the interplay among exchange interaction, interfacial DMI,

perpendicular magnetic anisotropy, and Zeeman energy.

The observed field-driven evolution of the magnetic textures demonstrates that AB′ stacked $FeTe_2$/Pt(111) with three Pt monolayers resides in a parameter regime favorable for stabilizing topologically nontrivial chiral spin states. In particular, the relatively large value of $|d_{\parallel}/J| \sim 0.27$ obtained for this structure substantially enhances the tendency toward noncollinear spin ordering. The strong DMI induced by the Pt substrate competes effectively with the ferromagnetic exchange interaction and magnetic anisotropy, thereby enabling the stabilization of isolated skyrmions under experimentally accessible magnetic fields.

To further characterize the topological nature of the stabilized chiral spin texture, we evaluated the topological charge (skyrmion number), defined as

$$Q = \frac{1}{4\pi} \int \mathbf{S} \cdot \left(\frac{\partial \mathbf{S}}{\partial x} \times \frac{\partial \mathbf{S}}{\partial y} \right) dx\, dy, \tag{6.14}$$

where $\mathbf{S}$ denotes the normalized spin vector field. A finite integer value of Q confirms the presence of a topologically nontrivial magnetic texture. For the stabilized magnetic configuration obtained at 60 mT, the calculated topological charge approaches $|Q| \approx 1$, confirming the formation of an isolated Néel-type skyrmion in the $FeTe_2$/Pt(111) heterostructure.

6.4 Conclusions

In this chapter, we investigated the emergence of chiral magnetic textures in centrosymmetric $FeTe_2$ through vdW heterostructure engineering with Pt(111). While pristine 1T-$FeTe_2$ lacks intrinsic DMI due to inversion symmetry, interfacing with Pt induces strong interfacial SOC and symmetry breaking, resulting in finite DMI and enhanced magnetic anisotropy. Our first-principles calculations reveal that the magnetic interactions strongly depend on both the stacking configuration and Pt thickness. The exchange interaction is dominated by the nearest-neighbor coupling J_1, while the DMI exhibits a pronounced enhancement at

intermediate Pt thickness. In particular, the AB stacking at 3 ML Pt thickness exhibits the largest DMI, with $d_{\parallel} = 1.75$ meV and micromagnetic DMI constant $D = 4.50$ mJ m^{-2}. Correspondingly, the ratio $|d_{\parallel}/J|$ reaches ~ 0.27, placing the system within the regime favorable for stabilizing chiral magnetic textures. Micromagnetic simulations based on the extracted first-principles parameters demonstrate the field-driven evolution of spin textures from a disordered noncollinear magnetic state to a stabilized isolated Néel-type skyrmion. Under an external magnetic field of $B_{\text{ext}} = 60$ mT, the AB′ stacked $FeTe_2$/Pt(111) heterostructure stabilizes a skyrmion with characteristic radius $r_{\text{sk}} \approx 5.1$ nm. The corresponding topological charge approaches $|Q| \approx 1$, confirming the formation of a topologically nontrivial skyrmionic state.

Overall, the results establish $FeTe_2$/Pt(111) as a promising platform for interfacial DMI-driven skyrmions in centrosymmetric 2D systems. The combined effect of strong SOC, interfacial inversion symmetry breaking, and sizable DMI enables the stabilization of nanoscale skyrmions under experimentally accessible magnetic fields, providing a viable pathway toward ultrathin skyrmion-based spintronic devices.

Chapter 7

Activating DMI in 2D Silicide Ti_2Si via Co and Pt Doping

In the previous chapters, we showed that DMI and MAE arise either intrinsically in non-centrosymmetric H-$FeTe_2$ or via inversion symmetry breaking in the T-$FeTe_2$/Pt(111) heterostructure. In both cases, strong SOC from heavy elements such as Te and Pt plays a crucial role. Here, we address the more challenging case of a centrosymmetric system with weak intrinsic SOC. To this end, we introduce heavy dopants (Co and Pt) into the Ti_2Si monolayer to simultaneously break local symmetry and enhance SOC. Using first-principles calculations and an orbital-resolved tight-binding model, we investigate the emergence and microscopic origin of DMI in doped Ti_2Si.

This chapter is based on the following published work:

[1] **D. Rani**, Gayatri Panda, Subrata Jana, and Prasanjit Samal, *ACS Applied Nano Materials*, 2026, 9, 5423–5434.

7.1 Introdution

In recent years, 2D magnetism has revealed a diverse range of materials capable of hosting DMI-driven spin textures [312, 263, 313, 314]. Beyond the well-studied CrI_3 [283], Fe_3GeTe_2 [269], $MnSe_2$ [315], and $FeTe_2$ [298], long-range magnetic order has also been reported in layered halides such as $CrBr_3$, CrI_3 and $CrCl_3$ [316, 317, 318], Janus MnSTe [319], and metallic systems including monolayer VSe_2 [271] and $NbSe_2$ [320]. Transition-metal dichalcogenides (TMDs), in particular, provide a versatile platform for engineering chiral magnetism, where heavy-element substitution [321, 250], Janus engineering [e.g.,

$Cr_2X_3Y_3$ (X, Y = Cl, Br, I; X $\neq$ Y) [272], MnXY (X, Y = S, Se, Te; X $\neq$ Y) [273], and CrXTe (X = S, Se) [274]], or interfacing with high-SOC substrates such as Pt, W, and Ir [252, 48, 267] can significantly enhance the DMI.

2D silicides remain largely unexplored in the context of chiral magnetism and DMI. While bulk and thin-film silicides have been extensively investigated for their electronic, catalytic, and thermoelectric properties [322, 323], their magnetic behaviour, particularly SOC-driven effects has received comparatively little attention. Reported magnetic silicides such as $GdSi_2$ and TbSi typically exhibit conventional magnetic ordering without evidence of chiral spin textures [324, 325]. Experimental demonstrations of DMI in silicide systems have mainly been restricted to MnSi-based bulk crystals and epitaxial films [326, 327]. Whether monolayer or quasi-2D silicides can host DMI-driven chiral magnetism, where reduced dimensionality and symmetry breaking may play a decisive role, remains an open question.

Recently, binary silicon-based 2D materials have attracted growing interest due to their structural stability and tunable electronic properties [328, 329]. Several transition-metal silicide monolayers have been theoretically predicted and, in some cases, experimentally explored, exhibiting metallic or semiconducting behaviour and, in certain cases, intrinsic magnetism. These advances suggest that silicon-based monolayers can serve as promising nanoscale platforms for functional magnetic materials. Among these systems, titanium silicide (Ti_2Si) monolayers have been predicted to possess intrinsic ferromagnetism, dynamical stability, and tunable electronic phases [330, 331]. The partially filled Ti $3d$ orbitals generate local magnetic moments, and the electronic structure can be effectively modulated by strain or chemical substitution. However, the impact of symmetry breaking and SOC on the emergence of chiral magnetic interactions in Ti_2Si has not yet been systematically explored.

Titanium silicides are well-known materials in the Ti-Si system and can be synthesized

using common solid-state reaction methods. One possible way to obtain Ti_2Si is through self-propagating high-temperature synthesis, where Ti and Si powders are mixed in the correct ratio and heated to trigger a solid-state reaction [332, 333]. Similar silicides, such as $TiSi_2$, have already been grown as thin films and nanostructures using chemical vapor deposition (CVD), where the structure and morphology are controlled by the choice of precursors and growth conditions [334, 335]. Based on these established techniques, Ti_2Si thin films or nanoscale structures could also be produced using controlled vapor-phase growth methods.

First-principles evolutionary structure studies show that Ti_2Si is a low-energy metastable phase in the Ti-Si system [336, 337]. This suggests that it may be experimentally realized under non-equilibrium conditions, such as rapid solidification or thin-film deposition. For doped structures, transition-metal atoms like Co or Pt can be introduced either during growth (by co-deposition or alloying) or after synthesis through diffusion processes. Molten-salt-assisted diffusion has been successfully used to insert metal atoms into silicon-based materials in a controlled way [338]. In addition, studies of Pt thin films reacting with Si substrates show that silicide formation occurs through interfacial diffusion, supporting the possibility of dopant incorporation via reactive diffusion pathways [339]. Together, these well-established synthesis approaches indicate that doped Ti_2Si-based nanoscale structures could be experimentally achievable.

In this work, we demonstrate that controlled Pt and Co substitution [303, 340] at Ti sites provides an effective route to break inversion symmetry and enhance SOC, thereby inducing sizable DMI in Ti_2Si-based monolayers. This strategy establishes Ti_2Si as a tunable silicon-based nanoscale platform for engineering chiral magnetism, with potential applications in chiral magnetism-based memory devices, racetrack logic architectures [341], and electrically controllable spintronic elements. Further, our study focuses on the microscopic origin of the DMI in two-dimensional silicides. We employ first-principles calculations together

with a Wannier based tight-binding (TB) model [342, 343] to analyze orbital dependent interlayer and intralayer superexchange pathways in the layered structure. This microscopic perspective naturally connects to the emerging field of orbitronics, which seeks to exploit the generation, transport, and manipulation of orbital angular momentum in solids [344]. Recent advances in orbitronics have underscored the importance of two-dimensional materials as platforms where orbital geometry, symmetry breaking, and chemical engineering can be harnessed to control relativistic and chiral phenomena [345]. In this context, identifying how orbital resolved superexchange pathways govern interlayer and intralayer DMI in 2D silicides not only advances the understanding of chiral magnetism, but also provides insight into orbital-driven functionality in low-dimensional materials.

7.2 Model and Computational Details

We investigate the 2D Ti_2Si, which crystallizes in a tetragonal structure belonging to the centrosymmetric space group $P4/mmm$, with optimized lattice constants $a = b = 2.73$ with vacumm slab 20 . All first-principles calculations are performed within the framework of DFT using the VASP package [156]. The electron ion interactions are described using the PAW method [108, 109], and the exchange correlation energy is treated within the GGA of PBE [145]. To account for on-site Coulomb interactions among Ti $3d$ states, we employ the DFT+U method [330] in the Dudarev formulation [346] with an effective $U_{\text{eff}} = 2$ eV, which correctly reproduces the ground-state magnetic configuration of Ti_2Si monolayers. The plane-wave basis set is truncated at a kinetic energy cutoff of 420 eV, and Brillouin-zone integrations are performed using a Γ-centered $16 \times 16 \times 1$ Monkhorst-Pack k-point grid. All calculations are spin-polarized unless otherwise stated. A Gaussian smearing of 0.05 eV is used for Brillouin-zone integration. A dipole correction is applied along the out-of-plane direction to avoid spurious interactions between periodic slabs. The DMI is

extracted by enforcing opposite spin rotation chiralities (clockwise and counterclockwise) in a 4×1 supercell for pristine Ti_2Si and a 4×2 supercell for Pt- and Co-doped structures. The resulting energy differences yield both the direction and magnitude of the DMI vectors with high accuracy. To estimate the magnetic transition temperature, Classical Monte Carlo simulations were performed using the Metropolis algorithm [347]. The magnetic susceptibility was calculated from thermal fluctuations as [348]

$$\chi = \frac{N}{k_B T} \left(\langle M^2 \rangle - \langle M \rangle^2 \right). \tag{7.1}$$

where N is the total number of spins and M is the magnetization per spin. The Curie (or Néel) temperature was determined from the peak position of the susceptibility curve. All Monte Carlo simulations were performed using the JuMag package [349].

To compute the orbital-resolved DMI, we construct a tight-binding (TB) Hamiltonian from maximally localized Wannier functions (MLWFs) generated using the Wannier90 package [342]. The formalism is based on the Anderson superexchange mechanism [350], extended by Moriya [256] and Dzyaloshinskii [255] to account for antisymmetric exchange interactions in the presence of SOC. The Wannier-based TB Hamiltonian faithfully reproduces the *ab initio* electronic structure and provides orbital-resolved hopping parameters, obtained using TBMODELS [351]. These hopping integrals form the basis for evaluating both symmetric (Heisenberg) and antisymmetric (DMI) exchange interactions. In this framework, the MLWFs represent localized orbitals on magnetic cations and ligand atoms, naturally incorporating crystal symmetry and enabling a systematic analysis of orbital overlaps. SOC is explicitly included in the effective Hamiltonian, and interactions among all relevant nearest neighbors are considered. By analyzing the complex hopping amplitudes between orbital pairs, we extract the orbital-resolved DMI contributions for Ti_2Si and its doped derivatives.

7.3 Results and Discussions

7.3.1 Structural, Electronic, and Magnetic Properties

In this work, we have investigated the monolayer Ti_2Si, shown in Fig. 7.1(a), which consists of a Ti-Si-Ti trilayer with a bond angle $\theta = 63°$, indicating a slight deviation from ideal planarity. The phonon dispersion calculated using a 4×4 supercell [Fig. 7.1(b)] displays no imaginary frequencies throughout the Brillouin zone, confirming the dynamical stability of the Ti_2Si monolayer. The orbital-resolved DOS in Fig. 7.1(c) shows that the states near

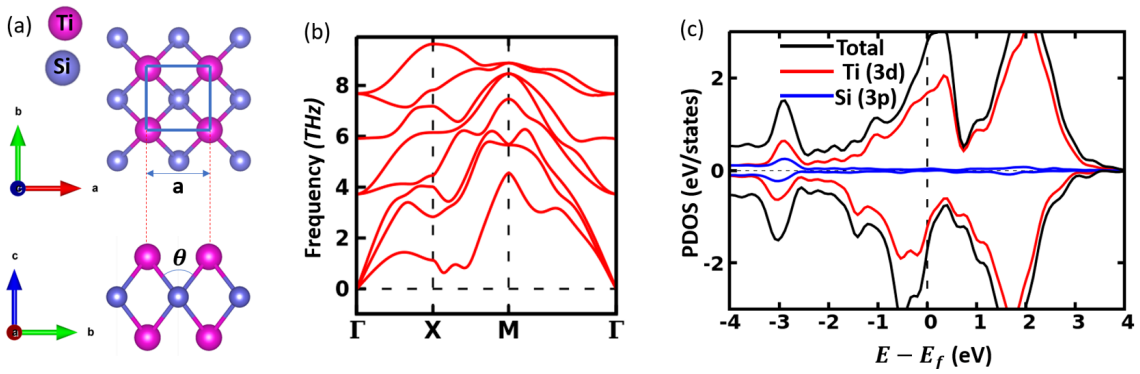

Figure 7.1: (a) Top and side views of the Ti_2Si monolayer, where a denotes the lattice constant and θ represents the bond angle. (b) Phonon dispersion confirming the dynamical stability of the system. (c) Spin-polarized projected density of states (PDOS) of the Ti_2Si monolayer.

the Fermi level are mainly contributed by the Ti $3d$ orbitals, with noticeable hybridization from the Si $3p$ states. The exchange splitting of the Ti $3d$ orbitals produces a spin-polarized electronic structure, confirming that Ti_2Si behaves as an itinerant ferromagnetic metal. The total magnetic moment is about $1.43\ \mu_B$ per unit cell, concentrated mostly on the Ti atoms, with the Si p orbitals contributing through an indirect superexchange pathway. To understand how Ti_2Si responds to external perturbations, we applied a perpendicular electric field ($\vec{E}$) and examined how it affects the electronic and magnetic properties.

In order to understand the magnetic interactions in Ti_2Si monolayers, we consider the

generalized spin Hamiltonian,

$$H = \frac{1}{2}\sum_{i,j} J_{ij}\,\mathbf{S}_i \cdot \mathbf{S}_j - K_\mu \sum_i \left(S_i^z\right)^2 + \frac{1}{2}\sum_{i,j} \mathbf{d}_{ij} \cdot \left(\mathbf{S}_i \times \mathbf{S}_j\right) \ , \tag{7.2}$$

where J_{ij} represents the isotropic Heisenberg exchange coupling, K_μ denotes the uniaxial single-ion anisotropy constant, and $\mathbf{d}_{ij}$ is the Dzyaloshinskii-Moriya vector. The anisotropy term governs the preferred spin orientation, stabilizing out-of-plane alignment for $K_\mu > 0$ and in-plane orientation for $K_\mu < 0$. The DMI contribution encodes the antisymmetric exchange that favors chiral spin textures.

To extract the exchange interactions, we constructed a 4×1 supercell to capture up to fourth-nearest-neighbor Ti–Ti interactions. Several collinear magnetic configurations were considered, including the ferromagnetic (FM) state and four distinct antiferromagnetic orderings (AFM_1–AFM_4), as illustrated in Figs. 7.2(a)–(e). Mapping the DFT total energies onto the Heisenberg Hamiltonian [Eq. (11)], the total energies for the different spin configurations can be expressed as

$$E_{\mathrm{FM}} = \frac{1}{4}S^2\left(2J_1 + J_2 + 2J_3 + J_4\right) + E_0, \tag{7.3}$$

$$E_{\mathrm{AFM_1}} = \frac{1}{4}S^2\left(-2J_1 + J_2 - 2J_3 + J_4\right) + E_0, \tag{7.4}$$

$$E_{\mathrm{AFM_2}} = \frac{1}{4}S^2\left(2J_1 - J_2 - 2J_3 + J_4\right) + E_0, \tag{7.5}$$

$$E_{\mathrm{AFM_3}} = \frac{1}{4}S^2\left(-J_2 - J_4\right) + E_0, \tag{7.6}$$

$$E_{\mathrm{AFM_4}} = \frac{1}{4}S^2\left(-2J_1 + J_2 - J_4\right) + E_0. \tag{7.7}$$

Here, S denotes the local magnetic moment on Ti, and E_0 represents the nonmagnetic reference energy. The set of linear equations in Eqs. (7.3)–(7.7) enables an unambiguous determination of the exchange parameters J_1–J_4. Among them, J_1, J_2, and J_4 correspond to direct Heisenberg exchange between Ti atoms, whereas J_3 originates from Ti–Si–Ti superexchange pathways.

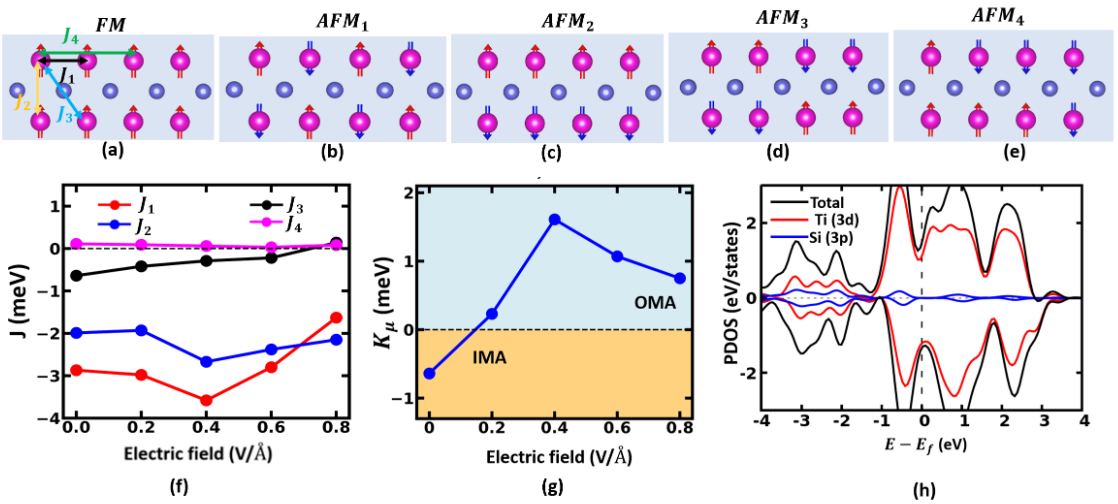

Figure 7.2: (a-e) Schematic spin configurations used for extracting exchange parameters in Ti_2Si, including the FM and four AFM states (AFM_1-AFM4). The exchange pathways corresponding to J_1, J_2, J_3, and J_4 are illustrated in panel (a).(f) Heisenberg exchange interaction parameter $J_i^{'s}$ as a function of external electric field. (g) Single-ion anisotropy as a function of external electric field, where the blue region indicates out-of-plane magnetic anisotropy (OMA) and the yellow region corresponds to in-plane magnetic anisotropy (IMA). (h) Spin-resolved density of states of the Ti_2Si monolayer calculated under an applied electric field of 0.4 V/Å.

As shown in Fig. 7.2(f), J_1 and J_2 remain negative throughout the electric-field range of 0–0.8 V/Å, indicating robust ferromagnetic (FM) coupling. Among these, J_1 exhibits the strongest FM interaction and shows a pronounced nonmonotonic variation with increasing electric field, reaching its maximum magnitude near 0.4 V/Å. A similar trend is observed for J_2, though with smaller magnitude. In contrast, J_3 is significantly weaker and gradually approaches zero as the electric field increases, eventually becoming slightly positive at 0.8 V/Å, signalling a crossover from weak FM to weak antiferromagnetic (AFM) coupling. The fourth nearest neighbor interaction J_4 remains very small across the entire field range and exhibits weak AFM character at higher electric fields. Overall, the dominant contributions from J_1 and J_2 stabilize the ferromagnetic ground state under applied electric fields. The nonmonotonic behavior of J_1 and J_2 reflects the field-induced modulation of the Ti-3d

and Si-$3p$ orbital hybridization, which governs the superexchange interaction and magnetic coupling strength.

The single-ion magnetic anisotropy constant (K_μ) is evaluated as

$$K_\mu = E_\parallel - E_\perp, \tag{7.8}$$

where $E_\parallel$ and $E_\perp$ denote the total energies with magnetization oriented in-plane and out-of-plane, respectively. A positive K_μ indicates an easy-axis anisotropy along the out-of-plane direction, which is favorable for skyrmion formation. As shown in Fig. 7.2(g), K_μ exhibits strong field dependence: at zero electric field, $K_\mu < 0$ corresponds to an in-plane magnetic anisotropy (IMA), while increasing the field drives a sign reversal, marking a transition to out-of-plane magnetic anisotropy (OMA). This reorientation originates from an electric field-induced redistribution of Ti 3d orbital occupations, which alters the SOC contribution to the total anisotropy energy. Such $\vec{E}$ controlled modulation of K_μ highlights the potential of Ti_2Si as a platform for tunable spintronic phenomena.

At $E = 0.4$ V/Å, the PDOS as shown in Fig. 7.2 (h), reveals a clear field-induced redistribution of the Ti–3d states near the Fermi level, accompanied by changes in Ti–Si hybridization and local bond geometry. This electronic rearrangement modifies the relative strength of the competing superexchange channels, leading to a pronounced minimum in the magnitude of the ferromagnetic exchange interaction J_1 and J_2. The magnetic anisotropy K_μ exhibits a similar nonmonotonic response: it increases with the applied field and reaches its maximum at $E = 0.4$ V/Å, after which it decreases but remains positive. This behavior reflects the enhanced occupation of Ti–3d states around E_F at moderate fields, which strengthens the out-of-plane anisotropy before weakening again at higher fields. Overall, the nonmonotonic evolution of J_1, J_2 and K_μ originates from the electric-field-driven reshaping of the Ti–3d electronic structure.

Overall, the $\vec{E}$ dependent modulation of both J_1, J_2 and K_μ demonstrates that Ti_2Si is

a promising two-dimensional magnetic system with electrically controllable exchange and anisotropy energies. Such tunability suggests potential applications of Ti_2Si in voltage-controlled spintronic and magnetoelectric devices. We have also explored the possibility of inducing inversion symmetry breaking in the Ti_2Si monolayer by applying an external electric field, aiming to generate a finite DMI. However, even under a relatively strong electric field of 0.8 V/Å, the structural inversion symmetry remained preserved, as no significant atomic displacement or potential asymmetry was observed between the two Ti sublayers. This indicates that the intrinsic crystal field and strong covalent bonding in Ti-Si layers effectively screen the external perturbation, thereby suppressing $\vec{E}$ driven inversion asymmetry and, consequently, the emergence of DMI.

7.3.2 Influence of Doping on Exchange interactions and anisotropy

Even when an external electric field is applied, the inversion symmetry of pristine Ti_2Si remains intact, preventing the formation of any finite DMI. To lift this intrinsic symmetry constraint and strengthen the magnetic interactions, we introduce Transition Metal (TM) substitution at the Ti sites. Co-doping generates substantial local magnetic moments and enhances the exchange coupling, while Pt, owing to its strong SOC, supplies the relativistic contribution required to produce a finite DMI. The schematic Illusration of Co and Pt doping in Ti_2Si monolayer is shown in Fig. 7.3 (a).

To investigate the combined influence of magnetism and SOC, we constructed a 4×2 Ti_2Si supercell and examined several substitutional configurations, including $Pt_{0.5}Ti_{1.5}Si$, $Pt_{0.5}Co_{0.5}TiSi$, $Pt_{0.5}CoTi_{0.5}Si$, and $Pt_1Co_{0.5}Ti_{0.5}Si$, together with the limiting cases CoTiSi, PtTiSi. An ab initio molecular dynamics (AIMD) simulations were performed for the Ti_2Si monolayer and its doped structures within the canonical (NVT) ensemble at 300 K for a total duration of 10 ps, using a time step of 1 fs and the Nosé–Hoover thermostat [352] as shown in Fig. 7.4 The temperature fluctuates mildly around 300 K without abrupt deviations, con-

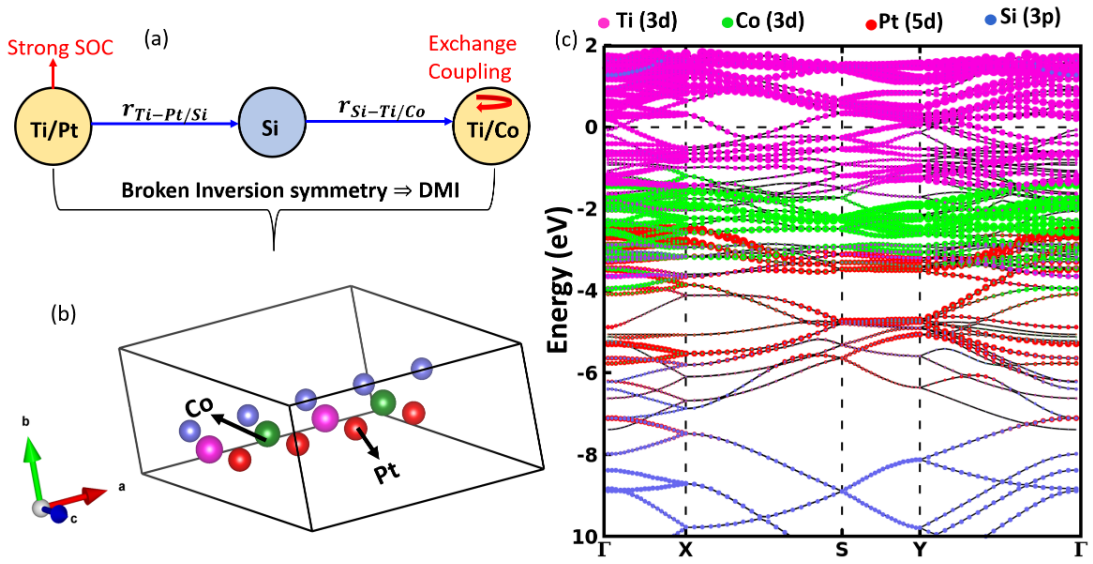

Figure 7.3: (a)Schematic representation of the asymmetric Ti/Pt-Si-Ti/Co exchange pathway in the doped Ti_2Si monolayer. Pt provides strong SOC on one side and Co strengthens the exchange interact in on the other, together creating the conditions required for a finite DMI. (b) Relaxed atomic structure of the $Pt_{0.5}CoTi_{0.5}Si$ configuration, illustrating the asymmetric coordination created by simultaneous Pt and Co substitution. (c) Orbital-projected band structure of $Pt_{0.5}CoTi_{0.5}Si$ strcuture.

firming proper thermal equilibration throughout the simulation.No structural distortions, bond breaking, or significant atomic rearrangements are observed during the entire simulation period. The normalized total energy per atom exhibits only small fluctuations with no systematic drift, indicating good numerical stability of the calculations [353, 354]. These results demonstrate that the Ti_2Si monolayer and its doped variants are thermally stable at room temperature. This systematic chemical substitution provides a controlled route for tuning the balance between exchange interactions and SOC, offering a microscopic basis for identifying how each contribution influences the emergence and stabilisation of chiral magnetic textures. The optimised atomic configuration of $Pt_{0.5}CoTi_{0.5}Si$ is illustrated in Fig. 7.3 (b), where Co and Pt atoms are distributed asymmetrically within a 4×2 supercell of Ti_2Si, thereby breaking local inversion symmetry and providing a natural environment

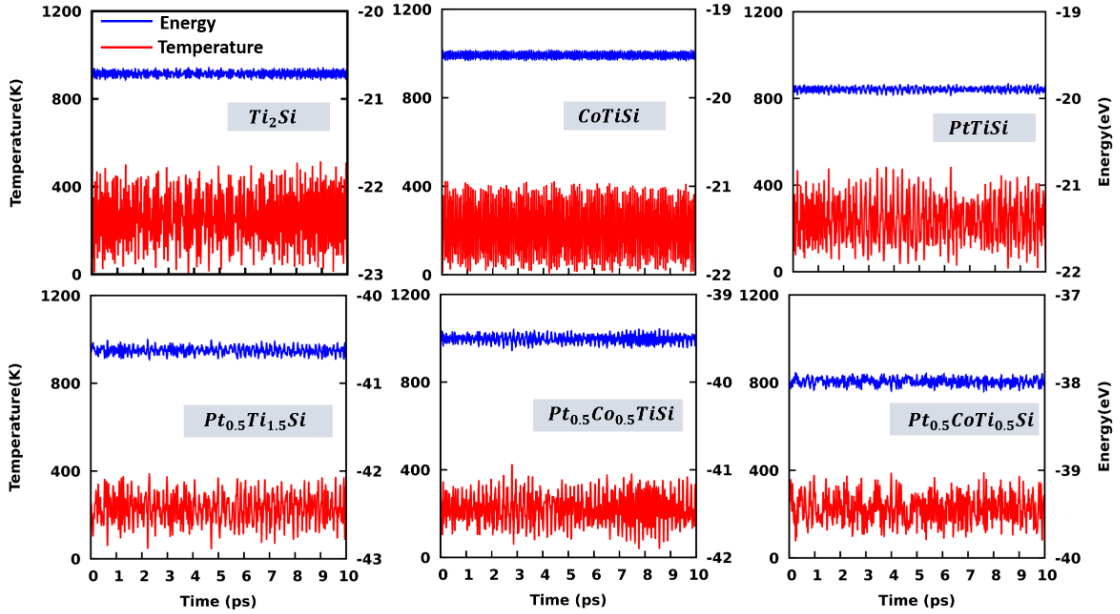

Figure 7.4: Time evolution of temperature (red) and total energy (blue) obtained from 10 ps ab initio molecular dynamics (AIMD) simulations at 300 K for pristine and doped Ti_2Si monolayers.

for DMI to emerge.

Fig. 7.3 (c) shows the orbital-projected band structure of the $Pt_{0.5}CoTi_{0.5}Si$ configuration, revealing how TM substitution modifies the electronic states of the Ti_2Si host. The Pt-derived $5d$ states strongly hybridize with the Si $3p$ manifold in the energy window below the Fermi level, reflecting the substantial SOC introduced by Pt. In parallel, the Co $3d$ orbitals couple predominantly with the Ti $3d$ states, forming a broadened d-band complex that enhances the exchange-splitting within the magnetic sublattice. The coexistence of these two distinct types of hybridization, Pt-induced strong SOC on one side and Co-driven magnetic exchange on the other, breaks the local chemical environment and reshapes the low-energy band dispersion. This asymmetric redistribution of orbital character provides the microscopic origin for the emergence of finite DMI in the doped Ti_2Si system, as it modifies both the relativistic hopping amplitudes and the exchange pathways responsible

for chiral magnetic interactions.

Table 7.1: Calculated element-resolved magnetic moments on Ti (M_{Ti}) and Co (M_{Co}), induced magnetic moment in Pt (M_{Pt}), exchange coupling parameters J_1–J_4, single-ion anisotropy energy K_μ, DMI constants d_1 and d_2, corresponding micromagnetic DMI strengths D_1 and D_2, and Monte Carlo estimated Curie temperature T_C for the different Pt/Co/Ti/Si compositions considered.

Material	M_{Ti} (μ_B)	M_{Co} (μ_B)	M_{Pt} (μ_B)	J_1 (meV)	J_2 (meV)	J_3 (meV)	J_4 (meV)	K_μ (meV)	d_1 (meV)	d_2 (meV)	D_1 (mJ/m^2)	D_2 (mJ/m^2)	T_C (K)
$Pt_{0.5}Ti_{1.5}Si$	1.24	0.00	0.02	-2.85	-0.98	-0.32	0.25	0.72	0.03	-0.12	0.05	-0.23	38
$Pt_{0.5}Co_{0.5}TiSi$	1.17	1.05	0.05	-1.25	-1.09	-0.53	-0.11	1.41	0.09	-0.17	0.17	-0.33	40
$Pt_{0.5}CoTi_{0.5}Si$	0.52	1.55	0.06	-5.55	-4.40	0.24	0.09	-2.31	0.11	-0.26	0.21	-0.50	110
CoTiSi	0.82	0.97	0.00	-3.33	-1.98	-0.76	0.08	1.19	-0.04	0.00	0.08	0.00	56
PtTiSi	0.89	0.00	0.02	-2.18	0.00	0.00	0.00	1.50	0.00	-0.02	0.00	-0.04	42

The element-resolved magnetic moments listed in Table 7.1 show a clear dependence on the local Pt/Co/Ti coordination around the magnetic sites. In the Ti-rich composition $Pt_{0.5}Ti_{1.5}Si$, the Ti atoms carry a sizeable M_{Ti} of 1.24 μ_B, while Co is absent and Pt hosts only a very small induced moment of 0.02 μ_B, reflecting the weak polarization of Pt-5d states. Introducing Co into the lattice, as in $Pt_{0.5}Co_{0.5}Ti_1Si$, leads to the development of a substantial Co moment and a moderate Ti moment, indicating that the spin density becomes redistributed between Co and Ti through hybridization. The induced Pt moment also increases slightly, highlighting the sensitivity of Pt-5d polarization to the presence of magnetic Co neighbors. Upon further increasing the Co concentration to $Pt_{0.5}Co_1Ti_{0.5}Si$, the Co moment reaches its maximum value (1.55 μ_B), while the Ti moment drops significantly to 0.52 μ_B, demonstrating that the magnetic character becomes increasingly dominated by the Co network. The induced Pt moment is also the largest in this composition (0.06 μ_B), consistent with stronger Co-Pt hybridization. In the CoTiSi compound, the Co and Ti moments remain sizable, while in PtTiSi, where Co is absent, Ti retains a moderate moment (0.89 μ_B) and Pt acquires only a small induced moment (0.02 μ_B). Overall, the data reveal a systematic evolution of the magnetic moments: Ti carries the dominant moment in Ti-rich compositions, Co becomes the primary magnetic contributor as its concentration increases, and Pt consistently hosts only a small induced moment whose magnitude reflects the de-

gree of Co-Pt hybridization. These trends highlight the interplay between local chemical coordination and the distribution of spin density across the Pt/Co/Ti sublattice.

To understand how the local chemical environment influences the magnetic interactions, we analyze the extracted exchange parameters J_1-J_4 for the five $Pt_xCo_yTi_zSi$ compositions listed in Table 7.1, with the with the spin arrangment for FM and AFM states shown in Fig. 7.5. For CoTiSi, where the number and spatial arrangement of magnetic atoms remain

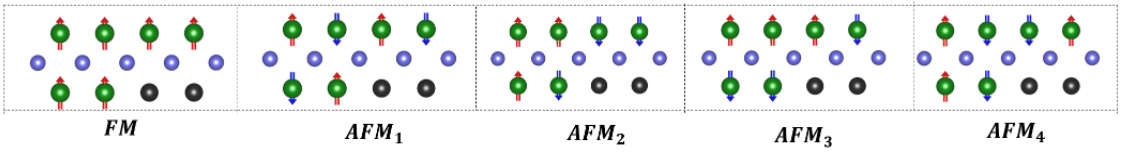

Figure 7.5: Spin arrangements of the ferromagnetic (FM) and four antiferromagnetic (AFM_1–AFM_4) configurations considered for the Pt- and Co-doped structures, namely $Pt_{0.5}Ti_{1.5}Si$, $Pt_{0.5}Co_{0.5}TiSi$, and $Pt_{0.5}CoTi_{0.5}Si$. Green spheres represent magnetic atoms, while black spheres denote nonmagnetic atoms.

unchanged within the supercell, the total energies of the five magnetic configurations are mapped onto the Heisenberg model described in Eqs. 7.3-7.7. In contrast, for PtTiSi only a single magnetic Ti layer remains after Pt substitution, while the remaining layers become nonmagnetic. In this situation, only the nearest-neighbor AFM_1 configuration can be meaningfully constructed. Therefore, only J_1 can be reliably extracted for this composition. For the Pt-containing doped systems ($Pt_{0.5}Ti_{1.5}Si$, $Pt_{0.5}Ti_{1.5}Si$ and $Pt_{0.5}Co_{0.5}Ti_1Si$), the substitution modifies both the number and spatial distribution of magnetic atoms. As a result, certain exchange pathways are altered and the magnetic connectivity changes. Consequently, the energy-mapping equations are adjusted to reflect the modified bond counting:

$$E_{\mathrm{FM}} = \frac{1}{4}S^2\left(2J_1 + J_2 + J_3 + J_4\right) + E_0, \tag{7.9}$$

$$E_{\mathrm{AFM_1}} = \frac{1}{4}S^2\left(-2J_1 - J_2 + J_3 + J_4\right) + E_0, \tag{7.10}$$

$$E_{\mathrm{AFM_2}} = \frac{1}{4}S^2\left(-J_2 + J_3 - J_4\right) + E_0, \tag{7.11}$$

$$E_{\mathrm{AFM_3}} = \frac{1}{4}S^2\left(-J_2 - J_3 + J_4\right) + E_0, \tag{7.12}$$

$$E_{\mathrm{AFM_4}} = \frac{1}{4}S^2\left(J_2 - J_3 - J_4\right) + E_0. \tag{7.13}$$

This ensures that the exchange parameters are extracted consistently with the actual magnetic topology of each composition. The resulting J_1-J_4 values are summarized in Table 7.1. The corresponding spin arrangements (FM and $\mathrm{AFM_1}$-$\mathrm{AFM_4}$) are illustrated in Fig. 7.5. From Table 7.1, J_1 is negative for all compositions, indicating dominant nearest-neighbor ferromagnetic coupling. Its magnitude increases significantly upon Co substitution and reaches the largest value (-5.55 meV) in $Pt_{0.5}CoTi_{0.5}Si$, reflecting enhanced exchange due to increased magnetic moment and stronger magnetic connectivity. A similar trend is observed for J_2, which becomes particularly strong in $Pt_{0.5}CoTi_{0.5}Si$, confirming reinforced longer-range ferromagnetic interactions. In contrast, for PtTiSi only J_1 remains finite because Pt substitution leaves a single magnetic Ti layer, eliminating extended exchange pathways. The variation and occasional sign change of J_3 and J_4 indicate modified exchange channels induced by Pt and Co incorporation.

As shown in Fig. 7.6, the magnetic anisotropy constants K_μ are presented graphically, with their numerical values summarized in Table 7.1. the first two compositions, $Pt_{0.5}Ti_{1.5}Si$ and $Pt_{0.5}Co_{0.5}TiSi$, exhibit positive K_μ values, indicating out-of-plane magnetic anisotropy (OMA). In these systems, the combined effect of Ti-driven hybridization and SOC favors perpendicular magnetization. When the Co concentration increases further, as in $Pt_{0.5}CoTi_{0.5}Si$, the magnetic behavior changes markedly. The anisotropy constant K_μ becomes negative,

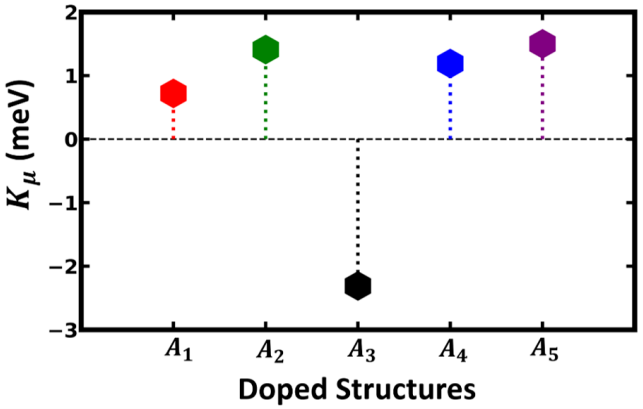

Figure 7.6: Evolution of the magnetic anisotropy K_μ across different doped Ti_2Si configurations. The abbreviations correspond to: A_1 = $Pt_{0.5}Ti_{1.5}Si$, A_2 = $Pt_{0.5}Co_{0.5}Ti_1Si$, A_3 = $Pt_{0.5}Co_1Ti_{0.5}Si$, A_4 = CoTiSi, and A_5 = PtTiSi.

signaling a transition from OMA to in-plane magnetic anisotropy (IMA), which is consistent with the more planar bonding environment around the closely spaced Co atoms. The two end-member compounds, CoTiSi and PtTiSi, retain positive K_μ values, showing that although ferromagnetic exchange dominates, the magnetic anisotropy is primarily governed by the local Ti/Pt coordination and the associated spin-orbit interaction. Overall, the sign of K_μ reflects how the local spin-orbit environment stabilizes either out-of-plane or in-plane magnetization.

The Curie temperatures (T_C) estimated from classical Monte Carlo simulations further reflect the composition-dependent magnetic strength. As summarized in Table 7.1, T_C increases with enhanced exchange interactions and reaches its highest value for $Pt_{0.5}CoTi_{0.5}Si$, consistent with its large J_1 and J_2 values. In contrast, compositions with weaker exchange interactions exhibit lower transition temperatures. These results confirm that Co substitution effectively strengthens ferromagnetic coupling and improves thermal stability, while Pt primarily modifies the SOC. Overall, the variation in T_C follows the trend of the dominant exchange parameters, demonstrating a clear correlation between chemical composition and magnetic robustness.

7.3.3 Orbital-Resolved Pathways of the DMI

Tight Binding Methodology

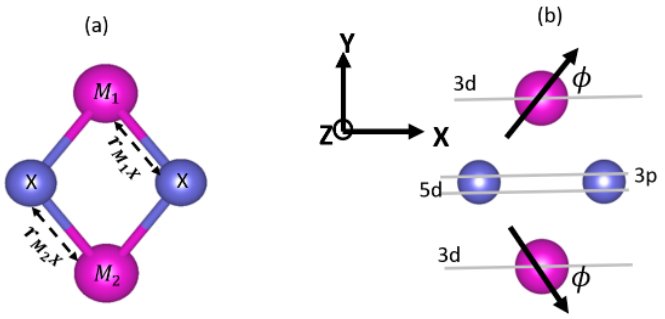

Figure 7.7: (a) Schematic representation of a TM silicide, where M_1 and M_2 are magnetic transition-metal sites and X is a nonmagnetic ligand. (b) The minimal trimer model consisting of two magnetic sites, M_1 and M_2, each hosting a d orbital, bridged by a nonmagnetic ligand X carrying either a p or d orbital. The magnetic moments on M_1 and M_2 are canted by an angle ϕ with respect to the x-axis.

The third term of the Hamiltonian in Eq. 7.2 corresponds to DMI, which arises from SOC in systems without inversion symmetry and plays a crucial role in stabilizing chiral magnetic textures such as skyrmions [226, 283]. In the doped Ti_2Si lattice considered here, the top and bottom Ti layers are separated by a nonmagnetic Si spacer, while Pt/Co substitution breaks the horizontal mirror plane of the pristine Ti_2Si structure. Consequently, the system is both intralayer and interlayer asymmetric [355]:

(1) Within each magnetic Ti (or Ti/Co) layer, local bond distortions generated by Pt/Co doping breaks inversion symmetry, giving rise to intralayer DMI; and

(2) The two magnetic layers become chemically and structurally inequivalent, allowing a distinct interlayer DMI across the Si layer.

To understand the microscopic origin of the resulting noncollinear exchange, we construct a minimal TB Hamiltonian based on MLWFs [342]. The model is built on a trimer M_1-X-M_2 cluster, where two magnetic sites M_1 and M_2 are bridged by a nonmagnetic ligand

X, mimicking the Ti-Si-Ti link in the monolayer geometry [Fig. 7.7]. The TB Hamiltonian takes the form

$$\hat{H} = \hat{H}_0 + \hat{H}_t + \hat{H}_{\text{SOC}}, \tag{7.14}$$

where $\hat{H}_0$ contains the on-site energies, $\hat{H}_t$ describes ligand-mediated hopping, and $\hat{H}_{\text{SOC}}$ introduces SOC. The interplay of SOC with the broken inversion symmetry in the asymmetric M_1-X-M_2 geometry generates the antisymmetric exchange responsible for the DMI.

The on-site term corresponds to:

$$\hat{H}_0 = \sum_{im,\sigma} \varepsilon_{d,m}\, d^\dagger_{im\sigma} d_{im\sigma} + \sum_{\alpha,\sigma} \varepsilon_{p,\alpha}\, p^\dagger_{\alpha\sigma} p_{\alpha\sigma} + \sum_{\alpha,\sigma} \varepsilon_{d,\alpha}\, d^\dagger_{\alpha\sigma} d_{\alpha\sigma} \tag{7.15}$$

where $\varepsilon_{d,m}$ and $\varepsilon_{p,\alpha}$ denote the on-site energies of the m-th M-d and α-th X-p (or or X-d) orbitals. The operators $d^\dagger_{m\sigma}$ ($d_{m\sigma}$) and $p^\dagger_{\alpha\sigma}$ ($p_{\alpha\sigma}$) create (annihilate) an electron with spin σ in the corresponding orbitals. The ligand-mediated hopping between the magnetic and nonmagnetic sites is given by

$$\hat{H}_t = \sum_{i,m,\alpha,\sigma} \left(H^{(iX)}_{m\alpha}\, d^\dagger_{im\sigma} p_{\alpha\sigma} + H^{(iX)}_{m\alpha}\, d^\dagger_{im\sigma} d_{\alpha\sigma} + \text{h.c.} \right), \tag{7.16}$$

while SOC contributes via

$$\hat{H}_{\text{SOC}} = \lambda_X \sum_{\alpha,\beta,\sigma,\sigma'} (p^\dagger_{\alpha\sigma} \langle p_\alpha | \mathbf{L} | p_\beta \rangle \cdot \langle \sigma | \mathbf{S} | \sigma' \rangle p_{\beta\sigma'} \tag{7.17}$$

$$+ d^\dagger_{\alpha\sigma} \langle d_\alpha | \mathbf{L} | d_\beta \rangle \cdot \langle \sigma | \mathbf{S} | \sigma' \rangle d_{\beta\sigma'}). \tag{7.18}$$

with analogous terms on the metal sites.

From the Wannier representation, we extract the orbital-resolved hopping matrix elements for both Si and Pt ligands:

$$\begin{aligned} t^{(M_1\text{Si})}_{m,\alpha} &= \langle d^{(M_1)}_m | \hat{H} | p^{(\text{Si})}_\alpha \rangle, \qquad t^{(M_2\text{Si})}_{n,\beta} = \langle d^{(M_2)}_n | \hat{H} | p^{(\text{Si})}_\beta \rangle, \\ t^{(M_1\text{Pt})}_{m,\alpha} &= \langle d^{(M_1)}_m | \hat{H} | d^{(\text{Pt})}_\alpha \rangle, \qquad t^{(M_2\text{Pt})}_{n,\beta} = \langle d^{(M_2)}_n | \hat{H} | d^{(\text{Pt})}_\beta \rangle, \end{aligned} \tag{7.19}$$

where $m, n, \alpha, \beta \in \{xy, yz, xz, x^2 - y^2, z^2\}$ for d-type orbitals, and $\alpha, \beta \in \{x, y, z\}$ for p-type orbitals.

From the Wannier-based TB Hamiltonian, we extract all orbital-resolved hopping amplitudes t_{ij} between orbitals i and j. For each hopping channel, the associated geometric direction is defined as

$$\vec{\mathbf{R}} = \mathbf{a}_{\text{lat}} + (\mathbf{r}_i - \mathbf{r}_j), \tag{7.20}$$

where $\mathbf{a}_{\text{lat}}$ connects the unit cells of the two orbitals, and $\mathbf{r}_i$, $\mathbf{r}_j$ denote their intracell coordinates. The corresponding hopping vector is then written as

$$\vec{\mathbf{R}}_{ij} = t_{ij}\,\vec{\mathbf{R}}, \tag{7.21}$$

which carries units of (eV · Å) and encodes both the magnitude and the spatial orientation of the orbital couplings along the M_1-X-M_2 superexchange pathway, the microscopic origin of DMI.

Following Blügel [356], the emergence of antisymmetric exchange is governed by the noncollinearity of such hopping channels. For the M_1-X-M_2 trimer, the site-dependent orbital moments $\vec{\theta}_i$ can be expressed as

$$\vec{\theta}_i = \theta_i(\cos\phi\,\hat{\mathbf{e}}_x \pm \sin\phi\,\hat{\mathbf{e}}_y),$$

where ϕ is the canting angle defined in Fig. 7.7(b). SOC and local inversion-symmetry breaking modify the orientation of the M_i-X hybrid orbitals, and the resulting hopping vectors may be represented as

$$\vec{\mathbf{R}}_{ij} = R^x_{ij}\hat{\mathbf{e}}_x \pm R^y_{ij}\hat{\mathbf{e}}_y,$$

with approximate magnitudes $|R^x_{ij}| \approx |\theta_i \cos\phi|$ and $|R^y_{ij}| \approx |\theta_i \sin\phi|$. Once all hopping vectors are expressed in a common global coordinate frame, the microscopic chirality of a given superexchange path is evaluated from the cross product of the hopping channels involving the ligand,

$$d^{\text{TB}}_{ij} \propto \mathbf{R}_{ik} \times \mathbf{R}_{kj}, \tag{7.22}$$

where $i \in M_1$, $j \in M_2$, and k labels the ligand orbital. This quantity has units of ($eV^2Å^2$) but is used only as a dimensionless chirality indicator: its sign and relative magnitude reveal whether a particular M-X-M pathway supports finite antisymmetric exchange. It is directly analogous to the DMI term in Eq. 7.2, although it is not a physical DMI coefficient. The TB model is constructed from Wannier90-derived hopping parameters [342],

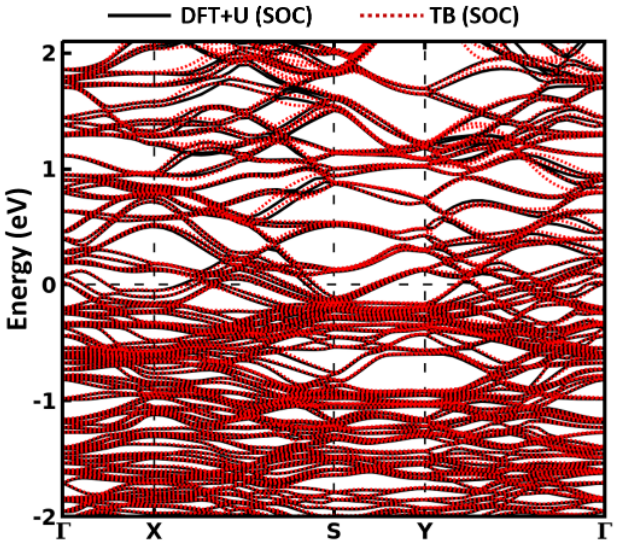

Figure 7.8: Fitted band structures of the $Pt_{0.5}Co_1Ti_0.5Si$ monolayer obtained from DFT+U and tight-binding calculations with SOC.

with SOC strengths. The TB eigenvalues and eigenfunctions are fitted to the DFT band structure, and excellent agreement is obtained for $Pt_{0.5}Co_1Ti_{0.5}Si$, as shown in Fig. 7.8. This Wannier-based TB analysis identifies two distinct antisymmetric exchange paths: a weak Si-mediated channel and a dominant Pt-mediated interlayer channel. Using Eq. 7.22, we compute the chirality indicators for the Co-Si-Co, Co-Pt-Co, Ti-Si-Ti, and Ti-Pt-Ti paths (in both intralayer and interlayer geometries) across all Pt/Co-substituted Ti_2Si compositions. The results in Table 7.2 show that nonzero entries identify symmetry allowed chiral pathways, whereas the Ti–Si–Ti channel vanishes for all compositions except $Pt_{0.5}Ti_{1.5}Si$. This composition behaves differently because, in the absence of Co, only the weaker Ti-mediated

Table 7.2: Tight-binding chirality indicators using Eq. 7.22 for the Co-Si-Co, Co-Pt-Co, Ti-Si-Ti, and Ti-Pt-Ti superexchange pathways in Pt/Co-substituted Ti_2Si. These quantities have units of ($eV^2Å^2$) but are reported in arbitrary units, since only their sign and relative magnitude determine whether a given M_1–X–M_2 pathway supports antisymmetric exchange.

Material	Co-Si-Co	Co-Pt-Co	Ti-Si-Ti	Ti-Pt-Ti
$Pt_{0.5}Ti_{1.5}Si$	0.00	0.00	-0.90	-2.08
$Pt_{0.5}Co_{0.5}Ti_1Si$	0.89	-2.96	-0.002	0.00
$Pt_{0.5}Co_1Ti_{0.5}Si$	4.38	-6.44	-0.00	0.00
CoTiSi	-1.68	0.00	0.00	0.00
PtTiSi	0.00	0.00	0.00	0.00

pathways are active, yielding smaller DMI signatures compared to the Co-containing systems. The sign of d_{ij}^{TB} follows the right-hand convention, with positive (negative) values indicating CCW (CW) rotation around the $+\hat{z}$ ($-\hat{z}$) direction.

Density functional results

The TB model provides the microscopic chirality signatures, while the actual DMI vectors are obtained from a symmetry analysis of the real-space atomic geometry. Following Moriya's symmetry rules [255, 256], the DMI interaction between two magnetic atoms M_1 and M_2 located at sites i and j arises through the M_1–X–M_2 superexchange pathways mediated by the nonmagnetic atom(s) X, as illustrated in Fig. 7.7. For each exchange path, the corresponding DMI vector takes the minimal symmetry-allowed form:

$$\vec{d}_{ij} = d_{ij}\,(\hat{r}_{iX} \times \hat{r}_{jX}), \tag{7.23}$$

where $\hat{r}_{iX}$ and $\hat{r}_{jX}$ are the unit vectors from the mediating atom X toward the magnetic sites i and j. As illustrated in Fig. 7.9 (a), the present geometry contains two symmetry related M_1–X–M_2 pathways, giving rise to two independent DMI vectors: $\vec{d}_1$, which originates predominantly from the Si-mediated intralayer and interlayer exchange, and $\vec{d}_2$, which is

dominated by the Pt-mediated interlayer interaction.

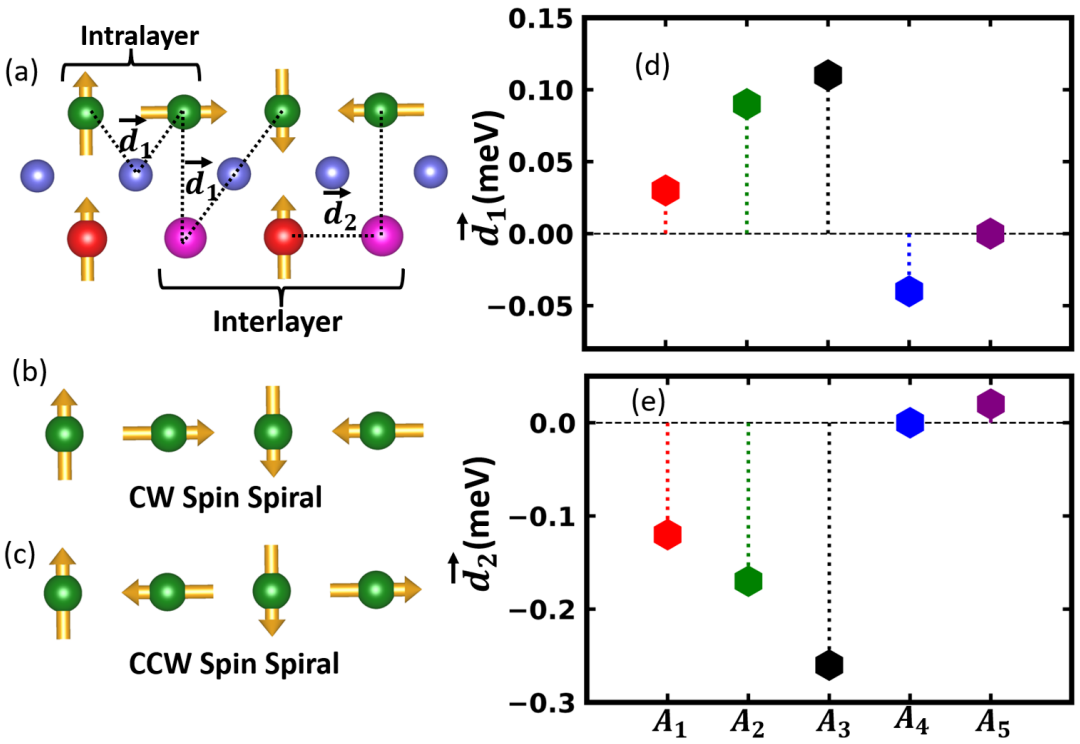

Figure 7.9: (a) Schematic illustration of the two symmetry-allowed DMI pathways in doped Ti_2Si. The first pathway, $\vec{d_1}$, contains both intralayer and weak interlayer contributions transmitted primarily through Si and Pt, whereas the second pathway, $\vec{d_2}$, is a predominantly interlayer DMI mediated by Pt. (b) - (c) show the clockwise (CW) and Counter-clockwise (CCW) spin spirals configurations. (d) and (e) Evolution of the calculated d_1 and d_2 values, respectively, for the configurations A_1 = $Pt_{0.5}Ti_{1.5}Si$, A_2 = $Pt_{0.5}Co_{0.5}Ti_1Si$, A_3 = $Pt_{0.5}Co_1Ti_{0.5}Si$, A_4 = CoTiSi, and A_5 = PtTiSi.

The layer-resolved DMI constants are extracted using the spin-spiral method, where each component ($\vec{d_1}$ or $\vec{d_2}$) is obtained from the energy difference between clockwise (CW) and counterclockwise (CCW) spirals,

$$d = \frac{E_{\mathrm{CW}} - E_{\mathrm{CCW}}}{m},$$

with m denoting the number of chiral magnetic bonds participating in the imposed spiral. The CW and CCW spin-spiral configurations used to extract the DMI constants are shown in

Fig. 7.9 (b) - (c). Since the structural models for the doped systems are already constructed using a 4×2 supercell, no additional supercell is required for the DMI calculations. Where $m = 16$ for the Si mediated DMI vector $\vec{d}_1$, and $m = 2\sqrt{2}$ for the Pt mediated interlayer DMI vector $\vec{d}_2$, as derived in Section B.1 of Appendix B.

The resulting DMI vectors $\vec{d}_1$ and $\vec{d}_2$ are illustrated in Fig. 7.9 (d) - (e), and their magnitudes are summarized in Table 7.1. A clear hierarchy emerges: $\vec{d}_2$ is consistently and substantially larger than $\vec{d}_1$, reflecting the much stronger SOC on Pt and the more efficient chiral exchange it mediates across the spacer. This trend is fully consistent with our TB analysis, which shows that the Co-Pt-Co exchange channel carries a much larger antisymmetric DMI exchange energy compared to the Ti-Si-Ti channel as shown in Table 7.2. For Pt containing compositions such as $Pt_{0.5}Ti_{1.5}Si$, $Pt_{0.5}Co_{0.5}Ti_1Si$, and $Pt_{0.5}Co_1Ti_{0.5}Si$, the Pt assisted interlayer DMI dominates the total chiral interaction, in agreement with the TB prediction that Co-Pt-Co couplings exhibit the strongest SOC-induced asymmetry. In contrast, Si-mediated DMI remains weak: in CoTiSi, the absence of Pt leads to a small $\vec{d}_1$ due to Co-Si-Co consistent with TB results as shown in Table 7.2 and vanishing $\vec{d}_2$. Even in PtTiSi (where Co is absent), the Pt-mediated long-range pathway produces a very small but finite DMI contribution, $d_2 = -0.02$, while the Si-mediated term d_1 essentially vanishes. The corresponding TB chirality indicators for this composition appear nearly zero, reflecting the fact that both channels are extremely weak and fall below the TB model's numerical resolution. Nevertheless, the sign of the finite DFT-derived d_2 remains consistent with the general TB trend that the Pt-mediated exchange is intrinsically stronger than the Si-mediated one. Taken together, these results demonstrate that Pt driven interlayer DMI is the primary source of chirality in doped Ti_2Si, while Si-mediated intralayer and interlayer contributions are intrinsically weak.

In the micromagnetic limit, the discrete lattice spins $\vec{S}_i$ are replaced by a continuous magnetization field $\vec{m}(\mathbf{r})$. Under this transformation, the DMI contribution arising from

the third term of the Hamiltonian in Eq. 7.2 can be expressed as

$$E_{\text{DMI}} = \int d\mathbf{r}\epsilon_{\text{DMI}} = \int d\mathbf{r} \sum_{\mu} D_{\mu}\big[\vec{m} \times \partial_{\mu}\vec{m}\big], \tag{7.24}$$

where $\epsilon_{\text{DMI}} = \sum_{\mu} D_{\mu}, (\vec{m} \times \partial_{\mu}\vec{m})$ is the micromagnetic DMI energy density, ∂_{μ} denotes the spatial derivative along direction μ, and D_{μ} is the corresponding micromagnetic DMI vector. For interfacial systems, this expression reduces to the widely used form [357, 259, 53, 358]

$$E_{\text{DMI}} = \int d\mathbf{r} D\left[\hat{\mathbf{m}} \cdot (\nabla \times \hat{\mathbf{m}}) - (\hat{\mathbf{m}} \cdot \nabla)\hat{\mathbf{m}}\right] \cdot \hat{\mathbf{z}}, \tag{7.25}$$

where D is the effective interfacial micromagnetic DMI constant. The micromagnetic coefficients D_1 and D_2 are connected to their corresponding atomistic DMI vectors $\vec{d_1}$ and $\vec{d_2}$ (derived in Section B.2 of Appendix B) through

$$D_1 = \frac{d_1 N}{at}, \tag{7.26}$$

$$D_2 = \frac{d_2 N}{at}, \tag{7.27}$$

where N is the number of magnetic atoms per unit cell, a is the in-plane lattice parameter, and t is the monolayer thickness. The extracted micromagnetic DMI values are listed in Table 7.1.

Among all compositions, $Pt_{0.5}Co_1Ti_{0.5}Si$ exhibits the strongest chiral interaction, with $D_1 = 0.21$ mJ/m^2 and $D_2 = -0.50$ mJ/m^2. The opposite signs of D_1 and D_2 reflect their distinct rotational preferences: D_1 favors a CCW spin spiral, whereas D_2 favors a CW spiral, consistent with the conventions used in Eqs. 7.26 and 7.27. $Pt_{0.5}Co_{0.5}Ti_1Si$ likewise displays finite chirality, with $D_1 = 0.17$ mJ/m^2 (CCW) and $D_2 = -0.33$ mJ/m^2 (CW). These results show that both intralayer (Si-mediated) and interlayer (Si- and Pt-mediated) exchange pathways contribute to the total DMI, with the Pt-assisted path dominant in magnitude. The rotation senses extracted from D_1 and D_2 are also fully consistent with the TB

chirality analysis as shown in Table 7.2. Overall, the atomistic and micromagnetic results demonstrate that Pt-driven interlayer DMI is the primary source of chiral exchange in doped Ti_2Si, whereas the Si-mediated intralayer contribution remains intrinsically weak. This establishes Ti_2Si monolayers with controlled Pt and Co substitution as a robust platform for engineering sizable and tunable DMI, enabling the stabilization of chiral spin textures in centrosymmetry broken 2D TMS.

7.4 Conclusion

In summary, we employed density-functional theory, micromagnetic analysis, and Wannier-based tight-binding modeling to investigate chiral magnetic interactions in monolayer Ti_2Si. The pristine material is identified as a ferromagnetic metal whose exchange interaction and magnetic anisotropy can be effectively tuned by an external electric field. However, due to its centrosymmetric structure, DMI is absent in the undoped system. By introducing controlled Pt and Co substitution at Ti sites, inversion symmetry is broken. At the same time, Co enhances magnetic exchange while Pt strengthens SOC. This combined effect generates a finite DMI, with the dominant contribution arising from Pt-mediated interlayer superexchange pathways. Among the investigated compositions, $Pt_{0.5}CoTi_{0.5}Si$ exhibits the largest DMI. This work provides a microscopic understanding of DMI engineering in Ti_2Si within the framework of density-functional theory and an effective Heisenberg model. The present analysis focuses on the intrinsic properties of free-standing monolayers, which serve as a reference for understanding symmetry-driven chiral interactions. While the DFT-based Heisenberg model captures the dominant exchange mechanisms, substrate effects and large-scale finite-temperature spin dynamics were not explicitly considered. These aspects offer natural directions for future research. Overall, our results provide theoretical guidance for the nanoscale design of two-dimensional silicides with tunable chiral magnetism. The

ability to control DMI through symmetry engineering and chemical substitution highlights the potential of doped Ti_2Si monolayers for compact, energy-efficient spintronic technologies, such as ultrathin chiral magnetic memory elements, racetrack-type logic architectures, and electrically programmable magnetic nanostructures. Their reduced dimensionality and interface sensitivity make them promising candidates for integration into next-generation nanoscale spintronic devices.

Chapter 8

Conclusion and Future Prospects

8.1 Summary and Conclusions

This thesis investigates the electronic structure, transport properties, and chiral magnetism in two complementary classes of quantum materials: bulk chalcopyrite semiconductors and 2D magnetic systems. A central outcome of this work is that emergent functionalities, including thermoelectric efficiency and topological spin textures, are fundamentally governed by the interplay of orbital hybridization, SOC, and symmetry. By combining advanced density functional theory with spin-Hamiltonian modeling, micromagnetic simulations, and Wannier-based analysis, this work establishes predictive links between electronic structure and macroscopic physical properties.

In bulk chalcopyrites, a systematic comparison of XC functionals reveals that accurate electronic structure depends critically on the treatment of d-state localization and p–d hybridization. The PBE functional significantly underestimates band gaps due to over-delocalization of d-electrons, while meta-GGA functionals reduce this error. Among these, rMGGAC yields band gaps in close agreement with experiment, comparable to HSE06, whereas r^{2}SCAN provides a reliable description of thermodynamic phase stability. Together, these functionals establish an efficient and accurate computational framework for chalcopyrite materials.

Building on this foundation, the thermoelectric properties of Ag-based chalcopyrites were analyzed using the DDH functional and Boltzmann transport theory. The results show that high thermoelectric performance arises from the combined effect of multi-band electronic structure near the valence band maximum and low lattice thermal conductivity.

In particular, the quaternary compound Ag_2ZnGeS_4 achieves a maximum $ZT = 2.57$ at 800 K, with related quaternary systems also exhibiting similarly high performance. These findings establish quaternary Ag-based chalcopyrites as promising candidates for high-temperature thermoelectric applications.

In 2D systems, reduced dimensionality and symmetry breaking give rise to chiral magnetic interactions. In the H-phase $FeTe_2$ monolayer, intrinsic inversion symmetry breaking leads to finite DMI, which can be continuously tuned by biaxial strain and electronic correlation. The MAE and DMI exhibit strong sensitivity to strain, with the micromagnetic DMI constant reaching 3.06 mJ/m^2. Atom-resolved analysis identifies Te atoms as the dominant contributors through their strong SOC.

For centrosymmetric systems, DMI can be induced through interfacial engineering. In T-$FeTe_2$/Pt heterostructures, inversion symmetry breaking at the interface and strong SOC from Pt generate a large DMI of up to 1.75 meV. The origin of this interaction is traced to hybridization between Fe, Te, and Pt orbitals, consistent with the Fert–Levy mechanism. Monte Carlo simulations confirm that these heterostructures support Néel-type skyrmions of radius 5.1 nm under an applied magnetic field of 60 mT, demonstrating a viable platform for skyrmion-based spintronic applications.

Chemical modification provides an additional route for engineering chiral magnetism. In the centrosymmetric Ti_2Si monolayer, Co and Pt co-doping simultaneously break inversion symmetry and enhance SOC, leading to finite DMI. Wannier-based analysis reveals that Pt-mediated superexchange pathways dominate the DMI, while Si-mediated contributions remain weak. The composition $Pt_{0.5}CoTi_{0.5}Si$ exhibits the largest DMI and supports chiral spin textures, establishing doped 2D silicides as tunable platforms for chiral magnetism.

Overall, this thesis demonstrates that electronic structure, particularly the interplay between orbital hybridization, SOC, and symmetry, provides a unifying and predictive framework for understanding and designing quantum materials. By linking microscopic interac-

tions to macroscopic properties across different dimensional regimes, this work contributes to the rational design of materials for thermoelectric and spintronic applications.

8.2 Future Outlook

The results of this thesis open several promising directions for future research across both bulk and low-dimensional quantum materials.

In bulk chalcopyrite semiconductors, further improvements in electronic structure accuracy can be achieved using many-body approaches such as the GW approximation, enabling reliable quasiparticle corrections and optical predictions. In addition, machine-learning-assisted exchange–correlation functionals offer a pathway for improved transferability and high-throughput materials discovery. For thermoelectric materials, extending the present study to low-dimensional systems, including two-dimensional and quasi-one-dimensional materials, is a promising direction. Reduced dimensionality and quantum confinement can enhance the Seebeck coefficient through modified electronic density of states, while interfaces and structural complexity can suppress lattice thermal conductivity. Exploring layered heterostructures and mixed-composition systems for band convergence, combined with controlled doping, may enable thermoelectric performance beyond bulk limits.

In two-dimensional systems, incorporating finite-temperature effects through Monte Carlo simulations will be essential for understanding magnetic ordering and the stability of chiral spin textures. Electric-field control of magnetic interactions provides an additional route for tuning exchange interactions, magnetic anisotropy, and DMI, enabling energy-efficient manipulation of spin textures. A natural extension of this work is the exploration of altermagnetism and topological transport phenomena in two-dimensional materials. In systems with broken symmetry and strong SOC, nontrivial Berry curvature can give rise to anomalous Hall conductivity and related responses. Investigating these effects

within the present framework will deepen the understanding of the connection between electronic structure, symmetry, and topological behavior. The stabilization of skyrmions in $FeTe_2$-based heterostructures motivates further exploration of moiré engineering, where twist-induced superlattices can modify electronic structure, enhance correlations, and tune magnetic interactions. Such systems may provide additional control over DMI, skyrmion size, and stability. A complementary direction is the development of Wannier-based tight-binding models to bridge first-principles calculations with large-scale simulations. These models enable efficient evaluation of Berry curvature, anomalous Hall conductivity, and magnetic interactions, while providing an orbital-resolved understanding of emergent phenomena across extended length scales.

Overall, the methodologies and design principles developed in this thesis provide a foundation for predictive materials design, enabling the discovery of quantum materials with tunable electronic, thermoelectric, and spintronic functionalities.

Appendix A

Exploring Skyrmion Stability in Centrosymmetric Monolayers

A.1 Exchange Stifness Constant (A)

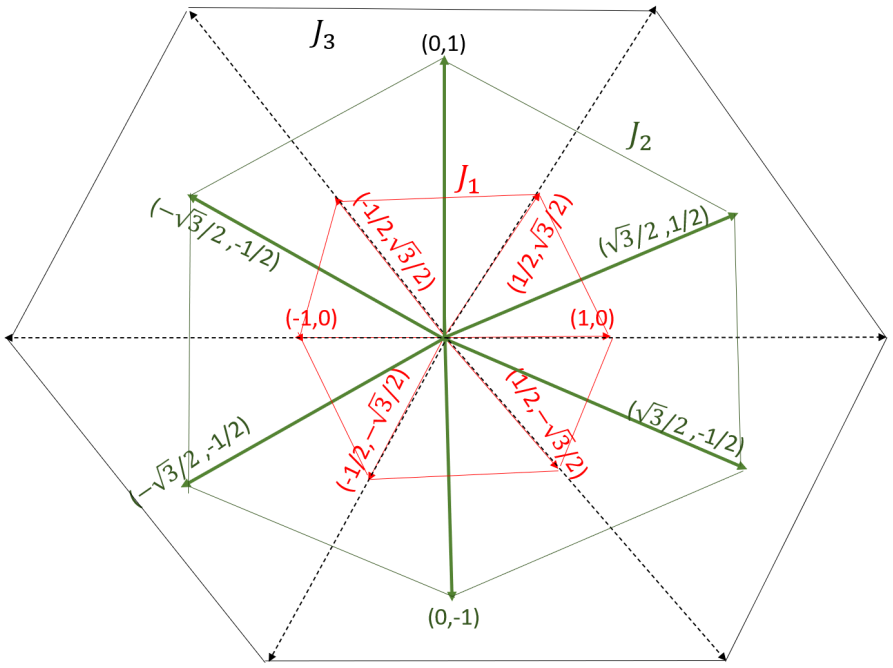

Figure A.1: Magnetic Continum for J_1, J_2 and J_3

For the Heisenberg exchange interaction, the exchange energy associated with atom i is given by

$$E_{\text{ex},i} = \frac{1}{2}\sum_{j=1}^{6} J\,\mathbf{S}_i \cdot \mathbf{S}_j, \tag{A.1}$$

where J represents the isotropic exchange interaction between neighboring spins. Expand-

ing the neighboring spins up to second order yields

$$\mathbf{S}_j = \mathbf{S}_i + re_{ij}^x \frac{\partial \mathbf{S}_i}{\partial x} + re_{ij}^y \frac{\partial \mathbf{S}_i}{\partial y} + \frac{r^2}{2}\left[(e_{ij}^x)^2 \frac{\partial^2 \mathbf{S}_i}{\partial x^2} + (e_{ij}^y)^2 \frac{\partial^2 \mathbf{S}_i}{\partial y^2}\right] + \cdots, \tag{A.2}$$

The first and second term is zero because magentic atoms are centrosymmetric, so we get:

$$E_{\text{ex},i} = \frac{1}{2} J \sum_{j=1}^{6} \mathbf{S}_i \cdot \left[\frac{1}{2}\left(re_{ij}^x\right)^2 \frac{\partial^2 \mathbf{S}_i}{\partial x^2} + \frac{1}{2}\left(re_{ij}^y\right)^2 \frac{\partial^2 \mathbf{S}_i}{\partial y^2}\right] \tag{A.3}$$

$$= \frac{1}{4} r^2 J \sum_{j=1}^{6} \mathbf{S}_i \cdot \left[\left(e_{ij}^x\right)^2 \frac{\partial^2 \mathbf{S}_i}{\partial x^2} + \left(e_{ij}^y\right)^2 \frac{\partial^2 \mathbf{S}_i}{\partial y^2}\right]. \tag{A.4}$$

Substituting these values from Fig. A.1, into the exchange Hamiltonian and retaining only the leading nonvanishing terms gives

$$\begin{aligned} E_{\text{ex},i} = {} & \frac{1}{4} r^2 J_1 \mathbf{S}_i \cdot \left[2\left(\frac{\partial^2 \mathbf{S}_i}{\partial x^2}\right) + 4\left(\frac{1}{4}\frac{\partial^2 \mathbf{S}_i}{\partial x^2}\right) + 4\left(\frac{3}{4}\frac{\partial^2 \mathbf{S}_i}{\partial y^2}\right)\right] \\ & + \frac{1}{4} r^2 J_2 \mathbf{S}_i \cdot \left[2\left(\frac{\partial^2 \mathbf{S}_i}{\partial y^2}\right) + 4\left(\frac{3}{4}\frac{\partial^2 \mathbf{S}_i}{\partial x^2}\right) + 4\left(\frac{1}{4}\frac{\partial^2 \mathbf{S}_i}{\partial y^2}\right)\right] \\ & + \frac{1}{4} r^2 J_3 \mathbf{S}_i \cdot \left[2\left(\frac{\partial^2 \mathbf{S}_i}{\partial x^2}\right) + 4\left(\frac{1}{4}\frac{\partial^2 \mathbf{S}_i}{\partial x^2}\right) + 4\left(\frac{3}{4}\frac{\partial^2 \mathbf{S}_i}{\partial y^2}\right)\right]. \end{aligned} \tag{A.5}$$

This leads to

$$E_{\text{ex},i} = \frac{3}{4} r^2 (J_1 + J_2 + J + 3)(\Delta S_i)^2 \tag{A.6}$$

where r= a and after divided this Equation with volume V, where V= $\frac{\sqrt{3}a^2 t}{2}$ the energy denisty becomes:

$$\epsilon_{\text{ex}} = \frac{\sqrt{3}}{2} r^2 (J_1 + J_2 + J + 3)(\Delta S_i)^2 \tag{A.7}$$

the energy density of exchange interaction is:

$$\epsilon_{\text{ex}}(\mathbf{r}) = A(\nabla \mathbf{M})^2, \tag{A.8}$$

Comapring Eqns. A.7 and A.8 with the exchange stiffness parameter

$$A = \frac{\sqrt{3}(J_1 + J_2 + J_3)}{2t}, \tag{A.9}$$

where J_1, J_2, and J_3 correspond to the exchange interactions up to third nearest neighbors.

For the magnetic anisotropy, the continuum anisotropy constant is related to the atomistic anisotropy energy through

$$K = \frac{2K_\mu}{\sqrt{3}a^2 t}, \tag{A.10}$$

where K_μ is the magnetic anisotropy energy per magnetic atom.

Similarly, the saturation magnetization is expressed as

$$M_s = \frac{2m}{\sqrt{3}a^2 t}, \tag{A.11}$$

where m denotes the magnetic moment per magnetic atom.

Using these relations, the atomistic magnetic interactions obtained from first-principles calculations are mapped onto the continuum micromagnetic model employed in the Mumax3 simulations.

Appendix B

Activating DMI in 2D Silicide Ti_2Si via Co and Pt Doping

B.1 Dzyloshinskii Moriya Interaction (Intralayer and Interlayer Contribution)

$$d^{tot} = \frac{E_{CW} - E_{CCW}}{m} \tag{B.1}$$

The constant m depends on the crystal structure and the wavelength of the magnetic spiral. The energies of the clockwise (CW) and counterclockwise (CCW) spin configurations, denoted as E_{CW} and E_{ACW} respectively, can be obtained using first-principles calculations [145]. The contribution of magnetic interactions can be evaluated by considering the intra-layer spin interaction energy. when there is DMI which is mediated through the Si atoms the DMI constant (d_1) can be calculated as follows:. For atom 2, as illustrated in Figure B.1, the spin-interaction energy can be written as:

$$E^{(2)} = \frac{1}{2}\Big[J\Big(S_2 \cdot S_3 + S_2 \cdot S_1 + S_2 \cdot S_6 + S_2 \cdot S_{2'}\Big] + A_\mu \left(S_1^z\right)^2 + \frac{1}{2}\Big[d_1 \cdot (S_2 \times S_3) + d_1 \cdot (S_2 \times S_1) + d_1 \cdot (S_2 \times S_6) + d_1 \cdot (S_2 \times S_{6'})\Big] + \mu\nu B S_1^z.$$

where Heisenberg exchange interaction and DMI energy sharing between the two sites of each bond so factor 1/2 is included.

According to Moriya's symmetry rules for DMI interactions [255], $\mathbf{d}_{ij}$ between two magnetic atoms i and j is restricted in direction based on the symmetry of the bond connecting them. Specifically, when there is no inversion symmetry at the midpoint between i

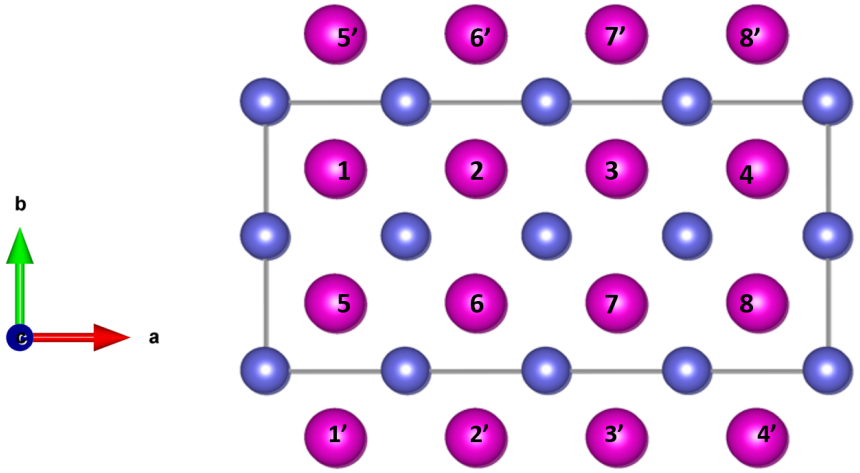

Figure B.1: Top view of the 4×1 Ti_2Si supercell showing the spin configuration used for the DMI calculations.

and j, Moriya's third rule states that $\mathbf{d}_{ij}$ must be oriented perpendicular to the bond direction $\hat{\mathbf{u}}_{ij}$, which is the unit vector connecting sites i and j. DMI vector $\mathbf{d}_{ij}$ takes the form $\hat{\mathbf{z}} \times \hat{\mathbf{u}}_{ij}$, where $\hat{\mathbf{z}}$ is the unit vector normal to the film, oriented from the adjacent nonmagnetic layer towards the magnetic film. As per figure B.1, the spin interaction energy for atom 2 can be written as:

$$E^{(2)} = \frac{1}{2}[J_] + A_\mu \left(S_1^z\right)^2 + \frac{1}{2} d_1 \left[\cos(0^\circ) - \cos(180^\circ) - \cos(270^\circ) + \cos(90^\circ)\right] + \mu\nu B S_1^z. \tag{B.2}$$

Based on this rule, the energy contributions for a selected atom 2 for both clockwise (E_{CW}) and counterclockwise (E_{CCW}) spin configurations is given by:

$$E_{CW}^2 = \frac{1}{2}[J] + A_\mu \left(S_1^z\right)^2 + \frac{1}{2}[2d_1] + \mu\nu B S_1^z. \tag{B.3}$$

$$E_{CCW}^1 = \frac{1}{2}[2J_1] + A_\mu \left(S_1^z\right)^2 + \frac{1}{2}[-2d_1] + \mu\nu B S_1^z. \tag{B.4}$$

Add Equations B.13 and B.4

$$d_1 = \frac{E_{CW}^1 - E_{CCW}^1}{2} \tag{B.5}$$

The total opposite chirality energy difference in the supercell using Eqns B.13 and B.4:

$$\Delta E_{DMI} = \frac{E_{CW} - E_{CCW}}{2} = 8d_1 \tag{B.6}$$

Total DMI strength $d_{\parallel}$ for n=8 can be expressed as:

$$d_1 = \frac{E_{CW} - E_{CCW}}{16} \tag{B.7}$$

Now when the DMI is mediated through Pt atoms, the DMI vector d_2 can be evaluated when atom 5 and 7 is replaced by Pt atoms then the atom 1 will interact with atom 6 through Pt atom (in place of atom 5)and the simillarly atom 3 will interact with atom 8 through Pt atom (in place of atom 7), then the DMI vector d_2 will be mediated through Pt can be evaluated as the sum of spin interaction energy of atom 6 ($E^{(6)}$) and atom 8($E^{(8)}$):

$$E^{(6)} + E^{(8)} = \tfrac{1}{2}\Big[\mathbf{d}_2\cdot(\mathbf{S}_1 \times \mathbf{S}_6) + \mathbf{d}_2\cdot(\mathbf{S}_1 \times \mathbf{S}_{6'}) + \mathbf{d}_2\cdot(\mathbf{S}_3 \times \mathbf{S}_8) + \mathbf{d}_2\cdot(\mathbf{S}_3 \times \mathbf{S}_{8'})\Big] \tag{B.8}$$

$$= \tfrac{1}{2}d_2\big[\cos(45^\circ) + \cos(135^\circ) + \cos(45^\circ) + \cos(135^\circ)\big] \tag{B.9}$$

$$= \tfrac{1}{2}d_2\big[\tfrac{1}{\sqrt{2}} + \tfrac{1}{\sqrt{2}} + \tfrac{1}{\sqrt{2}} + \tfrac{1}{\sqrt{2}}\big] \tag{B.10}$$

$$= \tfrac{1}{2}d_2\big[\tfrac{4}{\sqrt{2}}\big] = \frac{2}{\sqrt{2}}\,d_2 = \sqrt{2}\,d_2. \tag{B.11}$$

$$E_{CW}^{6+8} = \frac{1}{2}[2\sqrt{2}d_2] \tag{B.12}$$

$$E_{CCW}^{6+8} = -\frac{1}{2}[2\sqrt{2}d_2] \tag{B.13}$$

$$d_2 = \frac{E_{CW} - E_{CCW}}{2\sqrt{2}} \tag{B.14}$$

B.2 The Micromagnetic DMI D

In micromagnetics, we assume that the spins $\mathbf{S}_i$ change gradually across atomic distances. This allows us to approximate $\mathbf{S}_i$ by a smooth, continuous function $\mathbf{m}(\mathbf{r}_i)$, where $\mathbf{m}(\mathbf{r})$ describes the local magnetization. Since the variation is slow and we ignore any change

along the z direction, the spin at a neighbouring site $\mathbf{r}_j$ can be approximated using a first-order Taylor expansion:

$$\mathbf{m}(\mathbf{r}_j) \simeq \mathbf{m}(\mathbf{r}_i) + ru_{ij}^{x}\frac{\partial \mathbf{m}}{\partial x}(\mathbf{r}_i) + ru_{ij}^{y}\frac{\partial \mathbf{m}}{\partial y}(\mathbf{r}_i)$$

The DMI energy for atom i corresponds to all six nearest neighbouring Fe atoms is:

$$E_{i,\mathrm{DMI}} = \frac{1}{2}rd_{\mathrm{tot}}\sum_{n=1}^{4}(\vec{z}\times\vec{u}_n)\cdot\left[\vec{m}(\vec{r}_i)\times\left(u_n^{x}\frac{\partial\vec{m}}{\partial x}\bigg|_{\vec{r}_i} + u_n^{y}\frac{\partial\vec{m}}{\partial y}\bigg|_{\vec{r}_i}\right)\right]. \tag{B.15}$$

since the $d_{\parallel}$ is the dominant DMI component so, the micromagnetic DMI energy density, $\varepsilon_{\mathrm{DMI}}$, is generally determined by the crystallographic point-group symmetry.

$$E_{i,\mathrm{DMI}} = \frac{1}{2}rd_1\sum_{n=1}^{4}(\vec{z}\times\vec{u}_n)\cdot\left[\vec{m}(\vec{r}_i)\times\frac{\partial\vec{m}}{\partial u_n}\right] \tag{B.16}$$

Here the cross product $\vec{m}\times\vec{m} = 0$ and the cross product of $\vec{m}(\vec{r}_i)\times\frac{\partial\vec{m}}{\partial u}$ is given by:

$$\vec{m}(\vec{r}_i)\times\frac{\partial\vec{m}}{\partial u} = (L_{yz}^{(u)}, L_{zx}^{(u)}, L_{xy}^{(u)})$$

where Lifshitz invariants can be written as;

$$L_{pq}^{(u)} = \vec{m}_p\frac{\partial\vec{m}_q}{\partial u} - \vec{m}_q\frac{\partial\vec{m}_p}{\partial u},$$

where p, q represent arbitrary Cartesian coordinates, such as x and y. As per figure B.1, the energy value for 4 nearest neigbouring astoms can be calculating by subsitituing u into

equation B.16 where

$$E_{i,DMI} = \epsilon_3 + \epsilon_1 + \epsilon_6 + \epsilon_{2'} \tag{B.17}$$
$$= \frac{1}{2} r d_1 \left[L_{zx}^{(x)} + L_{zx}^{(x)} + L_{zy}^{(y)} + L_{zy}^{(y)} \right] \tag{B.18}$$
$$= \frac{1}{2} r d_1 \left[2L_{zx}^{(x)} + 2L_{zy}^{(y)} \right] \tag{B.19}$$
$$= r d_1 \left[L_{zx}^{(x)} + L_{zy}^{(y)} \right] \tag{B.20}$$
$$\tag{B.21}$$

Comparing Eqs. B.21 and Eq.7.25 of chapter7, we can evaluate dmi strength D_1 normalized by number of magnetic atoms N and volume corresponding to a Ti atom in the magnetic film, where V = $a^2 \cdot$ t for tetragonal structure, where a^2 is the atomic surface area for a tetragonal lattice and t is the thickness of the magnetic layer :

$$D_1 = \frac{r d_1 N}{V} = \frac{r d_1 N}{a^2 \cdot t} \tag{B.22}$$

where r = a is the in plane atomic distance for tetragonal Ti_2Si magnetic film following that the DMI strength for Ti_2Si monolayer can be written as:

$$D_1 = \frac{d_1 N}{a \cdot t}. \tag{B.23}$$

The Micromagnetic DMI strength D_2 where the DMI strength is governed by Pt.

$$E_{i,DMI} = \epsilon_1 + \epsilon_{1'} + \epsilon_3 + \epsilon_{3'} \tag{B.24}$$
$$= \frac{1}{2} r d_2 \left[4(\frac{1}{2} L_{zx}^{(x)} + \frac{1}{2} L_{zy}^{(y)}) \right] \tag{B.25}$$
$$= r d_2 \left[L_{zx}^{(x)} + L_{zy}^{(y)} \right] \tag{B.26}$$

simillarly we get D_2

$$D_2 = \frac{r d_2 N}{V} = \frac{d_2 N}{a \cdot t} \tag{B.27}$$

References

[1] Namhoon Kim, Pamela Pena Martin, Angus A Rockett, and Elif Ertekin. Screened-exchange density functional theory description of the electronic structure and phase stability of the chalcopyrite materials aginse 2 and auinse 2. *Physical Review B*, 93(16):165202, 2016.

[2] TJ Anderson, OD Crisalle, SS Li, and PH Holloway. Future cis manufacturing technology development: Final report, 8 july 1998–17 october 2001. Technical report, National Renewable Energy Lab.(NREL), Golden, CO (United States), 2003.

[3] Donald D Wagman, William H Evans, Vivian B Parker, Richard H Schumm, Iva Halow, Sylvia M Bailey, Kenneth L Churney, and Ralph L Nuttall. Erratum: The nbs tables of chemical thermodynamic properties. selected values for inorganic and c1 and c2 organic substances in si units [j. phys. chem. ref. data 11, suppl. 2 (1982)]. *Journal of physical and chemical reference data*, 18(4):1807–1812, 1989.

[4] Neil W. Ashcroft and N. David Mermin. *Solid State Physics*. Harcourt College Publishers, 1976.

[5] Charles Kittel. *Introduction to Solid State Physics*. Wiley, 8 edition, 2005.

[6] Bernhard Keimer and Joel E. Moore. The physics of quantum materials. *Nature Physics*, 13:1045–1055, 2017.

[7] Yoshinori Tokura, Kensuke Yasuda, and Atsushi Tsukazaki. Magnetic topological insulators. *Nature Reviews Physics*, 1:126–143, 2019.

[8] Masatoshi Imada, Atsushi Fujimori, and Yoshinori Tokura. Metal-insulator transitions. *Reviews of Modern Physics*, 70:1039–1263, 1998.

[9] Elbio Dagotto. Complexity in strongly correlated electronic systems. *Science*, 309:257–262, 2005.

[10] M. Zahid Hasan and Charles L. Kane. Colloquium: Topological insulators. *Reviews of Modern Physics*, 82:3045–3067, 2010.

[11] Xiao-Liang Qi and Shou-Cheng Zhang. Topological insulators and superconductors. *Reviews of Modern Physics*, 83:1057–1110, 2011.

[12] K. S. Novoselov, A. Mishchenko, A. Carvalho, and A. H. Castro Neto. 2d materials and van der waals heterostructures. *Science*, 353:aac9439, 2016.

[13] A. K. Geim and I. V. Grigorieva. Van der waals heterostructures. *Nature*, 499:419–425, 2013.

[14] Libor Šmejkal, Yuriy Mokrousov, Binghai Yan, and Allan H. MacDonald. Emerging research landscape of altermagnetism. *Nature Physics*, 18:1090–1098, 2022.

[15] S. M. Sze and Kwok K. Ng. *Physics of Semiconductor Devices*. Wiley, 2006.

[16] K. S. et al. Novoselov. Two-dimensional gas of massless dirac fermions in graphene. *Nature*, 438:197–200, 2005.

[17] A. et al. Splendiani. Emerging photoluminescence in monolayer mos_2. *Nano Letters*, 10:1271–1275, 2010.

[18] Xiaodong Xu, Wang Yao, Di Xiao, and Tony F. Heinz. Spin and pseudospins in layered transition metal dichalcogenides. *Nature Physics*, 10:343–350, 2014.

[19] H. Morkoc, S. Strite, G. B. Gao, M. E. Lin, B. Sverdlov, and M. Burns. Large-band-gap sic, iii-v nitride, and ii-vi znse-based semiconductor device technologies. *Journal of Applied Physics*, 76:1363–1398, 1994.

[20] J. B. Casady and R. W. Johnson. Status of silicon carbide (sic) as a wide-bandgap semiconductor for high-temperature applications. *Solid-State Electronics*, 39:1409–1422, 1996.

[21] P. Y. Yu and M. Cardona. *Fundamentals of Semiconductors*. Springer, 2010.

[22] M. Lundstrom. *Fundamentals of Carrier Transport*. Cambridge University Press, 2000.

[23] A. Damascelli, Z. Hussain, and Z.-X. Shen. Angle-resolved photoemission studies of the cuprate superconductors. *Reviews of Modern Physics*, 75:473, 2003.

[24] F. J. Himpsel. Angle-resolved measurements of the photoemission of electrons in the study of solids. *Advances in Physics*, 32:1–51, 1983.

[25] P. Hohenberg and W. Kohn. Inhomogeneous electron gas. *Physical Review*, 136:B864, 1964.

[26] W. Kohn and L. J. Sham. Self-consistent equations including exchange and correlation effects. *Physical Review*, 140:A1133, 1965.

[27] L. Hedin. New method for calculating the one-particle green's function with application to the electron-gas problem. *Physical Review*, 139:A796, 1965.

[28] M. S. Hybertsen and S. G. Louie. Electron correlation in semiconductors and insulators: Band gaps and quasiparticle energies. *Physical Review B*, 34:5390, 1986.

[29] M. A. Green, A. Ho-Baillie, and H. J. Snaith. The emergence of perovskite solar cells. *Nature Photonics*, 8:506–514, 2014.

[30] H. J. Snaith. Perovskites: The emergence of a new era for low-cost, high-efficiency solar cells. *Journal of Physical Chemistry Letters*, 4:3623–3630, 2013.

[31] H. Julian Goldsmid. *Introduction to Thermoelectricity*. Springer, 2010.

[32] Mildred S. et al. Dresselhaus. New directions for low-dimensional thermoelectric materials. *Advanced Materials*, 19:1043–1053, 2007.

[33] K. Biswas et al. High-performance bulk thermoelectrics with all-scale hierarchical architectures. *Nature*, 489:414–418, 2012.

[34] Li-Dong et al. Zhao. Ultralow thermal conductivity and high thermoelectric figure of merit in snse crystals. *Nature*, 508:373–377, 2014.

[35] G. J. Snyder and E. S. Toberer. Complex thermoelectric materials. *Nature Materials*, 7:105–114, 2008.

[36] A. Fujishima and K. Honda. Electrochemical photolysis of water at a semiconductor electrode. *Nature*, 238:37–38, 1972.

[37] A. Kudo and Y. Miseki. Heterogeneous photocatalyst materials for water splitting. *Chemical Society Reviews*, 38:253–278, 2009.

[38] A. et al. Manchon. New perspectives for rashba spin–orbit coupling. *Nature Materials*, 14:871–882, 2015.

[39] Y. et al. Cao. Unconventional superconductivity in magic-angle graphene superlattices. *Nature*, 556:43–50, 2018.

[40] C. Huang et al. Lateral heterojunctions within monolayer $mose_2$–wse_2 semiconductors. *Nature Materials*, 13:1096–1101, 2014.

[41] S. Manzeli, D. Ovchinnikov, D. Pasquier, O. V. Yazyev, and A. Kis. 2d transition metal dichalcogenides. *Nature Reviews Materials*, 2:17033, 2017.

[42] C. Ataca, H. Şahin, and S. Ciraci. Stable, single-layer mx2 transition-metal oxides and dichalcogenides in a honeycomb-like structure. *The Journal of Physical Chemistry C*, 116(16):8983–8999, 2012.

[43] Roland Winkler. *Spin-Orbit Coupling Effects in Two-Dimensional Electron and Hole Systems*. Springer, 2003.

[44] N. D. Mermin and H. Wagner. Absence of ferromagnetism or antiferromagnetism in one- or two-dimensional isotropic heisenberg models. *Physical Review Letters*, 17:1133–1136, 1966.

[45] C. et al. Gong. Discovery of intrinsic ferromagnetism in two-dimensional van der waals crystals. *Nature*, 546:265–269, 2017.

[46] B. et al. Huang. Layer-dependent ferromagnetism in a van der waals crystal down to the monolayer limit. *Nature*, 546:270–273, 2017.

[47] Y. et al. Deng. Gate-tunable room-temperature ferromagnetism in two-dimensional fe_3gete_2. *Nature*, 563:94–99, 2018.

[48] S. Heinze et al. Spontaneous atomic-scale magnetic skyrmion lattice in two dimensions. *Nature Physics*, 7:713–718, 2011.

[49] Albert Fert, Nicolas Reyren, and Vincent Cros. Magnetic skyrmions: advances in physics and potential applications. *Nature Reviews Materials*, 2:17031, 2017.

[50] I. Dzyaloshinskii. A thermodynamic theory of weak ferromagnetism of antiferromagnetics. *Journal of Physics and Chemistry of Solids*, 4:241–255, 1958.

[51] T. Moriya. Anisotropic superexchange interaction and weak ferromagnetism. *Physical Review*, 120:91, 1960.

[52] S. et al. Mühlbauer. Skyrmion lattice in a chiral magnet. *Science*, 323:915–919, 2009.

[53] A. Fert, V. Cros, and J. Sampaio. Skyrmions on the track. *Nature Nanotechnology*, 8:152–156, 2013.

[54] A. N. Bogdanov and U. K. Rößler. Chiral symmetry breaking in magnetic thin films and multilayers. *Physical Review Letters*, 87:037203, 2001.

[55] N. Nagaosa and Y. Tokura. Topological properties and dynamics of magnetic skyrmions. *Nature Nanotechnology*, 8:899–911, 2013.

[56] A. K. Nayak et al. Discovery of magnetic antiskyrmions beyond room temperature in tetragonal heusler magnets. *Nature*, 548:561–566, 2017.

[57] Paul Drude. Zur elektronentheorie der metalle. *Annalen der Physik*, 306(3):566–613, 1900.

[58] Hendrik A. Lorentz. The theory of electrons and its applications to the phenomena of light and radiant heat. *Teubner, Leipzig*, 1909.

[59] Neil W. Ashcroft and N. David Mermin. *Solid State Physics*. Holt, Rinehart and Winston, 1976.

[60] Charles Kittel. *Introduction to Solid State Physics*. Wiley, 2005.

[61] Attila Szabo and Neil S. Ostlund. *Modern Quantum Chemistry*. Dover, 1996.

[62] Trygve Helgaker, Poul Jørgensen, and Jeppe Olsen. *Molecular Electronic-Structure Theory*. Wiley, 2000.

[63] Isaiah Shavitt and Rodney J. Bartlett. *Many-Body Methods in Chemistry and Physics*. Cambridge University Press, 2009.

[64] P. Hohenberg and W. Kohn. Inhomogeneous electron gas. *Physical Review*, 136:B864–B871, 1964.

[65] W. Kohn and L. J. Sham. Self-consistent equations including exchange and correlation effects. *Physical Review*, 140:A1133–A1138, 1965.

[66] Robert G. Parr and Weitao Yang. *Density-Functional Theory of Atoms and Molecules*. Oxford University Press, 1989.

[67] R. O. Jones and O. Gunnarsson. The density functional formalism, its applications and prospects. *Reviews of Modern Physics*, 61:689–746, 1989.

[68] Richard M. Martin. *Electronic Structure: Basic Theory and Practical Methods*. Cambridge University Press, 2004.

[69] Erwin Schrödinger. An undulatory theory of the mechanics of atoms and molecules. *Phys. Rev.*, 28(6):1049–1070, 1926.

[70] David J. Griffiths. *Introduction to Quantum Mechanics*. Pearson, 2018.

[71] Max Born and Robert Oppenheimer. Zur quantentheorie der molekeln. *Annalen der Physik*, 389(20):457–484, 1927.

[72] D. R. Hartree. The wave mechanics of an atom with a non-coulomb central field. *Mathematical Proceedings of the Cambridge Philosophical Society*, 24:89–110, 1928.

[73] V. Fock. Näherungsmethode zur lösung des quantenmechanischen mehrkörperproblems. *Zeitschrift für Physik*, 61:126–148, 1930.

[74] P. Hohenberg and W. Kohn. Inhomogeneous electron gas. *Phys. Rev.*, 136:B864, 1964.

[75] W. Kohn and L. J. Sham. Self-consistent equations including exchange and correlation effects. *Phys. Rev.*, 140:A1133, 1965.

[76] Robert G. Parr and Weitao Yang. *Density-Functional Theory of Atoms and Molecules*. Oxford University Press, 1989.

[77] P. A. M. Dirac. Note on exchange phenomena in the thomas atom. *Math. Proc. Cambridge Phil. Soc.*, 26:376, 1930.

[78] D. M. Ceperley and B. J. Alder. Ground state of the electron gas by a stochastic method. *Phys. Rev. Lett.*, 45:566, 1980.

[79] J. P. Perdew and A. Zunger. Self-interaction correction to density-functional approximations. *Phys. Rev. B*, 23:5048, 1981.

[80] J. P. Perdew. Electronic structure of solids '91. *Akademie Verlag*, 1992.

[81] C. Fiolhais, F. Nogueira, and M. A. L. Marques. A primer in density functional theory. *Springer*, 2003.

[82] J. P. Perdew, K. Burke, and M. Ernzerhof. Generalized gradient approximation made simple. *Phys. Rev. Lett.*, 77:3865–3868, 1996.

[83] J. P. Perdew and Y. Wang. Accurate and simple analytic representation of the electron-gas correlation energy. *Phys. Rev. B*, 45:13244, 1992.

[84] J. P. Perdew and K. Schmidt. Jacob's ladder of density functional approximations for the exchange-correlation energy. *AIP Conference Proceedings*, 577:1, 2001.

[85] Jianwei Sun, Adrienn Ruzsinszky, and John P. Perdew. Strongly constrained and appropriately normed semilocal density functional. *Phys. Rev. Lett.*, 115:036402, 2015.

[86] C. F. von Weizsäcker. Zur theorie der kernmassen. *Zeitschrift für Physik*, 96:431, 1935.

[87] Jianwei Sun, Adrienn Ruzsinszky, and John P Perdew. Strongly constrained and appropriately normed semilocal density functional. *Physical review letters*, 115(3):036402, 2015.

[88] James W Furness, Aaron D Kaplan, Jinliang Ning, John P Perdew, and Jianwei Sun. Accurate and numerically efficient r2scan meta-generalized gradient approximation. *The journal of physical chemistry letters*, 11(19):8208–8215, 2020.

[89] Bikash Patra, Subrata Jana, Lucian A. Constantin, and Prasanjit Samal. Relevance of the pauli kinetic energy density for semilocal functionals. *Phys. Rev. B*, 100:155140, Oct 2019.

[90] Subrata Jana, Sushant Kumar Behera, Szymon Śmiga, Lucian A. Constantin, and Prasanjit Samal. Accurate density functional made more versatile. *The Journal of Chemical Physics*, 155(2), 07 2021. 024103.

[91] Aaron D Kaplan and John P Perdew. Laplacian-level meta-generalized gradient approximation for solid and liquid metals. *Physical Review Materials*, 6(8):083803, 2022.

[92] Daniel Mejía-Rodríguez and SB Trickey. Meta-gga performance in solids at almost gga cost. *Physical Review B*, 102(12):121109, 2020.

[93] Jochen Heyd, Gustavo E. Scuseria, and Matthias Ernzerhof. Hybrid functionals based on a screened coulomb potential. *The Journal of Chemical Physics*, 118(18):8207–8215, 2003.

[94] Jochen Heyd, Gustavo E. Scuseria, and Matthias Ernzerhof. Erratum: Hybrid functionals based on a screened coulomb potential. *The Journal of Chemical Physics*, 124(21):219906, 2006.

[95] S. Refaely-Abramson, S. Sharifzadeh, M. Jain, R. Baer, L. Kronik, and J. B. Neaton. Gap renormalization of molecular crystals from density-functional theory. *Physical Review B*, 88:081204, 2012.

[96] Subrata Jana, Arghya Ghosh, Lucian A. Constantin, and Prasanjit Samal. Simple and effective screening parameter for range-separated dielectric-dependent hybrids. *Physical Review B*, 108:045101, 2023.

[97] V. I. Anisimov, J. Zaanen, and O. K. Andersen. Band theory and mott insulators: Hubbard u instead of stoner i. *Physical Review B*, 44:943–954, 1991.

[98] V. I. Anisimov, F. Aryasetiawan, and A. I. Lichtenstein. First-principles calculations of the electronic structure and spectra of strongly correlated systems: The lda+u method. *Journal of Physics: Condensed Matter*, 9:767–808, 1997.

[99] S. L. Dudarev, G. A. Botton, S. Y. Savrasov, C. J. Humphreys, and A. P. Sutton. Electron-energy-loss spectra and the structural stability of nickel oxide: An lsda+u study. *Physical Review B*, 57:1505–1509, 1998.

[100] Richard M. Martin. *Electronic Structure: Basic Theory and Practical Methods*. Cambridge University Press, 2004.

[101] P. E. Blöchl. Projector augmented-wave method. *Physical Review B*, 50:17953, 1994.

[102] M. C. Payne, M. P. Teter, D. C. Allan, T. A. Arias, and J. D. Joannopoulos. *Iterative minimization techniques for ab initio total-energy calculations*, volume 64. 1992.

[103] Stefan Grimme. Density functional theory with london dispersion corrections. *Wiley Interdisciplinary Reviews: Computational Molecular Science*, 1:211–228, 2016.

[104] Jiří Klimeš and Angelos Michaelides. Perspective: Advances and challenges in treating van der waals dispersion forces in density functional theory. *Journal of Chemical Physics*, 137:120901, 2012.

[105] Stefan Grimme, Jens Antony, Stephan Ehrlich, and Helge Krieg. A consistent and accurate ab initio parametrization of density functional dispersion correction (dft-d). *Journal of Chemical Physics*, 132:154104, 2010.

[106] Nicola Marzari and David Vanderbilt. Maximally localized generalized wannier functions for composite energy bands. *Physical Review B*, 56:12847–12865, 1997.

[107] Ivo Souza, Nicola Marzari, and David Vanderbilt. Maximally localized wannier functions for entangled energy bands. *Physical Review B*, 65:035109, 2001.

[108] Georg Kresse and Jürgen Furthmüller. Efficient iterative schemes for ab initio total-energy calculations using a plane-wave basis set. *Physical review B*, 54(16):11169, 1996.

[109] Georg Kresse and Daniel Joubert. From ultrasoft pseudopotentials to the projector augmented-wave method. *Physical review b*, 59(3):1758, 1999.

[110] Sergey N Rashkeev and Walter RL Lambrecht. Second-harmonic generation of i-iii-vi 2 chalcopyrite semiconductors: Effects of chemical substitutions. *Physical Review B*, 63(16):165212, 2001.

[111] Martin Green, Ewan Dunlop, Jochen Hohl-Ebinger, Masahiro Yoshita, Nikos Kopidakis, and Xiaojing Hao. Solar cell efficiency tables (version 57). *Progress in photovoltaics: research and applications*, 29(1):3–15, 2021.

[112] Aron Walsh, Shiyou Chen, Su-Huai Wei, and Xin-Gao Gong. Kesterite thin-film solar cells: Advances in materials modelling of cu2znsns4. *Advanced Energy Materials*, 2(4):400–409, 2012.

[113] Wanxiang Feng, Di Xiao, Jun Ding, and Yugui Yao. Three-dimensional topological insulators in i- iii- vi 2 and ii- iv- v 2 chalcopyrite semiconductors. *Physical review letters*, 106(1):016402, 2011.

[114] JC Rife, RN Dexter, PM Bridenbaugh, and BW Veal. Optical properties of the chalcopyrite semiconductors znge p 2, znge as 2, cuga s 2, cual s 2, cuin se 2, and agin se 2. *Physical Review B*, 16(10):4491, 1977.

[115] Philip Jackson, Dimitrios Hariskos, Erwin Lotter, Stefan Paetel, Roland Wuerz, Richard Menner, Wiltraud Wischmann, and Michael Powalla. New world record efficiency for cu (in, ga) se2 thin-film solar cells beyond 20%. *Progress in photovoltaics: research and applications*, 19(7):894–897, 2011.

[116] MI Alonso, K Wakita, J Pascual, M Garriga, and N Yamamoto. Optical functions and electronic structure of cuinse 2, cugase 2, cuins 2, and cugas 2. *Physical Review B*, 63(7):075203, 2001.

[117] Ingrid Repins, Miguel A Contreras, Brian Egaas, Clay DeHart, John Scharf, Craig L Perkins, Bobby To, and Rommel Noufi. 19· 9%-efficient zno/cds/cuingase2 solar cell with 81· 2% fill factor. *Progress in Photovoltaics: Research and applications*, 16(3):235–239, 2008.

[118] Hans W Spiess, Ulrich Haeberlen, G Brandt, A Räuber, and J Schneider. Nuclear magnetic resonance in ib–iii–vi2 semiconductors. *Physica Status Solidi B*, 62(1):183–192, 1974.

[119] KL Chopra, PD Paulson, and V Dutta. Thin-film solar cells: an overview. *Progress in Photovoltaics: Research and applications*, 12(2-3):69–92, 2004.

[120] Frank Hergert, Stefan Jost, Rainer Hock, and Michael Purwins. Prediction of solid-state reactions for the formation of the chalcopyrites cuins2, cugas2, cuals2 and cualse2 starting from binary compounds. *physica status solidi (a)*, 203(11):2598–2602, 2006.

[121] Robert W Birkmire and Erten Eser. Polycrystalline thin film solar cells: present status and future potential. *Annual Review of Materials Science*, 27(1):625–653, 1997.

[122] Weiru Chen, Wei Cao, Talaat A Hameed, Sylvain Marsillac, and Hani E Elsayed-Ali. Properties of cu (in, ga, al) se 2 thin films fabricated by pulsed laser deposition. *Journal of Materials Science: Materials in Electronics*, 26:1743–1747, 2015.

[123] ShigeFusa Chichibu, Yoshiyuki Harada, Mutsumi Sugiyama, and Hisayuki Nakanishi. Metalorganic vapor phase epitaxy of cu (alxga1- x)(syse1- y) 2 chalcopyrite semiconductors and their band offsets. *Journal of Physics and Chemistry of Solids*, 64(9-10):1481–1489, 2003.

[124] Kannan Ramanathan, Miguel A Contreras, Craig L Perkins, Sally Asher, Falah S Hasoon, James Keane, David Young, Manuel Romero, Wyatt Metzger, Rommel Noufi, et al. Properties of 19.2% efficiency zno/cds/cuingase2 thin-film solar cells. *Progress in Photovoltaics: research and applications*, 11(4):225–230, 2003.

[125] R Brini, G Schmerber, M Kanzari, J Werckmann, and B Rezig. Study of the growth of cuals2 thin films on oriented silicon (111). *Thin Solid Films*, 517(7):2191–2194, 2009.

[126] KS Knight. The crystal structures of cuinse2 and cuinte2. *Materials Research Bulletin*, 27(2):161–167, 1992.

[127] SC Abrahams and JL Bernstein. Piezoelectric nonlinear optic cugas2 and cuins2 crystal structure: Sublattice distortion in aib iii c 2 vi and a ii b iv c 2 v type chalcopyrites. *The Journal of Chemical Physics*, 59(10):5415–5422, 1973.

[128] WN Honeyman. Preparation and properties of single crystal cuals2 and cualse2. *Journal of Physics and Chemistry of Solids*, 30(8):1935–1940, 1969.

[129] T Maeda, T Takeichi, and T Wada. Systematic studies on electronic structures of cuinse2 and the other chalcopyrite related compounds by first principles calculations. *physica status solidi (a)*, 203(11):2634–2638, 2006.

[130] Pamela Peña Martin, Angus A Rockett, and Joseph Lyding. Growth mechanism and surface atomic structure of aginse2. *Journal of Vacuum Science & Technology A*, 30(4), 2012.

[131] P Benoit, P Charpin, R Lesueur, and C Djega-Mariadassou. Crystal structure of chalcopyrite aginse2. *Japanese Journal of Applied Physics*, 19(S3):85, 1980.

[132] Peter T Erslev, JinWoo Lee, Gregory M Hanket, William N Shafarman, and J David Cohen. The electronic structure of cu (in1- xgax) se2 alloyed with silver. *Thin Solid Films*, 519(21):7296–7299, 2011.

[133] JG Albornoz, JM Merino, M León, et al. Structural, thermal and electrical properties of the semiconductor system ag (1- x) cuxinse2. *Journal of Physics and Chemistry of Solids*, 75(1):1–7, 2014.

[134] Saeed Ullah, Haleem Ud Din, G Murtaza, T Ouahrani, R Khenata, S Bin Omran, et al. Structural, electronic and optical properties of agxy2 (x= al, ga, in and y= s, se, te). *Journal of alloys and compounds*, 617:575–583, 2014.

[135] Iman H Khudayer and Bushra H Hussien. Study of some structural and optical properties of agalse2 thin films. *Ibn AL-Haitham Journal For Pure and Applied Science*, 29(2):41–51, 2017.

[136] H Karaagac, Murat Kaleli, and Mehmet Parlak. Characterization of agga0. 5in0. 5se2 thin films deposited by electron-beam technique. *Journal of Physics D: Applied Physics*, 42(16):165413, 2009.

[137] C Merschjann, M Mews, T Mete, A Karkatzinou, M Rusu, BV Korzun, S Schorr, P Schubert-Bischoff, S Seeger, Th Schedel-Niedrig, et al. Aggase2 thin films grown by chemical close-spaced vapor transport for photovoltaic applications: structural, compositional and optical properties. *Journal of Physics: Condensed Matter*, 24(17):175801, 2012.

[138] Baodong Mao, Chi-Hung Chuang, Junwei Wang, and Clemens Burda. Synthesis and photophysical properties of ternary i–iii–vi agins2 nanocrystals: intrinsic versus surface states. *The Journal of Physical Chemistry C*, 115(18):8945–8954, 2011.

[139] Julien Vidal, Silvana Botti, Pär Olsson, Jean-Francois Guillemoles, and Lucia Reining. Strong interplay between structure and electronic properties in cuin (s, se) 2: a first-principles study. *Physical review letters*, 104(5):056401, 2010.

[140] Susanne Siebentritt, Malgorzata Igalson, Clas Persson, and Stephan Lany. The electronic structure of chalcopyrites—bands, point defects and grain boundaries. *Progress in Photovoltaics: Research and Applications*, 18(6):390–410, 2010.

[141] JE Jaffe and Alex Zunger. Theory of the band-gap anomaly in ab c 2 chalcopyrite semiconductors. *Physical Review B*, 29(4):1882, 1984.

[142] JE Jaffe and Alex Zunger. Electronic structure of the ternary chalcopyrite semiconductors cual s 2, cuga s 2, cuin s 2, cual se 2, cuga se 2, and cuin se 2. *Physical Review B*, 28(10):5822, 1983.

[143] JE Jaffe and Alex Zunger. Anion displacements and the band-gap anomaly in ternary ab c 2 chalcopyrite semiconductors. *Physical Review B*, 27(8):5176, 1983.

[144] John P Perdew and Yue Wang. Erratum: Accurate and simple analytic representation of the electron-gas correlation energy [phys. rev. b 45, 13244 (1992)]. *Physical Review B*, 98(7):079904, 2018.

[145] John P Perdew, Kieron Burke, and Yue Wang. Generalized gradient approximation for the exchange-correlation hole of a many-electron system. *Physical review B*, 54(23):16533, 1996.

[146] Jochen Heyd, Gustavo E Scuseria, and Matthias Ernzerhof. Hybrid functionals based on a screened coulomb potential. *The Journal of chemical physics*, 118(18):8207–8215, 2003.

[147] Jochen Heyd and Gustavo E Scuseria. Efficient hybrid density functional calculations in solids: Assessment of the heyd–scuseria–ernzerhof screened coulomb hybrid functional. *The Journal of chemical physics*, 121(3):1187–1192, 2004.

[148] Aliaksandr V Krukau, Oleg A Vydrov, Artur F Izmaylov, and Gustavo E Scuseria. Influence of the exchange screening parameter on the performance of screened hybrid functionals. *The Journal of chemical physics*, 125(22), 2006.

[149] Joachim Paier, Martijn Marsman, K Hummer, Georg Kresse, Iann C Gerber, and János G Ángyán. Screened hybrid density functionals applied to solids. *The Journal of chemical physics*, 124(15), 2006.

[150] Subrata Jana, Abhilash Patra, and Prasanjit Samal. Efficient lattice constants and energy bandgaps for condensed systems from a meta-gga level screened range-separated hybrid functional. *The Journal of Chemical Physics*, 149(9), 2018.

[151] Subrata Jana and Prasanjit Samal. Screened hybrid meta-gga exchange–correlation functionals for extended systems. *Physical Chemistry Chemical Physics*, 21(6):3002–3015, 2019.

[152] Subrata Jana, Abhilash Patra, Lucian A Constantin, and Prasanjit Samal. Screened range-separated hybrid by balancing the compact and slowly varying density regimes: Satisfaction of local density linear response. *The Journal of Chemical Physics*, 152(4), 2020.

[153] John P Perdew and Karla Schmidt. Jacob's ladder of density functional approximations for the exchange-correlation energy. In *AIP Conference Proceedings*, volume 577, pages 1–20. American Institute of Physics, 2001.

[154] Carlo Adamo, Matthias Ernzerhof, and Gustavo E Scuseria. The meta-gga functional: Thermochemistry with a kinetic energy density dependent exchange-correlation functional. *The Journal of Chemical Physics*, 112(6):2643–2649, 2000.

[155] Arghya Ghosh, Subrata Jana, Manish K Niranjan, Sushant Kumar Behera, Lucian A Constantin, and Prasanjit Samal. Improved electronic structure prediction of chalcopyrite semiconductors from a semilocal density functional based on pauli kinetic energy enhancement factor. *Journal of Physics: Condensed Matter*, 34(7):075501, 2021.

[156] Georg Kresse and Jürgen Furthmüller. Efficiency of ab-initio total energy calculations for metals and semiconductors using a plane-wave basis set. *Computational materials science*, 6(1):15–50, 1996.

[157] Tom K Woo, Peter M Margl, Peter E Blöchl, and Tom Ziegler. A combined car-parrinello qm/mm implementation for ab initio molecular dynamics simulations of extended systems: Application to transition metal catalysis. *The Journal of Physical Chemistry B*, 101(40):7877–7880, 1997.

[158] Koichi Momma and Fujio Izumi. Vesta 3 for three-dimensional visualization of crystal, volumetric and morphology data. *Journal of applied crystallography*, 44(6):1272–1276, 2011.

[159] H Hahn. G. frank, w. klingler. *A.-D. Meyer, and G. St6rger, Z. anorg allg. Chem*, 271:153, 1953.

[160] G Brandt, A Räuber, and J Schneider. Esr and x-ray analysis of the ternary semiconductors cuals2, cuins2 and aggas2. *Solid State Communications*, 12(6):481–483, 1973.

[161] J Schneider, A Räuber, and G Brandt. Esr-analysis of the chalcopyrite structure: Cugas2: Fe3+. *Journal of Physics and Chemistry of Solids*, 34(3):443–450, 1973.

[162] John D Meakin. Status of cuinse2 solar cells. In *Photovoltaics*, volume 543, pages 108–118. SPIE, 1985.

[163] Yubo Zhang, Xun Yuan, Xiudong Sun, Bi-Ching Shih, Peihong Zhang, and Wenqing Zhang. Comparative study of structural and electronic properties of cu-based multinary semiconductors. *Physical Review B*, 84(7):075127, 2011.

[164] Kanghyeon Park, Byeong-Hyeon Jeong, and Ji-Sang Park. Search of chalcopyrite materials based on hybrid density functional theory calculation. *Journal of Physics Communications*, 6(6):065001, 2022.

[165] GM Dongho Nguimdo and Daniel P Joubert. A density functional (pbe, pbesol, hse06) study of the structural, electronic and optical properties of the ternary compounds agalx 2 (x= s, se, te). *The European Physical Journal B*, 88:1–10, 2015.

[166] Sihan Wang, Haijun Li, Xiuping Sun, and Ying Xu. Novel structure of agins2 compound under high pressure: First principles calculations. *Solid State Communications*, 284:20–24, 2018.

[167] Mark Asta. Computational materials discovery and design. *JOM*, 66(3):364–365, 2014.

[168] Anubhav Jain, Shyue Ping Ong, Geoffroy Hautier, Wei Chen, William Davidson Richards, Stephen Dacek, Shreyas Cholia, Dan Gunter, David Skinner, Gerbrand Ceder, et al. Commentary: The materials project: A materials genome approach to accelerating materials innovation. *APL materials*, 1(1), 2013.

[169] Vladan Stevanović, Stephan Lany, Xiuwen Zhang, and Alex Zunger. Correcting density functional theory for accurate predictions of compound enthalpies of formation: Fitted elemental-phase reference energies. *Physical Review B*, 85(11):115104, 2012.

[170] H Neumann, G Kühn, and B Schumann. Adamantine ternary epitaxial layers. *Progress in Crystal Growth and Characterization*, 3(2-3):157–178, 1980.

[171] Yu-Jun Zhao and Alex Zunger. Site preference for mn substitution in spintronic cum iii x 2 vi chalcopyrite semiconductors. *Physical Review B*, 69(7):075208, 2004.

[172] Dan Huang, Yang Xue, Wentong Zhou, Jingwen Jiang, Hua Ning, Jin Guo, Yu-Jun Zhao, Rongzhen Chen, and Clas Persson. Ideal half-filled intermediate band position in cugas2 generated by sb-related defect complex: a first-principles study. *Applied Physics Express*, 12(2):021002, 2019.

[173] Leandro M Liborio, Christine L Bailey, Giuseppe Mallia, Stanko Tomić, and Nicholas M Harrison. Chemistry of defect induced photoluminescence in chalcopyrites: The case of cuals2. *Journal of Applied Physics*, 109(2), 2011.

[174] Leandro Liborio, Su Chuen Chew, and Nicholas Harrison. Atomic structure of the (001) surface of cugase2. *Surface science*, 606(3-4):496–504, 2012.

[175] Tingting Wang, Xiaoguang Li, Wenjie Li, Li Huang, Cencen Ma, Ya Cheng, Jun Cui, Hailin Luo, Guohua Zhong, and Chunlei Yang. Transition metals doped cualse2 for promising intermediate band materials. *Materials Research Express*, 3(4):045905, 2016.

[176] Jingwen Jiang, Xiaoxia Cen, Wenquan Dong, Wenzheng Zhou, Xianqing Liang, Yixin Liu, Jin Guo, and Dan Huang. Theoretical design of the absorber for intermediate band solar cells from group-iv (si, ge, and sn)-doped agalse2. *physica status solidi (b)*, 255(7):1800031, 2018.

[177] Francis J DiSalvo. Thermoelectric cooling and power generation. *Science*, 285(5428):703–706, 1999.

[178] Lon E Bell. Cooling, heating, generating power, and recovering waste heat with thermoelectric systems. *Science*, 321(5895):1457–1461, 2008.

[179] Vladimir Leonov and Ruud J. M. Vullers. Wearable electronics self-powered by using human body heat: The state of the art and the perspective. *Journal of Renewable and Sustainable Energy*, 1(6):062701, 11 2009.

[180] A Boyer and E Cisse. Properties of thin film thermoelectric materials: application to sensors using the seebeck effect. *Materials Science and Engineering: B*, 13(2):103–111, 1992.

[181] Ling-Yu Lv, Cheng-Fei Cao, Yong-Xiang Qu, Guo-Dong Zhang, Li Zhao, Kun Cao, Pingan Song, and Long-Cheng Tang. Smart fire-warning materials and sensors: Design principle, performances, and applications. *Materials Science and Engineering: R: Reports*, 150:100690, 2022.

[182] GD Mahan and JO Sofo. The best thermoelectric. *Proceedings of the National Academy of Sciences*, 93(15):7436–7439, 1996.

[183] Joseph P Heremans, Vladimir Jovovic, Eric S Toberer, Ali Saramat, Ken Kurosaki, Anek Charoenphakdee, Shinsuke Yamanaka, and G Jeffrey Snyder. Enhancement of thermoelectric efficiency in pbte by distortion of the electronic density of states. *Science*, 321(5888):554–557, 2008.

[184] Min Hong, Zhi-Gang Chen, and Jin Zou. Fundamental and progress of bi2te3-based thermoelectric materials. *Chinese Physics B*, 27(4):048403, 2018.

[185] Y Gelbstein, Z Dashevsky, and MP Dariel. High performance n-type pbte-based materials for thermoelectric applications. *Physica B: Condensed Matter*, 363(1-4):196–205, 2005.

[186] RA Downie, DA MacLaren, and J-WG Bos. Thermoelectric performance of multiphase xnisn (x= ti, zr, hf) half-heusler alloys. *Journal of Materials Chemistry A*, 2(17):6107–6114, 2014.

[187] Yu Cao, Xianli Su, Fanchen Meng, Trevor P Bailey, Jinggeng Zhao, Hongyao Xie, Jian He, Ctirad Uher, and Xinfeng Tang. Origin of the distinct thermoelectric transport properties of chalcopyrite abte2 (a= cu, ag; b= ga, in). *Advanced Functional Materials*, 30(51):2005861, 2020.

[188] David Parker and David J Singh. Thermoelectric properties of aggate 2 and related chalcopyrite structure materials. *Physical Review B*, 85(12):125209, 2012.

[189] Dimple Rani, Subrata Jana, Manish K Niranjan, and Prasanjit Samal. First-principle investigation of structural, electronic, and phase stabilities in chalcopyrite semiconductors: insights from meta-gga functionals. *Journal of Physics: Condensed Matter*, 36(16):165502, 2024.

[190] Subrata Jana, Arghya Ghosh, Abhishek Bhattacharjee, Dimple Rani, Manoar Hossain, and Prasanjit Samal. Nonempirical dielectric dependent hybrid as an accurate starting point for the single shot g0w0 calculation of chalcopyrite semiconductors. *The Journal of Chemical Physics*, 162(6), 2025.

[191] Anek Charoenphakdee, Ken Kurosaki, Hiroaki Muta, Masayoshi Uno, and Shinsuke Yamanaka. Thermal conductivity of the ternary compounds: Agmte2 and agm5te8 (m= ga or in). *Materials transactions*, 50(7):1603–1606, 2009.

[192] Sheetal Sharma, AS Verma, and VK Jindal. Ab initio studies of structural, electronic, optical, elastic and thermal properties of silver gallium dichalcogenides (aggax2: X= s, se, te). *Materials Research Bulletin*, 53:218–233, 2014.

[193] H Peng, CL Wang, and JC Li. Enhanced thermoelectric properties of aggate2 utilizing carrier concentration adjusting. *Physica B: Condensed Matter*, 441:68–71, 2014.

[194] Jianhui Yang, Qiang Fan, and Xinlu Cheng. Prediction for electronic, vibrational and thermoelectric properties of chalcopyrite agx (x= in, ga) te2: Pbe+ u approach. *Royal Society Open Science*, 4(10):170750, 2017.

[195] Kan Li, Bo Chai, Tianyou Peng, Jin Mao, and Ling Zan. Synthesis of multicomponent sulfide ag 2 znsns 4 as an efficient photocatalyst for h 2 production under visible light irradiation. *Rsc Advances*, 3(1):253–258, 2013.

[196] Kaya Wei and George S. Nolas. Synthesis and characterization of nanostructured stannite cu2znsnse4 and ag2znsnse4 for thermoelectric applications. *ACS Applied Materials & Interfaces*, 7(18):9752–9757, 2015. PMID: 25894101.

[197] Evgueni Chagarov, Kasra Sardashti, Andrew C. Kummel, Yun Seog Lee, Richard Haight, and Talia S. Gershon. Ag2znsn(s,se)4: A highly promising absorber for thin film photovoltaics. *The Journal of Chemical Physics*, 144(10):104704, 03 2016.

[198] Zhang Xianfeng, Tsuyoshi Kobayashi, Yasuyoshi Kurokawa, Shinsuke Miyajima, and Akira Yamada. Deposition of ag(in,ga)se2 solar cells by a modified three-stage method using a low-temperature-deposited ag–se cap layer. *Japanese Journal of Applied Physics*, 52(5R):055801, apr 2013.

[199] Lin-Ya Yeh and Kong-Wei Cheng. Preparation of the ag–zn–sn–s quaternary photoelectrodes using chemical bath deposition for photoelectrochemical applications. *Thin Solid Films*, 558:289–293, 2014.

[200] Shiyou Chen, X. G. Gong, Aron Walsh, and Su-Huai Wei. Crystal and electronic band structure of cu2znsnx4 (x=s and se) photovoltaic absorbers: First-principles insights. *Applied Physics Letters*, 94(4):041903, 01 2009.

[201] O.V. Parasyuk, A.O. Fedorchuk, Yu.M. Kogut, L.V. Piskach, and I.D. Olekseyuk. The ag2s–zns–ges2 system: Phase diagram, glass-formation region and crystal structure of ag2znges4. *Journal of Alloys and Compounds*, 500(1):26–29, 2010.

[202] Fatima Zahra Nainaa, Naoual Bekkioui, Abderrahman Abbassi, and Hamid Ez-Zahraouy. First principle study of structural, electronic, optical and electric properties of ag2zngex4 (s, se). *Computational Condensed Matter*, 19:e00364, 2019.

[203] Jun Zhou, Xiaobo Li, Gang Chen, and Ronggui Yang. Semiclassical model for thermoelectric transport in nanocomposites. *Physical Review B*, 82(11):115308, 2010.

[204] DH Chung and WR Buessem. The voigt-reuss-hill approximation and elastic moduli of polycrystalline mgo, caf2, β-zns, znse, and cdte. *Journal of Applied Physics*, 38(6):2535–2540, 1967.

[205] Wei Chen, Giacomo Miceli, Gian-Marco Rignanese, and Alfredo Pasquarello. Nonempirical dielectric-dependent hybrid functional with range separation for semiconductors and insulators. *Phys. Rev. Mater.*, 2:073803, Jul 2018.

[206] Zhi-Hao Cui, Yue-Chao Wang, Min-Ye Zhang, Xi Xu, and Hong Jiang. Doubly screened hybrid functional: An accurate first-principles approach for both narrow- and wide-gap semiconductors. *The Journal of Physical Chemistry Letters*, 9(9):2338–2345, 2018.

[207] Arghya Ghosh, Subrata Jana, Dimple Rani, Manoar Hossain, Manish K Niranjan, and Prasanjit Samal. Accurate and efficient prediction of the band gaps and optical spectra of chalcopyrite semiconductors from a nonempirical range-separated dielectric-dependent hybrid: Comparison with many-body perturbation theory. *Physical Review B*, 109(4):045133, 2024.

[208] Subrata Jana, Arghya Ghosh, Lucian A Constantin, and Prasanjit Samal. Simple and effective screening parameter for range-separated dielectric-dependent hybrids. *Physical Review B*, 108(4):045101, 2023.

[209] A. Ferreira da Silva, C. Persson, Rajeev Ahuja, and B. Johansson. Effective electron and hole masses in intrinsic and heavily n-type doped gan and aln. *Journal of Physics: Condensed Matter*, 13(8):4385, 2001.

[210] JMJ Den Toonder, JAW Van Dommelen, and FPT Baaijens. The relation between single crystal elasticity and the effective elastic behaviour of polycrystalline materials: theory, measurement and computation. *Modelling and Simulation in Materials Science and Engineering*, 7(6):909, 1999.

[211] VL Shaposhnikov, AV Krivosheeva, VE Borisenko, J-L Lazzari, and F Arnaud d'Avitaya. Ab initio modeling of the structural, electronic, and optical properties of a ii b iv c 2 v semiconductors. *Physical Review B*, 85(20):205201, 2012.

[212] Takahiro Wada. Materials science of chalcopyrite-type and multinary solar cells compounds: crystal structure and electronic structure of cise, czts, cts, and the related compounds. *JSAP Review*, 2022:220204, 2022.

[213] Hai Xiao, Jamil Tahir-Kheli, and William A Goddard III. Accurate band gaps for semiconductors from density functional theory. *The Journal of Physical Chemistry Letters*, 2(3):212–217, 2011.

[214] Paul Picot and Zdenek Johan. La pirquitasite, ag2znsns4, un nouveau membre du groupe de la stannite. *Bulletin de Minéralogie*, 105(3):229–235, 1982.

[215] Kaya Wei, Artem R Khabibullin, Troy Stedman, Lilia M Woods, and George S Nolas. Polaronic transport in ag-based quaternary chalcogenides. *Journal of Applied Physics*, 122(10), 2017.

[216] Zhen-Kun Yuan, Shiyou Chen, Hongjun Xiang, Xin-Gao Gong, Aron Walsh, Ji-Sang Park, Ingrid Repins, and Su-Huai Wei. Engineering solar cell absorbers by exploring the band alignment and defect disparity: The case of cu- and ag-based kesterite compounds. *Advanced Functional Materials*, 25(43):6733–6743, 2015.

[217] Amanda J Souna, Kaya Wei, and George S Nolas. The effect on the optical modes of quaternary chalcogenides upon metal and chalcogen substitution. *Applied Physics Letters*, 116(8), 2020.

[218] Shinya Arai, Shunji Ozaki, and Sadao Adachi. Optical properties and electronic band structure of aggate 2 chalcopyrite semiconductor. *Applied optics*, 49(5):829–837, 2010.

[219] Yanzhong Pei, Xiaoya Shi, Aaron LaLonde, Heng Wang, Lidong Chen, and G Jeffrey Snyder. Convergence of electronic bands for high performance bulk thermoelectrics. *Nature*, 473(7345):66–69, 2011.

[220] Jiawei Zhang, Ruiheng Liu, Nian Cheng, Yubo Zhang, Jihui Yang, Ctirad Uher, Xun Shi, Lidong Chen, and Wenqing Zhang. High-performance pseudocubic thermoelectric materials from non-cubic chalcopyrite compounds. 2014.

[221] Yanzhong Pei, Aaron D. LaLonde, Heng Wang, and G. Jeffrey Snyder. Low effective mass leading to high thermoelectric performance. *Energy Environ. Sci.*, 5:7963–7969, 2012.

[222] Richard C Remsing and Jefferson E Bates. Effective mass path integral simulations of quasiparticles in condensed phases. *The Journal of Chemical Physics*, 153(12), 2020.

[223] Georg KH Madsen, Jesús Carrete, and Matthieu J Verstraete. Boltztrap2, a program for interpolating band structures and calculating semi-classical transport coefficients. *Computer Physics Communications*, 231:140–145, 2018.

[224] Biswaranjan R Nag. *Electron transport in compound semiconductors*, volume 11. Springer Science & Business Media, 2012.

[225] Koushik Pal, Xia Hua, Yi Xia, and Christopher Wolverton. Unraveling the structure-valence-property relationships in amm q3 chalcogenides with promising thermoelectric performance. *ACS Applied Energy Materials*, 3(3):2110–2119, 2019.

[226] Sahib Hasan, Saro San, Khagendra Baral, Neng Li, Paul Rulis, and Wai-Yim Ching. First-principles calculations of thermoelectric transport properties of quaternary and ternary bulk chalcogenide crystals. *Materials*, 15(8):2843, 2022.

[227] Shiqiang Hao, Logan Ward, Zhongzhen Luo, Vidvuds Ozolins, Vinayak P Dravid, Mercouri G Kanatzidis, and Christopher Wolverton. Design strategy for high-performance thermoelectric materials: The prediction of electron-doped kzrcuse3. *Chemistry of Materials*, 31(8):3018–3024, 2019.

[228] J Bardeen and WJPR Shockley. Deformation potentials and mobilities in non-polar crystals. *Physical review*, 80(1):72, 1950.

[229] Jinyang Xi, Mengqiu Long, Ling Tang, Dong Wang, and Zhigang Shuai. First-principles prediction of charge mobility in carbon and organic nanomaterials. *Nanoscale*, 4(15):4348–4369, 2012.

[230] Suiting Ning, Shan Huang, Ziye Zhang, Renqi Zhang, Ning Qi, and Zhiquan Chen. High thermoelectric performance of topological half-heusler compound laptbi achieved by hydrostatic pressure. *Physical Chemistry Chemical Physics*, 22(26):14621–14629, 2020.

[231] Zhigang Shuai, Linjun Wang, and Chenchen Song. *Theory of charge transport in carbon electronic materials*. Springer Science & Business Media, 2012.

[232] John M Ziman. *Electrons and phonons: the theory of transport phenomena in solids*. Oxford university press, 2001.

[233] Wu Li, Jesús Carrete, Nebil A Katcho, and Natalio Mingo. Shengbte: A solver of the boltzmann transport equation for phonons. *Computer Physics Communications*, 185(6):1747–1758, 2014.

[234] Tiantian Jia, Gang Chen, and Yongsheng Zhang. Lattice thermal conductivity evaluated using elastic properties. *Physical Review B*, 95(15):155206, 2017.

[235] DT Morelli, V Jovovic, and JP Heremans. Intrinsically minimal thermal conductivity in cubic i- v- vi 2 semiconductors. *Physical review letters*, 101(3):035901, 2008.

[236] Yu Xiao, Cheng Chang, Yanling Pei, Di Wu, Kunling Peng, Xiaoyuan Zhou, Shengkai Gong, Jiaqing He, Yongsheng Zhang, Zhi Zeng, et al. Origin of low thermal conductivity in snse. *Physical Review B*, 94(12):125203, 2016.

[237] Ponniah Vajeeston and Helmer Fjellvåg. First-principles study of structural stability, dynamical and mechanical properties of li 2 fesio 4 polymorphs. *RSC advances*, 7(27):16843–16853, 2017.

[238] András Reuß. Berechnung der fließgrenze von mischkristallen auf grund der plastizitätsbedingung für einkristalle. *ZAMM-Journal of Applied Mathematics and Mechanics/Zeitschrift für Angewandte Mathematik und Mechanik*, 9(1):49–58, 1929.

[239] Richard Hill. The elastic behaviour of a crystalline aggregate. *Proceedings of the Physical Society. Section A*, 65(5):349, 1952.

[240] Aikebaier Yusufu, Ken Kurosaki, Atsuko Kosuga, Tohru Sugahara, Yuji Ohishi, Hiroaki Muta, and Shinsuke Yamanaka. Thermoelectric properties of ag1- xgate2 with chalcopyrite structure. *Applied Physics Letters*, 99(6), 2011.

[241] Yaqiong Zhong, Yong Luo, Xie Li, and Jiaolin Cui. Silver vacancy concentration engineering leading to the ultralow lattice thermal conductivity and improved thermoelectric performance of ag1-xinte2. *Scientific reports*, 9(1):18879, 2019.

[242] Kun Huang and Bangfen Zhu. Dielectric continuum model and fröhlich interaction in superlattices. *Physical Review B*, 38(18):13377, 1988.

[243] Tianqi Deng, Jose Recatala-Gomez, Masato Ohnishi, DV Maheswar Repaka, Pawan Kumar, Ady Suwardi, Anas Abutaha, Iris Nandhakumar, Kanishka Biswas, Michael B Sullivan, et al. Electronic transport descriptors for the rapid screening of thermoelectric materials. *Materials Horizons*, 8(9):2463–2474, 2021.

[244] Jose J Plata, Ernesto J Blancas, Antonio M Márquez, Victor Posligua, Javier Fdez Sanz, and Ricardo Grau-Crespo. Harnessing the unusually strong improvement of thermoelectric performance of aginte 2 with nanostructuring. *Journal of Materials Chemistry A*, 11(31):16734–16742, 2023.

[245] Yaqiong Zhong, Debalaya Sarker, Tao Fan, Liangliang Xu, Xie Li, Guang-Zhao Qin, Zhong-Kang Han, and Jiaolin Cui. Computationally guided synthesis of high performance thermoelectric materials: Defect engineering in aggate2. *Advanced Electronic Materials*, 7(4):2001262, 2021.

[246] M. Heide, G. Bihlmayer, and S. Blügel. Dzyaloshinskii-moriya interaction accounting for the orientation of magnetic domains in ultrathin films: Fe/w(110). *Phys. Rev. B*, 78:140403, Oct 2008.

[247] Zhong Shen, Changsheng Song, Yufei Xue, Zebin Wu, Jiqing Wang, and Zhicheng Zhong. Strain-tunable dzyaloshinskii-moriya interaction and skyrmions in two-dimensional janus $cr_2X_3Y_3$ (x, y = cl, br, i, $x \neq y$) trihalide monolayers. *Phys. Rev. B*, 106:094403, Sep 2022.

[248] Kenneth S Burch, David Mandrus, and Je-Geun Park. Magnetism in two-dimensional van der waals materials. *Nature*, 563(7729):47–52, 2018.

[249] Mehmet Aras, Çetin Kılıç, and S. Ciraci. Planar heterostructures of single-layer transition metal dichalcogenides: Composite structures, schottky junctions, tunneling barriers, and half metals. *Phys. Rev. B*, 95:075434, Feb 2017.

[250] Xuelei Sui, Tao Hu, Jianfeng Wang, Bing-Lin Gu, Wenhui Duan, and Mao-sheng Miao. Voltage-controllable colossal magnetocrystalline anisotropy in single-layer transition metal dichalcogenides. *Phys. Rev. B*, 96:041410, Jul 2017.

[251] L. Powalla, M. T. Birch, K. Litzius, S. Wintz, S. Satheesh, M. Weigand, E. Goering, G. Schütz, and M. Burghard. Skyrmion and skyrmionium formation in the two-dimensional magnet $cr_2ge_2te_6$. *Phys. Rev. B*, 108:214417, Dec 2023.

[252] Constance Moreau-Luchaire, Christoforos Moutafis, Nicolas Reyren, João Sampaio, CAF Vaz, N Van Horne, Karim Bouzehouane, K Garcia, C Deranlot, P Warnicke, et al. Additive interfacial chiral interaction in multilayers for stabilization of small individual skyrmions at room temperature. *Nature nanotechnology*, 11(5):444–448, 2016.

[253] Tae-Eon Park, Licong Peng, Jinghua Liang, Ali Hallal, Fehmi Sami Yasin, Xichao Zhang, Kyung Mee Song, Sung Jong Kim, Kwangsu Kim, Markus Weigand, Gisela Schütz, Simone Finizio, Jörg Raabe, Karin Garcia, Jing Xia, Yan Zhou, Motohiko Ezawa, Xiaoxi Liu, Joonyeon Chang, Hyun Cheol Koo, Young Duck Kim, Mairbek Chshiev, Albert Fert, Hongxin Yang, Xiuzhen Yu, and Seonghoon Woo. Néel-type skyrmions and their current-induced motion in van der waals ferromagnet-based heterostructures. *Phys. Rev. B*, 103:104410, Mar 2021.

[254] Igor Dzyaloshinsky. A thermodynamic theory of "weak" ferromagnetism of antiferromagnetics. *Journal of physics and chemistry of solids*, 4(4):241–255, 1958.

[255] Tôru Moriya. Anisotropic superexchange interaction and weak ferromagnetism. *Phys. Rev.*, 120:91–98, Oct 1960.

[256] A. Fert and Peter M. Levy. Role of anisotropic exchange interactions in determining the properties of spin-glasses. *Phys. Rev. Lett.*, 44:1538–1541, Jun 1980.

[257] Alexei N Bogdanov and DA Yablonskii. Thermodynamically stable "vortices" in magnetically ordered crystals. the mixed state of magnets. *Zh. Eksp. Teor. Fiz*, 95(1):178, 1989.

[258] André Thiaville, Stanislas Rohart, Émilie Jué, Vincent Cros, and Albert Fert. Dynamics of dzyaloshinskii domain walls in ultrathin magnetic films. *Europhysics Letters*, 100(5):57002, 2012.

[259] J. Sampaio, V. Cros, S. Rohart, A. Thiaville, and A. Fert. Nucleation, stability and current-induced motion of isolated magnetic skyrmions in nanostructures. *Nature Nanotechnology*, 8:839–844, 2013.

[260] Dongzhe Li, Soumyajyoti Haldar, Tim Drevelow, and Stefan Heinze. Tuning the magnetic interactions in van der waals fe_3gete_2 heterostructures: A comparative study of ab initio methods. *Phys. Rev. B*, 107:104428, Mar 2023.

[261] Dongzhe Li, Soumyajyoti Haldar, and Stefan Heinze. Strain-driven zero-field near-10 nm skyrmions in two-dimensional van der waals heterostructures. *Nano Letters*, 22(18):7706–7713, 2022. PMID: 36121771.

[262] Christian Back, Vincent Cros, Hubert Ebert, Karin Everschor-Sitte, Albert Fert, Markus Garst, Tianping Ma, Sergiy Mankovsky, TL Monchesky, Maxim Mostovoy, et al. The 2020 skyrmionics roadmap. *Journal of Physics D: Applied Physics*, 53(36):363001, 2020.

[263] XZ Yu, Naoya Kanazawa, Yoshinori Onose, K Kimoto, WZ Zhang, Shintaro Ishiwata, Yoshio Matsui, and Yoshinori Tokura. Near room-temperature formation of a skyrmion crystal in thin-films of the helimagnet fege. *Nature materials*, 10(2):106–109, 2011.

[264] XZ Yu, Yoshinori Onose, Naoya Kanazawa, Joung Hwan Park, JH Han, Yoshio Matsui, Naoto Nagaosa, and Yoshinori Tokura. Real-space observation of a two-dimensional skyrmion crystal. *Nature*, 465(7300):901–904, 2010.

[265] Sebastian Mühlbauer, Benedikt Binz, Florian Jonietz, Christian Pfleiderer, Achim Rosch, Anja Neubauer, Robert Georgii, and Peter Böni. Skyrmion lattice in a chiral magnet. *Science*, 323(5916):915–919, 2009.

[266] Duck-Ho Kim, Mitsutaka Haruta, Hye-Won Ko, Gyungchoon Go, Hyeon-Jong Park, Tomoe Nishimura, Dae-Yun Kim, Takaya Okuno, Yuushou Hirata, Yasuhiro Futakawa, et al. Bulk dzyaloshinskii–moriya interaction in amorphous ferrimagnetic alloys. *Nature materials*, 18(7):685–690, 2019.

[267] Satoru Emori, Uwe Bauer, Sung-Min Ahn, Eduardo Martinez, and Geoffrey SD Beach. Current-driven dynamics of chiral ferromagnetic domain walls. *Nature materials*, 12(7):611–616, 2013.

[268] Bing Li, J.-Q. Yan, D. M. Pajerowski, Elijah Gordon, A.-M. Nedić, Y. Sizyuk, Liqin Ke, P. P. Orth, D. Vaknin, and R. J. McQueeney. Competing magnetic interactions in the antiferromagnetic topological insulator $mnbi_2te_4$. *Phys. Rev. Lett.*, 124:167204, Apr 2020.

[269] Yang Gao, Shaohua Yan, Qiangwei Yin, He Huang, Zhuolin Li, Zhaozhao Zhu, Jianwang Cai, Baogen Shen, Hechang Lei, Ying Zhang, and Shouguo Wang. Manipulation of topological spin configuration via tailoring thickness in van der waals ferromagnetic $fe_{5-x}gete_2$. *Phys. Rev. B*, 105:014426, Jan 2022.

[270] Weiyan Gong, Takahiro Tabata, Koji Takei, Masaru Morihama, Tsuyoshi Maeda, and Takahiro Wada. Crystallographic and optical properties of (cu, ag) 2znsns4 and (cu, ag) 2znsnse4 solid solutions. *physica status solidi (c)*, 12(6):700–703, 2015.

[271] Jinghua Liang, Weiwei Wang, Haifeng Du, Ali Hallal, Karin Garcia, Mairbek Chshiev, Albert Fert, and Hongxin Yang. Very large dzyaloshinskii-moriya interaction in two-dimensional janus manganese dichalcogenides and its application to realize skyrmion states. *Phys. Rev. B*, 101:184401, May 2020.

[272] Zhong Shen, Changsheng Song, Yufei Xue, Zebin Wu, Jiqing Wang, and Zhicheng Zhong. Strain-tunable dzyaloshinskii-moriya interaction and skyrmions in two-dimensional janus $cr_2X_3Y_3$ (x, y = cl, br, i, $x \neq y$) trihalide monolayers. *Phys. Rev. B*, 106:094403, Sep 2022.

[273] Jinghua Liang, Weiwei Wang, Haifeng Du, Ali Hallal, Karin Garcia, Mairbek Chshiev, Albert Fert, and Hongxin Yang. Very large dzyaloshinskii-moriya interaction in two-dimensional janus manganese dichalcogenides and its application to realize skyrmion states. *Phys. Rev. B*, 101:184401, May 2020.

[274] Qirui Cui, Jinghua Liang, Ziji Shao, Ping Cui, and Hongxin Yang. Strain-tunable ferromagnetism and chiral spin textures in two-dimensional janus chromium dichalcogenides. *Phys. Rev. B*, 102:094425, Sep 2020.

[275] C. Ataca, H. Şahin, and S. Ciraci. Stable, single-layer mx2 transition-metal oxides and dichalcogenides in a honeycomb-like structure. *The Journal of Physical Chemistry C*, 116(16):8983–8999, 2012.

[276] Mehmet Aras, Çetin Kılıç, and S. Ciraci. Magnetic ground state in $fete_2$, vs_2, and $nite_2$ monolayers: Antiparallel magnetic moments at chalcogen atoms. *Phys. Rev. B*, 101:054429, Feb 2020.

[277] Atsushi Togo and Isao Tanaka. First principles phonon calculations in materials science. *Scripta Materialia*, 108:1–5, 2015.

[278] H. J. Xiang, E. J. Kan, Su-Huai Wei, M.-H. Whangbo, and X. G. Gong. Predicting the spin-lattice order of frustrated systems from first principles. *Phys. Rev. B*, 84:224429, Dec 2011.

[279] V. I. Anisimov, I. V. Solovyev, M. A. Korotin, M. T. Czyżyk, and G. A. Sawatzky. Density-functional theory and nio photoemission spectra. *Phys. Rev. B*, 48:16929–16934, Dec 1993.

[280] Matteo Cococcioni and Stefano de Gironcoli. Linear response approach to the calculation of the effective interaction parameters in the LDA + U method. *Phys. Rev. B*, 71:035105, Jan 2005.

[281] Louis Noodleman. Valence bond description of antiferromagnetic coupling in transition metal dimers. *The Journal of Chemical Physics*, 74(10):5737–5743, 1981.

[282] Ding-sheng Wang, Ruqian Wu, and A. J. Freeman. First-principles theory of surface magnetocrystalline anisotropy and the diatomic-pair model. *Phys. Rev. B*, 47:14932–14947, Jun 1993.

[283] Yan Zhou. Magnetic skyrmions: intriguing physics and new spintronic device concepts. *National Science Review*, 6(2):210–212, 10 2018.

[284] Yoshinori Tokura and Naoya Kanazawa. Magnetic skyrmion materials. *Chemical Reviews*, 121:2857–2897, 2021.

[285] D. Zhu, W. Kang, S. Li, Y. Huang, X. Zhang, Y. Zhou, and W. Zhao. Skyrmion racetrack memory with random information update/deletion/insertion. *IEEE Transactions on Electron Devices*, 65:87–95, 2018.

[286] W. Kang, C. Zheng, Y. Huang, X. Zhang, Y. Zhou, W. Lv, and W. Zhao. Complementary skyrmion racetrack memory with voltage manipulation. *IEEE Electron Device Letters*, 37:924–927, 2016.

[287] W. Koshibae, Y. Kaneko, J. Iwasaki, M. Kawasaki, Y. Tokura, and N. Nagaosa. Memory functions of magnetic skyrmions. *Japanese Journal of Applied Physics*, 54:053001, 2015.

[288] A. Fert, N. Reyren, and V. Cros. Magnetic skyrmions: Advances in physics and potential applications. *Nature Reviews Materials*, 2:17031, 2017.

[289] Albert Fert, Vincent Cros, and João Sampaio. Skyrmions on the track. *Nature Nanotechnology*, 8(3):152–156, 2013.

[290] Naoto Nagaosa and Yoshinori Tokura. Topological properties and dynamics of magnetic skyrmions. *Nature Nanotechnology*, 8:899–911, 2013.

[291] João Sampaio, Vincent Cros, Stéphane Rohart, André Thiaville, and Albert Fert. Nucleation, stability and current-induced motion of isolated magnetic skyrmions in nanostructures. *Nature Nanotechnology*, 8:839–844, 2013.

[292] I. Dzyaloshinsky. A thermodynamic theory of "weak" ferromagnetism of antiferromagnetics. *Journal of Physics and Chemistry of Solids*, 4:241–255, 1958.

[293] T. Moriya. Anisotropic exchange interaction. *Phys. Rev.*, 120:91, 1960.

[294] A. Kundu and S. Zhang. Dzyaloshinskii-moriya interaction mediated by spin-orbit scattering. *Physical Review B*, 92:094434, 2015.

[295] Stefan Heinze, Kirsten von Bergmann, Matthias Menzel, and et al. Spontaneous atomic-scale magnetic skyrmion lattice in two dimensions. *Nature Physics*, 7:713–718, 2011.

[296] Camille Moreau-Luchaire, Christos Moutafis, Nicolas Reyren, and et al. Additive interfacial chiral interaction in multilayers for stabilization of small individual skyrmions at room temperature. *Nature Nanotechnology*, 11:444–448, 2016.

[297] A. Soumyanarayanan, N. Reyren, A. Fert, and C. Panagopoulos. Tunable room-temperature magnetic skyrmions in ir/fe/co/pt multilayers. *Nature Materials*, 16:898–904, 2017.

[298] Dimple Rani, B. R. K. Nanda, and Prasanjit Samal. Strain- and correlation-tuned magnetic anisotropy and dzyaloshinskii-moriya interaction in two-dimensional d_{3h}fete$_2$. *Phys. Rev. B*, 112:174401, Nov 2025.

[299] Olivier Boulle, Julien Vogel, Hua Yang, and et al. Room-temperature chiral magnetic skyrmions in ultrathin magnetic nanostructures. *Nature Nanotechnology*, 11:449–454, 2016.

[300] Stefan Grimme, Jens Antony, Stephan Ehrlich, and Helge Krieg. A consistent and accurate ab initio parametrization of density functional dispersion correction (dft-d) for the 94 elements h-pu. *Journal of Chemical Physics*, 132:154104, 2010.

[301] Stefan Grimme, Stephan Ehrlich, and Lars Goerigk. Effect of the damping function in dispersion corrected density functional theory. *Journal of Computational Chemistry*, 32:1456–1465, 2011.

[302] Guifang Xu, Fan Zhang, Xue Jiang, Yi Wang, Weiwei Gao, and Jijun Zhao. Tunable multi-q states caused by frustrated and long-range exchange interactions in monolayer $1t-$CrTe$_2$ and related heterostructures. *Phys. Rev. B*, 111:024419, Jan 2025.

[303] Hongxin Yang, André Thiaville, Stanislas Rohart, Albert Fert, and Mairbek Chshiev. Anatomy of dzyaloshinskii-moriya interaction at Co/Pt interfaces. *Phys. Rev. Lett.*, 115:267210, Dec 2015.

[304] Arne Vansteenkiste, Jonathan Leliaert, Mykola Dvornik, Mathias Helsen, Felipe Garcia-Sanchez, and Bartel Van Waeyenberge. The design and verification of mumax3. *AIP Advances*, 4(10):107133, 10 2014.

[305] Liang Liu, Songsong Chen, Zezhou Lin, and Xi Zhang. A symmetry-breaking phase in two-dimensional fete2 with ferromagnetism above room temperature. *The Journal of Physical Chemistry Letters*, 11(18):7893–7900, 2020. PMID: 32787292.

[306] Pooja Jamdagni, Ashok Kumar, Anil Thakur, Ravindra Pandey, and P. K. Ahluwalia. Energetics and electronic properties of pt wires of different topologies on monolayer mose2. *AIP Conference Proceedings*, 1731(1):090028, 05 2016.

[307] Cheng Ma, Kuijuan Jin, Chen Ge, Er-Jia Guo, Can Wang, and Xiulai Xu. Strong dzyaloshinskii-moriya interaction in two-dimensional magnets via lithium absorption. *Phys. Rev. B*, 108:134405, Oct 2023.

[308] Hongxin Yang, Gong Chen, Alexandre A. C. Cotta, Alpha T. N'Diaye, Sergey A. Nikolaev, Edmar A. Soares, Waldemar A. A. Macedo, Kai Liu, Andreas K. Schmid, Albert Fert, and Mairbek Chshiev. Significant dzyaloshinskii–moriya interaction at graphene–ferromagnet interfaces due to the rashba effect. *Nature Materials*, 17(7):605–609, 2018.

[309] Khimananda Acharya, Kai Huang, Evgeny Y. Tsymbal, and Tula R. Paudel. First-principles investigation of the emergence of multiferroicity and skyrmions in Cri_2. *Phys. Rev. B*, 111:094435, Mar 2025.

[310] R. Caglayan, A. Mogulkoc, Y. Mogulkoc, M. Modarresi, and A. N. Rudenko. Dzyaloshinskii-moriya interaction and nontrivial spin textures in the janus semiconductor monolayers Vxy (x = Cl, Br, I; y = S, Se, Te). *Phys. Rev. B*, 110:094440, Sep 2024.

[311] A. Fert and Peter M. Levy. Role of anisotropic exchange interactions in determining the properties of spin-glasses. *Phys. Rev. Lett.*, 44:1538–1541, Jun 1980.

[312] S. Mühlbauer, B. Binz, F. Jonietz, C. Pfleiderer, A. Rosch, A. Neubauer, R. Georgii, and P. Böni. Skyrmion lattice in a chiral magnet. *Science*, 323(5916):915–919, 2009.

[313] Eugen Ruff, Peter Lunkenheimer, Alois Loidl, H Berger, and Stephan Krohns. Magnetoelectric effects in the skyrmion host material cu2oseo3. *Scientific reports*, 5(1):15025, 2015.

[314] O. L. Makarova, A. V. Tsvyashchenko, G. Andre, F. Porcher, L. N. Fomicheva, N. Rey, and I. Mirebeau. Neutron diffraction study of the chiral magnet mnge. *Phys. Rev. B*, 85:205205, May 2012.

[315] Dante J. O'Hara, Tiancong Zhu, Amanda H. Trout, Adam S. Ahmed, Yunqiu Kelly Luo, Choong Hee Lee, Mark R. Brenner, Siddharth Rajan, Jay A. Gupta, David W. McComb, and Roland K. Kawakami. Room temperature intrinsic ferromagnetism in epitaxial manganese selenide films in the monolayer limit. *Nano Letters*, 18(5):3125–3131, 2018. PMID: 29608316.

[316] Yonglong Ga, Qirui Cui, Jinghua Liang, Dongxing Yu, Yingmei Zhu, Liming Wang, and Hongxin Yang. Dzyaloshinskii-moriya interaction and magnetic skyrmions induced by curvature. *Phys. Rev. B*, 106:054426, Aug 2022.

[317] Lucas Webster and Jia-An Yan. Strain-tunable magnetic anisotropy in monolayer $crcl_3$, $crbr_3$, and cri_3. *Phys. Rev. B*, 98:144411, Oct 2018.

[318] J L Lado and J Fernández-Rossier. On the origin of magnetic anisotropy in two dimensional cri3. *2D Materials*, 4(3):035002, jun 2017.

[319] Yonglong Ga, Dongxing Yu, Liming Wang, Peng Li, Jinghua Liang, and Hongxin Yang. Layer-dependent dzyaloshinskii–moriya interaction and field-free topological magnetism in two-dimensional janus mnste. *2D Materials*, 10(3):035020, may 2023.

[320] Menashe Haim, Alex Levchenko, and Maxim Khodas. Mechanisms of in-plane magnetic anisotropy in superconducting $nbse_2$. *Phys. Rev. B*, 105:024515, Jan 2022.

[321] Arghya Ghosh, Subrata Jana, Manoar Hossain, Dimple Rani, Szymon Śmiga, and Prasanjit Samal. Advancing excited-state properties of two-dimensional materials using a dielectric-dependent hybrid functional. *Phys. Rev. B*, 112:045128, Jul 2025.

[322] Xiao Chen and Changhai Liang. Transition metal silicides: fundamentals, preparation and catalytic applications. *Catal. Sci. Technol.*, 9:4785–4820, 2019.

[323] H. Ihou Mouko, K. Romanjek, M. Mejri, M. Oulfarsi, S. El Oualid, P. Malinconi, Y. Thimont, B. Malard, C. Estournès, N. David, and A. Dauscher. Manufacturing and performances of silicide-based thermoelectric modules. *Energy Conversion and Management*, 242:114304, 2021.

[324] Won Seok Yun, Gi-Beom Cha, and Soon Cheol Hong. The electronic structure and magnetism of gdsi2 by first-principles study. *Journal of Magnetism and Magnetic Materials*, 304(1):e31–e33, 2006. International Symposium on Spintronics and Advanced Magnetic Technologies and International Symposium on Magnetic Materials and Applications 2005.

[325] Ajay Kumar, Prashant Singh, Andrew Doyle, Deborah L. Schlagel, and Yaroslav Mudryk. Multiple magnetic interactions and large inverse magnetocaloric effect in tbsi and $tbsi_{0.6}ge_{0.4}$. *Phys. Rev. B*, 109:214410, Jun 2024.

[326] E. A. Karhu, U. K. Rößler, A. N. Bogdanov, S. Kahwaji, B. J. Kirby, H. Fritzsche, M. D. Robertson, C. F. Majkrzak, and T. L. Monchesky. Chiral modulations and reorientation effects in mnsi thin films. *Phys. Rev. B*, 85:094429, Mar 2012.

[327] Andrey O. Leonov, Ivan M. Tambovtcev, Igor S. Lobanov, and Valery M. Uzdin. Stability of in-plane and out-of-plane chiral skyrmions in epitaxial mnsi(111)/si(111) thin films: Surface twists versus easy-plane anisotropy. *Phys. Rev. B*, 102:174415, Nov 2020.

[328] Xi Fu, Jian Lin, Guangyao Liang, Wenhu Liao, Xiaowu Li, and Liming Li. Density functional theory study of phosphorus silicide monolayers as anodes for lithium-ion batteries and electrocatalysts for co2 reduction. *ACS Applied Nano Materials*, 7(22):26267–26275, 2024.

[329] Xi Fu, Guangyao Liang, Jian Lin, Wenhu Liao, and Liming Li. Research progress on predicting binary nanosheet monolayers using the calypso methodology: Implications for nano-materials, optoelectronics, catalysis and energy science. *Physica B: Condensed Matter*, 721:418039, 2026.

[330] Qisheng Wu, Jun-Jie Zhang, Peipei Hao, Zhongyang Ji, Shuai Dong, Chongyi Ling, Qian Chen, and Jinlan Wang. Versatile titanium silicide monolayers with prominent ferromagnetic, catalytic, and superconducting properties: Theoretical prediction. *The Journal of Physical Chemistry Letters*, 7(19):3723–3729, 2016. PMID: 27603004.

[331] Xiaoli Lan, Linke Yu, Xiaodong Lv, and Fengyu Li. 2d transition-metal silicides as analogs of mxenes: A first-principles exploration. *physica status solidi (RRL)–Rapid Research Letters*, 15(6):2100048, 2021.

[332] C.L. Yeh, W.H. Chen, and C.C. Hsu. Formation of titanium silicides ti5si3 and tisi2 by self-propagating combustion synthesis. *Journal of Alloys and Compounds*, 432(1):90–95, 2007.

[333] Arvind Varma, Alexander S. Rogachev, Alexander S. Mukasyan, and Stephen Hwang. Combustion synthesis of advanced materials: Principles and applications. volume 24 of *Advances in Chemical Engineering*, pages 79–226. Academic Press, 1998.

[334] Sa Zhou, Xiaohua Liu, Yongjing Lin, and Dunwei Wang. Rational synthesis and structural characterizations of complex tisi2 nanostructures. *Chemistry of Materials*, 21(6):1023–1027, 2009.

[335] Leo Miglio, M. Iannuzzi, M.G. Grimaldi, F. La Via, F. Marabelli, S. Bocelli, S. Santucci, and A.R. Phani. Texturing, surface energetics and morphology in the c49–c54 transformation of tisi2. *Solid-State Electronics*, 43(6):1069–1074, 1999.

[336] Catherine Colinet and Jean-Claude Tedenac. Structural stability of intermetallic phases in the si–ti system. point defects and chemical potentials in d88-si3ti5 phase. *Intermetallics*, 18(8):1444–1454, 2010.

[337] P.L. Tam, Y. Cao, and L. Nyborg. Xrd and xps characterisation of transition metal silicide thin films. *Surface Science*, 606(3):329–336, 2012.

[338] Yang Song, Isabel Gómez-Recio, Anissa Ghoridi, Fernando Igoa Saldaña, Daniel Janisch, Capucine Sassoye, Vincent Dupuis, David Hrabovsky, M. Luisa Ruiz-González, José M. González-Calbet, Sandra Casale, Andrea Zitolo, Benedikt Lassalle-Kaiser, Christel Laberty-Robert, and David Portehault. Heterostructured cobalt silicide nanocrystals: Synthesis in molten salts, ferromagnetism, and electrocatalysis. *Journal of the American Chemical Society*, 145(35):19207–19217, 2023. PMID: 37615605.

[339] Omar Abbes, Khalid Hoummada, Dominique Mangelinck, and Véronique Carron. Formation of pt silicide on doped si: Kinetics and stress. *Thin Solid Films*, 542:174–179, 2013.

[340] Vladislav Borisov, Qichen Xu, Nikolaos Ntallis, Rebecca Clulow, Vitalii Shtender, Johan Cedervall, Martin Sahlberg, Kjartan Thor Wikfeldt, Danny Thonig, Manuel Pereiro, Anders Bergman, Anna Delin, and Olle Eriksson. Tuning skyrmions in b20 compounds by $4d$ and $5d$ doping. *Phys. Rev. Mater.*, 6:084401, Aug 2022.

[341] Ke Gu, Yicheng Guan, Binoy Krishna Hazra, Hakan Deniz, Andrea Migliorini, Wenjie Zhang, and Stuart S. P. Parkin. Three-dimensional racetrack memory devices designed from freestanding magnetic heterostructures. *Nature Nanotechnology*, 17(10):1065–1071, 2022.

[342] Giovanni Pizzi, Valerio Vitale, Ryotaro Arita, Stefan Blügel, Frank Freimuth, Guillaume Géranton, Marco Gibertini, Dominik Gresch, Charles Johnson, Takashi Koretsune, et al. Wannier90 as a community code: new features and applications. *Journal of Physics: Condensed Matter*, 32(16):165902, 2020.

[343] Arash A. Mostofi, Jonathan R. Yates, Young-Su Lee, Ivo Souza, David Vanderbilt, and Nicola Marzari. wannier90: A tool for obtaining maximally-localised wannier functions. *Computer Physics Communications*, 178(9):685–699, 2008.

[344] Donguk Jo, Dongwook Go, G. M. Choi, et al. Spintronics meets orbitronics: Emergence of orbital angular momentum in solids. *npj Spintronics*, 2:19, 2024.

[345] Tarik P. Cysne, Luis M. Canonico, Marcio Costa, R. B. Muniz, and Tatiana G. Rappoport. Orbitronics in two-dimensional materials. *npj Spintronics*, 3(1):39, 2025.

[346] S. L. Dudarev, G. A. Botton, S. Y. Savrasov, C. J. Humphreys, and A. P. Sutton. Electron-energy-loss spectra and the structural stability of nickel oxide: An lsda+u study. *Phys. Rev. B*, 57:1505–1509, Jan 1998.

[347] N. Metropolis, A. W. Rosenbluth, M. N. Rosenbluth, A. H. Teller, and E. Teller. Equation of state calculations by fast computing machines. *The Journal of Chemical Physics*, 21(6):1087–1092, 1953.

[348] D. P. Landau and K. Binder. *A Guide to Monte Carlo Simulations in Statistical Physics*. Cambridge University Press, 4 edition, 2014.

[349] JuMag Development Team. Jumag: A julia package for micromagnetic and monte carlo simulations. https://github.com/JuMag/JuMag, 2023. Accessed Month Year.

[350] P. W. Anderson. New approach to the theory of superexchange interactions. *Phys. Rev.*, 115:2–13, Jul 1959.

[351] Dominik Gresch, QuanSheng Wu, Georg W. Winkler, Rico Häuselmann, Matthias Troyer, and Alexey A. Soluyanov. Automated construction of symmetrized wannier-like tight-binding models from ab initio calculations. *Phys. Rev. Mater.*, 2:103805, Oct 2018.

[352] Glenn J. Martyna, Michael L. Klein, and Mark Tuckerman. Nosé–hoover chains: The canonical ensemble via continuous dynamics. *The Journal of Chemical Physics*, 97(4):2635–2643, 1992.

[353] Asadollah Bafekry, Mehmet Yagmurcukardes, Berna Akgenc, Mitra Ghergherehchi, and Bohayra Mortazavi. First-principles investigation of electronic, mechanical and thermoelectric properties of graphene-like xbi (x = si, ge, sn) monolayers. *Phys. Chem. Chem. Phys.*, 23:12471–12478, 2021.

[354] Yan Qian, Haiping Wu, Erjun Kan, and Kaiming Deng. Graphene-like quaternary compound sibcn: A new wide direct band gap semiconductor predicted by a first-principles study. *Europhysics Letters*, 118(1):17002, may 2017.

[355] Tim Matthies, Levente Rózsa, László Szunyogh, Roland Wiesendanger, and Elena Y. Vedmedenko. Interlayer and interfacial dzyaloshinskii-moriya interaction in magnetic trilayers: First-principles calculations. *Phys. Rev. Res.*, 6:043158, Nov 2024.

[356] Vikas Kashid, Timo Schena, Bernd Zimmermann, Yuriy Mokrousov, Stefan Blügel, Vaishali Shah, and H. G. Salunke. Dzyaloshinskii-moriya interaction and chiral magnetism in $3d-5d$ zigzag chains: Tight-binding model and ab initio calculations. *Phys. Rev. B*, 90:054412, Aug 2014.

[357] Junichi Iwasaki, Masahito Mochizuki, and Naoto Nagaosa. Current-induced skyrmion dynamics in constricted geometries. *Nature nanotechnology*, 8(10):742–747, 2013.

[358] Hongxin Yang, Jinghua Liang, and Qirui Cui. First-principles calculations for dzyaloshinskii–moriya interaction. *Nature Reviews Physics*, 5(1):43–61, 2023.